# Study on a test rig of dynamic tyre/road contact forces at the origin of rolling noise

Yuanfang Zhang

UNIVERSITE BRETAGNE LOIRE

Centrale Nantes

# Thèse de Doctorat

Yuanfang ZHANG

*Mémoire présenté en vue de l'obtention*
***du grade de Docteur de l'École Centrale de Nantes***
*sous le sceau de l'Université Bretagne Loire*

**École doctorale : Sciences Pour l'Ingénieur, Géosciences, Architecture**

***Discipline : Sciences pour l'ingénieur***
***Unité de recherche : Institut Français des Sciences et Technologies des Transports, de l'Aménagement et des Réseaux***

**Soutenue le 21 octobre 2016**

# Étude sur banc d'essai des forces de contact dynamique pneumatique/chaussée à l'origine du bruit de roulement

## JURY

| | |
|---|---|
| Président : | **Denis DUHAMEL**, Professeur assimilé, École des Ponts ParisTech, Marne-La-Vallée |
| Rapporteurs : | **Wolfgang KROPP**, Professeur, Chalmers University of Technology, Göteborg (Suède)<br>**Daniel NÉLIAS**, Professeur des universités, INSA de Lyon, Villeurbanne |
| Examinateurs : | **Patrice CARTRAUD**, Professeur des universités, École Centrale de Nantes, GeM, Nantes<br>**Alain LE BOT**, Directeur de recherche, École Centrale de Lyon, Ecully |
| Directeur de thèse : | **Michel BÉRENGIER**, Directeur de recherche, IFSTTAR, Bouguenais |
| Co-directeur de thèse : | **Honoré YIN**, Directeur de recherche, École des Ponts ParisTech, Marne-La-Vallée |
| Co-encadrant de thèse : | **Julien CESBRON**, Chargé de recherche, IFSTTAR, Bouguenais |

**Abstract :** The dynamic contact models for tyre/road noise are often based on a quasi-static assumption and a half-space approximation for the tyre. The aim of the thesis is to assess these assumptions by measuring contact forces on a test rig composed of a smooth reduced-sized tyre rolling on a cylindrical basis. Beforehand, the experimental modal analysis of the tyre allows the identification of eigenmodes of classical shapes. Although a finite element model based on a homogeneous elastic tyre section yields satisfactory modes, a hyper-viscoelastic heterogeneous section provides a good compromise between vibrations and static contact. The dynamic contact force on a single spherical or conical asperity during rolling of the tyre is then measured. The relationship between the maximum force and the height of the asperity is consistent with theoretical contact laws. The contact duration on the asperity is inversely proportional to the speed. The contact calculations based on an elastic half-space assumption lead to a proper estimation of the maximum force measured on high asperity heights, but not on low asperity heights. The dissymmetry of the force time signal is well modelled by introducing the viscoelasticity in the model. The dynamic contact forces measured between the tyre and several asperities of simple shapes confirm the previous results, demonstrating the quasi-static nature of the rolling contact. However, the calculated forces are underestimated at the edges of the contact area, showing a limitation of the half-space assumption to describe the tyre structure.

**Keywords :** dynamic tyre/road contact, modal analysis, viscoelasticity, contact forces measurements, rolling contact, tyre/road test rig, tyre/road noise

**Résumé :** Les modèles de contact dynamique pour le bruit de roulement reposent souvent sur une hypothèse quasi-statique et une approximation de massif semi-infini pour le pneu. L'objectif de la thèse est de vérifier ces hypothèses par la mesure de forces de contact sur un banc d'essai constitué d'un pneu lisse de taille réduite roulant sur un bâti cylindrique. Au préalable, l'analyse modale expérimentale du pneu permet d'identifier des modes propres de formes classiques. Bien qu'un modèle éléments finis basé sur une section de pneu homogène élastique donne des modes satisfaisants, une section hétérogène hyper-viscoélastique permet d'obtenir un bon compromis entre vibrations et contact statique. La force de contact dynamique lors du roulement du pneu sur une seule aspérité sphérique ou conique est ensuite mesurée. La relation entre la force maximale et la hauteur de l'aspérité est conforme aux lois de contact théoriques. La durée de contact sur l'aspérité est inversement proportionnelle à la vitesse. Les calculs de contact basés sur un massif semi-infini élastique permettent d'approcher correctement la force maximale mesurée pour les fortes hauteurs d'aspérités, mais pas pour les faibles. La dissymétrie du signal temporel de force est bien modélisée en introduisant la viscoélasticité dans le modèle. Les forces de contact dynamique mesurées entre le pneu et plusieurs aspérités de formes simples confirment les résultats précédents, démontrant dans l'ensemble la nature quasi-statique du contact roulant. Toutefois, les forces calculées sont sous-estimées sur les bords de l'aire de contact, montrant une limitation de l'hypothèse de massif semi-infini pour décrire la structure du pneu.

**Mots-clés :** contact dynamique pneumatique/chaussée, analyse modale, viscoélasticité, mesures de forces de contact, contact roulant, banc d'essai pneumatique/chaussée, bruit de roulement.

# Acknowledgements

First and foremost, I would like to thank my advisors Michel Bérengier and Honoré Yin and my supervisor Julien Cesbron for always being available and ready to give valuable advice and mentoring throughout the three years of my thesis. They have demonstrated to me the qualities that make a good researcher. It has also been an honour for me to be Michel's very last PhD student.

I am sincerely thankful to Wolfgang Kropp and Daniel Nélias for having spent their precious time to review my thesis and to Denis Duhamel, Patrice Cartraud and Alain Le Bot for their being members of the jury together with the formers.

I thank all the colleagues of the Environmental Acoustics Laboratory of IFSTTAR for their friendliness and support, especially when I encountered difficulties in my life. I am grateful to Judicaël Picaut for having given me various opportunities to attend conferences, seminars and summer schools. My heartfelt thanks go to colleagues whose technical expertise was essential for the successful completion of the thesis: colleagues from the Structures and Integrated Instrumentation Laboratory who helped design and fabricate the test rig; Vincent Gary who collaborated with me in the measurements of forces and accelerations; colleagues from the Advanced Materials for Transportation Infrastructure Laboratory who helped us with the material charaterisation tests; colleagues from École des Ponts ParisTech for the assistance in the experimental modal analysis of the tyre.

I am thankful to IFSTTAR and the Région Pays de la Loire for having jointly funded the thesis and the test rig.

Finally, I thank my parents for giving my life, for educating me to be a righteous person, for encouraging me to pursue my interests especially during all my years abroad. Thank you!

# Table of Contents

# Résumé long en français (Executive summary in French)

## Inroduction

Le trafic routier est la cause de diverses nuisances environnementales, en particulier son émission acoustique. Le bruit de roulement est une source principale du bruit routier, en hausse dans les zones urbaines au cours des dernières décennies. Le contact dynamique entre le pneumatique et la chaussée est un contributeur majeur à des phénomènes tels que les mécanismes vibratoire et aérodynamique à l'origine du bruit pneumatique/chaussée.

Pour réduire le bruit de roulement à la source, il est essentiel de bien comprendre l'interaction pneumatique/chaussée. Il existe des modèles numériques pour prédire les niveaux de force de contact pneumatique/chaussée. Cependant, ces modèles sont souvent basés sur une description quasi-statique du contact dynamique et utilisent une hypothèse de massif semi-infini. Des vérifications expérimentales manquent cependant pour valider ces modèles, puisque l'étude de l'interaction pneumatique/chaussée dans des conditions de laboratoire bien maîtrisées s'avère difficile.

Pour faire face à ce problème, un nouveau banc d'essai a été conçu et fabriqué au Laboratoire d'Acoustique Environnementale de l'IFSTTAR, où le bruit du trafic routier est une préoccupation majeure dans ses activités de recherche depuis de nombreuses années. Ce dispositif permet de mesurer directement les forces de contact dynamiques entre un pneumatique et une ou plusieurs aspérités. Ces mesures serviront à la vérification de la nature quasi-statique du contact, ainsi qu'à l'évaluation des modèles numériques basés sur l'hypothèse de massif semi-infini.

Cette thèse contient 4 chapitres. Le chapitre 1 développe une étude bibliographique qui résume les modèles numériques et les travaux expérimentaux existants. Les principaux objectifs de la thèse sont identifiés à la fin de ce chapitre. Le chapitre 2 justifie le choix d'un pneumatique de taille réduite à utiliser sur le banc d'essai et concerne ensuite la caractérisation vibratoire ainsi que l'analyse du contact statique entre le pneumatique et une surface lisse. Dans le chapitre 3, le banc d'essai est utilisé pour étudier la force de contact dynamique entre le pneumatique de taille réduite et une seule aspérité de forme sphérique ou conique. Suivant une approche similaire au chapitre 3, le chapitre 4 concerne le contact dynamique entre le pneumatique et de multiples aspérités. Dans les deux derniers chapitres, la nature quasi-statique du contact est étudiée pour les deux configurations respectives et l'hypothèse de massif semi-infini est évaluée pour un modèle élastique de contact statique et un modèle viscoélastique de contact avec roulement. Des perspectives sont proposées à la fin de la thèse concernant l'amélioration du modèle dynamique de contact et de l'utilisation du banc d'essai dans le futur.

# Chapitre 1 : étude bibliographique

A partir de 50 km/h, le bruit de contact pneumatique/chaussée est la source prédominante du bruit du trafic routier en conditions de trafic fluide. Son spectre large bande, compris entre 100 Hz et 5000 Hz, est principalement généré par les vibrations radiales du pneumatique en-dessous de 1000 Hz et par le pompage d'air au-delà de 1000 Hz. Ces deux types de sources sont amplifiées par l'effet dièdre. Les mécanismes de génération du bruit de roulement sont fortement influencés par les efforts de contact dynamique entre le pneumatique et la surface de la chaussée. L'étude bibliographique se focalise sur les modèles de contact développés pour la prévision du bruit et sur les études expérimentales menées jusqu'à présent pour leur validation.

Dans un premier temps, les procédures d'enveloppement de profil de texture de chaussée sont rappelées. Bien que basées sur un contact statique, ces dernières permettent l'estimation rapide du bruit de roulement par approche statistique hybride, dont le modèle HyRoNE de l'Ifsttar est un exemple opérationnel.

Les modèles de contact dynamique développés pour la prévision du bruit de roulement sont pour la plupart basés sur une description quasi-statique du contact. En raison de la nature non-linéaire du contact, le problème doit être résolu dans le domaine temporel. Certaines approches couplent les conditions de contact unilatéral avec la réponse impulsionnelle du pneumatique (fonction de Green). Il existe différents modèles vibratoires de pneumatique : plaque orthotrope, structure double couches élastique, modèles éléments finis en guide d'onde ou périodique. La bande de roulement du pneumatique est très souvent approchée par un massif semi-infini élastique qui permet de prendre en compte l'interaction entre les points de contact. La nature multi-échelle des surfaces de chaussée nécessite un traitement préalable pour une résolution efficace du problème, soit par le calcul de raideur de contact non-linéaire à partir des petites échelles de texture (approche de l'université de Chalmers), soit par une décomposition multi-aspérités de la surface de chaussée (approche Ifsttar/ENPC). Cette dernière nécessite également la connaissance des lois de contact locales sur chacune des aspérités. Les forces de contact dynamique calculées sont utilisées pour la prévision du bruit d'origine vibratoire, soit par méthode statistique hybride, soit par méthode physique déterministe.

Pour des conditions de chargement statique, les études expérimentales ont permis de valider les lois de contact ponctuel et l'hypothèse de massif semi-infini pour des configurations simplifiées entre un pavé de gomme et des aspérités sphériques. Les empreintes de contact statique entre un pneumatique et différentes surfaces de chaussée rugueuse ont également permis d'estimer la précision du modèle multi-aspérités de l'Ifsttar. De plus, les mesures de force de contact dynamique en conditions de roulement sur piste, plus difficiles à réaliser, ont montré une diminution de l'ordre de 20 % de l'aire de contact pneumatique/chaussée lors du roulement. Ce phénomène est attribué à la viscoélasticité de la gomme composant le pneumatique. En revanche, les mesures sur piste n'ont pas permis de démontrer clairement le caractère quasi-statique du contact.

Au regard de ce chapitre, la modélisation du contact dynamique pour la prévision du bruit de roulement nécessite des hypothèses simplificatrices dont une partie reste à valider expérimentalement. À cet effet, un banc d'essai spécifique a été développé à l'Ifsttar afin de réaliser des mesures en conditions de laboratoire maîtrisées. À l'aide de cet équipement, les objectifs de la thèse sont d'une part d'étudier l'influence de la vitesse de roulement sur les forces de contact dynamique, incluant l'effet de la vitesse sur l'amplitude des forces de contact et sur les lois de contact local, et d'autre part d'étudier l'interaction entre les aspérités et la distribution des forces de contact dynamique en conditions de roulement.

## Chapitre 2 : Caractérisation du pneumatique de taille réduite intégré au banc d'essai

Afin d'étudier les forces de contact dynamique en conditions de laboratoire maîtrisées, un banc d'essai cylindrique a été développé à l'Ifsttar afin de simuler une surface de chaussée sur laquelle un pneumatique de taille réduite roule. Il s'agit d'un pneumatique de karting de surface lisse et de taille 114/55 R5, soit des dimensions environ réduites de moitié par rapport à un pneumatique de véhicule léger standard. Ce chapitre concerne la caractérisation vibratoire du pneumatique ainsi que l'analyse du contact statique entre le pneumatique et une surface lisse.

Dans un premier temps, l'analyse modale expérimentale du pneu en conditions libres est menée. Une approche SIMO (Single-Input Multiple-Output) classique est utilisée pour les essais. Le pneu est suspendu à l'aide de tendeurs à une structure rigide et excité par un pot vibrant délivrant un signal aléatoire. Les accélérations sont mesurées en plusieurs points à l'aide d'accéléromètres collés à la surface du pneu. Les propriétés de symétrie sont vérifiées et exploitées lors des essais. Trois pressions de gonflage différentes (0, 1 et 2 bars) sont étudiées. Les Fonctions de Réponse en Fréquence (FRF) mesurées sont traitées afin d'extraire les fréquences propres et les taux d'amortissement du pneu. La méthode RFP (Rational Fraction Polynomial) globale est utilisée et consiste à utiliser une fraction rationnelle polynomiale pour identifier les paramètres modaux. Au final, 8 modes propres sont identifiés entre 280 Hz et 1200 Hz. Leur forme est conforme aux résultats de la littérature, de même que l'influence de la pression de gonflage est retrouvée. L'accord entre FRF mesurées et synthétisées est bon, aussi bien au point d'excitation qu'aux points de transfert.

Une modélisation par éléments finis sous Abaqus est ensuite proposée pour l'analyse modale du pneu. Plusieurs degrés de complexité sont testés pour la structure interne du pneu : section composée d'un matériau homogène élastique, puis viscoélastique, avant de terminer par une section hétérogène constituée d'une bande de roulement viscoélastique et de couches de nylon constituant la ceinture du pneu. Dans le cas homogène élastique, un bon accord avec les résultats expérimentaux est obtenu, mais d'une part l'amortissement expérimental doit être utilisé pour calculer les FRF et d'autre part le modèle, trop rigide, sous-estime l'empreinte de contact statique. Le modèle homogène viscoélastique permet d'intégrer la dissipation intrinsèque à la gomme en se basant sur une série de Prony identifiée à partir du module complexe mesuré sur visco-analyseur. Les taux d'amortissement sont alors conformes à l'expérience mais, la structure devenant moins rigide, les fréquences propres sont décalées vers les basses fréquences. L'introduction des couches de nylon dans le modèle hétérogène permet de compenser cet effet et donne des FRF proches de l'expérience. De plus, l'ajout de l'hyper-viscoélasticité permet d'obtenir une empreinte de contact conforme aux mesures.

La dernière partie du chapitre s'intéresse au contact statique entre le pneu et une surface lisse. Les mesures d'empreinte au papier Fuji sur une plaque montrent une diminution de l'aire de contact totale lorsque la pression de gonflage du pneu augmente. L'aire de contact augmente avec la charge totale appliquée, en raison d'une augmentation de la largeur de l'empreinte dans le sens longitudinal (la dimension transversale varie peu). La Méthode d'Inversion de Matrice (MIM), basée sur une hypothèse de massif semi-infini, est ensuite optimisée en exploitant les symétries des géométries en contact. Les résultats de la MIM montrent qu'il est possible d'obtenir des empreintes de contact similaires à l'expérience en adaptant convenablement le module élastique pour chaque configuration. Enfin, des mesures de contact statique sont effectuées sur le bâti cylindrique du banc d'essai. La courbure de ce dernier influence peu les aires de contact dont la dimension longitudinale diminue toujours lorsque la charge totale augmente. Le contact est également mesuré

après avoir atteint une température stabilisée de la gomme pour différentes vitesse de roulement (5, 10 et 15 m/s). Les aires de contact diminuent légèrement avec la vitesse, démontrant une diminution du module élastique de la gomme avec la température (effet viscoélastique).

## Chapitre 3 : Contact dynamique avec une seule aspérité

Dans ce chapitre, le banc d'essai est utilisé pour étudier la force de contact dynamique entre le pneumatique de taille réduite et une seule aspérité de forme sphérique ou conique. Les essais sont réalisés en conditions de roulement. La force de contact dynamique est mesurée à l'aide d'un capteur de force piezo-électrique intégré au bâti cylindrique du banc d'essai, sans l'ajout de papier ou de capteur de pression à l'interface de contact. L'aspérité consiste en un embout de forme sphérique ou conique vissé à la surface du capteur de force dont la hauteur est variable et connue avec précision à l'aide d'une mesure par capteur à faisceau laser. La répétabilité des essais est évaluée à partir de 100 impacts successifs à une même vitesse de roulement. En prenant garde de bien respecter le temps de chauffe du pneumatique, les résultats sont satisfaisants aussi bien pour les signaux temporels que pour le maximum de la force de contact.

Les résultats expérimentaux sont ensuite présentés en s'intéressant à différents paramètres. Dans un premier temps, l'influence de la géométrie de l'aspérité sur la force de contact dynamique est étudiée. À hauteur équivalente, la force de contact sur la sphère est plus élevée que sur le cone mais l'allure des signaux temporels est très similaire et les durées de contact sont très proches. L'analyse spectrale de la force d'impact donne des résultats proches de ceux pour un demi-sinus, à savoir un spectre plat jusqu'à une fréquence critique égale à l'inverse de la durée de contact, puis des pics d'amplitude décroissante aux harmoniques de cette fréquence. La relation entre la force de contact maximale et la hauteur de l'aspérité est étudiée pour les deux géométries. Moyennant un recalage du module élastique, les courbes expérimentales sont cohérentes avec les lois de puissance analytiques issues de la théorie de Boussinesq. L'influence de la charge totale sur la force de contact dynamique est ensuite étudiée. L'amplitude maximale de la force diminue lorsque la charge augmente, alors que la durée de contact diminue avec la charge, ce qui est cohérent avec les empreintes de contact mesurées en statique. Enfin, l'influence de la vitesse de roulement sur la force de contact est analysée. Il apparaît que la durée de contact est inversement proportionnelle à la vitesse et que les spectres aux différentes vitesses, modifiés en fréquence, coïncident jusqu'à 350 Hz. Ces résultats illustrent la nature quasi-statique du contact dynamique sur une seule aspérité.

Dans la dernière partie du chapitre, la Méthode d'Inversion de Matrice (MIM) basée sur l'hypothèse de massif semi-infini est confrontée aux résultats expérimentaux. Le modèle élastique est premièrement testé. Des empreintes de contact statique sont calculées pour différentes hauteurs d'aspérité puis la force de contact locale sur l'aspérité est comparée aux résultats expérimentaux. Moyennant un recalage du module d'Young, le modèle élastique permet d'approcher la force maximale mesurée pour les fortes hauteurs, mais l'erreur est plus élevée pour les faibles hauteurs, notamment lorsque la charge totale appliquée augmente. La comparaison avec des empreintes de contact, mesurées en statique à l'aide de papier Fuji, indique que le problème pourrait être dû à une sous-estimation des pressions de contact au niveau des flancs du pneumatique, comme déjà observé au chapitre 2. Le fait que la force de contact maximale sur l'aspérité soit plus élevée pour une charge totale plus faible est ensuite expliqué par une effet thermo-rhéologique de la gomme constituant le pneumatique. En effet, lorsque la charge augmente, la température de la gomme lors du roulement augmente et cette dernière devient moins rigide de par ses propriétés viscoélastiques. Un module d'Young adapté à chaque charge permet d'approcher ces résultats à l'aide du modèle

élastique. Des calculs temporels quasi-statiques montrent clairement que la MIM élastique ne permet pas de retrouver la dissymétrie temporelle du signal de force mesuré. Cette dissymétrie est attribuée à la viscoélasticité de la gomme qui est alors introduite dans le modèle.

Après un rappel des relations constitutives entre contrainte et déplacement pour un matériau viscoélastique, le problème de contact avec roulement est formulé puis discrétisé afin d'appliquer la MIM dans le cas viscoélastique. Les calculs de la force de contact temporelle sont effectués en utilisant un modèle simplifié de Zener. Le modèle permet d'obtenir des signaux temporels dissymétriques par rapport au maximum de la force de contact, ce qui est conforme aux résultats expérimentaux. En recalant convenablement le module long-terme et le temps caractéristique du modèle de Zener, la MIM donne des résultats en très bon accord avec l'expérience pour une charge totale de 500 N et une hauteur d'aspérité élevée. L'accord essai/calcul est cependant moins bon pour les faibles hauteurs d'aspérité, comme dans le cas élastique. Pour une charge totale de 1000 N, le modèle donne des résultats satisfaisants, mais la durée de contact est sous-estimée, donnant une incertitude plus importante par rapport à l'expérience. Cet écart pourrait être réduit en utilisant un modèle de Kelvin généralisé à la place du modèle de Zener. Il pourrait aussi s'agir d'un effet des flancs du pneumatique ou de l'hyperélasticité, plus marqués lorsque la charge totale augmente et non pris en compte dans le modèle de contact basé sur une hypothèse de massif semi-infini.

## Chapitre 4 : Contact dynamique avec plusieurs aspérités

Dans ce dernier chapitre, le banc d'essai est utilisé pour étudier les forces de contact dynamique entre le pneumatique de taille réduite et plusieurs aspérités de forme sphérique ou conique. Les essais sont réalisés en conditions de roulement. Comme au chapitre précédent, les forces de contact dynamique sont mesurées à l'aide d'un ensemble de capteurs de force piezo-électriques intégrés au bâti cylindrique du banc d'essai. Toutes les aspérités sont situées à la même hauteur, qui est contrôlée avec précision à l'aide d'une mesure par capteur à faisceau laser. La répétabilité des essais sur chaque aspérité est vérifiée à partir de 100 impacts successifs à une même vitesse de roulement. La symétrie des forces de contact par rapport à l'axe de roulement n'est pas parfaitement vérifiée en raison de défauts de montage du système et de l'apparition de forces de contact négatives sur certaines aspérités, dont l'origine reste à expliquer.

Les résultats expérimentaux sont ensuite présentés en s'intéressant à différents paramètres. Dans un premier temps, l'influence de la géométrie de l'aspérité sur la distribution des forces de contact dynamique est étudiée. Comme au chapitre 3, à hauteur équivalente, les forces de contact sur les sphères sont plus élevées que sur les cônes mais l'allure des signaux temporels est similaire et les durées de contact sont proches. L'influence de la charge totale sur la distribution des forces de contact dynamique est ensuite étudiée. La durée de contact augmente avec la charge totale, ce qui est cohérent avec la configuration d'une seule aspérité. Cependant, bien que l'évolution temporelle de la force de contact soit dissymétrique, le temps nécessaire pour atteindre la force maximale sur une aspérité est presque le même pour toutes les charges testées. Enfin, l'influence de la vitesse de roulement sur la force de contact est analysée. La nature quasi-statique du contact dynamique sur plusieurs aspérités est ainsi vérifiée par le fait que la durée de contact est inversement proportionnelle à la vitesse de roulement.

Dans la dernière partie du chapitre, la Méthode d'Inversion de Matrice (MIM) basée sur l'hypothèse de massif semi-infini est confrontée aux résultats expérimentaux. Le modèle élastique est premièrement testé en utilisant les modules d'Young recalés au chapitre précédent. Des empreintes de contact statique sont calculées pour différentes charges totales sur le pneumatique

puis comparées aux empreintes mesurées à l'aide de papier Fuji. Les dimensions des empreintes et les aires de contact sur les aspérités sont assez bien estimées. Enfin, le problème de contact multi-aspérités avec roulement est résolu dans le cas viscoélastique en employant un modèle de Zener avec les mêmes paramètres recalés pour le contact avec une seule aspérité. L'accord essai/-calcul est meilleur pour les aspérités qui ont moins d'interactions avec les fortes concentrations de pressions de contact au niveau des flancs du pneumatique. Il pourrait aussi s'agir d'un effet des flancs et d'une limitation de l'hypothèse de massif semi-infini. Néanmoins, la dissymétrie des signaux temporels est bien estimée dans cette approche, ce qui est physiquement représentatif de l'interaction pneumatique/chaussée en conditions de roulement.

## Conclusions et perspectives

Au préalable, l'analyse modale expérimentale du pneu permet d'identifier des modes propres de formes classiques. Bien qu'un modèle éléments finis basé sur une section de pneu homogène élastique donne des modes satisfaisants, une section hétérogène hyper-viscoélastique permet d'obtenir un bon compromis entre vibrations et contact statique. La force de contact dynamique lors du roulement du pneu sur une seule aspérité sphérique ou conique est ensuite mesurée. La relation entre la force maximale et la hauteur de l'aspérité est conforme aux lois de contact théoriques. La durée de contact sur l'aspérité est inversement proportionnelle à la vitesse. Les calculs de contact basés sur un massif semi-infini élastique permettent d'approcher correctement la force maximale mesurée pour les fortes hauteurs d'aspérités, mais pas pour les faibles. La dissymétrie du signal temporel de force est bien modélisée en introduisant la viscoélasticité dans le modèle. Les forces de contact dynamique mesurées entre le pneu et plusieurs aspérités de formes simples confirment les résultats précédents, démontrant dans l'ensemble la nature quasi-statique du contact roulant. Toutefois, les forces calculées sont sous-estimées sur les bords de l'aire de contact, montrant une limitation de l'hypothèse de massif semi-infini pour décrire la structure du pneu.

Compte tenu du travail qui a été effectué au cours de la thèse, les aspects suivants pourraient être étudiés pour améliorer le modèle de contact dynamique :

- utiliser le modèle par éléments finis du pneumatique de taille réduite pour calculer la matrice d'influence utilisée dans le calcul de contact en remplacement de la matrice analytique basée sur l'hypothèse de massif semi-infini ;
- utiliser une fonction de fluage basée sur le modèle de Kelvin généralisé à la place du modèle de Zener pour améliorer la description de la viscoélasticité dans le modèle et améliorer l'accord entre les signaux temporels calculés et mesurés ;
- effectuer des mesures sur le banc d'essai pour une et plusieurs aspérités de formes aléatoires afin de valider l'approche multi-aspérités pour les surfaces de chaussées réelles ;
- effectuer des mesures dans des conditions plus réalistes à l'échelle d'un pneumatique de véhicule léger.

En outre, le banc d'essai ouvre plusieurs perspectives dans le domaine de l'interaction pneumatique/chaussée, parmi lesquels l'étude du mécanisme d'air-pumping dans des configurations simplifiées, la mesure du bruit ou la résistance au roulement en laboratoire pour le recalage des outils de prévision et la recherche académique pour l'optimisation acoustique des propriétés de texture de chaussée.

# Introduction

Road traffic is responsible for various environmental issues, especially road noise emission from an acoustical point of view. Tyre/road noise is a main cause of the increasing road noise exposure in urban areas over the last decades [EEA, 2014, Fritschi et al., 2011]. In particular, for passenger cars rolling at over 50 km/h, it dominates among all the road noise sources [Sandberg, 2001]. The dynamic contact between rolling tyres and road asperities is a major contributor to phenomena such as the vibrational and aerodynamic mechanisms at the origin of tyre/road noise.

To reduce rolling noise from sources, it is essential to understand tyre/road interaction in a proper way. There exist numerical models for predicting tyre/road contact force levels or even noise levels. However, quite often, these models are based on a quasi-static description of the dynamic contact and use an elastic or viscoelastic half-space assumption. The applicability of these assumptions lacks experimental verification, since experimental investigation of tyre/road interaction under well-controlled laboratory conditions remains a challenging task despite previous efforts.

To tackle this problem, a novel test rig has been designed and fabricated at the Environmental Acoustics Laboratory of IFSTTAR, where road traffic noise has been a major concern of the research for a long time. This apparatus allows direct measurements, without interfacial layer, of the dynamic contact forces between a tyre and a single asperity or multiples ones to be performed. These measurements will provide necessary elements for verifying the quasi-static nature of the contact and also for assessing numerical models in terms of the half-space assumption.

This thesis is divided into 4 chapters. Chapter 1 is a literature review which will first briefly describe the noise generation mechanisms. After that, existing models, as well as experimental set-ups and outcomes in laboratories, will be summarised. Following these surveys, the main aims of the thesis will be identified at the end of this chapter. For the sake of simplicity, a reduced-sized tyre is chosen to be used on the test rig. Chapter 2 involves the characterisation of the dynamic and the contact behaviours of the tyre. A modal analysis is carried out to investigate the vibrational nature of the tyre structure, and the materials properties of the tread rubber are also measured. A finite-element model is then built as a reference method that offers a good compromise between the modal frequencies and the contact patch. A static contact analysis is conducted to study the influence of various parameters on the contact area and to calibrate a numerical model based on the elastic half-space assumption. In Chapter 3, the test rig is used to investigate the contact force between the tyre and a single asperity of simple geometric shape under rolling conditions. The experimental set-up is presented and the measurement repeatability is verified. Tests are performed to study the influences of different parameters on the peak contact force, such as the geometric shape of indenter, the asperity height, the total load on the tyre and the rolling speed. Then, the experimental results are used to assess numerical models, namely an elastic model for static contact comparisons and a viscoelastic model for the rolling contact analysis. Similar to Chapter 3, Chapter 4 deals with the dynamic contact between the tyre and multiple asperities.

In addition to parametric studies, this chapter also focusses on the interaction between asperities. Finally, numerical models based on the elastic or viscoelastic half-space assumption are assessed in the case of the multiple asperities. Concluding remarks are then given on the verification of the quasi-static nature of the contact and the performance of the half-space assumption. Outlooks are also proposed with respect to the improvement of the dynamic contact model and to the future utility of the test rig.

# Chapitre 1 : Étude bibliographique

A partir de 50 km/h, le bruit de contact pneumatique/chaussée est la source prédominante du bruit du trafic routier en conditions de trafic fluide. Son spectre large bande, compris entre 100 Hz et 5000 Hz, est principalement généré par les vibrations radiales du pneumatique en-dessous de 1000 Hz et par le pompage d'air au-delà de 1000 Hz. Ces deux types de sources sont amplifiées par l'effet dièdre. Les mécanismes de génération du bruit de roulement sont fortement influencés par les efforts de contact dynamique entre le pneumatique et la surface de la chaussée. L'étude bibliographique se focalise sur les modèles de contact développés pour la prévision du bruit et sur les études expérimentales menées jusqu'à présent pour leur validation.

Dans un premier temps, les procédures d'enveloppement de profil de texture de chaussée sont rappelées. Bien que basées sur un contact statique, ces dernières permettent l'estimation rapide du bruit de roulement par approche statistique hybride, dont le modèle HyRoNE de l'Ifsttar est un exemple opérationnel.

Les modèles de contact dynamique développés pour la prévision du bruit de roulement sont pour la plupart basés sur une description quasi-statique du contact. En raison de la nature non-linéaire du contact, le problème doit être résolu dans le domaine temporel. Certaines approches couplent les conditions de contact unilatéral avec la réponse impulsionnelle du pneumatique (fonction de Green). Il existe différents modèles vibratoires de pneumatique : plaque orthotrope, structure double couches élastique, modèles éléments finis en guide d'onde ou périodique. La bande de roulement du pneumatique est très souvent approchée par un massif semi-infini élastique qui permet de prendre en compte l'interaction entre les points de contact. La nature multi-échelle des surfaces de chaussée nécessite un traitement préalable pour une résolution efficace du problème, soit par le calcul de raideur de contact non-linéaire à partir des petites échelles de texture (approche de l'université de Chalmers), soit par une décomposition multi-aspérités de la surface de chaussée (approche Ifsttar/ENPC). Cette dernière nécessite également la connaissance des lois de contact locales sur chacune des aspérités. Les forces de contact dynamique calculées sont utilisées pour la prévision du bruit d'origine vibratoire, soit par méthode statistique hybride, soit par méthode physique déterministe.

Pour des conditions de chargement statique, les études expérimentales ont permis de valider les lois de contact ponctuel et l'hypothèse de massif semi-infini pour des configurations simplifiées entre un pavé de gomme et des aspérités sphériques. Les empreintes de contact statique entre un pneumatique et différentes surfaces de chaussée rugueuse ont également permis d'estimer la précision du modèle multi-aspérités de l'Ifsttar. De plus, les mesures de force de contact dynamique en conditions de roulement sur piste, plus difficiles à réaliser, ont montré une diminution de l'ordre de 20 % de l'aire de contact pneumatique/chaussée lors du roulement. Ce phénomène est attribué à la viscoélasticité de la gomme composant le pneumatique. En revanche, les mesures sur piste n'ont pas permis de démontrer clairement le caractère quasi-statique du contact.

Au regard de ce chapitre, la modélisation du contact dynamique pour la prévision du bruit de roulement nécessite des hypothèses simplificatrices dont une partie reste à valider expérimentalement. À cet effet, un banc d'essai spécifique a été développé à l'Ifsttar afin de réaliser des mesures en conditions de laboratoire maîtrisées. À l'aide de cet équipement, les objectifs de la thèse sont d'une part d'étudier l'influence de la vitesse de roulement sur les forces de contact dynamique, incluant l'effet de la vitesse sur l'amplitude des forces de contact et sur les lois de contact local, et d'autre part d'étudier l'interaction entre les aspérités et la distribution des forces de contact dynamique en conditions de roulement.

# Chapter 1

# Literature review

People are getting more exposed to road traffic noise in urban areas over the last decades. Tyre/road noise is a major contributor to this environmental issue. In particular, for passenger cars rolling at over 50 km/h, it dominates among all the road noise sources [Sandberg, 2001].

Various models have been established using different theories and analysing different aspects of noise generation, with the final aim to predict the tyre/road noise and to control the noise emission by, for instance, optimizing road surface structures. These aspects include a thorough understanding of pressure distribution over the tyre/road contact patch and its correlation with noise, tyre's structure-borne noise radiation, horn effect amplification as well as aerodynamic issues, namely air-pumping, Helmholtz resonance and pipe resonance.

The present literature review will first briefly describe the aforementioned noise generation mechanisms. After that, existing models, as well as experimental set-ups and outcomes in laboratories, will be summarised in two sections. The final section will identify and discuss areas yet to be explored, explaining why the work of the present thesis is of special scientific interest.

## 1.1 Noise generation mechanisms

Rolling noise is generated by different sources located separately around the tyre at various frequency ranges. Meanwhile, most generation mechanisms can be classified into 3 main categories: structural, aerodynamic and amplification effects. Understanding these aspects helps diagnose the most critical research challenges.

### 1.1.1 Sources of rolling noise

Generally speaking, for a passenger car under the cruise-by condition, i.e. a constant rolling speed above 50 km/h, rolling noise is stated to be a wide-band noise ranging from 100 Hz to 5000 Hz. The maximum of acoustic energy is usually situated between 700 Hz and 1500 Hz.

Iwao and Yamazaki [1996] distinguished four main sources of tyre/road noise, as shown in Figure 1.1, based on measurements carried out on a car rolling at 50 km/h. The first-order frequency component of the tread pattern, included between 400 Hz and 600 Hz, is radiated by the sidewall. Two zones very near the contact patch on each side, the leading edge and the trailing edge, generate noise from 500 to 2 kHz, covering the second-order component. The last source is

the resonance phenomenon due to the upper part of the wheel housing and radiates noise between 500 Hz and 600 Hz. In practice, rolling noise is reduced by treating physical processes from which it arises.

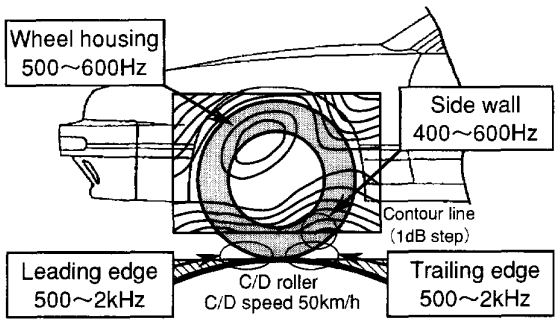


Figure 1.1 – Contour map of sound intensity level in the case of a car tyre rolling on a chassis dynamometer drum [Iwao and Yamazaki, 1996].

### 1.1.2 Mechanisms of noise generation

Rolling noise is due to a combination of complex physical phenomena that go into two categories: mechanical or structural mechanisms and aerodynamic mechanisms. Additional amplification effects are not to be ignored as well.

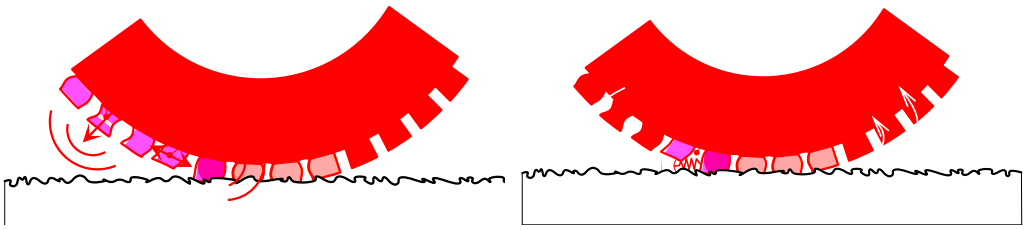

(a) Mechanical mechanisms (b) Aerodynamic Mechanisms

Figure 1.2 – Mechanisms of noise generation [Kuijpers and van Blokland, 2001].

Mechanical mechanisms (Figure 1.2a) mainly include radial and tangential vibrations, stick-slip and stick-snap effects. The most common aerodynamic noise sources (Figure 1.2b) are air-pumping, Helmholtz resonances and pipe resonances. The generated noise is then amplified by the multiple reflections within the tyre horn, named the horn effect.

### 1.1.3 Frequency ranges and speed exponents for the mechanisms

According to Kuijpers and van Blokland [2001], each mechanism is associated with a speed exponent $k$ and influences particularly a specific frequency range. Figure 1.3 summarises speed exponents and frequency ranges for major mechanisms. The sound level $L_p$ can be related to the so-called speed exponent $k$ with the following mathematical expression:

$$L_p \sim 10log(v/v_0)^k[dB] = 10klog(v/v_0)[dB] \tag{1.1}$$

Radial vibration of tyre is the main noise source at frequencies below 1 kHz while airflow related noise are dominant at frequencies above 1 kHz.

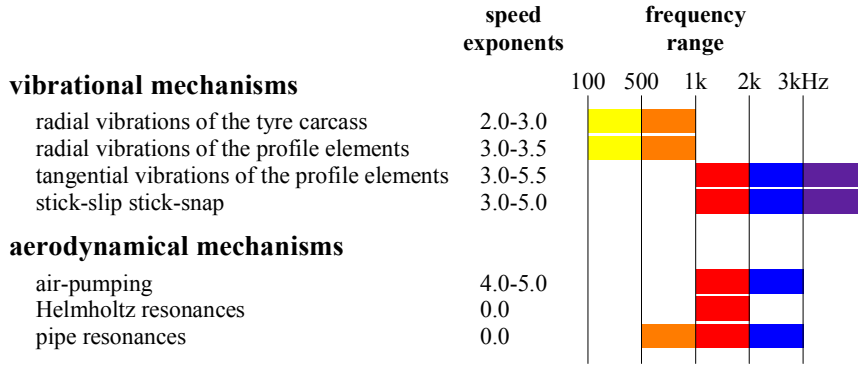


Figure 1.3 – Overview of speed exponents and frequency ranges for tyre/road noise generation mechanisms [Kuijpers and van Blokland, 2001].

## 1.2 Existing tyre/road contact models for rolling noise prediction

Facing the complexity of the whole problem, a number of theoretical models, taking into account one or several of the aforementioned aspects, have been proposed. These models are either physical or statistical (empirical or hybrid) with regard to how relationships between noise and influential factors, such as tyre tread patterns and road textures, are analysed. Deterministic physical models involve simplified yet reasonable approaches of the real physical problem to reduce the time of calculation while trying to retain a good approximation of the noise generation procedure. Statistical empirical models, on the contrary, bypass the physical mechanisms and seek directly the link between noise and parameters to be optimised for noise reduction, which are, most often, the road textures. Statistical hybrid models combine both physical models and statistical data to relate physical variables to noise measurement results. This section focuses on tyre/road contact models and how they can be used to assess rolling noise.

### 1.2.1 Envelopment procedures for hybrid models

Envelopment procedures are applied to determining the static contact pressure distribution of a tyre on a pavement and the corresponding rubber displacement when given the tyre's Young's modulus. The contact pressure tends to infinity at the edges limiting a profile with a finite length along the contact surface, represented in two dimensions [Johnson, 1985]. This problem is known as the edge effect. The word "envelopment" refers to methods aiming at omitting the boundary discontinuities. Accurate tyre/road noise prediction requires realistic modelling of the tyre deformation on texture profiles. Several methods have been proposed to this purpose and are either empirical or physical.

An empirical method by von Meier et al. [1992] is based on the idea of limiting the second-order derivative of texture profile. The envelopment profile thus obtained can then be correlated with noise. This procedure, however, is a purely statistical approach and does not involve the contact problem.

One physical method came from Clapp et al. [1988]. It deals with the classical contact mechanics problem in two dimensions between a rigid body (also called an indenter) subjected to normal loading and an elastic half-plane characterised by its Young's modulus $E$ and Poisson's ratio $\nu$, assumed to be equal to 0.5 [Johnson, 1985]. A third-order polynomial $u(x)$ is used to describe the vertical displacement of the tyre tread, from which the pressure distribution $p(x)$ can be determined. Digitised road surface texture data and an equilibrium pressure are used as input parameters. The computational algorithm then returns output information, including the deformed tyre geometry and the contact pressure distribution.

Another physical approach has been developed at the former INRETS by Klein and Hamet [2004] within the SILVIA research project. Similar to Clapp's model, this static approach evaluates the pressure distribution $p(x)$ on the contact area and the rubber displacement function $u(x)$ of the tyre tread. This model differs from the previous one since the road surface is discretised into elements of equal length $L$ and of height $z$ which is a continuous function of the longitudinal position $x$. The vertical displacement $\delta u$ at the contact interface of an elastic body due to a concentrated normal force $\delta F$ exerted at the origin is described as follows:

$$\delta u(x) = -\frac{2(1-\nu^2)}{\pi E} ln|x|\delta F + c, \tag{1.2}$$

where $c$ is an unknown constant. The global displacement function $u(x)$ for all points at the contact surface is expressed with help of a Green's function $g(x,\xi)$:

$$u(x) = \int_{\Gamma_c} g(x,\xi)p(\xi)\,\mathrm{d}\xi + c', \tag{1.3}$$

where $\Gamma_c$ is the contact area, $p(x)$ the pressure distribution function, $c'$ an unknown constant and $g(x,\xi)$ the Green's function defined as follows:

$$g(x,\xi) = -\frac{2(1-\nu^2)}{\pi E} ln|x-\xi|. \tag{1.4}$$

Discretisation of the contact surface results in an extreme overestimate at the boundaries (the so-called edge effect) and a slight underestimate in the middle in terms of pressure distribution, shown in Figure 1.4.

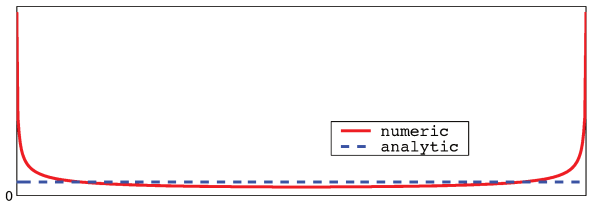


Figure 1.4 – Pressure distribution for a smooth plane profile [Klein and Hamet, 2004].

To omit the boundary conditions, the solution proposed is to repeat the same road texture infinitely. This can be mathematically interpreted by summing all influence functions shifted with a phase difference of multiple of $L$ to obtain a new function $G(x,\xi)$:

$$G(x,\xi) = \sum_{n=-\infty}^{+\infty} g(x,\xi - nL). \tag{1.5}$$

Knowing the vertical displacement $u(x_0)$ of a reference position $x_0$, $c'$ disappears from the following new equation:

$$u(x) - u(x_0) = \int_{\Gamma_c} [G(x,\xi) - G(x_0,\xi)]p(\xi)\,\mathrm{d}\xi. \tag{1.6}$$

At all contact points, the pressure should be positive. Also should the equilibrium condition be checked:

$$p_m = \frac{1}{L}\int_{\Gamma} p(x)\,\mathrm{d}x. \tag{1.7}$$

This approach requires two parameters, the Poisson's ratio $\nu$ and the rubber Young's modulus $E$. In fact, the latter has a significant impact on the penetration of road texture into the tyre, thus on the deformed tyre geometry and the pressure distribution. As the Young's modulus decreases, the penetration depth and contact area increase and the pressure distribution curve becomes smoother. Examples are shown in Figure 1.5.

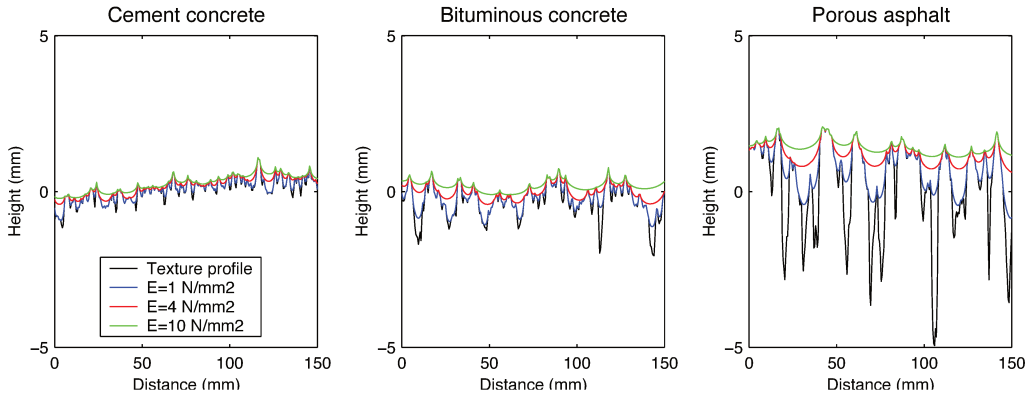


Figure 1.5 – Enveloped profiles for three road pavements and different values of Young's modulus [Klein and Hamet, 2004].

Envelopment methods are generally unsophisticated and not very time-consuming in terms of assessment of enveloped texture/noise relationships.

The INRETS 2D envelopment procedure is used in a hybrid model named HyRoNE (Hybrid Rolling Noise Estimation) whose structure is illustrated in Figure 1.6. This model developed at the French research institute IFSTTAR within the French PREDIT project Texture&Bruit and the French-German joint DEUFRAKO research project P2RN (Prediction and Propagation of Rolling Noise) includes in particular the noise attenuation aspect for porous pavements [Beckenbauer et al., 2008]. This feature requires absorption properties to be defined as input data using an absorption model specially dedicated to this issue, developed by Hamet and Bérengier [1993]. A 2D road texture description is sufficient for this model. The HyRoNE model is limited to predicting noise for three nominal speeds: 70 km/h, 90 km/h and 110 km/h.

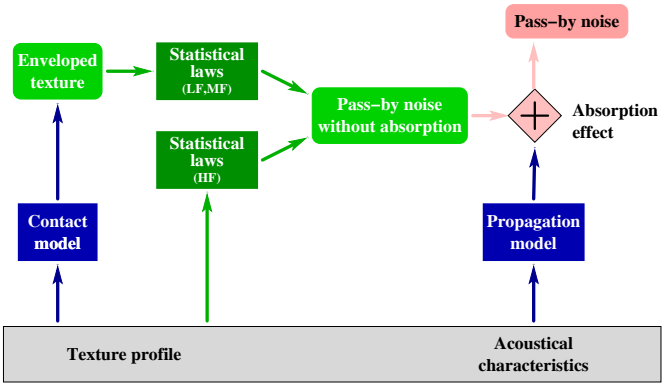


Figure 1.6 – HyRoNE structure [Beckenbauer et al., 2008].

Two rolling noise generation mechanisms, namely radial vibrations and air-pumping, are treated separately in the frequency ranges they predominate: 100 Hz to 1250 Hz for radial vibrations and 1250 Hz to 5 kHz for air-pumping. The INRETS static tyre envelopment model analyses the partial tyre/road contact. The statistical sub-model uses linear relations between contact forces and sound pressures and calculates the global pass-by noise levels in one-third octave bands. The noise absorption effect is then integrated and corrected to provide the final predicted noise level. The HyRoNE model handles only a limited numbers of road surface types and of rolling speeds, as well as one specific type of tyre.

### 1.2.2 Contact models developed at Chalmers University of Technology (Sweden)

Several models have been developed at Chalmers University in Sweden during a series of PhD theses. Based on an approach proposed by Kropp [1992], the tyre/road contact problem has been progressively modelled in a more realistic way by step-wise incorporation of previously unconsidered phenomena. The models are used either in hybrid approach (SPERoN model) or in deterministic physical models for rolling noise prediction.

#### 1.2.2.1 Kropp's model

Kropp [1992] first came up with a 2-D contact model based on which the following models are developed. For frequencies above 400 Hz, the curvature of tyre has little influence on structure-borne rolling noise and can hence be neglected, as the wavelengths are no longer significant compared with the radius of curvature. According to this observation, Kropp proposed to represent the tyre with an orthotropic plate using a Winkler bedding (elastic foundation) for modelling the contact between the rubber and the road surface. Nevertheless, tangential forces are not taken into account and the contact force is assumed to be uniformly distributed over the width of the rolling band.

The contact problem is to identify the radial contact force $F_e(\varphi_e, t)$ at point $e$ in the time domain. By dividing the rolling band into discrete elements along its circumference, the position of each point $e$ can be characterised by the angle $\varphi_e$ between the radius passing through it and the vertical direction. The contact force is a function of the tyre tread compression $\Delta y_e(t)$. The latter is given by the following equation:

$$\Delta y_e(t) = y_0(t) + k_{10}(\varphi_e, t) + \xi_e(\varphi_e, t) - k_2(\varphi_e, t) \tag{1.8}$$

where $y_0(t)$ is the position of the rim center, $k_{10}(\varphi_e, t)$ the contour of the undeformed tyre, $\xi_e(\varphi_e, t)$ the vibration of tyre belt and $k_2(\varphi_e, t)$ the roughness of the road surface as illustrated in Figure 1.7.

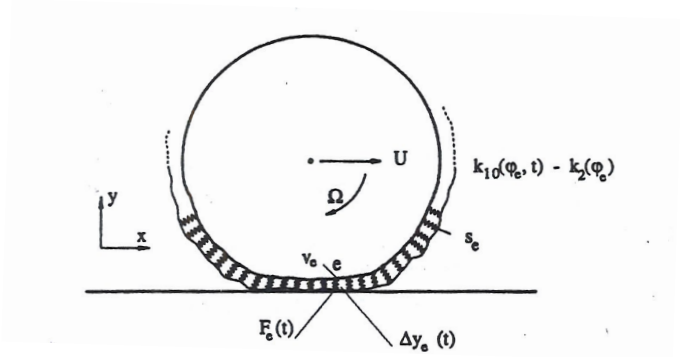


Figure 1.7 – Winkler bedding model for the tyre/road contact [Kropp, 1992].

As the contact configuration varies from one point to another and therefore leads to a non-linear contact problem, the use of a Winkler bedding [Johnson, 1985] allows the calculation time to be reduced. The contact between rolling band and road surface is modelled by a series of isolated, uncoupled springs, as shown in Figure 1.7. The contact force $F_e(\varphi_e, t)$ exerted at point $e$ by a spring of stiffness $s_e$ is described as follows:

$$F_e(\varphi_e, t) = s_e \Delta y_e(t) H(\Delta y_e(t)) \tag{1.9}$$

where $H$ is the Heaviside function which retains only positive values since $F_e(\varphi_e, t)$ exists only when contact occurs and the spring is compressed.

The deformation of the tyre belt $\xi_e(\varphi_e, t)$ at point $e$ is calculated thanks to an orthotropic plate model supported by an elastic foundation. The latter, illustrated in Figure 1.8, represents the interior pressure of the tyre and the contribution of the side walls to the radial stiffness. The plate under tension lying on this elastic foundation is orthotropic, i.e. the bending stiffnesses are different along circumferential and lateral directions.

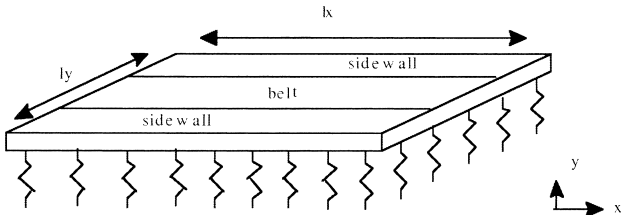


Figure 1.8 – Model of an orthotropic plate representing the belt of a tyre [Kropp, 1992].

The impulse response or the Green's function $g$ of an orthotropic plate can either be evaluated first in the frequency domain then transferred into the time domain with help of a Fast Fourier Transform [Kropp, 1992] or directly in the time domain [Hamet, 2001]. The following equation

expresses the convolution of the contact forces $F_e$ and the impulse response functions $g$ that describes $\xi_e$:

$$\xi_e(t) = \sum_m F_m(t) * g_{m,e}(t) = \sum_m \int_0^t F_m(\tau) g_{m,e}(t-\tau) d\tau \tag{1.10}$$

The system composed of equations (1.8), (1.9) and (1.10) defines the non-linear contact problem to be solved in the time domain. The resolution can be achieved by using the Newton-Raphson iterative scheme.

This model has been extended to a quasi 3D one [Kropp et al., 2001, Wullens, 2003] to introduce the roughness distribution in traversal direction into the contact problem. When the road surface is discretised into slices along its circumference, the non-linear local stiffness can be calculated from a Boussinesq's problem for each section, as schematically represented in Figure 1.9. Hence, the contact force $F_e(\varphi_e, t)$ at point $e$ becomes:

$$F_e(\varphi_e, t) = \int_0^{\Delta y_e(\varphi_e, t)} s_e(\eta) d\eta, \tag{1.11}$$

where $s_e$ is the characteristic function of stiffness and $\eta$ the displacement of the section in question. The contact force is assumed to be acting evenly over the width of the rolling band.

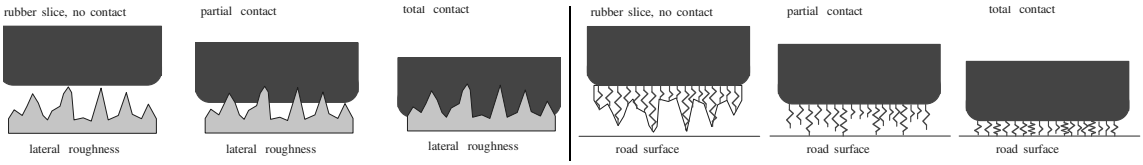


Figure 1.9 – Schematic representation of a lateral rubber slice in no, partial and total contact with the road surface (left) and realisation as a Winkler bedding [Wullens, 2003].

#### 1.2.2.2 Larsson's model

Kropp's model does not take into account the local deformation of the tyre tread which gains importance as the frequency rises, especially for small excitation areas. Therefore, it is only able to predict radial responses, but not tangential or lateral ones. To tackle this problem, Larsson proposed a high-frequency tyre model and has extended the contact model to a refined 3D one, considering the interaction between contact points.

The tyre model based on elastic field equations (1.12) is used to describe local deformations for excitations in both radial and tangential directions. Since the internal structure plays a relatively important role in the radiation of rolling noise at high frequencies, the tyre is modelled by two layers, each composed of an elastic homogeneous isotropic material, representing respectively the rubber rolling band and the stiff metal belt. The plates are under tension because of the inflation pressure in longitudinal and transverse directions. The bottom plate is placed on an elastic foundation to simulate the stiffness of sidewalls. Figure 1.10 illustrates the structure of the tyre model.

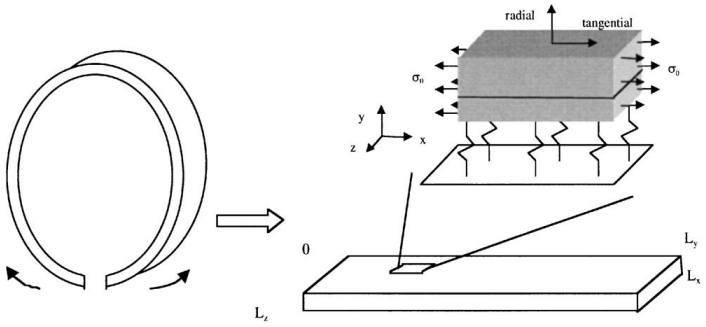


Figure 1.10 – Winkler spring model for the tyre [Larsson and Kropp, 2002].

The elastic field equations write as follows:

$$\begin{aligned} G\left[\Delta\xi + \frac{1}{1-2\nu}\frac{\partial}{\partial x}(\nabla\cdot\mathbf{u})\right] + \sigma_0\frac{\partial^2\xi}{\partial x^2} &= \rho\frac{\partial^2\xi}{\partial t^2} \\ G\left[\Delta\eta + \frac{1}{1-2\nu}\frac{\partial}{\partial y}(\nabla\cdot\mathbf{u})\right] + \sigma_0\frac{\partial^2\eta}{\partial x^2} &= \rho\frac{\partial^2\eta}{\partial t^2} \\ G\left[\Delta\zeta + \frac{1}{1-2\nu}\frac{\partial}{\partial z}(\nabla\cdot\mathbf{u})\right] + \sigma_0\frac{\partial^2\zeta}{\partial x^2} &= \rho\frac{\partial^2\zeta}{\partial t^2} \end{aligned} \tag{1.12}$$

where $\xi$, $\eta$ and $\zeta$ are displacements in x-, y- and z- directions respectively and $\mathbf{u}$ the corresponding velocity vector. $\Delta$ is the Laplace operator and $\nabla$ the nabla operator. $G$, $\nu$ and $\rho$ are the shear modulus, Poisson's ratio and the density respectively and, $\sigma_0$ the tension in the tangential direction. The equations fulfilling the boundary conditions are then solved with a Fourier transform. However, as the local deformation and stiffness are sensible to the unknown excitation area and pressure distribution, errors are induced while doing measurements. This problem has been treated by Andersson and Larsson [2005] who modelled the excitation used in measurements.

The tyre model has been experimentally validated [Andersson et al., 2004, Andersson and Larsson, 2005] and can thus be incorporated into the contact model to describe the deformation of the tyre surface. Equation (1.13) expresses the position $y_e$ of point $e$ on the rolling band as a function of time $t$:

$$y_e(t) = y_0 + k_{10}(\varphi_e, t) + u_e(t) \tag{1.13}$$

where $k_{10}(\varphi_e, t)$ is the geometry of the tyre before deformation and $u_e$ the displacement at the tyre surface due to contact forces. The stationary Green's function is obtained with the same Fast Fourier Transform method as in Kropp's model and leads to the Green's function $g$ of a rolling tyre by including the time phase shift due to tyre rotation. The convolution of the contact forces $F_e$ and the updated Green's function $g$ gives the aforementioned displacement $u_e$, as described in Equation (1.14).

$$u_e(t) = \sum_{m=1}^{N}\int_0^t F_m(\tau)g_{r,m,e}(t-\tau)d\tau \tag{1.14}$$

where $g_r(t) = g(t)\delta(\varphi - \Omega t)$, with $\Omega$ the angular velocity of the tyre. The contact boundary conditions are checked for each time step, and the problem is solved thanks to an iterative scheme proposed by Kalker [2013]. The quasi 3D model [Kropp et al., 2001] is applied to evaluating the contact forces.

Despite its consideration of local interaction at contact points between the rolling band and the road surface, this model appears to be computationally more expensive compared with Kropp's model. Its most important usage remains in the validation of simpler models including Kropp's one.

#### 1.2.2.3 Wullens and Kropp's model

Wullens and Kropp [2004] put forward another three-dimensional model capable of modelling the contact problem between a tyre and a rough road surface, assumed to be rigid, under rolling conditions in the time domain. It calculates the time history of dynamic radial contact forces and the local deformation of the tread. The orthotropic plate model is used to evaluate the response of the tyre structure, serving as an input data for the contact model. The rolling band of such a tyre is considered to be an elastic half-space in this model, and only normal contact forces are considered.

The non-linear contact problem is a classical one to be solved with the Matrix Inversion Method [Johnson, 1985]. The contact surface is divided into rectangular elements subjected to uniform pressures, and the influence matrix $\boldsymbol{C_p}$ relating pressure $\boldsymbol{u}$ and deformation of the elastic half-space $\boldsymbol{p}$ at equilibrium can be derived from analytical solutions to the contact problem for a single element:

$$\boldsymbol{u} = \boldsymbol{C_p p}. \tag{1.15}$$

When using this method, the elementary excitation area is incorporated into the influence matrix $\boldsymbol{C}$, and the relation between contact force $\boldsymbol{F}(t)$ and deformation of the elastic half-space $\boldsymbol{\Delta y}(t)$ is expressed as:

$$\boldsymbol{F}(t) = \boldsymbol{C}^{-1}\boldsymbol{\Delta y}(t) \tag{1.16}$$

Based on Equation (1.16), the iterative algorithm presented below is to be followed for each time step until $\boldsymbol{\Delta y}^{n+1}(t) = \boldsymbol{\Delta y}^{n}(t)$, providing the solution at step $n + 1$:

$$\left\{\boldsymbol{F}^{n+1}(t) = (\boldsymbol{C}^{n})^{-1}\boldsymbol{\Delta y}^{n}(t)\boldsymbol{\Delta y}^{n+1}(t) = \boldsymbol{C}\boldsymbol{F}^{n+1}(t)\forall n, \boldsymbol{\Delta y}^{n+1}(t) \geq \boldsymbol{\Delta y}^{n}(t)\right. \tag{1.17}$$

where $\boldsymbol{C}^{n}$ is a sub-matrix of $\boldsymbol{C}$ for points in contact at iteration $n$ and $\boldsymbol{\Delta y}^{0}(t)$ exactly the same notion as defined in Equation (1.8). The convolution product between the contact force $F_m(t)$ at point $m$ and the Green's function $g_{m,e}(t)$ of the normal displacement at point $e$ due to excitation at point $m$ gives the resulting displacement $\xi_e(t)$ at point $e$:

$$\xi_e(t) = \sum_m F_m(t) * g_{m,e}(t) \tag{1.18}$$

Measurements of accelerations carried out on an airplane tyre rolling on an ISO road show a good agreement for rotational velocities at 80 and 100 km/h, meanwhile a somewhat poorer quality of agreement at 60 km/h. Wullens [2003] compared this model with Kropp's and Larsson's model, hereinafter referred to as the 3D EHS, Q3D bedding and Q3D EHS models respectively. The time domain representation shows very similar results for the three models. However, more variations can be observed from the frequency content. For frequencies between 200 and 1000 Hz, the Q3D bedding model produces a higher force level explained by the absence of interaction between the non-linear springs.

This tyre/road contact model is then used to compute the force time-history with help of a tyre model in the hybrid model SPERoN (Statistical Physical Explanation of Rolling Noise) developed by Chalmers and Müller-BBM within the German project "Quiet Traffic", the EC project ITARI and the P2RN project [Beckenbauer et al., 2008]. The principle of the SPERoN model is shown in Figure 1.11. This model requires a quasi-3D description of non sound-absorbing road surface texture as one of the input data. Other ones are airflow resistance within a contact patch on a dense road surface, as well as tyre load and driving speed. The latter covers the whole speed range between 30 km/h and 120 km/h. Nevertheless, combinations of road and tyre characteristics and speeds need to be pre-processed based on comprehensive and well-documented data archived in the Sperenberg project measurements database. In addition, unlike HyRoNE, the version of SPERoN at that time was still limited to processing impervious road surfaces.

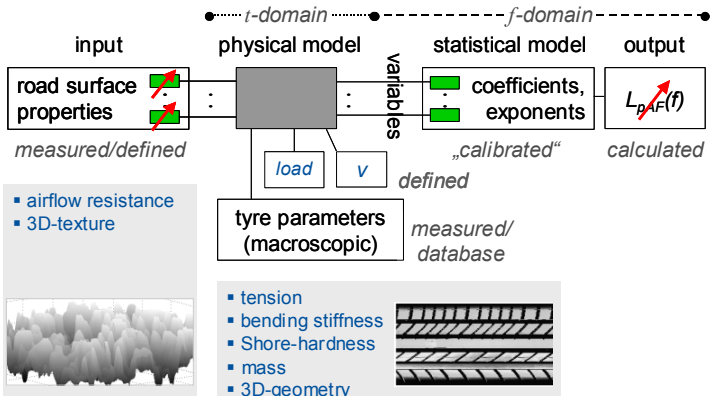


Figure 1.11 – SPERoN structure [Beckenbauer et al., 2008].

Based on the SPERoN contact model, Wullens and Kropp [2007] used the contact forces and the Green's functions of the tyre structure to calculate the vibration field of a rolling tyre in the wavenumber frequency domain, leading to a further step toward the understanding of rolling noise radiation. A new deterministic physical model for rolling noise prediction has been proposed by Kropp et al. [2012]. It combines the contact model described in this subsection, a wave guide finite element tyre model and a boundary element model for noise estimation. Calculated sound pressure levels are in good agreement with measured ones.

#### 1.2.2.4 Andersson and Kropp's model

Winroth et al. [2014] used a numerical contact model [Andersson and Kropp, 2008] to investigate the influence of tread inertia and material damping on dynamic response, that none of the aforementioned models have taken into account. The interfacial layer between the elastic rubber

and the rigid road surface is discretised into elements represented by pairs of matching points connected by non-linear contact springs. The contact problem for multiple contact elements is then solved numerically in the time domain.

In the first place, the contact patch needs to be divided into discrete elements to lower the computational expense. Figure 1.12b shows the discretisation of a detailed scan of the apparent contact area of $2 \times 2$ cm$^2$ used in the simulation. The sampled road surface geometry contains $20 \times 20$ "pixels" of $1 \times 1$ mm$^2$ each representing a pair of matching points, characterised by a non-linear contact spring. The height of a matching point is placed at the center of the element, and roughness at smaller length-scales than the element dimension is neglected. The use of non-linear springs is the most common method in contact modelling, and their stiffness can be approximately evaluated according to a detailed scan of road surface (Figure 1.12a) and material properties. A re-sampling process is necessary to ensure numerical stability during computation by increasing the time resolution.

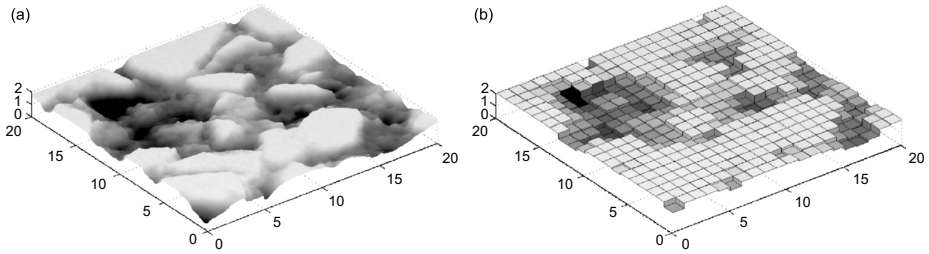


Figure 1.12 – (a) High resolution scan of the road surface and (b) sampled version of the road surface containing 400 elements [Andersson and Kropp, 2008].

Constitutive contact equations are then employed to establish the relation between contact force $F_m$, assumed to be evenly acting on an element of area $A_m$, and displacement $d_m$ of the latter, as expressed in the following equation:

$$F_m = A_m f(d_m) \quad \text{or} \quad d_m = h(F_m/A_m) \tag{1.19}$$

When ignoring very detailed roughness, the interaction between two rough surfaces in a single contact zone can be modelled as a pair of matching points linked by a non-linear spring (Figure 1.13), as in the case of a discrete element of tyre/road contact patch. The compression of spring $\zeta(t)$ is the negative separation distance expressed as:

$$\zeta(t) = -d(t) = -z_2 - w_2(t) + z_1(t) + w_1(t) \tag{1.20}$$

where $z_1$ and $z_2$ are respectively the positions of matching points belonging to body 1 and body 2 at rest, while $w_1(t)$ and $w_2(t)$ the displacements of matching points. In this very case, $w_1(t)$ is equal to zero, since the road surface is assumed to be rigid, and $w_2(t)$ is given by the convolution of the contact force $F(t)$ with the Green's function $g(t)$.

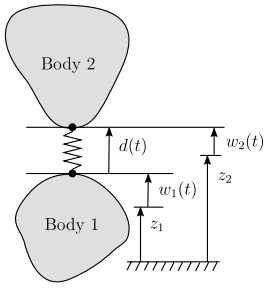


Figure 1.13 – Geometry and modelling approach of the problem [Andersson and Kropp, 2008].

Using Equation (1.20) and predetermined non-linear spring stiffness, the contact force $F(t)$ can then be written as:

$$F(t) = \int_{-\infty}^{\zeta(t)} k(x)dx \tag{1.21}$$

The contact problem is first sampled with low-pass filter and then re-sampled for time discretisation. All variables are thus expressed as functions of time step $N$. The Newton-Raphson numerical method is used to solve the system for a single contact element. Finally, the whole contact model deals with an equation system for multiple pairs of matching points.

Winroth et al. [2014] arranged and simulated two dynamic contact scenarios between a tyre tread block and a rough road surface for comparison with the quasi-static case. The influence of the mass is not taken into account in the latter, which is not the case for dynamic contact problems. In one scenario, representing an infinite impedance, the elastic layer is forced vertically into the road surface with a predetermined and constant indentation acceleration (50 m/s$^2$, 250 m/s$^2$ or 500 m/s$^2$). While in the other one, a mass of 5 grams assigned to the tread block is released from a certain height (0.1, 0.3 or 0.4 m) above the road surface. The set of Green's functions is obtained by using the model proposed by Larsson and Kropp [2002] and is transformed into the time domain. Simulations of the predetermined indentation scenario (Figure 1.14) show that contact force and stiffness increase with indentation acceleration and that dynamic contact cases yield higher values than the quasi-static case. When changing the loss factor, results indicate that material damping could be roughly modelled by a slightly augmented contact stiffness. The released mass scenario is a preliminary study of the inertial effect. It is believed that the latter only matters for highly detailed contact modelling.

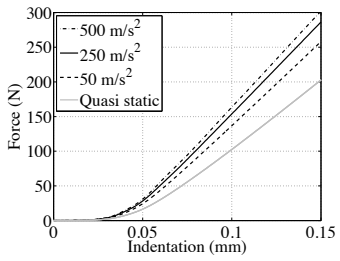


(a) Contact force as function of indentation for different predetermined indentation accelerations and the quasi static case.

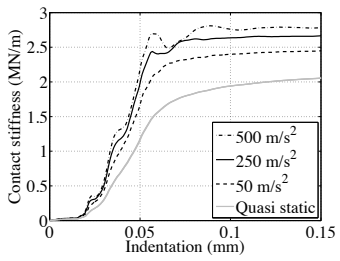


(b) Contact stiffness as function of indentation for different predetermined indentation accelerations and the quasi static case.

Figure 1.14 – Results for different predetermined indentation accelerations and the quasi static case [Winroth et al., 2014].

### 1.2.3 Multi-asperity contact models developed at IFSTTAR/ENPC

A multi-asperity tyre/road contact model has been developed at IFSTTAR in an active collaboration with the ENPC. First, Sameur [2004] proposed an analytical description of the load/penetration relationship while considering the interaction between asperities. Next, Cesbron [2007] developed a Two-Scale Iterative Method to find numerical solutions to the contact problem in statics efficiently. Finally, Dubois [2012] incorporated a road surface partitioning algorithm and introduced rubber viscoelasticity into the contact problem to obtain more accurate results with regards to geometrical and material properties. A summary of contact assumptions and applicable road surface geometry types at respectively macro- and micro-scales in the multi-asperity contact models is given in Table 1.1.

Table 1.1 – Summary of contact assumptions and applicable road surface geometry types at macro- and micro-scales in the multi-asperity contact models.

| | Macro scale (multi-point) | Micro scale |
|---|---|---|
| Sameur (2004) | Elastic<br>Simple geometries (spheres, cones) | |
| Cesbron (2007) | Elastic<br>Complex geometries (real road surfaces) | Elastic<br>Simple geometries: final contact pressure<br>Complex geometries : initial contact pressure |
| Dubois (2012) | Elastic/viscoelastic with/without tyre vibrations<br>Complex geometries | Elastic<br>Complex geometries: Small surfaces: final iteration<br>tyre/road contact: initial pressure |

#### 1.2.3.1 Sameur's model: multi-point elastic approach for tyre/road contact

Sameur [2004] proposed an analytical model to describe the load/penetration relationship for a 3-D multi-point frictionless elastic contact problem on simple shaped indenters. A theory of interaction potential is used to express the contact law between a single punch of arbitrary profile and an elastic half-space, based on the assumption that only normal loading is considered. The contact force $P$ is written as a function of the depth of penetration $\delta$ at the tip of the punch:

$$P(\delta) = \frac{\partial U(\delta)}{\partial \delta} \quad \text{with} \quad U = c\frac{8}{15\pi^{1/4}(\theta_1+\theta_2)}\frac{V_\Gamma^2 p_\Gamma^{1/2}}{S_\Gamma^{7/4}} \tag{1.22}$$

where $U$ is the potential, $V_\Gamma$ the volume of the contact domain $\Gamma$, $S_\Gamma$ the projected area of $\Gamma$ onto the tangent plane at the contact point and $p_\Gamma$ the projected perimeter.

After its experimental validation on single indenters of simple shapes, this analytical model serves to describe local contact laws in a multi-point contact problem. This formulation takes into account the interaction between $N$ asperities composing a surface in contact with an elastic half-space. The total normal load $P$ is divided into $N$ normal forces $P_i$ applied to the summit $M_i$ of each indenter. The local depth of penetration $\delta_i$ on the $i^{\text{th}}$ indenter is deduced from the total depth of penetration $\delta_0$, the height $H_i$ and the interaction displacement due to forces on other asperities $M_j$. The contact law for the $i^{\text{th}}$ asperity is then written as follows:

$$P_i(\delta) = \frac{\partial U}{\partial \delta}(\delta_0 - H_i - u_i) \quad \text{with} \quad u_i = \sum_{\substack{j=1 \\ j\neq i}}^{N} T_{ij}P_j \tag{1.23}$$

The interaction coefficients $T_{ij}$ are calculated using the influence function of Boussinesq [1885] for a concentrated normal force loading the surface of an elastic half-space:

$$T_{ij} = T(x_i, y_i; x_j, y_j) = \frac{1}{\pi E^* \sqrt{(x_i - x_j)^2 + (y_i - y_j)^2}} \quad \text{with} \quad E^* = \frac{E}{1 - \nu^2} \tag{1.24}$$

The contact is considered in statics for each time step, and the system of $N$ non-linear equations (1.23) is numerically solved using the Newton-Raphson iteration method.

When compared with a finite element model, the analytical model proves to be considerably more time-efficient. According to Sameur [2004], the results are in good agreement with those obtained from the FE model and experiments configured for contact between few indenters of simple shapes and a rubber block. Cesbron et al. [2006] obtained satisfactory results for measurements of contact forces and areas in the case of a periodic surface composed of 25 spherical indenters. This simplified analytical model dealing with the tyre/road contact problem at macro-scale is a first step towards a more reliable and more efficient one.

#### 1.2.3.2 Two-scale elastic approach for tyre/road contact

Based on the aforementioned method capable of calculating force distribution in the Boussinesq [1885] problem, Cesbron et al. [2009b] proposed a Two-scale Iterative Method (TIM) to fully solve this problem by introducing a second step for evaluation of pressure distribution at micro-scale, as depicted in Figure 1.15.

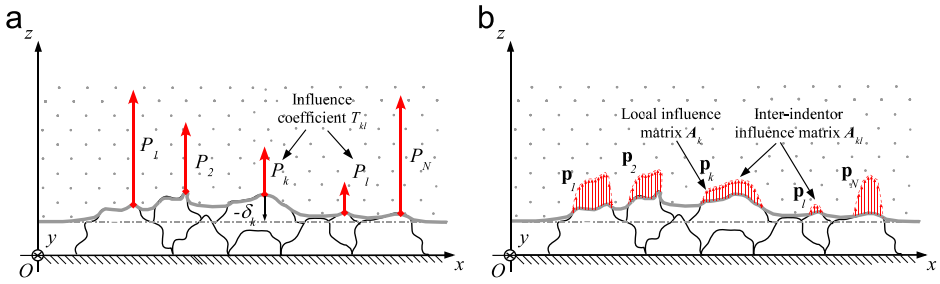


Figure 1.15 – Schematic view of the two-step iterative method, (a) macro-scale, (b) micro-scale [Dubois et al., 2012].

The contact forces $P_k$ at the summit of the asperities are calculated in the macro-scale step using the follow equation:

$$\forall k \in [1, N], \quad P_k = \begin{cases} f_k(\delta_k) & \text{if } \delta_k > 0 \\ 0 & \text{if } \delta_k \leq 0 \end{cases} \quad \text{and} \quad P + \sum_{k=1}^{N} P_k = 0 \tag{1.25}$$

In the micro-scale calculation step, the surface of the elastic half-space is divided into $n$ identical square elements with coordinates $(x_i, y_i, z_i)$ and size $h \times h$. A global influence matrix, denoted $\mathbf{A}$, is defined. Its coefficients are calculated using the analytical results of Love [1929] assuming that a uniform pressure is acting on each square element. Defining a global pressure vector $\mathbf{p} = \{p_i\}^{\mathrm{T}}_{i\in[1,n]}$ and a displacement vector $\mathbf{b} = \{\delta - z_i\}^{\mathrm{T}}_{i\in[1,n]}$ then the Boussinesq problem is written as a vector equation $\mathbf{Ap} = \mathbf{b}$. Matrix $\mathbf{A}$ is organised by blocks as follows:

$$\begin{pmatrix} \mathbf{A}_1 & \cdots & \mathbf{A}_{1k} & \cdots & \mathbf{A}_{1N} \\ \vdots & \ddots & \vdots & \ddots & \vdots \\ \mathbf{A}_{k1} & \cdots & \mathbf{A}_k & \cdots & \mathbf{A}_{kN} \\ \vdots & \ddots & \vdots & \ddots & \vdots \\ \mathbf{A}_{N1} & \cdots & \mathbf{A}_{Nk} & \cdots & \mathbf{A}_N \end{pmatrix} \begin{Bmatrix} \mathbf{p}_1 \\ \vdots \\ \mathbf{p}_k \\ \vdots \\ \mathbf{p}_N \end{Bmatrix} = \begin{Bmatrix} \mathbf{b}_1 \\ \vdots \\ \mathbf{b}_k \\ \vdots \\ \mathbf{b}_N \end{Bmatrix} \tag{1.26}$$

where $N$ is the number of indenters at macro-scale, $\mathbf{A}_{kk}$ the local influence matrix, $\mathbf{p}_k$ the local pressure vector and $\mathbf{b}_k$ the local displacement vector for the $k^{\text{th}}$ punch. The extra-diagonal block $\mathbf{A}_{kl}$ is the part of $\mathbf{A}$ relative to interaction of the $l^{\text{th}}$ punch on the $k^{\text{th}}$ punch. An initial approximation of the contact pressure distribution $\mathbf{p}^0 = \left\{\mathbf{p}_1^0(P_1)\cdots\mathbf{p}_k^0(P_k)\cdots\mathbf{p}_N^0(P_N)\right\}^{\mathrm{T}}$ is calculated based on the macro-scale forces $P_k$ using the classical matrix inversion method. For the $k$th punch, the equation is written as:

$$\begin{pmatrix} \mathrm{A}_{k_{11}} & \cdots & \mathrm{A}_{k_{1n_k}} & 1 \\ \vdots & \ddots & \vdots & \vdots \\ \mathrm{A}_{k_{n_k1}} & \cdots & \mathrm{A}_{k_{n_kn_k}} & 1 \\ 1 & \cdots & 1 & 0 \end{pmatrix} \begin{Bmatrix} p_{k_1}^0 \\ \vdots \\ p_{k_{n_k}}^0 \\ \delta + u_k \end{Bmatrix} = \begin{Bmatrix} z_{r,k_1} - z_{t,k_1} \\ \vdots \\ z_{r,k_{n_k}} - z_{t,k_{n_k}} \\ -\frac{P_k^0}{h_x h_y} \end{Bmatrix} \tag{1.27}$$

Equation (1.26) is then solved using a non-linear block Gauss-Seidel-like algorithm. The iteration starts from $\mathbf{p}^0$. At step $m+1$, the pressure distribution on each punch $k$, denoted $\mathbf{p_k^{m+1}}$, is calculated by inverting the following local linear problem:

$$\mathbf{A}_{kk}\mathbf{p}_k^{m+1} = \mathbf{b}_k^m - \sum_{l=1}^{k-1} \mathbf{A}_{kl}\mathbf{p}_l^{m+1} - \sum_{l=k+1}^{N} \mathbf{A}_{kl}\mathbf{p}_l^m \tag{1.28}$$

Negative pressures are replaced by zeros and the procedure is repeated for the other punches. It is stopped until no negative pressure is detected during an iteration and when the following convergence criterion is checked:

$$\frac{\| \mathbf{p}^{m+1} - \mathbf{p}^m \|}{\| \mathbf{p}^m \|} \leqslant \varepsilon \quad \text{with} \quad \| \mathbf{x} \| = \sum_{i=1}^{n} | x_i |^2 \tag{1.29}$$

The macro-scale step quickly provides a good estimation of the initial pressure distribution $\mathbf{p}^0$ for the micro-scale step, which saves time on the most time-consuming part of the whole calculation process by applying the iterative formula (1.28) instead of inverting the global influence matrix as in conventional methods. Comparison between numerical and experimental results for 3 configurations of spherical indenters loaded on a rubber block proves this model to be time-efficient and fairly accurate.

Although Cesbron's model shows several advantages, the macro-scale step identifies only the emergent part of asperities on road surface. Dubois et al. [2012] improved this approach by introducing an algorithm for partitioning the whole measured surface. A global flow chart (Figure 1.16) outlines the calculation steps in the whole modelling process and indicates the time cost on each step.

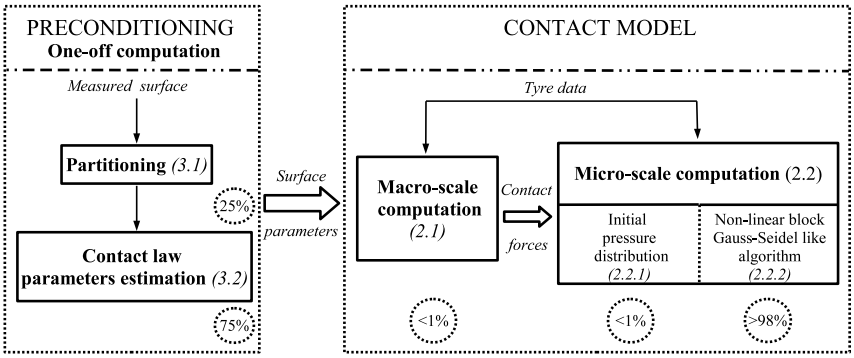


Figure 1.16 – Global flow chart of the method to evaluate numerically tyre/road contact pressures using a multi-asperity approach (the numbers in percentages are the relative computational effort in each part) [Dubois et al., 2012].

The measured road surface profile is first processed through a partitioning procedure as illustrated in Figure 1.17. Two image processing methods are used: an iterative labeling method [Cesbron et al., 2008] for binarizing the image of measured surface and the watershed segmentation method proposed by Vincent and Soille [1991]. Thus the surface is partitioned into segments, each associated to the summit of the asperity it surrounds. This is performed only once, and the results are saved for use as input data in contact calculations.

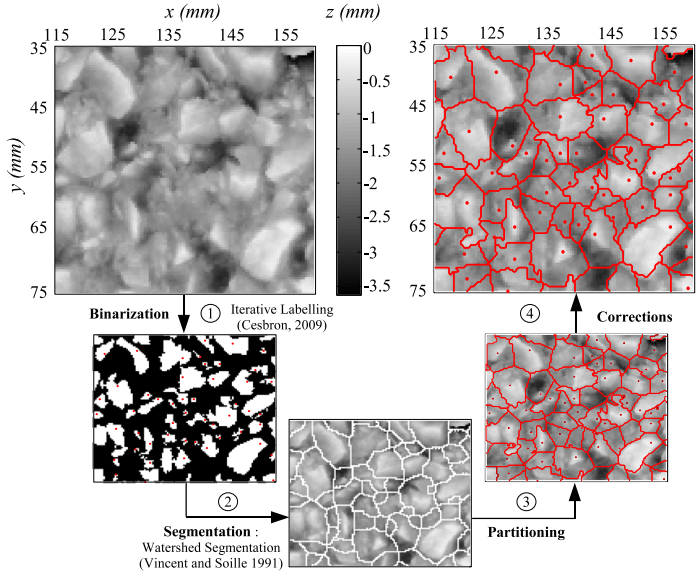


Figure 1.17 – Schematic view of the partitioning method for a real road surface [Dubois et al., 2012].

Dubois et al. [2012] extended the contact law on a single asperity to all situations (Figure 1.18), written as follows:

$$\forall k \in [1,N], \quad P_k = \begin{cases} 0 & \text{if } \delta_k \leq 0 \quad \text{Non-contact} \\ C_k E^* \delta_k^{\gamma_k} & \text{if } 0 < \delta_k < d_k \quad \text{Power law} \\ K_k E^* (\delta_k - d_k) + C_k E^* \delta_k^{\gamma_k} & \text{if } d_k \leq \delta_k \quad \text{Linear} \end{cases} \tag{1.30}$$

where $C_k$ and $\gamma_k$ are constants depending on the shape and size of the asperity, the constant $d_k$ is a critical depth above which the contact law becomes linear, and $K_k E^*$ corresponds to a linear stiffness. A local Boussinesq problem has to be solved individually for each asperity to obtain the numerical pairs ($\delta_k$,$P_k$), with which the aforementioned contact law parameters can be deduced from Equation (1.30).

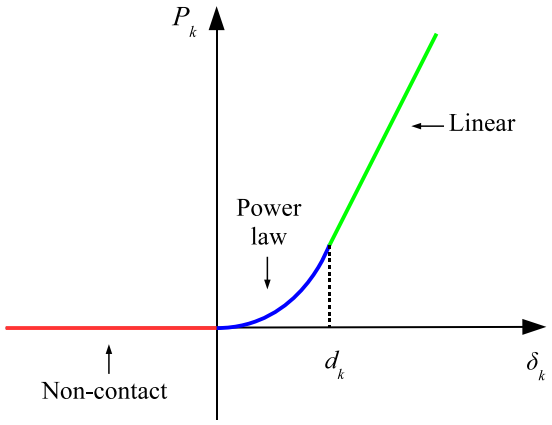


Figure 1.18 – Analytical contact law proposed for a single road asperity [Dubois et al., 2012]. In [Cesbron, 2007], the contact law was limited to the power law alone.

Dubois et al. [2012] computed the contact forces at macro-scale and the final pressure distribution at micro-scale for a small surface sample and compared results with those of the classical matrix inversion method. As shown in Figure 1.19, the comparisons are satisfactory. However, calculating the final pressure distribution within the full contact patch for real road surfaces is time-consuming. Bearing in mind that the contact forces evaluated at macro-scale are sufficiently accurate, the initial pressure distribution is used for noise estimation.

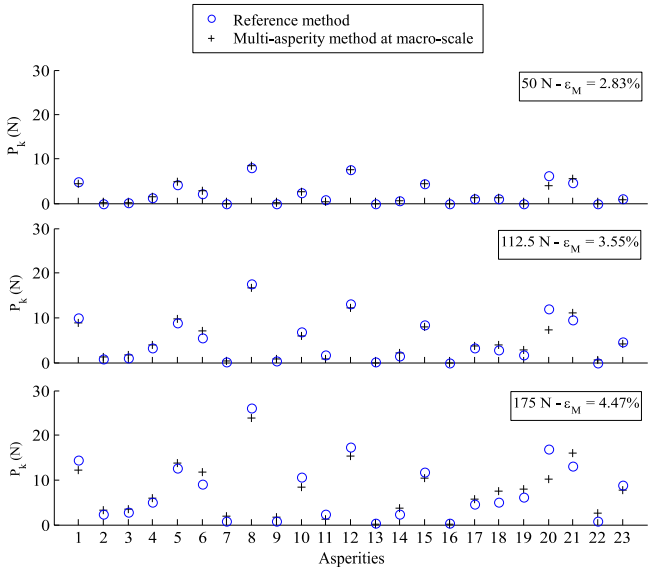


Figure 1.19 – Comparison of contact forces at the summit of each asperity between a reference method (matrix inversion method) and the multi-asperity method at macro-scale [Dubois et al., 2012].

Dubois et al. [2013] studied the relationship between tyre/road numerical contact data and close-proximity (CPX) rolling noise measurements at low frequencies and provided a statistical way to estimate the latter from the former. The complete procedure for the contact pressure calculation, considering a succession of static states in the rolling direction, is shown in Figure 1.20.

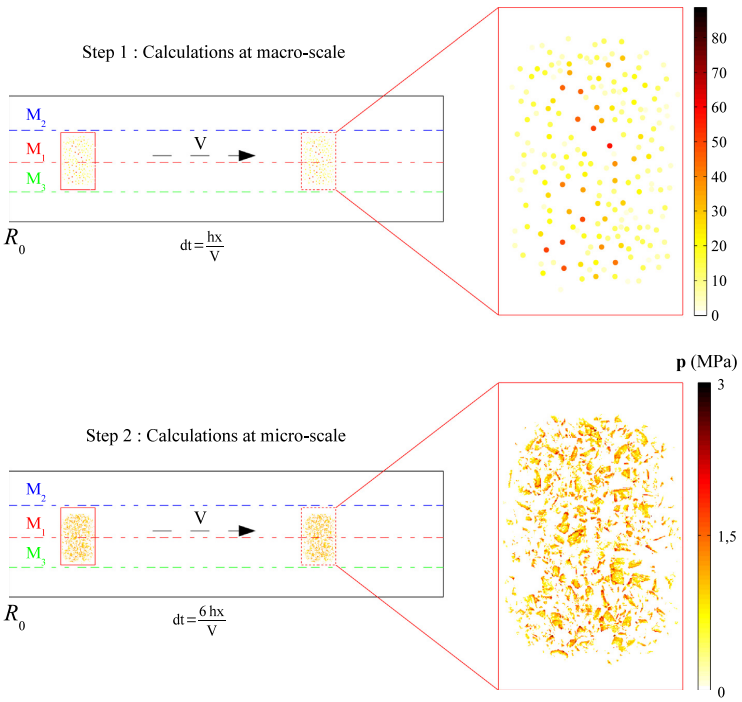


Figure 1.20 – Schematic view of the contact calculations on several metres of road surfaces [Dubois et al., 2013].

The pressure distribution is integrated and then transformed into contact force spectra represented in one-third octave bands. The contact force levels are calculated respectively for a slick tyre and a classic patterned tyre over all the tested road surfaces and for a rolling speed of 90 km/h and processed for correlation with the measured noise levels using a CPX equipment. Figure 1.21 shows the calculated force spectra for both tyres.

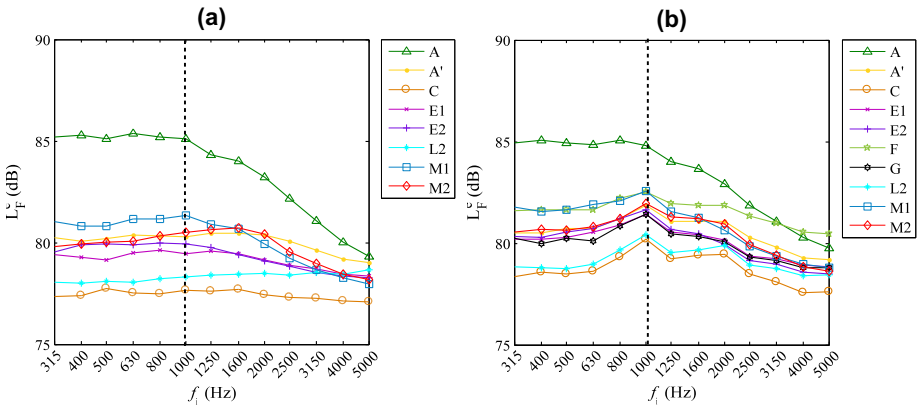


Figure 1.21 – Calculated one-third octave bands contact force levels at 90 km/h for each surface for a slick tyre (a) and for a classic patterned tyre (b) [Dubois et al., 2013].

The noise level can be estimated from the contact force levels using a weighted linear regression relation. The measured and estimated noise levels are then correlated in Figure 1.22. The mean absolute difference $\varepsilon$ is 1.50% for the slick tyre and 1.34% for the classic patterned tyre.

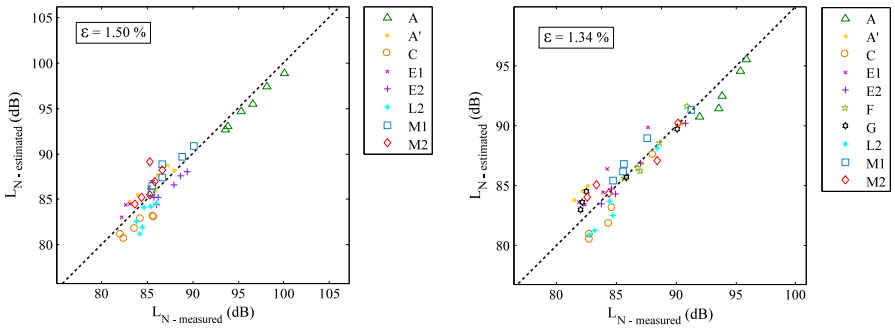


(a) Correlation between measured noise and estimated noise for a slick tyre.

(b) Correlation between measured noise and estimated noise for a classic patterned tyre.

Figure 1.22 – Correlation between measured noise and estimated noise from contact forces by hybrid method for a tyre at 90 km/h. Strong correlation is found within the frequency range between 315 and 1250 Hz for the slick tyre and between 315 and 800 Hz for the classic patterned tyre, by fixing a minimum threshold of correlation coefficient at 0.8 [Dubois et al., 2013].

#### 1.2.3.3 Multi-point viscoelastic approach

Dubois et al. [2011] presented a macro-scale approach capable of taking into account the viscoelastic behaviour of the tyre tread and how it influences the load/penetration relationship. To consider the time-dependent stress-strain($\sigma$-$\varepsilon$) relationship, rheological models such as Zener model and generalised Maxwell model are used to determine the creep compliance function $\Phi$ and the relaxation function $\Psi$, as depicted in Figure 1.23. Assuming that each time increment is short enough to treat $\Phi$ and $\Psi$ as constant functions very close to the initial instant, the numerical viscoelastic contact problem is turned into an elastic-like problem described by equations (1.31) and (1.32) for the whole road surface partitioned into N asperities. The latter, expressed as a Boussinesq problem, leads to an analytical elastic solution which will be transformed into a viscoelastic solution using Radok's technique [Radok, 1957].

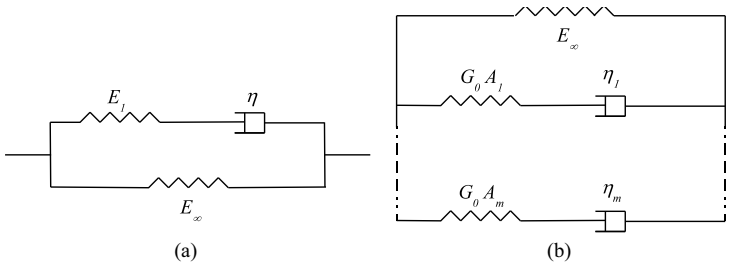


Figure 1.23 – Schematic view of both rheological models: (a) Zener model, (b) generalised Maxwell model [Dubois et al., 2011].

$$\forall k \in [1,N], \quad P_k(t) = \begin{cases} \psi(0) f_k(\delta_k(t)) + P^k_{old}(t) & \text{if } \delta_k(t) > 0 \\ 0 & \text{if } \delta_k(t) \leq 0 \end{cases} \tag{1.31}$$

with:

$$P^k_{old}(t) = \int_0^{t-\delta t} \psi(t-\tau)\frac{\mathrm{d}}{\mathrm{d}\tau}(f_k(\delta_k(\tau)))\mathrm{d}\tau - \psi(0)f_k(\delta_k(t-\delta t)) \tag{1.32}$$

where $P^k_{old}$ represents the known historical contact force on asperity $k$, whose penetration is given by the following equations:

$$\delta_k(t) = z^s_{r,k} - \delta(t) - z^s_{t,k} - u^k_{old}(t) - \phi(0)\sum_{\substack{l=1 \\ l\neq k}}^{N(t)} G_{kl}P_l(t) \tag{1.33}$$

where $u^k_{old}$ represents the known historic displacement on asperity $k$. Combining equations (1.31) and (1.33), a non-linear system of $N(t)+1$ equations with $N(t)+1$ unknowns $\{P_1(t), \ldots, P_N(t), \delta(t)\}$ is obtained. It is then solved using the Newton-Raphson iterative method at each time step.

This viscoelastic approach was numerically validated by comparison with a reference method proposed by Kozhevnikov et al. [2008] (Figure 1.24), showing an even considerably higher time-efficiency than an enhanced method based on the latter from Kozhevnikov et al. [2010]. When both the elastic and viscoelastic approaches are applied to real road surfaces, a decrease of about 20% in the contact areas can be observed between static and dynamic conditions. This result is in agreement with the experimental observation made by Cesbron et al. [2009a]. Thus, the static contact method can be a first approximation of the dynamic contact forces for tyre/road noise prediction at low frequencies, if the shear modulus is correctly chosen. A similar approach has been applied by Bui [2014] to investigate the influence of road textures on rolling resistance.

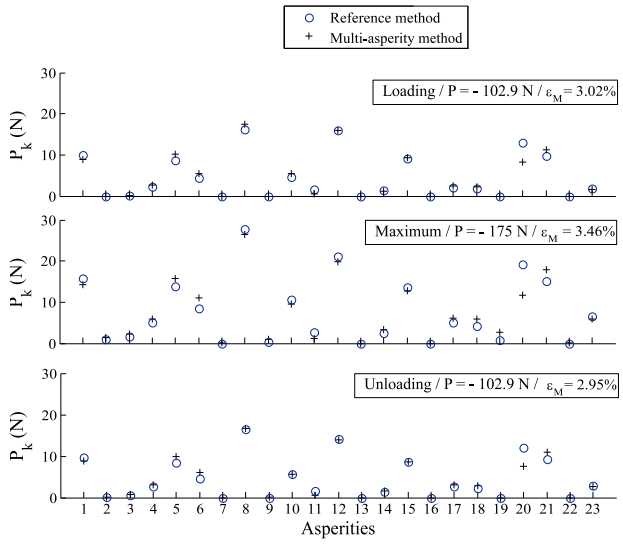


Figure 1.24 – Comparison of contact forces at the summit of each asperity between a reference method (matrix inversion method) and the multi-asperity method [Dubois et al., 2011].

#### 1.2.3.4 Reduced Green's formalism approach for dynamic contact

Meftah [2011] came up with another approach to study the dynamic tyre/road contact problem. The tyre response is calculated using an FE periodic model. To solve the contact problem,

a modal decomposition of the Green's function involved in the convolution technique is carried out, and modal parameters are used to construct a faster convolution. Meftah [2011] performed simulations of the dynamic contact between a tyre and a sinusoidal surface at different driving speeds while considering the tyre vibrations and calculated the contact force spectral content (Figure 1.25a). The results are compared with the contact force spectra calculated using the quasi-static multi-asperity model (Figure 1.25b , Cesbron et al. [2013]) for a tyre rolling on a similar periodic surface. A common result is that the frequency of the contact force peaks increases with the driving speed for both models. However, the peak magnitude increases according to Meftah [2011] but decreases according to Cesbron et al. [2013] as the speed increases. The same effect is observed for real road surfaces and may be due to a fundamental difference between a quasi-static contact model and a dynamic one, taking into account the vibrations of the tyre.

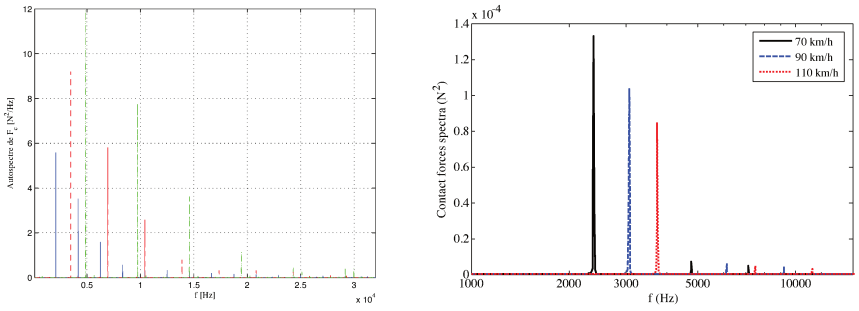


(a) Contact force spectral content obtained for a sinusoidal surface [Meftah et al., 2011].

(b) Contact force spectral content obtained for a periodic surface [Cesbron et al., 2013].

Figure 1.25 – Comparison of contact force spectral content at different driving speeds between a dynamic contact model [Meftah et al., 2011] and a quasi-static contact approach [Cesbron et al., 2013].

## 1.3 Experimental set-ups in laboratories

Although numerous experiments have been carried out on statistical estimation of noise from road texture, understanding the noise generation mechanisms would require experimental studies on physical laws, such as relationship between contact force levels and noise levels or influence of tyre vibrations on rolling noise. In the following, some few experiments found in the literature will be presented.

### 1.3.1 Tyre/road contact testing

#### 1.3.1.1 Single point contact testing

To validate the analytical contact law on a single punch in Sameur's model, Sameur [2004] carried out experiments to determine values of constant $c$ in Equation (1.22) for different punch shapes and compares them with analytical values. The Young's modulus of a rubber pad simulating the tyre tread material is first evaluated thanks to a relaxation test. A compression force is loaded onto the rubber pad with help of a compression testing machine *Instron*, as shown in Figure 1.26. When a certain deformation value is reached, it is maintained still until the stress value becomes

stable. Four characteristic relaxation times are identified, and a Prony's series is reconstructed to describe the stress as a function of the time parameter.

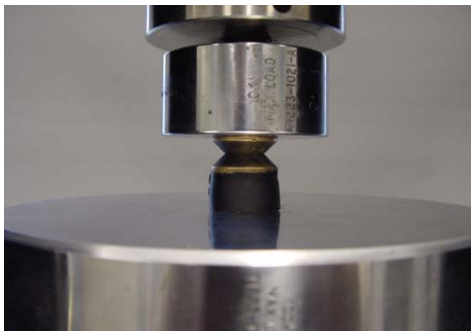

Figure 1.26 – Stress relaxation test for determination of the Young's modulus of rubber [Sameur, 2004].

The Young's modulus can also be determined using Hertzian contact theory, which is experimentally studied by pressing the rubber pad onto a steel ball (Figure 1.27). The force $P$ is proportional to $\delta^{3/2}$, where $\delta$ is the penetration depth. When $P$ is plotted versus $\delta$ using a logarithmic scale, the Young's modulus can be deduced from the slope of the linear relation. The test yields a very similar result to the relaxation test, and the one given by the latter is used for identification of constant $c$. A value of 0.34 that best fits the force/penetration curve is deduced according to Equation (1.22). Similar tests are done for steel cones with different angles ($\alpha = 45$ and $\alpha = 60$), as well as for a steel pyramid. Table 1.2 summarises experimental and analytical values of constant $c$ for all the three shapes of punch. The results are in good agreement.

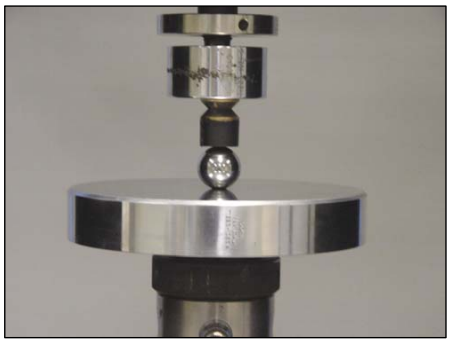

Figure 1.27 – Compress of a rubber pad on a spherical indenter for evaluation of the constant $c$ in equation (1.23) [Sameur, 2004].

Table 1.2 – Identification of the constant $c$ in Equation (1.22) [Sameur, 2004].

| | **Sphere** | **Cone** | | **Pyramid** |
|---|---|---|---|---|
| ***c*** | $c_s$ | $c_c$ | | $c_p$ |
| **Experimental** | 0.34 | **45°** | **60°** | 0.53 |
| | | 0.43 | 0.45 | |
| **Analytical** | 0.36 | 0.45 | | - |

A study carried out by Liu et al. [2012] also involves investigation of tyre/road contact forces at the asperity scale. By treating each stone chip as an asperity with a spherical top, they proposed a viscoelastic indentation model with edge effect correction capable of predicting dynamic contact forces. After validation of their proposed model by comparison with an FE model, a tread block rolling test rig is used to simulate the dynamic contact between a tread block and single asperities. A tread block sample is mounted on a bi-axial load cell in the smaller wheel, and the bigger wheel contains three holes equipped with holders. Light beam breakers and corresponding optical sensors mounted on the wheels detect contact, and the bi-axial load cell captures both the normal and tangential forces. Figure 1.28 shows a typical contact force time history of the contact over a spherical indenter. Real stone chips of different shapes are then used to validate the spherical top formulation, and good agreements are found between experiments, FE and viscoelastic indentation models at low force levels. Although tangential forces can be measured, friction is not taken into account in the model, and FE analysis in this study suggests that the effect of friction is negligible. In addition, tests on spherical indenters show that the rolling speed has a weak influence on contact forces. This model focuses on the dynamic response of a tread block in contact with an isolated road surface asperity. However, without consideration of the interaction between asperities, the estimate of force distribution would not be sufficiently accurate. And one drawback of the tests carried out on stone chips is that the smooth shapes are not fully representative of a real road aggregate.

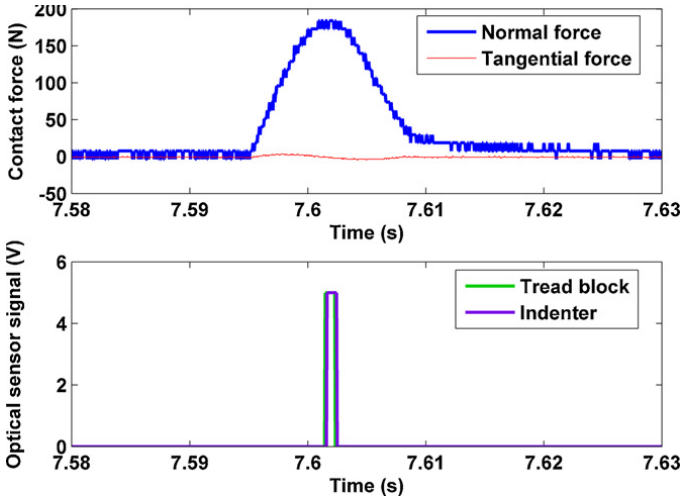


Figure 1.28 – Typical tread block contact force history. [Liu et al., 2012]

### 1.3.1.2 Multi-point contact testing

The single point contact law proposed by Sameur [2004] being rather accurate for a single asperity, it can be used to help study the interaction effect between asperities. Figure 1.29 illustrates how two identical steel balls are installed with a height gap of 0.2 mm between them and respectively labeled sphere 1 and sphere 2. The results show that there is a greater difference between experimental and analytical values on sphere 2 which is lower. This could reflect the importance of taking into account the interaction in modelling. More tests simulating double or triple contacts with mixed shapes of asperity confirm this conclusion, hence the multi-point contact law proposed by Sameur [2004] expressed as Equation (1.23).

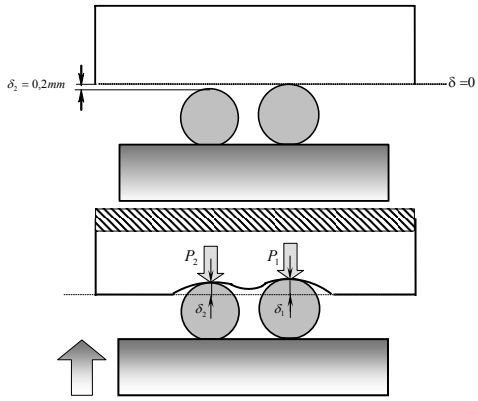


Figure 1.29 – Two spherical indenters installed with a height gap of 0.2 mm between them [Sameur, 2004].

Cesbron et al. [2006] measured contact forces and radii of contact areas using Fuji films to validate this new contact law. The contact area is between a rubber block and a periodic surface composed of 25 identical steel balls set at equal height (Figure 1.30). A press exerts a certain compression force on the contact surface and leaves prints on Fuji Prescale Films between the indenters and the rubber block. The prints are then converted to mean contact pressures or apparent radii. The latter yields coherent results with theoretical ones, whereas the differences can exceed 10% for contact forces (Figure 1.31).

Figure 1.30 – Periodic surface and experimental set-up for the contact tests with the rubber block [Cesbron et al., 2006].

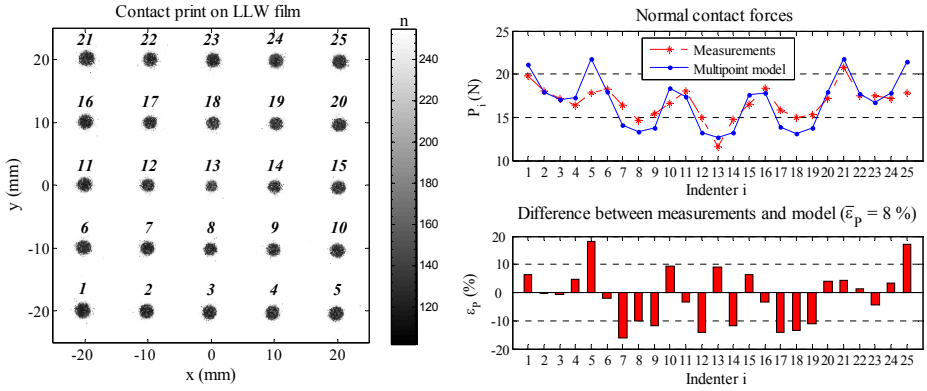


Figure 1.31 – Comparison between the experimental and the theoretical contact forces for P = 419 N [Cesbron et al., 2006].

Cesbron et al. [2009b] performed first an in-lab validation for the Two-scale Iterative Method proposed by himself. The experiment set-up is similar to the one explained above. A digital pressure sensing device I-Scan® developed by Tekscan© replaces Fuji films for force measurements. Three surfaces composed of spherical indenters are configured as depicted in Figure 1.32. Surface $S_1$ has seven identical and hexagonally arranged indenters. Surface $S_2$ is periodic and composed of 25 asperities of equal radius. Surface $S_3$ has 24 indenters with ramdom positions and three possible radii.

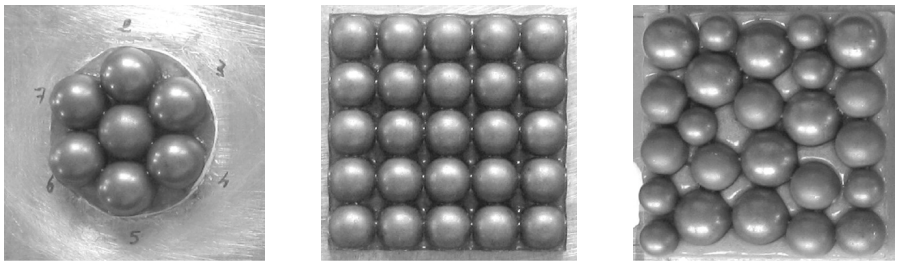

Figure 1.32 – Pictures of the three indenting surfaces $S_1$, $S_2$ and $S_3$ (top) and associated numbering (bottom). [Cesbron et al., 2009b]

The pressure distribution is measured in quasi-statics for each surface thanks to each sensor cell in the contact patch. The contact forces at the tips of asperities are calculated by integrating the measured pressure inside each local contact area. Two indicators $\varepsilon_M$ and $\varepsilon_m$ are defined to represent errors at macro-scale and micro-scale, respectively. The values of the indicators for each total load $P$ and each surface is summarised in Table 1.3. Since the precision of measurements is $\pm 10\%$, the results show that the proposed method could be relevant to modelling multi-contact problems at both scales.

Table 1.3 – Macro and micro-scale indicators for the three surfaces at the three loading cases. [Cesbron et al., 2009b]

| Surface | $S_1$ | | | $S_2$ | | | $S_3$ | | |
|---|---|---|---|---|---|---|---|---|---|
| $P$ (N) | 50 | 100 | 150 | 200 | 250 | 300 | 200 | 250 | 300 |
| $\bar{\varepsilon}_M$ (%) | 0.4 | 0.2 | 0.1 | 0.5 | 0.5 | 0.6 | 1.1 | 0.7 | 0.7 |
| $\bar{\varepsilon}_m$ (%) | 5.9 | 4.8 | 4.9 | 3.9 | 4.2 | 4.0 | 7.4 | 7.4 | 7.0 |

#### 1.3.1.3 Static tyre/road contact testing

Cesbron et al. [2008] then studied the influence of road texture on tyre/road contact in static conditions by making numerical and experimental comparisons. The experimental set-up for contact pressure measurement using a large Tekscan© device I-Scan® under static loading is shown in Figure 1.33. The tests were carried out on a passenger car fitted with two slick tyres on the rear wheels.

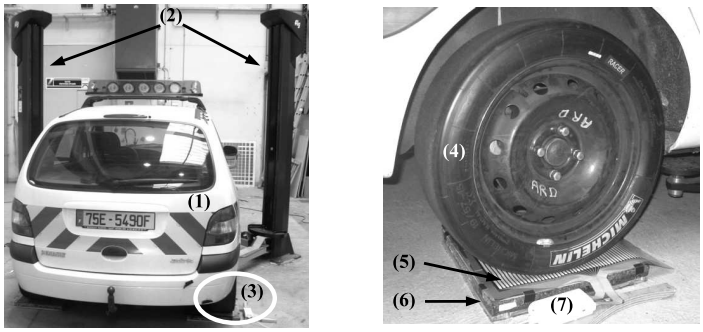


Figure 1.33 – Experimental setup: (1) Vehicle, (2) Lift system, (3) Measurement area, (4) Slick tyre, (5) Tekscan sensor 3150, (6) Tested surface, (7) Tekscan handle [Cesbron et al., 2008].

Figures 1.34a and 1.34b represent respectively measured and numerically calculated pressure distributions of three out of the eight tested road surfaces. The Model Surface MS 1 is composed of spheres with a periodic distribution. Each colored square element represents a cell of the Tekscan© sensor. Due to the low spatial resolution, the real contact area on each asperity cannot be identified in details. The pressure measured on a cell can be due to several asperities. Thus the total measured area, denoted $A$, is closer to the apparent contact area than to the real one.

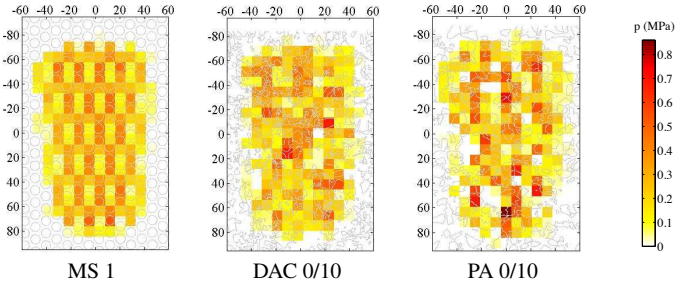


(a) Examples of measured normal pressure distribution.

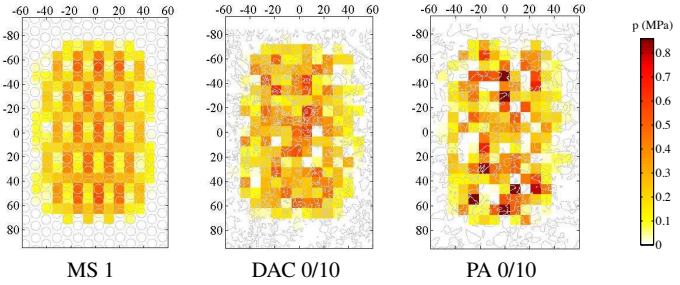


(b) Calculated numerical pressure integrated at Tekscan sensor scale.

Figure 1.34 – Comparison of measured and numerically calculated pressure distributions [Cesbron et al., 2008].

Correlations between calculated and measured contact areas $A$ and mean pressure values $p_{\mathrm{m}}$ are in good agreement. The best correlations for contact pressure distributions are obtained for model surfaces composed of spherical punches and real road surfaces of moderated or high macro-texture. The results are less conclusive for road surfaces of fine macro-texture. This may be explained by a limitation of the multi-asperity model when the surface is composed of very small protruding aggregates.

#### 1.3.1.4 Dynamic tyre/road contact testing

Encouraged by the efficiency of the TIM approach for analysing static tyre/road contact problems, Cesbron et al. [2009a] implements an experimental study of dynamic contact for noise prediction. The same passenger car and sensor are used for the measurement, but only a line of sensors is activated as illustrated in Figure 1.35. The sensor is taped on the road surface and calibrated according to the total load applied exerted on the tyre which is measured independently on a weighing device. At the same position, dynamic tests are performed for rolling speeds at 30, 40 and 50 km/h. First measurements, denoted "transverse tests", are performed with the active line of the sensor perpendicular to the rolling direction. Thus dynamic contact patches in rolling conditions can be estimated. Then measurements are performed with the active line along the rolling direction. These "longitudinal tests" are used to investigate variations of dynamic contact forces with speed on six different road surfaces.

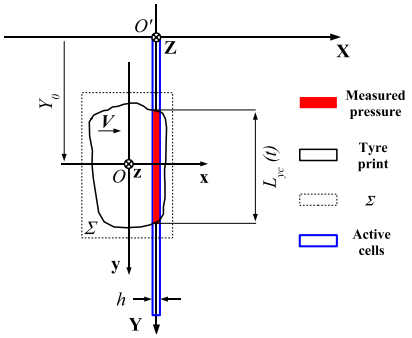


(a) Transverse tests.

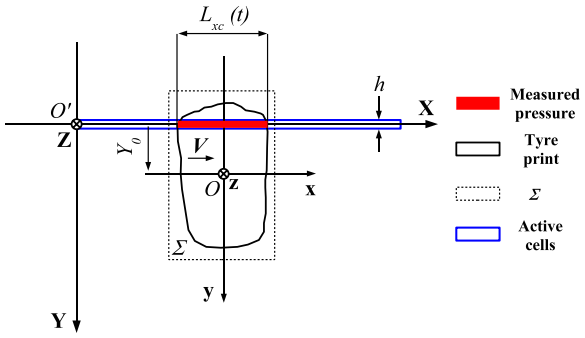


(b) Longitudinal tests.

Figure 1.35 – Position of the active line of cells for (a) the "transverse tests" and (b) the "longitudinal tests" [Cesbron et al., 2009a].

An example of the contact patches measured at different rolling speeds in "transverse tests" is given for one road surface in Figure 1.36. The results show that the contact areas are about 20% smaller in rolling than in static conditions. Moreover, the dynamic contact areas are in the same order for the three rolling speeds. The decrease in contact area is mainly explained by the dynamic properties of tyre compounds, like the viscoelastic behaviour of the rubber, whose influence is also observed in numerical studies carried out later by Dubois et al. [2011].

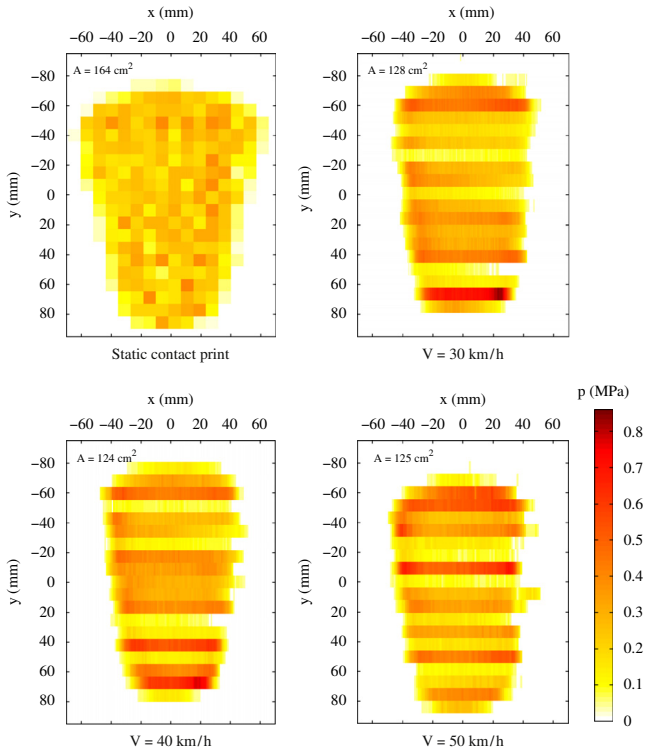


Figure 1.36 – Contact patches measured statically and reconstructed from the "transverse tests" at 30, 40 and 50 km/h for the DAC 0/10 (new) road surface [Cesbron et al., 2009a].

In the case of longitudinal tests, contact pressures are measured along the activated line of sensors at each time step. One example is given in Figure 1.37. Resultant contact forces calculated by integrating measured pressures for one road surface but different rolling speeds are plotted as a function of $t$ or $Vt$ in Figure 1.38. The signals are similar for the three rolling speeds, and this could be explained by the effect of the road texture. However, significant variations can be observed in the modified force spectra plotted in one-third octave bands for different rolling speeds (Figure 1.39). This result may be due to the dynamic characteristics of the tyre. Thus, the quasi-static contact assumption would not be verified experimentally.

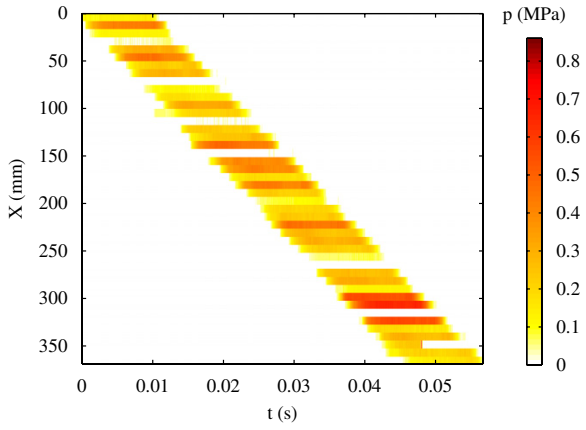


Figure 1.37 – Contact pressures measured at 3 km/h for the DAC 0/10 (old) road surface in the case of the "longitudinal tests" [Cesbron et al., 2009a].

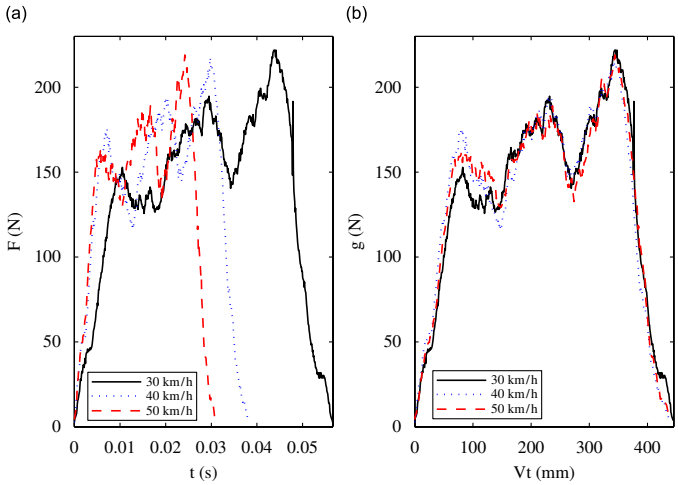


Figure 1.38 – Contact forces obtained from the "longitudinal tests" at 30, 40 and 50 km/h for the DAC 0/10 (old) road surface: (a) resultant contact forces $F(t)$ and (b) associated functions $g(Vt)$ [Cesbron et al., 2009a].

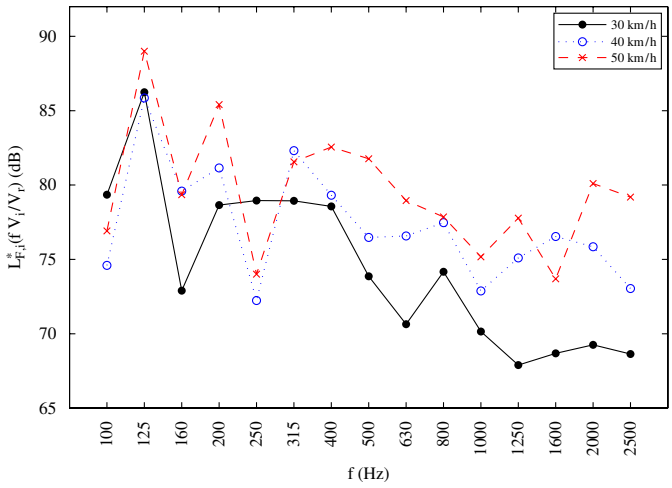


Figure 1.39 – Modified spectra in one-third octave bands of the resultant force at 30, 40 and 50 km/h for the DAC 0/10 (old) road surface with the reference speed $V_r$ = 30 km/h [Cesbron et al., 2009a].

### 1.3.2 Tyre vibrations and noise

Périsse [2002] investigated two motions composing the tyre vibrations: stationary motion of a smooth tyre rolling on a smooth road, bending wave motion due to unsteady tyre/road interactions. Two accelerometers, numbered 1 and 2 in Figure 1.40, are mounted onto the inner surface of the tread and the sidewall, respectively. The tyre first rolls on a smooth road surface. During the contact, a plateau phase can be observed for the acceleration. In Figure 1.41, the acceleration signals during one third revolution around the contact zone are compared for three different rolling speeds, i.e., 40, 60 and 80 km/h. Results show that the acceleration amplitude is proportional to the square of the tyre rolling speed.

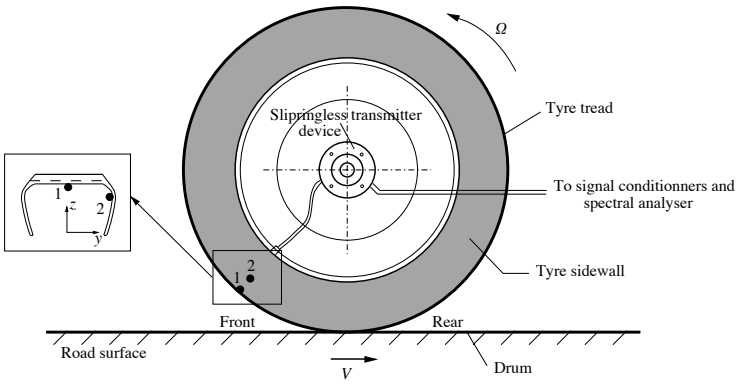


Figure 1.40 – Experimental set-up for tyre radial acceleration measurements [Périsse, 2002].

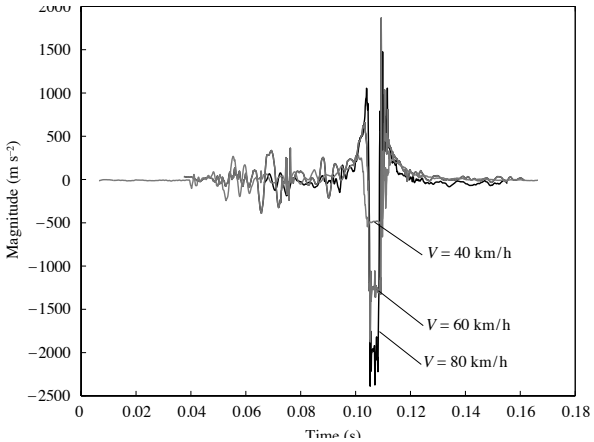


Figure 1.41 – Stationary acceleration signals of the tread in the vicinity of the contact area for three rolling speeds [Périsse, 2002].

Next, the tyre rolls on two rough surfaces composed of either an isolated step singularity or a set of such singularities. Acceleration signals measured from both accelerometers at a rolling speed of 60 km/h over one revolution represent a superimposition of the stationary acceleration signals and the vibration responses due to the road roughness.

Kindt et al. [2009b] performed experimental analysis of structure-borne tyre/road noise due to road discontinuities and parametric influences on noise generation. Two identical tyres rolling against each other are used. Thus, the static deformation of each tyre is equal to that of a tyre loaded on a flat road surface. For simulation of the impact on the tyre, a cleat is mounted onto the driven tyre and can easily be replaced by a cleat in another dimension. Photos of the experimental set-up and the measuring equipments are shown in Figure 1.42. The spindle forces and moments are measured by the multi-axial wheel hub dynamometer. Different influencing factors such as rolling speed, inflation pressure, static preload, temperature and cleat dimension are studied by analysing the spindle force spectra. The parameter causing the most significant variations is the rolling speed. The greatest peak values for the three rolling speeds (15.71, 26.18 and 31.42 rad/s) are identified for the (1,0) vertical resonance and appear around 80 Hz. The vertical resonances are found at low frequencies (below 400 Hz). Certain modes cannot be well excited by the cleat at certain speed.

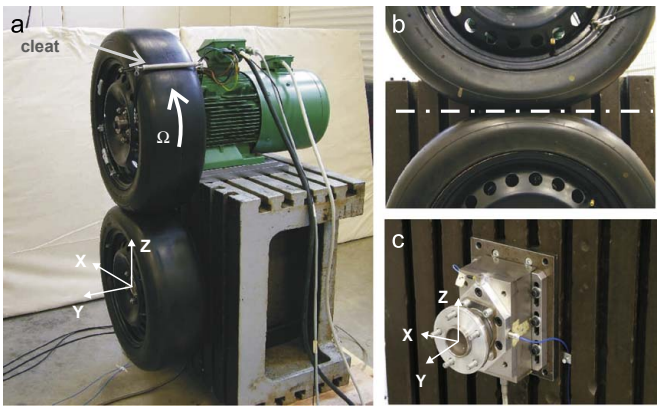


Figure 1.42 – (a) Test setup with two tyres mounted; (b) static tyre deformation due to preload; and (c) multi-axial wheel hub dynamometer [Kindt et al., 2009a].

## 1.4 Discussion and conclusions

This literature review tries to cover the major attempts to understand the rolling noise generation mechanisms using theoretical or experimental methods. Based on classical theories in contact mechanics, many studies have been carried out on the static tyre/road contact problem. Nevertheless, the dynamic contact problem has only been modelled under simplifying assumptions and little investigated through experiments.

Thus, the following chapters propose investigations into:

- the influence of rolling speed on dynamic contact forces, including the effect of speed on contact force magnitude and possible effect on the local load/penetration relationship;
- the interaction between asperities and the distribution of dynamic forces under rolling conditions;

For these purposes, a test rig has been designed and fabricated for experiments that are expected to provide an insight into the validity of the classical contact mechanics theories, and, if necessary, how they are to be corrected due to the influence of the speed on dynamics contact forces. Once the punctual contact law is established for the dynamic case, the test bench is to be used to analyse the interaction between asperities by measuring the distribution of dynamic forces for different combinations of asperity geometries.

# Chapitre 2 : Caractérisation du pneumatique de taille réduite intégré au banc d'essai

Afin d'étudier les forces de contact dynamique en conditions de laboratoire maîtrisées, un banc d'essai cylindrique a été développé à l'Ifsttar afin de simuler une surface de chaussée sur laquelle un pneumatique de taille réduite roule. Il s'agit d'un pneumatique de karting de surface lisse et de taille 114/55 R5, soit des dimensions environ réduites de moitié par rapport à un pneumatique de véhicule léger standard. Ce chapitre concerne la caractérisation vibratoire du pneumatique ainsi que l'analyse du contact statique entre le pneumatique et une surface lisse.

Dans un premier temps, l'analyse modale expérimentale du pneu en conditions libres est menée. Une approche SIMO (Single-Input Multiple-Output) classique est utilisée pour les essais. Le pneu est suspendu à l'aide de tendeurs à une structure rigide et excité par un pot vibrant délivrant un signal aléatoire. Les accélérations sont mesurées en plusieurs points à l'aide d'accéléromètres collés à la surface du pneu. Les propriétés de symétrie sont vérifiées et exploitées lors des essais. Trois pressions de gonflage différentes (0, 1 et 2 bars) sont étudiées. Les Fonctions de Réponse en Fréquence (FRF) mesurées sont traitées afin d'extraire les fréquences propres et les taux d'amortissement du pneu. La méthode RFP (Rational Fraction Polynomial) globale est utilisée et consiste à utiliser une fraction rationnelle polynomiale pour identifier les paramètres modaux. Au final, 8 modes propres sont identifiés entre 280 Hz et 1200 Hz. Leur forme est conforme aux résultats de la littérature, de même que l'influence de la pression de gonflage est retrouvée. L'accord entre FRF mesurées et synthétisées est bon, aussi bien au point d'excitation qu'aux points de transfert.

Une modélisation par éléments finis sous Abaqus est ensuite proposée pour l'analyse modale du pneu. Plusieurs degrés de complexité sont testés pour la structure interne du pneu : section composée d'un matériau homogène élastique, puis viscoélastique, avant de terminer par une section hétérogène constituée d'une bande de roulement viscoélastique et de couches de nylon constituant la ceinture du pneu. Dans le cas homogène élastique, un bon accord avec les résultats expérimentaux est obtenu, mais d'une part l'amortissement expérimental doit être utilisé pour calculer les FRF et d'autre part le modèle, trop rigide, sous-estime l'empreinte de contact statique. Le modèle homogène viscoélastique permet d'intégrer la dissipation intrinsèque à la gomme en se basant sur une série de Prony identifiée à partir du module complexe mesuré sur visco-analyseur. Les taux d'amortissement sont alors conformes à l'expérience mais, la structure devenant moins rigide, les fréquences propres sont décalées vers les basses fréquences. L'introduction des couches de nylon dans le modèle hétérogène permet de compenser cet effet et donne des FRF proches de l'expérience. De plus, l'ajout de l'hyper-viscoélasticité permet d'obtenir une empreinte de contact conforme aux mesures.

La dernière partie du chapitre s'intéresse au contact statique entre le pneu et une surface lisse. Les mesures d'empreinte au papier Fuji sur une plaque montrent une diminution de l'aire de contact totale lorsque la pression de gonflage du pneu augmente. L'aire de contact augmente avec la charge totale appliquée, en raison d'une augmentation de la largeur de l'empreinte dans le sens longitudinal (la dimension transversale varie peu). La Méthode d'Inversion de Matrice (MIM), basée sur une hypothèse de massif semi-infini, est ensuite optimisée en exploitant les symétries des géométries en contact. Les résultats de la MIM montrent qu'il est possible d'obtenir des empreintes de contact similaires à l'expérience en adaptant convenablement le module élastique pour chaque configuration. Enfin, des mesures de contact statique sont effectuées sur le bâti cylindrique du banc d'essai. La courbure de ce dernier influence peu les aires de contact dont la dimension longitudinale diminue toujours lorsque la charge totale augmente. Le contact est également mesuré

après avoir atteint une température stabilisée de la gomme pour différentes vitesse de roulement (5, 10 et 15 m/s). Les aires de contact diminuent légèrement avec la vitesse, démontrant une diminution du module élastique de la gomme avec la température (effet viscoélastique).

# Chapter 2

# Characterisation of the reduced-sized tyre incorporated to the test rig

## 2.1 Introduction

To examine the dynamic contact forces under well-controlled laboratory conditions, a cylindrical test rig has been built at IFSTTAR to simulate a road surface on which a smooth go-kart tyre will be rolling. The go-kart tyre, due to its reduced size and consequently its reduced mass, will be easier to manipulate in laboratory and will have less inertial effects during rotations, relative to a standard tyre. Moreover, the latter, composed of multiple layers of different materials, will present more difficulties in modelling, hence the choice of using a go-kart tyre with a simplified inner structure on the test rig. Figure 2.1 gives a picture of the whole system. A concrete ring with an outer diameter of 2 m is placed horizontally and remains immobile. A horizontal steel beam is maintained at a certain vertical distance above the concrete ring and can be driven to rotate about the axle of the latter by a motor. A reduced-sized pneumatic tyre, inflated to 1 bar, is mounted horizontally onto a vertical spindle which connects it to one end of the steel beam. The beam is free to translate longitudinally along a slide rail installed in the middle of the system and is actuated by a pneumatic jack installed beneath the beam to maintain a constant force exerted radially on the tyre. To balance the inertial effects during rotations, an extra mass is added to the other end of the beam with its weight so calculated that the centre of mass of the rotating components is on the axis of rotation. Thus, the system can be considered in equilibrium in the rotating reference frame because the resultant centrifugal force is zero for any rotational speed.

The exterior surface of the test rig simulates a concrete road surface on which the tyre will be driven to roll. The reduced-sized tyre used in this work is a slick commercial go-kart tyre from the manufacturer Duro. The tyre code indicating its size is 10-4.50-5: the first number (10) is the height of the tyre in inches, the second number (4.50) is the width of the tyre tread in inches and the last number (5) indicates the diameter of the rim in inches. These dimensions correspond to 114/55R5 in the ISO Metric sizing system. The dimensions are also illustrated in Figure 2.2[1]. Compared with a slick car tyre having a size of 205/55R16 used in another study [Kindt et al., 2006], the go-kart tyre is approximately 40% large in diameter and 56% in width. The tyre tread is composed of a thin rubber layer, the carcass has two rubber coated nylon layers and the bead is reinforced by steel wires. The maximal inflation pressure is 3.9 bars.

[1] Source: http://www.kartpartsdepot.com/Go_Kart_Wheels_s/1850.htm

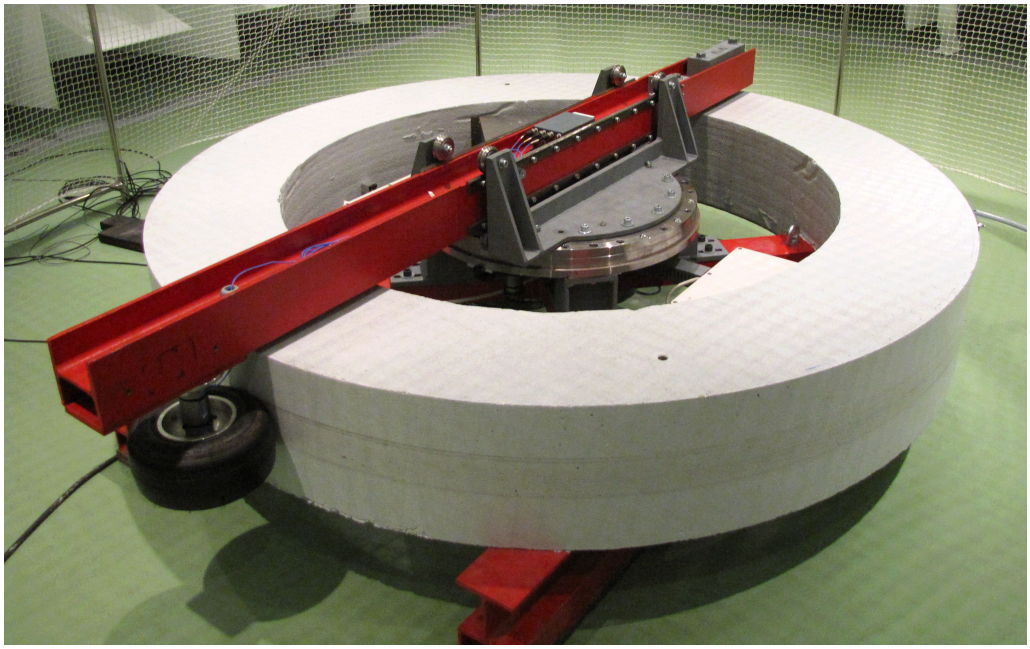

Figure 2.1 – Test rig designed at IFSTTAR for tyre/road dynamic contact measurements.


Figure 2.2 – Dimensions of the go-kart tyre incorportated to the test rig.

The choice of a reduced-sized tyre is on account of the ease of experimental manipulation and numerical modelling. During the concrete casting process, a rectangular parallelepiped volume was left out on the exterior surface of the test rig. This cavity allows a metallic plate hosting a set of asperities to be mounted, as shown in Figure 2.3 for a single asperity. The metallic plate was curved during machining to have the same curvature radius as the concrete ring.

## 2.2 Modal analysis of the reduced-sized tyre under free boundary conditions

The present section focusses on both experimental and FE (Finite-Element) modal analyses of the aforementioned pneumatic tyre, a reduced-sized one, to be used for experimental investigation of tyre/road interaction in laboratory. The section starts with a description of the modal testing technique and results. Next, FE tyre modelling approaches with increasing complexity are intro-

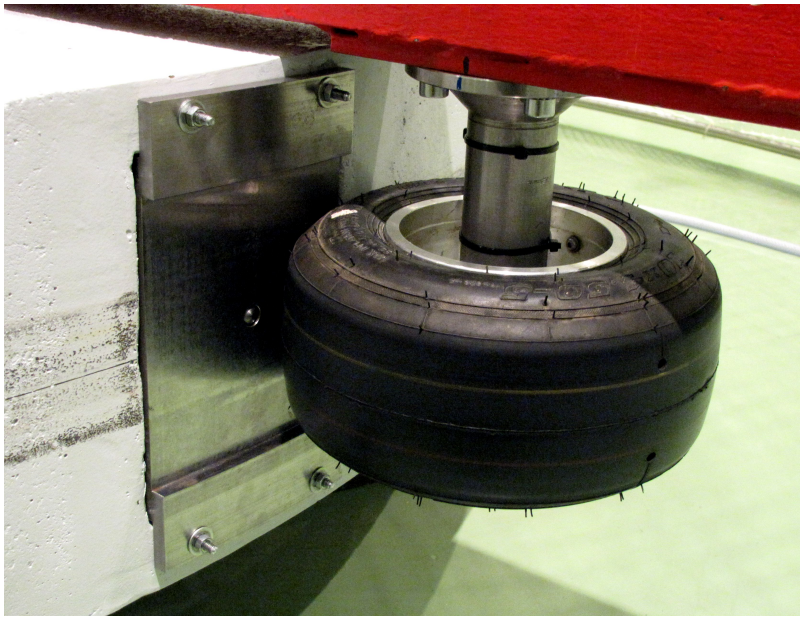

Figure 2.3 – A metallic plate hosts a single asperity connected to a force transducer for normal contact force measurement.

duced. For each model, a numerical modal analysis is carried out, and the results are compared with experiment. The possible uses of the models are discussed before concluding remarks.

### 2.2.1 Experimental modal analysis

#### 2.2.1.1 Experimental set-up

Modal tests with a classical SIMO (Single-Input Multiple-Output) approach were performed for 3 different tyre inflation pressures, respectively 0, 1 and 2 bars, at an ambient temperature of 20 °C. The experimental set-up shown in Figure 2.4 was similar to those used in the literature [Kindt et al., 2006, Andersson et al., 2004]. All the transducers were connected to a data acquisition front-end (hardware: Brüel & Kjær PULSE front-end; software: Brüel & Kjær PULSE Labshop v. 14.0.0.124) from which the data were saved and then processed with a software dedicated to modal analysis (Brüel & Kjær PULSE Reflex Modal Analysis Type 8721). To achieve a relatively complete and reliable exploration of the geometrical influences of the tyre on the modal parameters, measurements were carried out at points all around the tyre, spanning from the central rolling band to the sidewalls. The measurement points were marked on the outer contours of 48 cross-sections, evenly spaced in the circumferential direction, on each of which 5 equidistantly aligned points were symmetrically placed on both sides about the median point, leading to a total of 528 measurement points (Figure 2.5). The cross-sections were numbered from 0 to 47 with the median point of the cross-section number 0 being the drive point, onto which a square aluminium plate of edge length 10 mm was attached. An impedance head (PCB Piezotronics Model 288D01) was screwed onto the mounting plate. It measured the input force and the output acceleration at the drive point, thus the direct FRF (Frequency Response Function). The tyre, inflated to the desired pressure, was then horizontally suspended. A shaker (Brüel & Kjær Modal Exciter Type 4824) was connected to the impedance head by a stinger to exercise a radial excitation force on the tyre, as shown in Figure 2.4. Figure 2.5 illustrates how 5 lightweight single-axis accelerometers (PCB

Piezotronics Model 352A24) were repeatedly mounted onto a set of points on the upper or lower part of a cross-section with petro-wax, allowing a good temporary bonding that could be quickly removed.

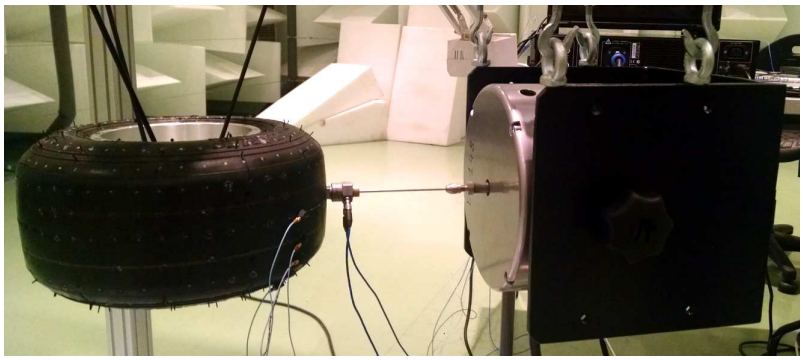

Figure 2.4 – Shaker attached to the suspended reduced-sized tyre.

Figure 2.5 – Impedance head and accelerometers mounted onto the suspended reduced-sized tyre.

To start a measurement, a random white noise signal between 0 and 6000 Hz was generated by the acquisition software and then increased by an amplifier to drive the shaker. Once the stationary state had been reached, the input force and the direct and transfer output accelerations served to calculate the complex accelerance FRFs $H_1(\omega) = S_{FA}(\omega)/S_{FF}(\omega)$ and $H_2(\omega) = S_{AA}(\omega)/S_{AF}(\omega)$, as defined in [Ewins, 2000], where $\omega = 2\pi f$ is the angular frequency, $S_{FF}$ is the power spectral density of the input signal $F$, $S_{AA}$ is the power spectral density of the output signal $A$, $S_{AF}$ and $S_{FA}$ are the cross power spectral density of the input and output signals. The coherence $C_{FA}(\omega)$ is classically defined by the ratio between $H_1(\omega)$ and $H_2(\omega)$. Its value is situated between 0 and 1 and helps verify the linear link between the drive point and the transfer points. Ideally, the two estimates of FRFs should be identical, thus the coherence should be 1.

All of the 528 measurement points were investigated for the tyre inflation pressure of 1 bar. The coherence value remained very close to 1 in most of the cases, especially under 3000 Hz, suggesting that using either $H_1(\omega)$ or $H_2(\omega)$ for modal parameter extraction was appropriate. The

magnitudes and the phase angles of the complex FRFs $H_1(\omega)$ were used for validations of geometrical symmetries. This was first done for the symmetry about the median plane of the tyre. The curves proved to be coherent and therefore allowed to check the symmetry of measurements about the excitation direction, which also turned out to be true. These symmetries led to the conclusion that the measurements for 0 and 2 bars needed only to be performed between 0 and 90° on a half section of the tyre. These symmetries will also be used in Section 2.2.2 for numerical modal analysis.

#### 2.2.1.2 Modal identification method

The measurement results were then imported into the software PULSE Reflex Modal Analysis[2]. The geometry of the quarter of the tyre was built and the FRFs were attributed to the associated point coordinates. The global RFP (Rational Fraction Polynomial) method was chosen to extract modal frequencies and damping ratios from the imaginary part of the complex FRFs, as recommended in [Ewins, 2000] and [Gatti, 2014]. In this method, the complex FRF in the frequency domain $H(\omega)$ generally expressed as:

$$H(\omega) = \sum_{k=1}^{N} \frac{A_k}{\omega_k^2 - \omega^2 + 2i\omega\omega_k\zeta_k}, \tag{2.1}$$

where $N$ is the number of modes composing the FRF, $A_k$ the $k$th complex modal constant, $\omega_k$ the $k$th natural frequency and $\zeta_k$ the $k$th modal damping ratio, is alternatively formulated as a rational fraction, i.e. a ratio of two polynomials:

$$H(\omega) = \frac{\sum_{k=0}^{2N-1} a_k(i\omega)^k}{\sum_{k=0}^{2N} b_k(i\omega)^k}, \tag{2.2}$$

where $a_k$ and $b_k$ are the polynomial coefficients. The coefficients are identified by minimising the error $e_f$ between the calculated FRF and the measured one $\tilde{H}(\omega_f)$ for each of the measured frequencies $\omega_f$:

$$e_f = \sum_{k=0}^{2m-1} a_k(i\omega_f)^k - \tilde{H}(\omega_f)\sum_{k=0}^{2m} b_k(i\omega_f)^k, \tag{2.3}$$

where $m$ is the mode order selected for analysis, and the subscript $f$ indicates variables related to measurements. In fact, the global curve-fitting approach in this method can be done in a frequency band chosen to include a certain number of modes. The CMIF (Complex Mode Indicator Function) was used for preliminary quality checks of the measured data. The curve-fitting frequency range was chosen to be from 280 to 1200 Hz to include the few modes that are identifiable from visual inspection, since peak magnitudes are found at natural frequencies in the imaginary part of accelerance [Ewins, 2000, Gatti, 2014].

[2]Product description available on: `http://www.bksv.com/Products/analysis-software/vibration/structural-dynamics/classical-modal-analysis/advanced-modal-analysis-8720-8721?tab=descriptions`

Based on the extracted modal parameters, a synthesised FRF was plotted for each measurement point for comparison with experiment. The extracted modal parameters could contain erroneous results, hence the validation step. The AutoMAC technique was used by looking at the correlation of a set of modes with themselves. The higher the mode order is, the more likely the mode is correlated with other ones. To determine which modes had to be eliminated, several factors needed to be considered: aberrant damping ratio; strong correlations with other modes; clearly false results from visual inspections of the FRFs; correlation degradation of the synthesised FRFs with the measured ones.

#### 2.2.1.3 Results

Finally, the frequencies and damping ratios of the retained eigenmodes were identified for each inflation pressure. They are given in Table 2.1 for the inflation pressure of 1 bar. The damping ratios are relatively homogeneous and ranged between 4.6% and 6.2%. It can be seen from Figure 2.6 that the modal frequency increases with the tyre inflation pressure at low frequencies due to the stiffening of the tyre structure with inflation pressure. This is consistent with literature results [Kung et al., 1985].

Table 2.1 – Modal parameters extracted from the measurements for the tyre inflation pressure of 1 bar.

| Mode | 1 | 2 | 3 | 4 | 5 | 6 | 7 | 8 |
|---|---|---|---|---|---|---|---|---|
| $f$(Hz) | 310 | 357 | 416 | 505 | 602 | 726 | 850 | 1000 |
| $\zeta$(%) | 4.9 | 5.4 | 4.6 | 6.2 | 5.9 | 5.6 | 5.8 | 5.3 |

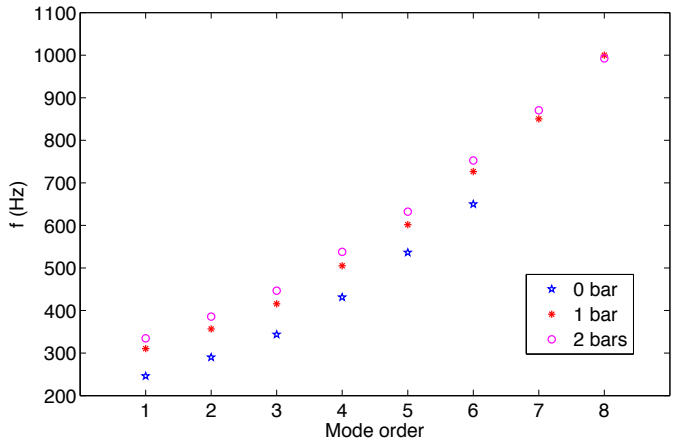


Figure 2.6 – Modal frequencies of the reduced-sized tyre for inflation pressures of 0, 1 and 2 bars. Eights modes are identified for 1 and 2 bars and six modes for 0 bar as higher modes are difficultly indentifiable in the latter case.

Mode shapes are plotted in two dimensions for the first five modes in Figure 2.7 by considering only the median measurement points. The mode shapes are simply the displacements of measurement points added to their initial positions around the tyre circumference. Having already calculated the complex accelerations due to a unit force, i.e. the accelerance FRFs, the displacements due to a unit force can be readily obtained by dividing the accelerance values by $-\omega^2$. Higher modes are not visually identifiable.

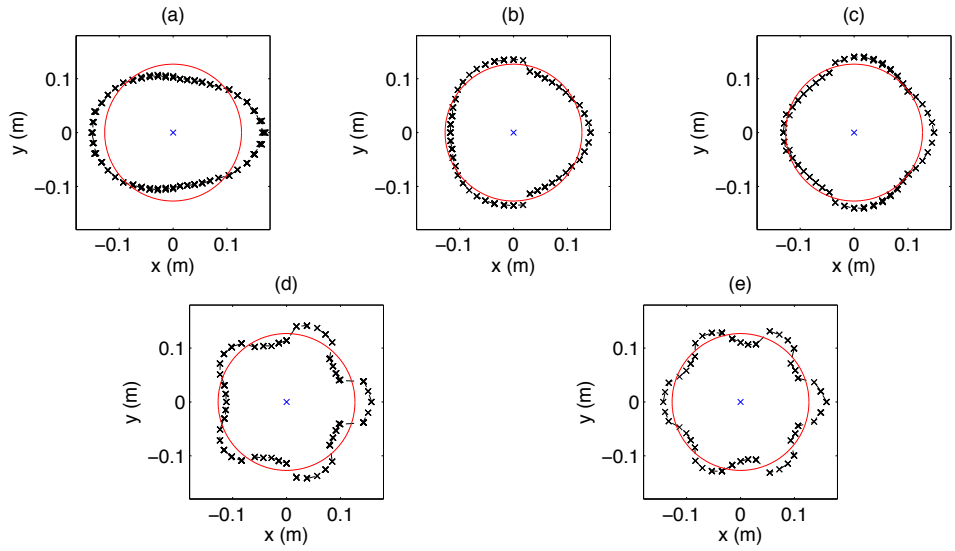


Figure 2.7 – Experimentally obtained mode shapes for mode orders $m = 1$ to 5: (a) oval ($m = 1$), (b) triangle ($m = 2$), (c) square ($m = 3$), (d) pentagon ($m = 4$) and (e) hexagon ($m = 5$).

Figures 2.8 and 2.9 represent the magnitude and the phase angle of the directly measured and the synthesised accelerance FRFs respectively at the drive point and at a point making an angle of 90° with the drive point about the tyre axle. The synthesised FRFs correlate well the experimental curves over the curve-fitting frequency range from 280 to 1200 Hz.

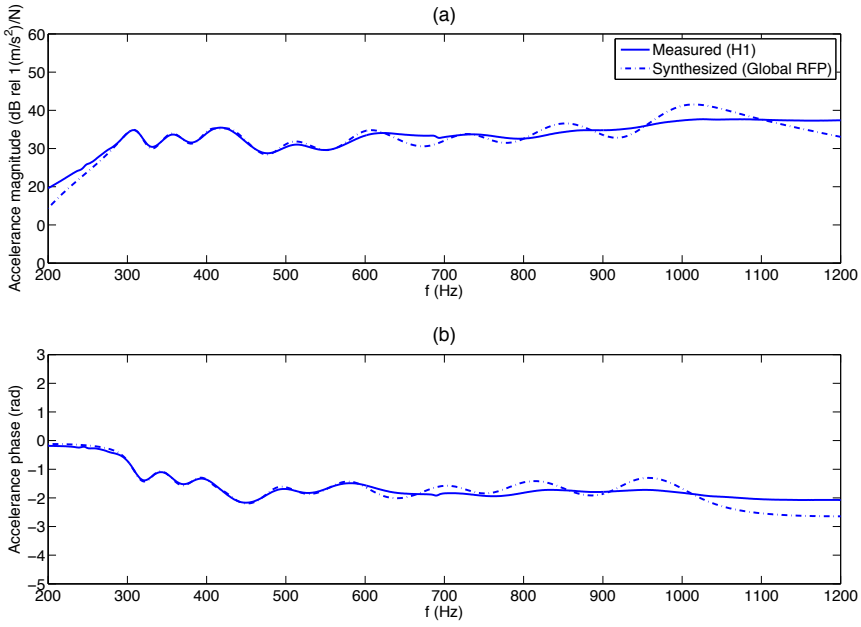


Figure 2.8 – Directly measured (H1) and synthesised (Global RFP) accelerance FRFs at the drive point for the tyre inflation pressure of 1 bar: (a) magnitude and (b) phase angle.

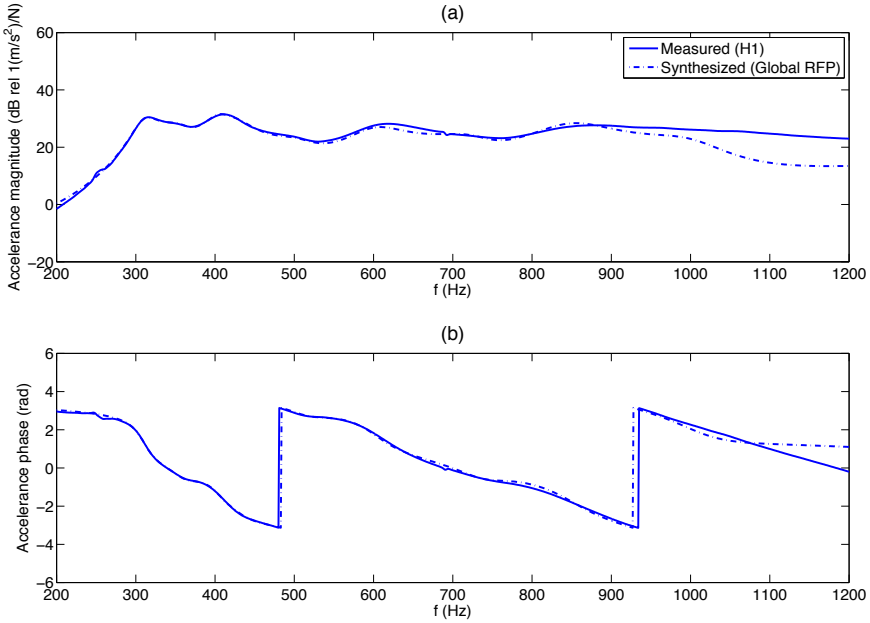


Figure 2.9 – Directly measured (H1) and synthesised (Global RFP) accelerance FRFs at a transfer point at 90° for the tyre inflation pressure of 1 bar: (a) magnitude and (b) phase angle.

## 2.2.2 Numerical modelling approaches

### 2.2.2.1 Elastic homogeneous model

A simplified FE modelling approach is first used to simulate the vibrational nature of the tyre carcass. The main idea is to model the tyre cross-section with a homogeneous and linearly elastic material and then seek a Young's modulus that allows the tyre model to reproduce similar vibrational characteristics as from the measurements. The FE model is developed using Abaqus software (v. 6.14) for the unloaded tyre on which a numerical frequency response analysis is carried out respectively for three inflation pressures: 0, 1 and 2 bars. On the one hand, the experimental and the numerical modal analysis results could be mutually validated with the calculated natural frequencies tuned to fit the measured ones; on the other hand, the numerical model could be used in combination with a contact model for further analyses of tyre/road rolling noise problem.

The geometry is constructed in three steps as shown in Figure 2.10. To take the pressurisation of the tyre into account, a distributed load corresponding to the tyre inflation pressure is applied onto the inner side of the tyre. First, an axisymmetric model representing a half cross-section is built and meshed; second, the geometrical deformations of the tyre under pressurisation are transferred into a partial 3D (three-dimensional) model by revolving the axisymmetric model about the tyre axle to form a half of the tyre; third, the results are transferred into a full 3D model by reflecting the geometry about the median plane of the tyre [Dassault Systèmes, 2014]. The structure of the tyre half cross-section is simplified as a single layer of rubber, considered as an elastic material. Its density is defined as being equal to 1100 kg/m$^3$, the Young's modulus 112 MPa and the Poisson's ratio 0.48. The half cross-section is composed of 129 CGAX4H (4-node bilinear, hybrid with constant pressure) elements. One revolution of the axisymmetric model results in 96 element subdivisions. The inflation pressure is applied once again in the new model to ensure the accuracy of calculation. The connection between the rim and the part of the tyre on which the rim

is mounted is defined as a rigid body constraint. The displacements of the nodes and elements in the median plane are confined within the plane due to the reflection symmetry.

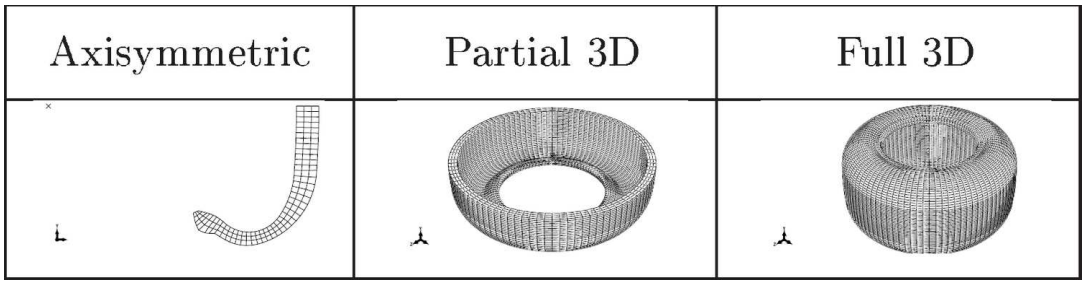


Figure 2.10 – Geometry construction using symmetric results transfer in Abaqus.

The natural frequencies between 0 and 1050 Hz were extracted for the full 3D model with the Lanczos eigensolver [Dassault Systèmes, 2014]. More frequencies were identified than experimentally. The additional modes include two modes with one wavelength and one axisymmetric mode with rotation. The frequency values are listed in Table 2.2. By comparing frequencies of mode orders $m$ = 3 to 10 with corresponding experimental values of mode orders $m$ = 1 to 8 presented in Table 2.1, a fairly positive correlation is observed. Except for the axisymmetric mode, at the same frequency, two different modes having the same mode shape with a phase shift appear due to the axisymmetry of the tyre model, as stated in [Kindt et al., 2006] and [Ewins, 2000].

Table 2.2 – Modal frequencies extracted from the elastic homogeneous FE model for the tyre inflation pressure of 1 bar.

| Mode | 1 | 2 | 3 | 4 | 5 | 6 | 7 | 8 | 9 | 10 |
|---|---|---|---|---|---|---|---|---|---|---|
| $f$(Hz) | 291 | 302 | 310 | 355 | 419 | 502 | 605 | 729 | 871 | 1031 |

Mode shapes ($m$ = 3 to 7) obtained with the FE model represented in Figure 2.11 are the same as those ($m$ = 1 to 5) in Figure 2.7. Mode shapes $m$ = 1 and 2 are illustrated in Figure 2.12.

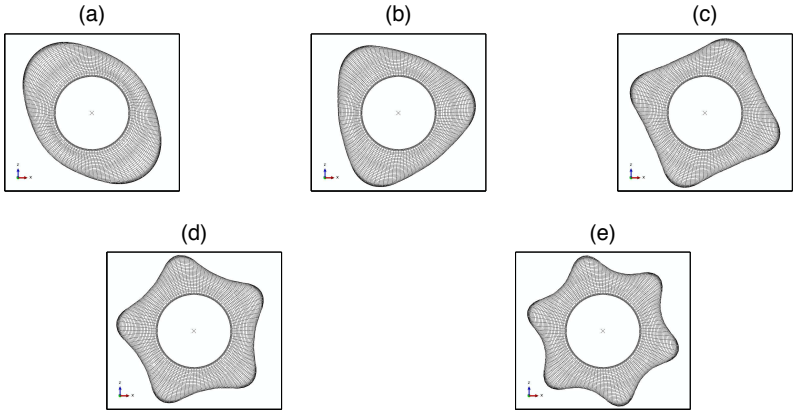


Figure 2.11 – Numerically calculated mode shapes for mode orders $m$ = 3 to 7: (a) oval ($m$ = 3), (b) triangle ($m$ = 4), (c) square ($m$ = 5), (d) pentagon ($m$ = 6) and (e) hexagon ($m$ = 7).

The next step was to perform a Steady-State Dynamic analysis of the tyre to calculate the FRFs from the FE model. The input excitation force was modelled by a unit force applied at

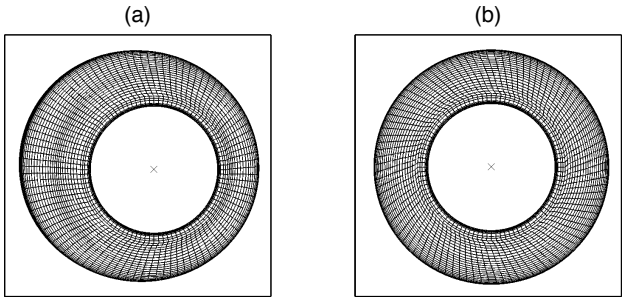


Figure 2.12 – Numerically calculated mode shapes for mode orders $m = 1$ and 2: (a) with one wavelength ($m = 1$), (b) axisymmetric ($m = 2$).

the drive point node in the middle of the tread. Thus, according to the definition of accelerance, the radial output accelerations at an investigated point gave directly the accelerance FRF. Abaqus allows the option to specify the modes to be considered in this analysis from the aforementioned frequency extraction step and to attribute an experimentally determined modal damping ratio to the corresponding mode. Figures 2.13 and 2.14 represent, in addition to experimental results, the numerically calculated accelerance at the drive point and the transfer point at 90° obtained by including only the modes reported in Table 2.2. The agreement is good from 280 Hz up to 800 Hz.

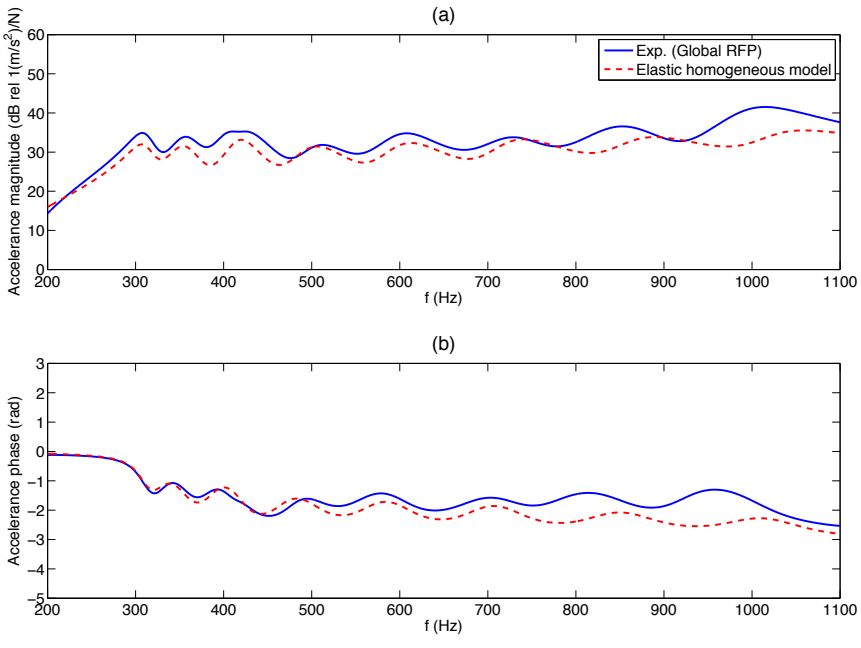


Figure 2.13 – Experimental accelerance FRFs at the drive point for the tyre inflation pressure of 1 bar in comparison with numerically calculated FRFs from the elastic homogeneous FE model: (a) magnitude and (b) phase angle.

When comparing the results obtained with the partial 3D and the full 3D model, no significant differences are stated. Therefore, further modal analyses will be carried out on partial 3D models.

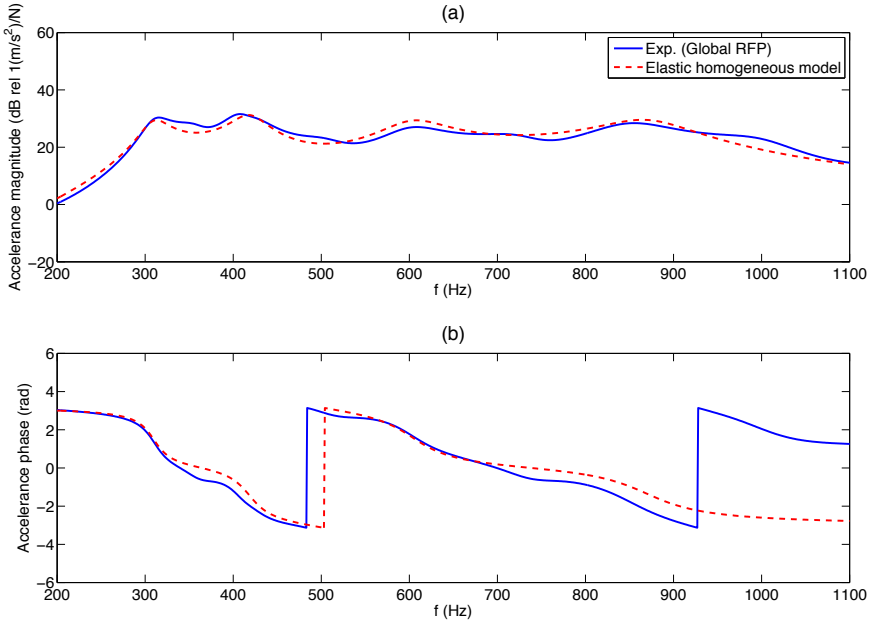


Figure 2.14 – Experimental accelerance FRFs at a transfer point at 90° for the tyre inflation pressure of 1 bar in comparison with numerically calculated FRFs from the elastic homogeneous FE model: (a) magnitude and (b) phase angle.

#### 2.2.2.2 Viscoelastic homogeneous model

The aforedescribed elastic homogeneous model uses a unified Young's modulus for the whole tyre structure. However, since rubber is a rate-dependent material, the damping of the tyre under small perturbations relies on the viscoelasticity of rubber. A second model takes into account this aspect and therefore tends to be closer to the reality. The rubber's viscoelasticity is described using a Prony series which was measured in a uniaxial tension test. A specimen of the rubber was taken from the central part of the rolling band of the tyre and cut into a 10 mm × 5 mm × 5 mm parallelepiped. The specimen was placed on a platform in a dynamic mechanical analyser (Metravib Viscoanalyser) as shown in Figure 2.15 and glued at both ends. The measurements were performed for five temperatures in the following order: 50, 40, 30, 20 and 10 °C. For each temperature, perturbations with a constant amplitude of 5 µm were applied to the specimen with 11 frequencies ranging from 1 to 120 Hz on a logarithmic scale, and the corresponding complex moduli $|E^*|$ and phase angles $\delta$ were measured.

The next step was to construct a master curve using the measured isotherms with the reference temperature equal to 20 °C, i.e. the ambient temperature at which the experimental modal tests were carried out. Having no knowledge beforehand on the type of rubber in question, this was done using a mathematical method [Chailleux et al., 2006] based on Booij and Thoone's approximation [Booij and Thoone, 1982] which yields the shift factor for a certain isotherm related to a reference temperature according to the time-temperature superposition principle. Figure 2.16 shows the continuous master curves formed with isotherms that overlap with neighbouring ones. The upper graph represents the complex modulus E* and the lower one, the phase angle $\delta$, both as functions of frequency. The complex modulus rises with frequency within the frequency range to be considered for modal analysis. The phase angle has a value situated between 8° and 9° which is almost constant over the frequency range concerned.

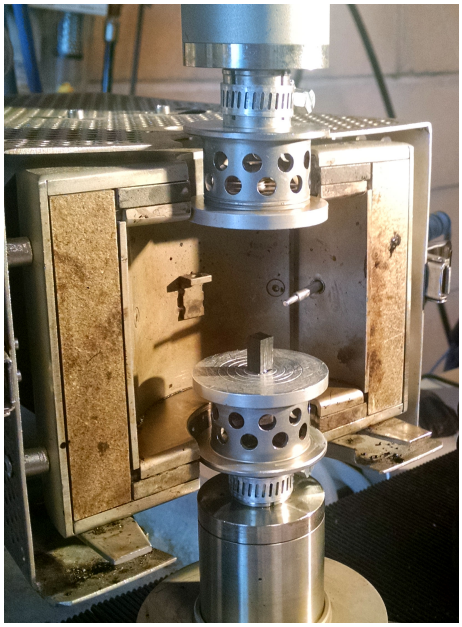

Figure 2.15 – A dynamic mechanical analyser (Metravib Viscoanalyser) in which a specimen prepared for a uniaxial tension test is placed.

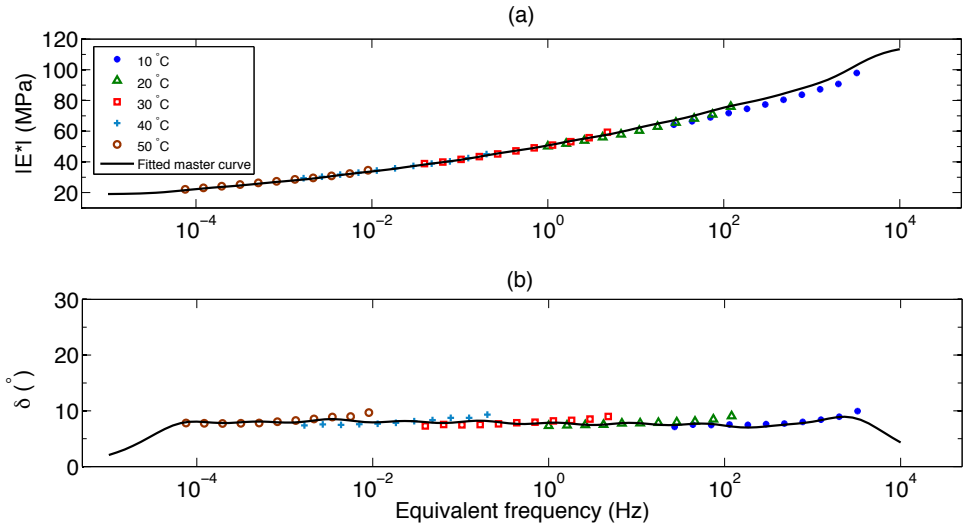


Figure 2.16 – Master curves constructed for a reference temperature of 20 °C based on the time-temperature superposition principle: (a) complex modulus $|E^*|$ (MPa) and (b) phase angle $\delta$ (°). The master curves constructed based on experimental data are plotted as dots, while the fitted curves are plotted as lines for comparison.

The frequency-dependent parameters $E^*(\omega)$ and $\delta(\omega)$ are related to the storage and loss moduli, $E_s(\omega)$ and $E_l(\omega)$, as described in the following equations:

$$E^*(\omega) = E_s(\omega) + iE_l(\omega), \tag{2.4}$$

$$\delta^*(\omega) = arctan\frac{E_l(\omega)}{E_s(\omega)}. \tag{2.5}$$

Abaqus systematically considers the Prony series parameters from a shear test. In the instance of an incompressible material like rubber, the shear storage and loss moduli, $G_s(\omega)$ and $G_l(\omega)$, are simply one third of the respective uniaxial storage and loss moduli, $E_s(\omega)$ and $E_l(\omega)$. Therefore, the relations that are valid for shear tests can also be used for the uniaxial tension test. By using a fitting method [Chailleux et al., 2010], parameters $E_\infty$, $\bar{g}_i^P$ and $\tau_i$ were determined based on the measured master curves. The term $E_\infty$ represents the modulus at $f = 0$, and $\bar{g}_i^P$ is the modulus ratio in the $i$th term in the Prony series expansion of the traction relaxation modulus whose corresponding relaxation time is $\tau_i$. These parameters describe the storage and loss moduli as follows:

$$E_s(\omega) = E_0[1 - \sum_{i=1}^{N} \bar{g}_i^P] + E_0 \sum_{i=1}^{N} \frac{\bar{g}_i^P \tau_i^2 \omega^2}{1 + \tau_i^2 \omega^2}, \tag{2.6}$$

$$E_l(\omega) = E_0 \sum_{i=1}^{N} \frac{\bar{g}_i^P \tau_i \omega}{1 + \tau_i^2 \omega^2}, \tag{2.7}$$

where $E_0$ is the instantaneous modulus, i.e. the modulus at $t = 0$, and is expressed as follows:

$$E_0 = \frac{E_\infty}{1 - \sum_{i=1}^{N} \bar{g}_i^P}, \tag{2.8}$$

The identified value of the long-term modulus $E_\infty$ is 18.97 MPa. A Prony series with 10 elements yields a good agreement between the experimental and calculated master curves as shown in Figure 2.16. The identified values of $\bar{g}_i^P$ and $\tau_i$ are presented in Table 2.3.

Table 2.3 – Prony series parameters $\bar{g}_i^P$ and $\tau_i$.

| $\bar{g}_i^P$ | $\tau_i$ |
|---|---|
| 0.2355 | 4.910E-05 |
| 0.0911 | 3.462E-04 |
| 0.1051 | 2.440E-03 |
| 0.0871 | 1.720E-02 |
| 0.0727 | 1.213E-01 |
| 0.0669 | 8.551E-01 |
| 0.0530 | 6.029E+00 |
| 0.0496 | 4.250E+01 |
| 0.0355 | 2.996E+02 |
| 0.0394 | 2.112E+03 |

The parameters $E_\infty$, $\bar{g}_i^P$ and $\tau_i$ replace therefore the linear elastic modulus of 112 MPa used in the elastic homogeneous model and describe the viscoelastic behaviour in the frequency domain of the rubber that fills the whole tyre section. The first eight circumferential modes were extracted for this viscoelastic homogeneous partial 3D tyre model. The natural frequencies obtained for the inflation pressure of 1 bar are listed in Table 2.4. The "oval" mode is of order $m = 3$. All the eigenvalues extracted are smaller than the experimental ones as presented in Table 2.1, meaning that the overall stiffness of the tyre structure is not high enough.

Table 2.4 – Modal frequencies extracted from the viscoelastic homogeneous FE model for the tyre inflation pressure of 1 bar.

| Mode | 1 | 2 | 3 | 4 | 5 | 6 | 7 | 8 | 9 | 10 |
|---|---|---|---|---|---|---|---|---|---|---|
| $f$(Hz) | 256 | 257 | 282 | 328 | 386 | 454 | 534 | 628 | 737 | 859 |

Another aspect to be considered in a modal analysis is the damping effect for which the viscosity of rubber is mainly responsible. The FRFs were evaluated for the same two points as in Figures 2.13 and 2.14, and the results are shown in Figures 2.17 and 2.18. Despite the fact that the calculated modes are not in phase with the experimental ones, the viscoelasticity of rubber alone yields comparable damping effects with the measurements, without having to introduce experimental structural damping into the Abaqus tyre model.

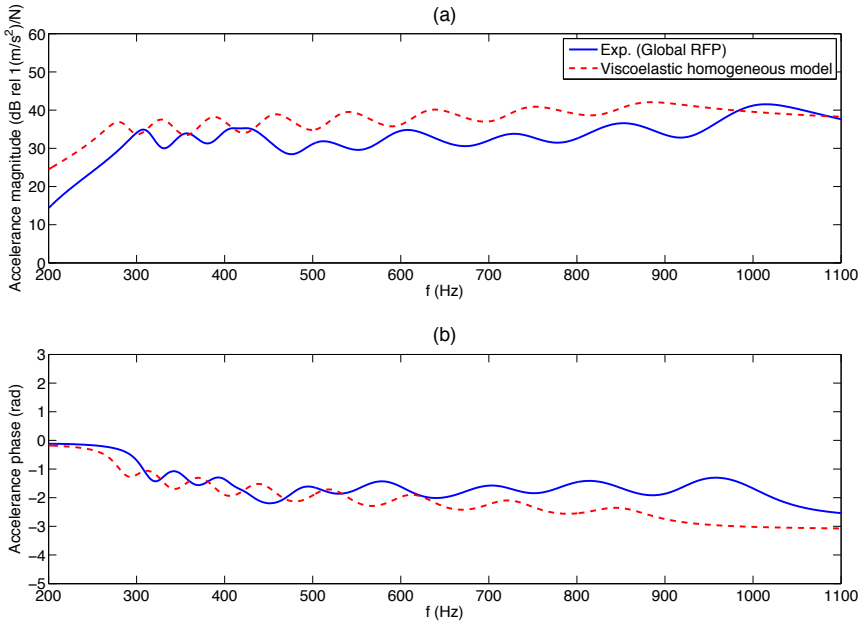


Figure 2.17 – Experimental accelerance FRFs at the drive point for the tyre inflation pressure of 1 bar in comparison with numerically calculated FRFs from the viscoelastic homogeneous FE model: (a) magnitude and (b) phase angle.

### 2.2.3 Viscoelastic heterogeneous model

Since the viscoelastic homogeneous tyre model is not rigid enough to reach the experimentally extracted natural frequencies for the corresponding modes yet capable of reproducing the correct damping effects, a viscoelastic heterogeneous model comprising the essential compounds in the real tyre is proposed to maintain the damping properties while enhancing the structural stiffness. Figure 2.19 depicts the inner structure of the tyre by displaying a half-section view of the real tyre in the left and the FE model geometry in the right. In the real tyre section, the carcass under the rubber tread occupies the innermost third of the tyre thickness and is made of rubber reinforced by two nylon layers. The nylon cords in the two layers are symmetrically oriented about the median plane of the tyre and both make an angle of about 35° with the circumferential

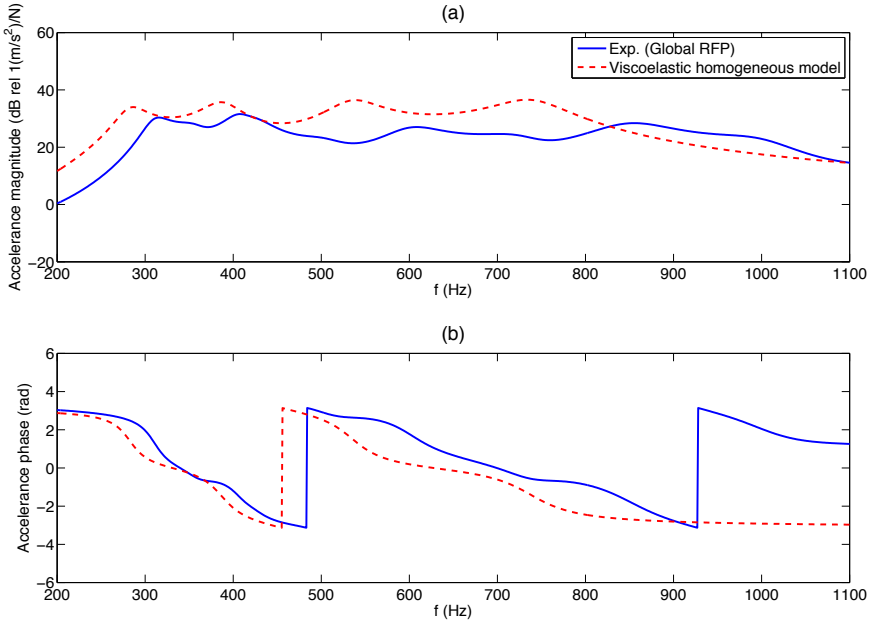


Figure 2.18 – Experimental accelerance FRFs at a transfer point at 90° for the tyre inflation pressure of 1 bar in comparison with numerically calculated FRFs from the viscoelastic homogeneous FE model: (a) magnitude and (b) phase angle.

direction in the flat rolling band. In the sidewalls, the number of nylon rebar layers is increased to four. The bead is reinforced by steel wires.

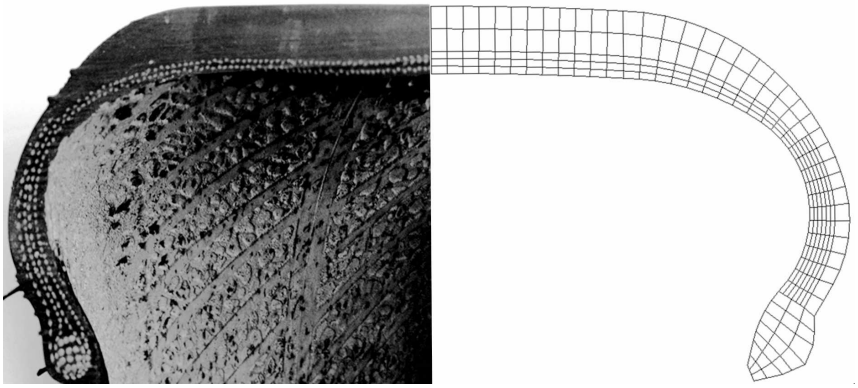

Figure 2.19 – Real and FE cross-sections of the tyre.

Figure 2.20 shows the material composition of the viscoelastic heterogeneous tyre model. The rubber has the same experimentally determined material properties as presented in the previous section. The material properties of the bead, which sits firmly on the rim, turn out to have no significant influence on the tyre dynamics, especially at high frequencies. Thus it is considered to be rubber for the sake of simplicity in modelling. The nylon layers are inserted as rebar layers composed of elastic cords having a diameter of 0.48 mm and a spacing of 0.82 mm and respecting the measured angular orientations. Its density is defined as being equal to 1100 kg/m$^3$ and the Poisson's ratio 0.4 which are classical values for nylon. The inflation pressure of the tyre leads to a pre-tension of the nylon cords, therefore the elastic modulus of the nylon cannot be experimen-

tally assessed. A value of 0.83 GPa is found to be a suitable fit for the inflation pressure of 1 bar by producing reasonably coherent natural frequencies with experiment as presented in Table 2.5. Two different values are also tested to show the sensitivity of the results to the variation of the nylon's modulus. It should be noted that for 0.42 GPa, the "oval" mode comes after the axisymmetric mode thus is of mode order $m = 3$, while for 0.83 and 1.63 GPa, the "oval" mode is between the mode with one wavelength and the axisymmetric mode and is of mode order $m = 2$.

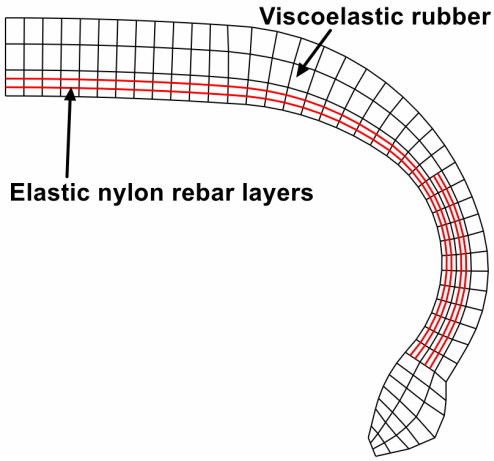


Figure 2.20 – Materials forming the heterogeneous half-section of the tyre.

Table 2.5 – Modal frequencies extracted from the viscoelastic heterogeneous FE model for the tyre inflation pressure of 1 bar with moduli of nylon equal to 0.42, 0.83 and 1.66 GPa for test of sensitivity. A modulus of 0.83 GPa is found to be a suitable fit to the experiments.

| | Mode | 1 | 2 | 3 | 4 | 5 | 6 | 7 | 8 | 9 | 10 |
|---|---|---|---|---|---|---|---|---|---|---|---|
| $E_{nylon}$ = 0.42 GPa | $f$(Hz) | 273 | 290 | 295 | 341 | 399 | 468 | 549 | 645 | 756 | 882 |
| $E_{nylon}$ = 0.83 GPa | $f$(Hz) | 291 | 310 | 319 | 357 | 416 | 485 | 568 | 667 | 782 | 911 |
| $E_{nylon}$ = 1.66 GPa | $f$(Hz) | 318 | 336 | 362 | 384 | 443 | 511 | 596 | 698 | 818 | 953 |

In Figures 2.21 and 2.22 are plotted the FRFs evaluated at the drive point and a transfer point at 90° on the tyre. The experimental and calculated curves show a good consistency for frequencies up to 500 Hz. Beyond this frequency range, a phase shift is observed.

### 2.2.4 Discussion

The discussion mainly concerns two of the aforedescribed FE models, the simplified elastic homogeneous model and the more complex viscoelastic heterogeneous model. The viscoelastic homogeneous model should rather be regarded as an intermediate step between the two other ones.

The elastic homogeneous model simulates the dynamic responses of the unloaded reduced-sized tyre's carcass and gives satisfying results in comparison with experiment, especially for the frequency range between 200 and 800 Hz. Nevertheless, the elastic modulus (112 MPa) chosen for the homogeneous half-section is too rigid when local deformations are considered, as loading the tyre model in Abaqus with 1000 N onto a rigid flat surface leads to a contact area of approximately

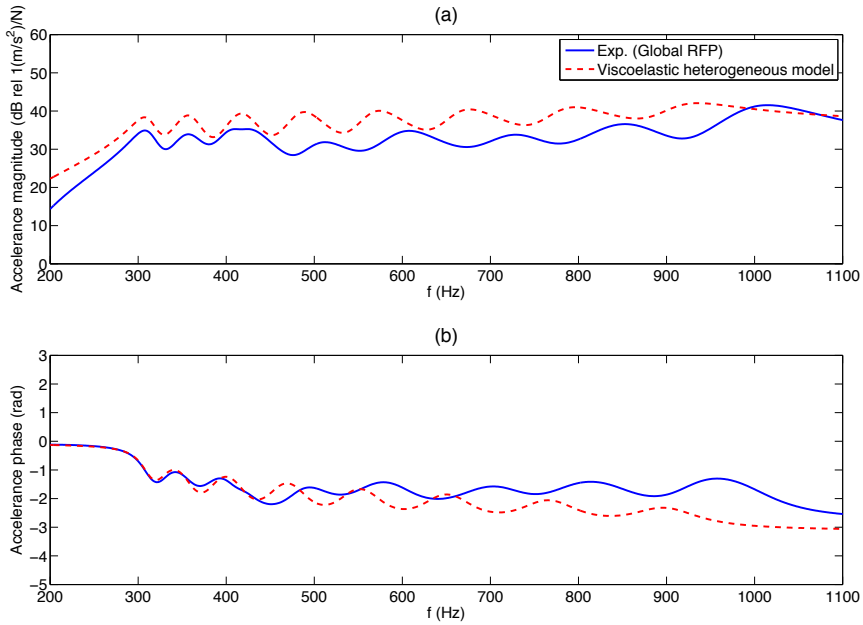


Figure 2.21 – Experimental accelerance FRFs at the drive point for the tyre inflation pressure of 1 bar in comparison with numerically calculated FRFs from the viscoelastic heterogeneous FE model: (a) magnitude and (b) phase angle.

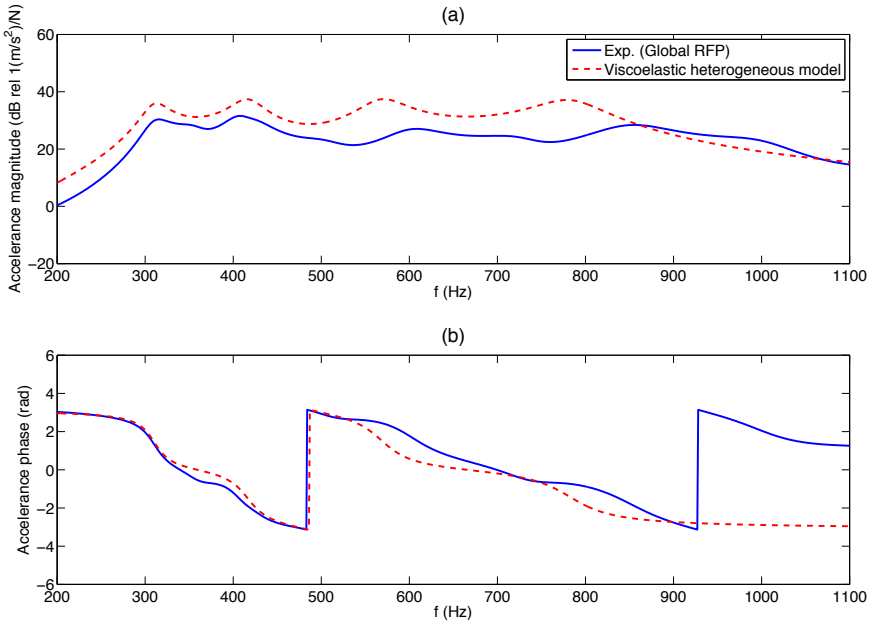


Figure 2.22 – Experimental accelerance FRFs at a transfer point at 90° for the tyre inflation pressure of 1 bar in comparison with numerically calculated FRFs from the viscoelastic heterogeneous FE model: (a) magnitude and (b) phase angle.

8 cm$^2$ which is too small in comparison with what will be presented in Section 2.3. An example of the calculated contact pressure distribution is given in Figure 2.23. Therefore, a more sophisticated

model is needed for a closer investigation of the contact problem.

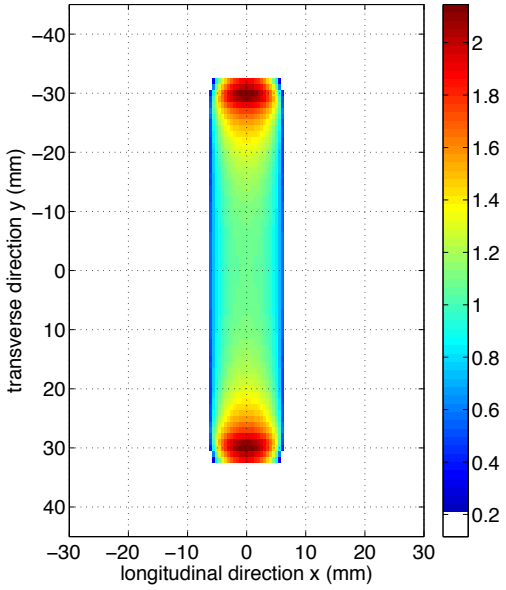


Figure 2.23 – Example of the contact pressure distribution calculated using the elastic homogeneous model in Abaqus for an inflation pressure of 1 bar and a static load of 1000 N.

The viscoelastic heterogeneous model considers the facts that rubber is a rate-dependent material and that the tyre cross-section is reinforced by nylon rebar layers which make it a robust model that can be tuned for different inflation pressures when simulating the vibration problem. The calculated dynamics responses, especially those for the transfer point where the influence of the mounting plate's size can be omitted, correlate well with experiment for frequencies up to 500 Hz, covering the first four modes which are visually identifiable, both in terms of amplitude and phase. To study dynamic contact laws or predict rolling resistance, it is necessary to investigate the contact problem with a detailed physical model of the tyre. A FE model could serve as a reference method. In this instance, the viscoelastic long-term modulus which is applicable for small strains may need to be described by a hyperelastic constitutive model since the material will undergo large deformations. Without exploring in depth, using a polynomial first-order strain energy potential with a coefficient $C_{10} = 3.5$ MPa combined with the experimentally determined Prony series yields a good compromise between the dynamic and the static behaviours. The modal frequencies are presented in Table 2.6. The "oval" mode is of order $m = 2$. Figure 2.24 shows a more reasonable contact patch than the one in Figure 2.23. The white areas within the contact zone corresponds to meshes having a slightly negative contact pressure due to calculation error in Abaqus or meshes having a very small positive pressure that cannot be distinguished from the non-contact area in the colormap in Matlab.

Table 2.6 – Modal frequencies extracted from the hyper-viscoelastic heterogeneous FE model for the tyre inflation pressure of 1 bar.

| Mode | 1 | 2 | 3 | 4 | 5 | 6 | 7 | 8 | 9 | 10 |
|---|---|---|---|---|---|---|---|---|---|---|
| $f$(Hz) | 304 | 326 | 328 | 377 | 441 | 517 | 609 | 718 | 843 | 984 |

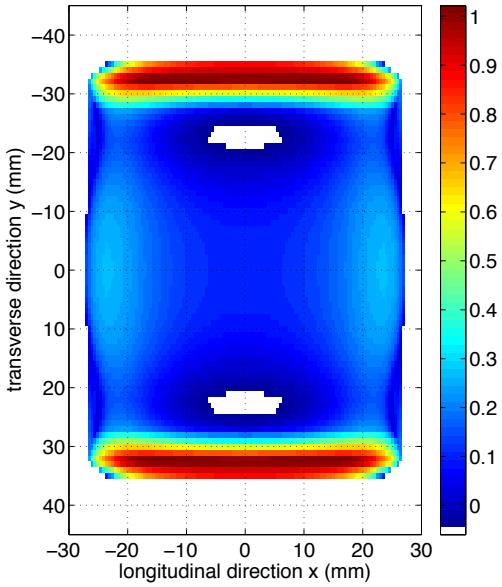


Figure 2.24 – Example of the contact pressure distribution calculated using the hyper-viscoelastic heterogeneous model in Abaqus for an inflation pressure of 1 bar and a static load of 1000 N.

## 2.3 Static contact analysis of the reduced-sized tyre

### 2.3.1 Static contact area measurement on a plane flat surface

In addition to modal analysis of the tyre, measuring its contact area under static loading also reveals the mechanical behaviour of the tyre structure and complements the basis for validation of numerical models. This was done by vertically pressing the tyre, inflated to various pressures, under different loads onto Fujifilm pressure sensitive papers[3] (type of Prescale: LLW) that were horizontally supported by a metal plate as shown in Figure 2.25. The two sheets of films react with each other when pressure is applied to give red patches. The vertical load was adjusted by a hydraulic pump and monitored by a vehicle scale system. A complete view of the experimental set-up is given in Figure 2.26.

The tested inflation pressures were 0.6, 0.8 and 1 bar and the vertical loads were 400, 600, 800 and 1000 N. The scanned images of the contact patches were processed to be displayed in gray scale. An example of the contact patch with an inflation pressure of 0.6 bar and a static load of 1000 N is presented in Figure 2.27. The contact patch is roughly rectangle in shape, considering the loss of area due to the pressures outside the sensitivity range of the Fujifilm. Its longitudinal size $l_x$, i.e. along the rolling direction, varies proportionally with the inflation pressure or the vertical load; the transverse size $l_y$ barely changes. The contact area $A$ can be estimated as the product of $l_x$ and $l_y$. The experimental values of $l_x$, $l_y$ and $A$ are summarised in Table 2.7. The highest pressures are mostly concentrated on the longitudinal borders. A certain pressure concentration can also be observed, though not clearly, within a transverse band in the middle of the contact patch. The dimensions of the contact patch in Figure 2.24 are comparable with the experimental ones.

[3]Product description available on: `http://www.fujifilm.com/products/prescale/prescalefilm`

Figure 2.25 – Measurement of contact area of the tyre loaded onto a flat surface using Fuji paper.

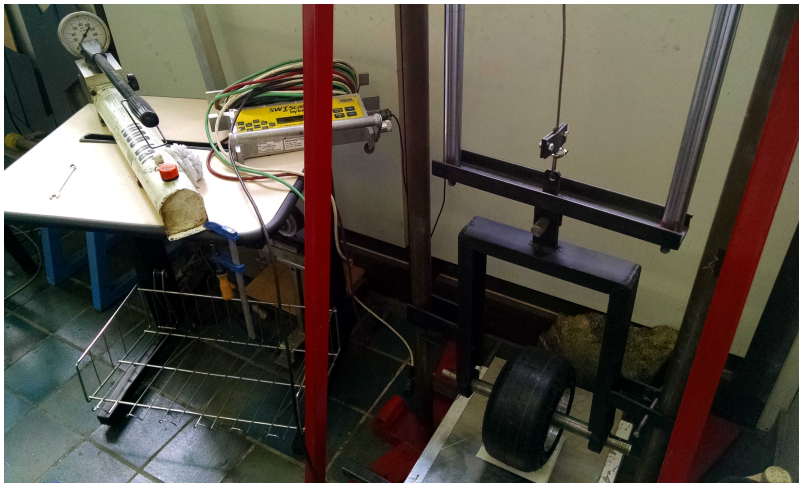

Figure 2.26 – Complete view of the experiemental set-up for static contact patch measurement on a flat surface using Fuji paper.

Table 2.7 – Summary of $l_x$ and $l_y$, widths of the go-kart tyre's static contact area respectively in the longitudinal and the transverse directions as well as $A$, the contact area, for the inflation pressures of 0.6, 0.8 and 1 bar and the static loads of 400, 600, 800 and 1000 N.

| | | 400 N | 600 N | 800 N | 1000 N |
|---|---|---|---|---|---|
| 0.6 bar | $l_x$ (cm) | 3.4 | 4.3 | 5.4 | 6.3 |
| | $l_y$ (cm) | 7.2 | 7.6 | 7.8 | 7.9 |
| | $A$ (cm$^2$) | 24.48 | 32.68 | 42.12 | 49.77 |
| 0.8 bar | $l_x$ (cm) | 2.8 | 3.4 | 4.7 | 5.4 |
| | $l_y$ (cm) | 7.2 | 7.3 | 7.5 | 7.7 |
| | $A$ (cm$^2$) | 20.16 | 24.82 | 35.25 | 41.58 |
| 1 bar | $l_x$ (cm) | 2.6 | 3.2 | 4.2 | 5 |
| | $l_y$ (cm) | 7.2 | 7.2 | 7.5 | 7.6 |
| | $A$ (cm$^2$) | 18.72 | 23.04 | 31.5 | 38 |

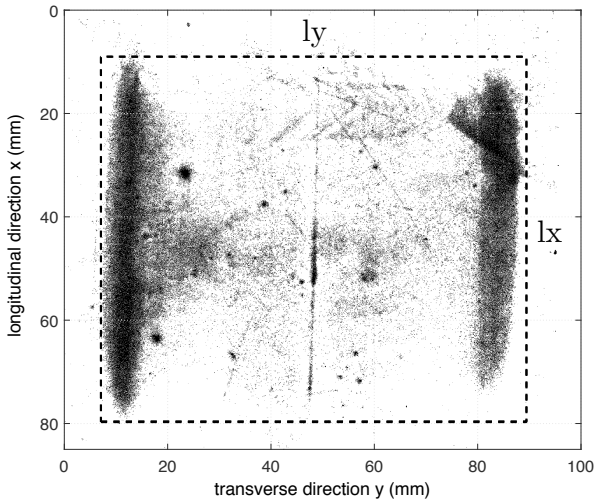


Figure 2.27 – Example of the contact patch measured in a compression test for an inflation pressure of 0.6 bar and a static load of 1000 N. $l_x$ is the longitudinal size, i.e. the dimension along the rolling direction; $l_y$ is the transverse size.

### 2.3.2 Matrix Inversion Method (MIM) used in static contact patch analysis

The FE (Finite-Element) model used for modal analysis represents well the dynamic behaviour of the tyre carcass. However, problems arise as we try to calculate the static footprint of the tyre pressed onto a smooth, rigid surface. While the transverse size of the contact area compares well with the experimentation for the loads and inflation pressures summarised in Table 2.7, the longitudinal size is almost one order of magnitude smaller. The elastic modulus chosen for the homogeneous half-section is thus too rigid when the local deformation is considered. Thus, in the present study, the half-space assumption was applied to the reduced-sized tyre and the static contact with a smooth rigid surface was studied using the MIM. The tyre contour geometry is depicted in Figure 2.28. The detailed numerical procedure used here for the MIM can be found in [Cesbron and Yin, 2010] and is summarised in Appendix A.

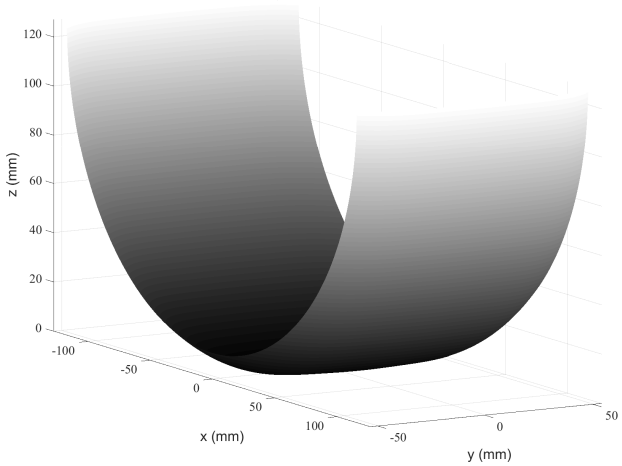


Figure 2.28 – Tyre contour used in the Matrix Inversion Method for the contact problem with a smooth rigid surface at $z = 0$.

### 2.3.3 Exploitation of symmetries

Theoretically, the contact pressure distribution should be symmetric about an axis parallel to the longitudinal direction and about another parallel to the transverse direction. By defining the centre of the contact patch as the origin of the coordinate system for the contact patch and the longitudinal and transverse symmetry axes as the x and y axes, the analysis of the contact problem can be confined to only a quarter of the original area of study. In this instance, the contact patch, originally having a roughly rectangular shape whose area $A = l_x \times l_y$, now becomes a $l_x/2 \times l_y/2$ rectangular shape. If the dimensions $h_x$ and $h_y$ of the mesh elements remain unchanged, the number of elements in question is also divided by 4, i.e. $n/4$. The original influence matrix $\mathbf{A}$ in Equation A.4 is an $n \times n$ matrix. When the symmetries are exploited, the dimensions of the new influence matrix are reduced to $n/4 \times n/4$, thus considerably saving its computation time and storage size.

To allow the symmetries to be exploited, any point $M_i$ ($i \in [1, n/4]$) around which an element $i$ is centred should have coordinates $(x_i, y_i)$ in which $x_i$ is an odd multiple of $h_x/2$ and $y_i$ an odd multiple of $h_y/2$. Naturally, $n$ is a multiple of 4. The new influence matrix $\mathbf{A_{sym}}$ considering the symmetries will have elements $A_{ij,sym}$ that are calculated as the sum of influences at element $i$ associated with point $M_i$ at coordinates $(x_i, y_i)$ by elements associated with point $(x_j, y_j)$ and its mirror points about the x axis $(x_j, -y_j)$, about the y axis $(-x_j, y_j)$ and about both the x and the y axes $(-x_j, -y_j)$.

$$
\begin{aligned}
\forall (i,j) \in [1, n/4]^2 \,,\; A_{ij,sym} = & \int_{y_j - h_y/2}^{y_j + h_y/2} \int_{x_j - h_x/2}^{x_j + h_x/2} T(x_i, y_i; \xi, \eta) d\xi d\eta \\
& + \int_{-y_j - h_y/2}^{-y_j + h_y/2} \int_{x_j - h_x/2}^{x_j + h_x/2} T(x_i, y_i; \xi, \eta) d\xi d\eta \\
& + \int_{y_j - h_y/2}^{y_j + h_y/2} \int_{-x_j - h_x/2}^{-x_j + h_x/2} T(x_i, y_i; \xi, \eta) d\xi d\eta \\
& + \int_{-y_j - h_y/2}^{-y_j + h_y/2} \int_{-x_j - h_x/2}^{-x_j + h_x/2} T(x_i, y_i; \xi, \eta) d\xi d\eta \,.
\end{aligned}
\tag{2.9}
$$

Figure 2.29 illustrate the meshing of the surface of the half-space and the elements to be considered for the calculation of the influence coefficient $A_{ij,sym}$.

It should be noted that the original influence matrix $\mathbf{A}$ is a Toeplitz-block Toeplitz matrix, i.e. a Toeplitz matrix composed of block that are themselves Toeplitz matrices. However, the new matrix $\mathbf{A_{sym}}$ no longer conserves this property. Meanwhile, since it is still a symmetric matrix, calculating the upper triangular matrix is sufficient to obtain all the influence coefficient values presents in the whole matrix and halves the computational labour. The aforedescribed optimisation does not only simplify the computation of the influence matrix, but also reduces the dimensions of the matrices to be inverted in solving Equation A.8. Any optimisation concerning the matrix factorisation algorithm is not within the scope of the present thesis.

### 2.3.4 Numerical results of static contact analysis using the optimised MIM.

After optimisation, this method yields a rough estimation of the contact area efficiently at little sacrifice of the spatial resolution. It also determines the pressure distribution covering the full

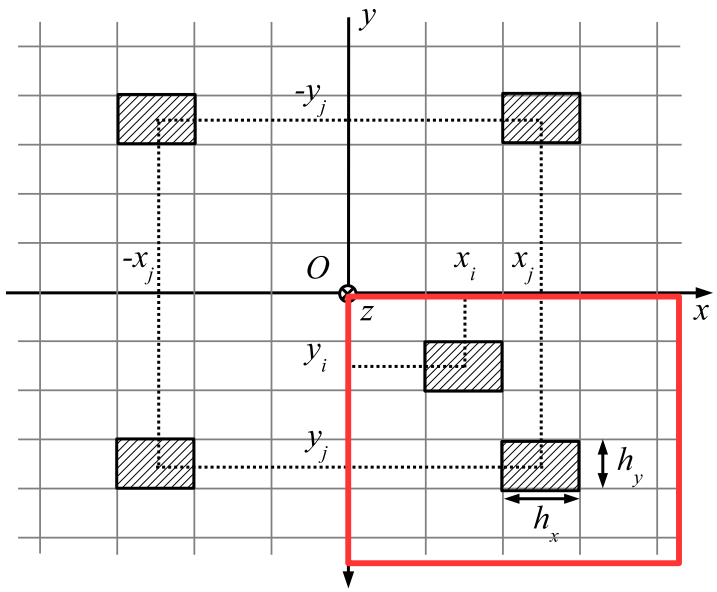


Figure 2.29 – Meshing of the surface of the half-space. The positions of the element $i$, element $j$ and its mirror elements for calculating $A_{ij,sym}$ are illustrated. The zone in red frame represents the elements used for the optimised MIM considering the contact symmetries.

pressure range. Although the MIM can be used for quick static contact analyses, its has limitations due to its simplicity. For example, since only the boundary values are considered, the modulus of rubber needs to be fitted for each contact configuration. Furthermore, the influence of the inflation pressure is not taken into account in the model. The local Young's modulus $E$ is thus determined by achieving the measured values of the contact area and the static load on a smooth plat surface in the calculations. Figure 2.30 plots $E$ as a function of load for the three inflation pressures: 0.6, 0.8 and 1 bar. The increase in $E$ with the inflation pressure confirms the stiffening effect of the air inside the tyre cavity which also explains the increase in the value of eigenfrequency.

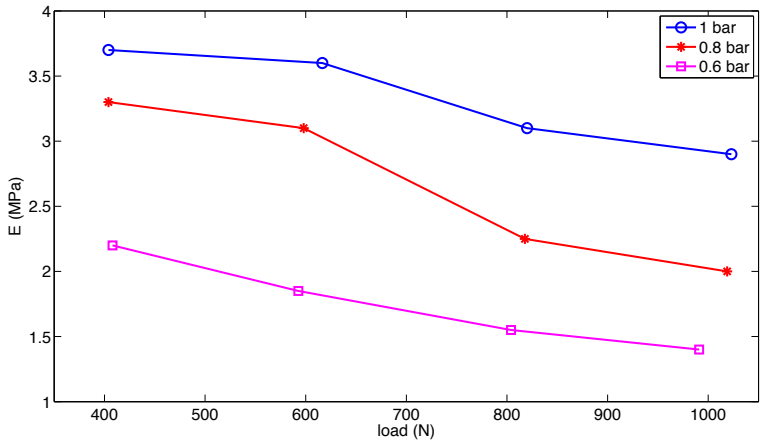


Figure 2.30 – Young's modulus $E$ determined using the Matrix Inversion Method and represented as a function of the static load.

Figure 2.31 shows numerically calculated contact patches of the tyre, inflated to 1 bar, loaded with 500, 750 and 1000 N onto a smooth flat surface. The corresponding Young's moduli are respectively 3.7, 3.3 and 2.9 MPa. The calculated results show that the highest contact pressures are concentrated along the longitudinal borders and in the middle of the contact patch which is consistent with the experimental results. As the load increases, the highest pressure tends to expand from the middle to the longitudinal borders.

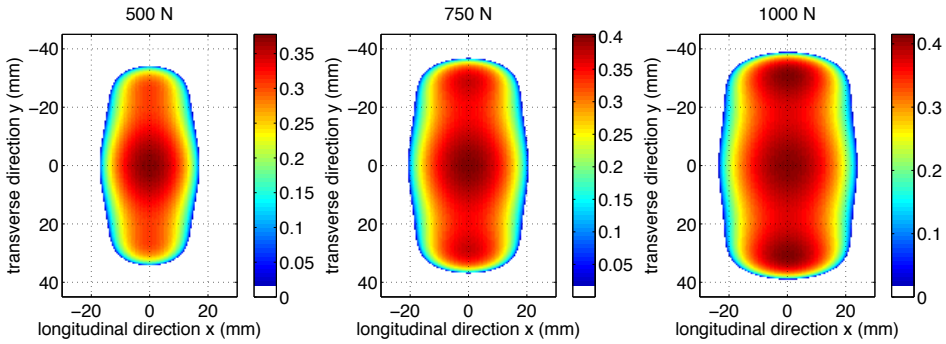


Figure 2.31 – Numerically determined contact patches based on the Method Inversion Method for an inflation pressure of 1 bar and static loads of 500, 750 and 1000 N. The tyre is loaded onto a smooth flat surface. The colours indicate the calculated contact pressure distribution (in MPa).

### 2.3.5 Static contact area measurement on the rolling surface

In the aforedescribed contact analysis, the contact patches were measured for the tyre loaded onto a flat and smooth surface. However, for the specific contact problem of the tyre rolling on the test rig, the curvature of the latter may affect the contact area and consequently the contact pressure distribution. Furthermore, in reality, the energy dissipation during rolling may cause the temperature at the surface of the tyre to vary, depending on the total load and the rolling speed. Although an experimental method to estimate the dynamic contact area has been proposed by Cesbron et al. [2009a], the novel test rig has the particular advantage of allowing direct measurements of contact forces without interfacial layer. Meanwhile, direct measurements of contact patches are not feasible.

Nevertheless, it is possible to measure the contact patch using Fuji pressure-sensitive paper on the test rig for a given loading condition and the tyre surface temperature corresponding to a certain rolling speed. The normal load applied on the tyre can be precisely controlled through a pneumatic jack. Contact patches were first measured for three loads, 500 , 750 and 1000 N, respectively, with the tyre surface temperature being equal to the room temperature, i.e. 20 °C. Then different combinations of load and rolling speed were tested: the tyre was driven to rolling under a given load and at a given speed until stabilisation of its surface temperature. The static contact patch was measured immediately after stopping the tyre from rolling. A photo of how the tyre was loaded for the static contact measurement is shown in Figure 2.32. The tyre was inflated to 1 bar for all the contact patch measurements performed on the test rig. An example of measured contact patch is given in Figure 2.33. The real geometry of the tyre comprises some irregularities and thus alters the pressure distribution from that of a completely smooth tyre to a slight extent by leaving a narrow blank stripe along the rolling direction in the middle of the contact patch.

The influence of load condition is analysed by comparing the contact patches measured with the tyre surface being at the room temperature as displayed in Figure 2.34. As the load increase,

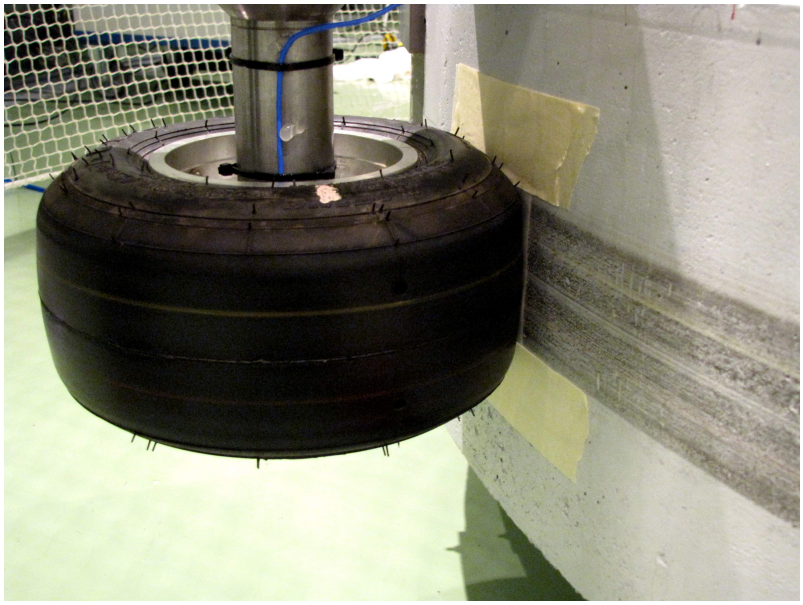

Figure 2.32 – Measurement of the contact area of the tyre loaded onto the rolling surface on the test rig using Fuji paper.

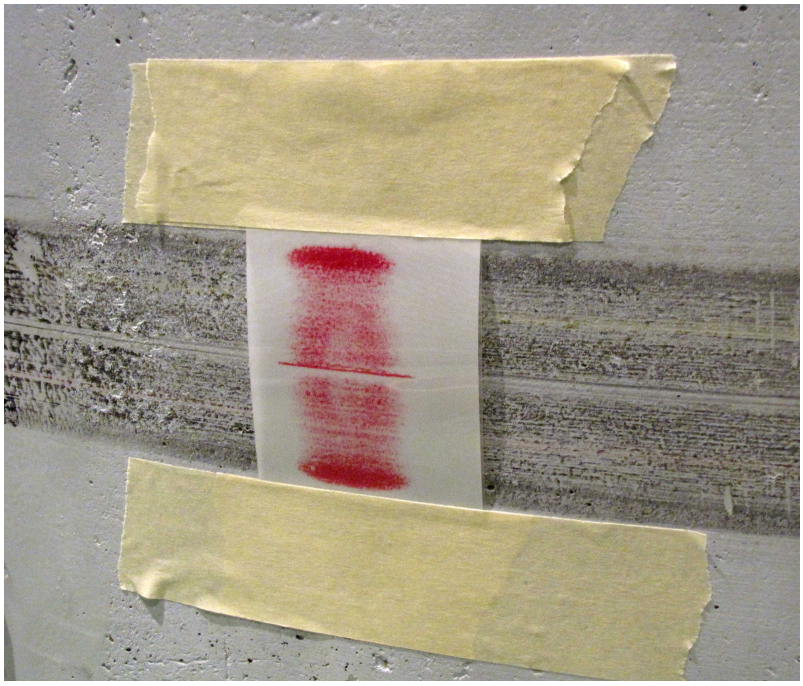

Figure 2.33 – Example of contact patch measured on the test rig using Fuji paper.

the contact patch tends to have a rectangular shape and the highest contact pressure moves from the middle of the contact patch to the borders along the x-axis, i.e. the rolling direction. The widths along the x-axis are slightly smaller than the values in Table 2.7 due to the curvature of the test rig in the circumferential direction.

Figure 2.35 shows numerically calculated contact patches of the tyre, inflated to 1 bar, loaded with 500, 750 and 1000 N onto a smooth surface having the same curvature of the test rig. The rubber modulus used for each respective loading condition is the same as for the contact simula-

tions in the case of a smooth flat surface (Figure 2.31), i.e. 3.7, 3.3 and 2.9 MPa for 500, 750 and 1000 N, respectively, when the tyre surface is at the room temperature. The contours of the numerical contact patches are added to Figure 2.34 for comparison of dimensions. The numerical results confirm the slight decrease in width along the longitudinal direction when the load decreases. Although the shapes and dimensions of the measured contact patches can be reproduced using the MIM with a carefully calibrated Young's modulus for the elastic half-space, the calculated contact pressure tends to be concentrated both in the middle and at the longitudinal borders of the contact patch, especially for high total loads on the tyre. This comparison shows some limitations of the MIM as a simplified approach that overlooks the influences of factors such as the inner structure of the tyre or the hyper-viscoelasticity of the tread rubber, which are taken into account in the FE model.

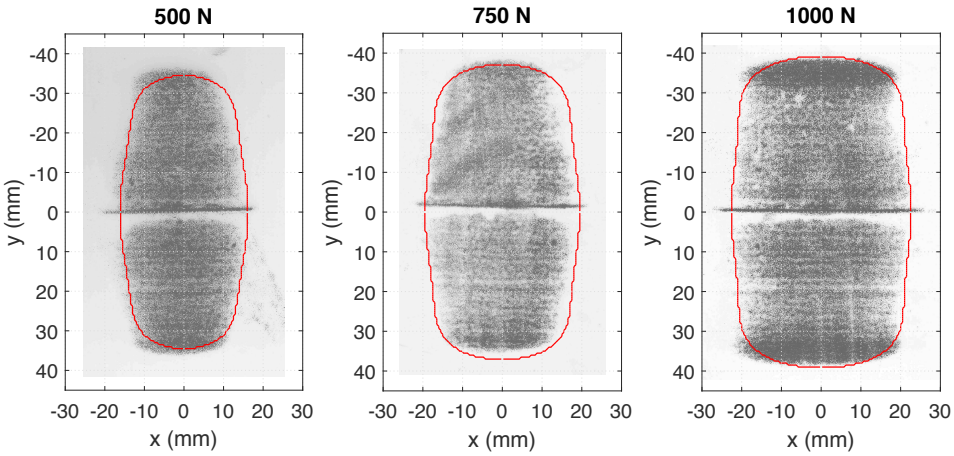


Figure 2.34 – Comparison of contact patches measured with the tyre surface being at the room temperature (20 °C) and under a load of 500, 750 and 1000 N, respectively. The contours of the numerical contact patches from Figure 2.35 are superposed for comparison of dimensions.

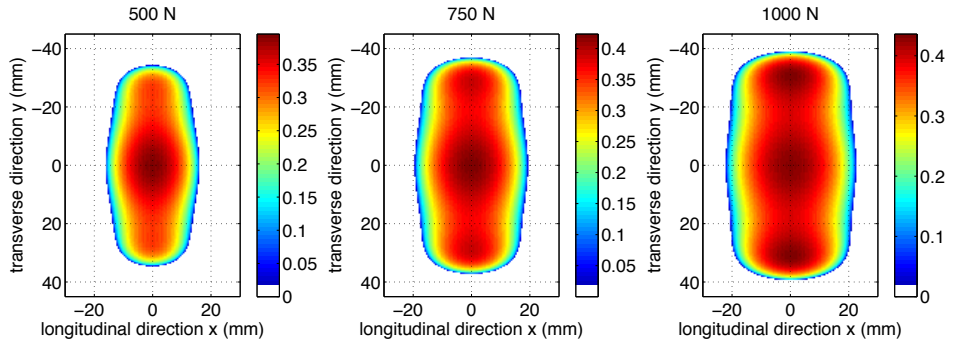


Figure 2.35 – Numerically determined contact patches based on the Method Inversion Method in the case where the tyre surface is at the room temperature (20 °C). The inflation pressure is 1 bar, and the static loads are 500, 750 and 1000 N. The corresponding Young's moduli are respectively 3.7, 3.3 and 2.9 MPa. The curvature of the test rig is taken into account in the geometry of the surface onto which the tyre is loaded. The colours indicate the calculated contact pressure distribution (in MPa).

The static contact patches measured under the same three loads, after the stabilisation of the tyre surface temperature induced by rolling at 10 m/s, are compared in Figure 2.36. Figure 2.37 shows numerically calculated static contact patches of the tyre, after rolling at 10 m/s, for 500, 750

and 1000 N. The fitted Young's moduli are respectively 7, 6 and 5 MPa. The widths along the x-axis are smaller than those shown in Figure 2.34. In the meantime, as the tyre surface temperature increases, the contact pressure tends to be more concentrated on the borders along the x-axis for the same loading condition. The increasing concentration of contact pressure on the borders along the x-axis and decreasing concentration in the middle of the contact patch due to increase in tyre surface temperature can also be seen from Figure 2.38, which represents the contact patches measured with the tyre surface temperature corresponding to different rolling speeds. However, the influence of the frequency of the cyclic loading on the rubber's viscoelastic modulus cannot be observed from the figure, as the static contact patch measurement reflects only the long-term value of the modulus.

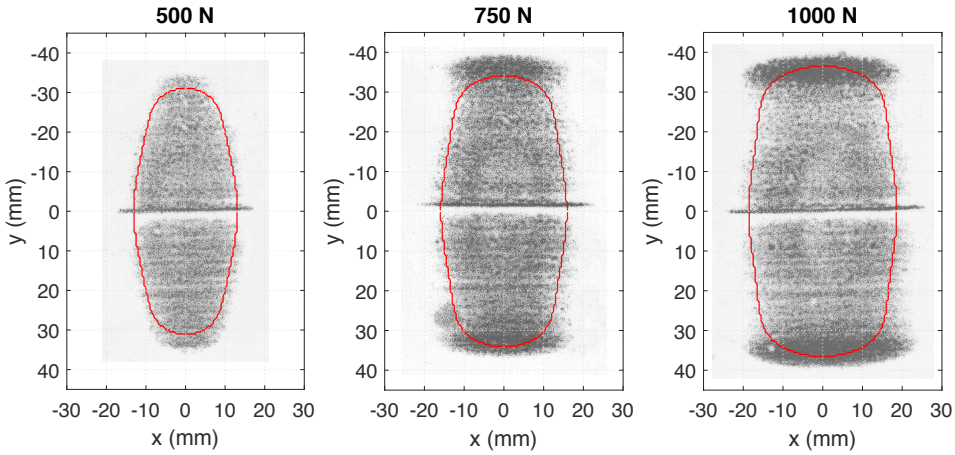


Figure 2.36 – Comparison of contact patches measured under a load of 500, 750 and 1000 N, respectively, with the tyre surface being at a stabilised temperature after rolling at 10 m/s and under the respective load. The contours of the numerical contact patches from Figure 2.37 are superposed for comparison of dimensions.

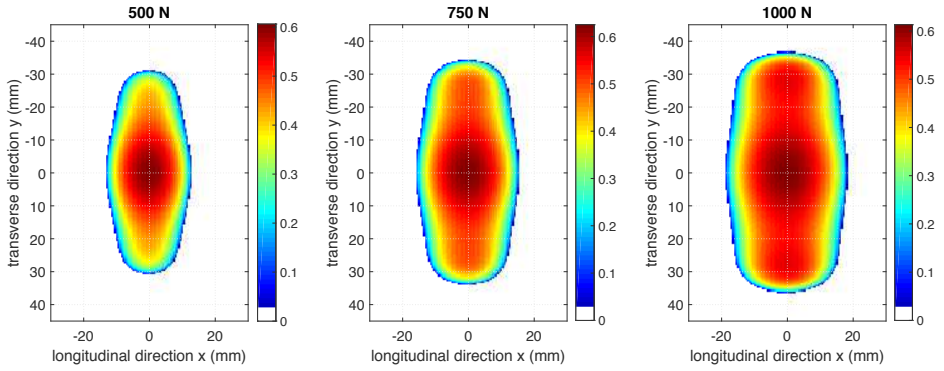


Figure 2.37 – Numerically determined contact patches based on the Method Inversion Method in the case where the tyre surface is at a stabilised temperature after rolling at 10 m/s. The inflation pressure is 1 bar, and the static loads are 500, 750 and 1000 N. The corresponding Young's moduli are respectively 7, 6 and 5 MPa. The curvature of the test rig is taken into account in the geometry of the surface onto which the tyre is loaded. The colours indicate the calculated contact pressure distribution (in MPa).

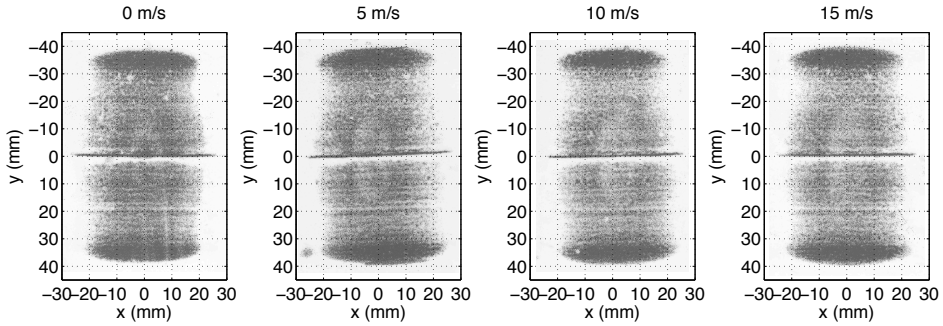


Figure 2.38 – Comparison of contact patches measured under a load of 1000 N with the tyre surface having reached a stabilised temperature after rolling at 0, 5, 10 and 15 m/s, respectively, and under a load of 1000 N.

## 2.4 Conclusions

This chapter involves the characterisation of the dynamic and contact behaviours of the reduced-sized tyre to be used on a novel test rig. The global structure and the working principle of the latter are presented, as well as the specifications of the tyre. For the dynamic aspect, modal tests are carried out using a shaker. The measured FRFs (Frequency Response Functions) are processed to extract 8 modal frequencies between 280 and 1200 Hz and the corresponding damping ratios. A simplified FE (finite-element) tyre model is built to first simulate the vibrational nature of the tyre. By treating the tyre as elastic and homogeneous and by calibrating a Young's modulus, this model yields modal frequencies that are in agreement with the experiment. However, the size of the numerical contact patch obtained is not reasonable. Thus, a more sophisticated model, taking into account the inner structure of the tyre and the properties of the different materials used in the tyre, including the measured viscoelasticity of the rubber, is proposed. The new model offers a good compromise between the modal frequencies and the contact patch and could serve as a reference method. For the contact calculations, the MIM (Matrix Inversion Method), based on the elastic half-space assumption, is used to predict the contact pressure distribution within the contact patch between the tyre and the rolling surface on the test rig. Real contact patches are measured using Fuji pressure-sensitive paper. The numerical model yields static contact patches of similar shapes and dimensions to the measured ones, while being time-efficient as the contact symmetries have been exploited. Meanwhile, it provides lesser accuracy in terms of contact pressure distribution for high loads, which could be due to the oversimplifying elastic half-space assumption and the underestimation of the sidewall effect. Contact patches have also been measured for different contact configurations to study the influences of factors such as the curvature of the test rig, the total load, the rolling speed and the consequent change in temperature at the tyre surface.

# Chapitre 3 : Contact dynamique avec une seule aspérité

Dans ce chapitre, le banc d'essai est utilisé pour étudier la force de contact dynamique entre le pneumatique de taille réduite et une seule aspérité de forme sphérique ou conique. Les essais sont réalisés en conditions de roulement. La force de contact dynamique est mesurée à l'aide d'un capteur de force piezo-électrique intégré au bâti cylindrique du banc d'essai, sans l'ajout de papier ou de capteur de pression à l'interface de contact. L'aspérité consiste en un embout de forme sphérique ou conique vissé à la surface du capteur de force dont la hauteur est variable et connue avec précision à l'aide d'une mesure par capteur à faisceau laser. La répétabilité des essais est évaluée à partir de 100 impacts successifs à une même vitesse de roulement. En prenant garde de bien respecter le temps de chauffe du pneumatique, les résultats sont satisfaisants aussi bien pour les signaux temporels que pour le maximum de la force de contact.

Les résultats expérimentaux sont ensuite présentés en s'intéressant à différents paramètres. Dans un premier temps, l'influence de la géométrie de l'aspérité sur la force de contact dynamique est étudiée. À hauteur équivalente, la force de contact sur la sphère est plus élevée que sur le cone mais l'allure des signaux temporels est très similaire et les durées de contact sont très proches. L'analyse spectrale de la force d'impact donne des résultats proches de ceux pour un demi-sinus, à savoir un spectre plat jusqu'à une fréquence critique égale à l'inverse de la durée de contact, puis des pics d'amplitude décroissante aux harmoniques de cette fréquence. La relation entre la force de contact maximale et la hauteur de l'aspérité est étudiée pour les deux géométries. Moyennant un recalage du module élastique, les courbes expérimentales sont cohérentes avec les lois de puissance analytiques issues de la théorie de Boussinesq. L'influence de la charge totale sur la force de contact dynamique est ensuite étudiée. L'amplitude maximale de la force diminue lorsque la charge augmente, alors que la durée de contact diminue avec la charge, ce qui est cohérent avec les empreintes de contact mesurées en statique. Enfin, l'influence de la vitesse de roulement sur la force de contact est analysée. Il apparaît que la durée de contact est inversement proportionnelle à la vitesse et que les spectres aux différentes vitesses, modifiés en fréquence, coïncident jusqu'à 350 Hz. Ces résultats illustrent la nature quasi-statique du contact dynamique sur une seule aspérité.

Dans la dernière partie du chapitre, la Méthode d'Inversion de Matrice (MIM) basée sur l'hypothèse de massif semi-infini est confrontée aux résultats expérimentaux. Le modèle élastique est premièrement testé. Des empreintes de contact statique sont calculées pour différentes hauteurs d'aspérité puis la force de contact locale sur l'aspérité est comparée aux résultats expérimentaux. Moyennant un recalage du module d'Young, le modèle élastique permet d'approcher la force maximale mesurée pour les fortes hauteurs, mais l'erreur est plus élevée pour les faibles hauteurs, notamment lorsque la charge totale appliquée augmente. La comparaison avec des empreintes de contact, mesurées en statique à l'aide de papier Fuji, indique que le problème pourrait être dû à une sous-estimation des pressions de contact au niveau des flancs du pneumatique, comme déjà observé au chapitre 2. Le fait que la force de contact maximale sur l'aspérité soit plus élevée pour une charge totale plus faible est ensuite expliqué par une effet thermo-rhéologique de la gomme constituant le pneumatique. En effet, lorsque la charge augmente, la température de la gomme lors du roulement augmente et cette dernière devient moins rigide de par ses propriétés viscoélastiques. Un module d'Young adapté à chaque charge permet d'approcher ces résultats à l'aide du modèle élastique. Des calculs temporels quasi-statiques montrent clairement que la MIM élastique ne permet pas de retrouver la dissymétrie temporelle du signal de force mesuré. Cette dissymétrie est attribuée à la viscoélasticité de la gomme qui est alors introduite dans le modèle.

Après un rappel des relations constitutives entre contrainte et déplacement pour un matériau

viscoélastique, le problème de contact avec roulement est formulé puis discrétisé afin d'appliquer la MIM dans le cas viscoélastique. Les calculs de la force de contact temporelle sont effectués en utilisant un modèle simplifié de Zener. Le modèle permet d'obtenir des signaux temporels dissymétriques par rapport au maximum de la force de contact, ce qui est conforme aux résultats expérimentaux. En recalant convenablement le module long-terme et le temps caractéristique du modèle de Zener, la MIM donne des résultats en très bon accord avec l'expérience pour une charge totale de 500 N et une hauteur d'aspérité élevée. L'accord essai/calcul est cependant moins bon pour les faibles hauteurs d'aspérité, comme dans le cas élastique. Pour une charge totale de 1000 N, le modèle donne des résultats satisfaisants, mais la durée de contact est sous-estimée, donnant une incertitude plus importante par rapport à l'expérience. Cet écart pourrait être réduit en utilisant un modèle de Kelvin généralisé à la place du modèle de Zener. Il pourrait aussi s'agir d'un effet des flancs du pneumatique ou de l'hyperélasticité, plus marqués lorsque la charge totale augmente et non pris en compte dans le modèle de contact basé sur une hypothèse de massif semi-infini.

# Chapter 3

# Dynamic contact with a single asperity

## 3.1 Introduction

In this chapter, the test rig is used to investigate the contact force between the reduced-sized pneumatic tyre and a single asperity of spherical or conical shape under rolling conditions. The influencing factors related to the solid indenter in static contact laws are the indenter height and the geometric shape. Similarly, peak dynamic contact forces are to be investigated by varying these two factors. Section 3.2 describes the experimental set-up and explains how contact forces and relative asperity heights are measured and analysed to verify the repeatability. In Section 3.3, experimental results are presented for studying the influences of different parameters on the peak contact force, such as the shape of the asperities, the total load and the rolling velocity. Section 3.4 concerns the contact model assessment and is divided into two parts. The first part concerns the comparison between experimental results on the influence of geometric shapes of indenter and solutions from a numerical model based on the elastic half-space assumption. The validity of the static contact assumptions in the rolling contact case is then discussed. In the second part, the influence of rubber viscoelasticity is introduced to discuss the results with varying loads and rolling speeds. Finally, concluding remarks are given.

## 3.2 Materials and Methods

### 3.2.1 Configurations for simple contact analysis

A detailed description of the operating principle of the test rig has been given in Section 2.1. Figure 2.3 shows the positions of the single asperity and of the tyre, sized 114/55R5, on the metallic plate. The asperity is screwed onto a uni-axial force transducer (PCB Model 208A12) which is embedded in the metallic plate. The force transducer is placed behind the metallic plate to facilitate the experimental set-up as depicted in Figure 3.1. The piezoelectric force transducer captures the dynamic normal force history throughout the contact duration. The height of the asperity tip can be adjusted by inserting metallic flat washers of different thicknesses under the transducer. The tyre comes into contact with the asperity once per revolution about the cylindrical axis of the test rig. The influencing factors related to the solid indenter in static contact laws are the indenter height and the geometric shape. Dynamic peak contact forces are also examined for different configurations involving these two factors.

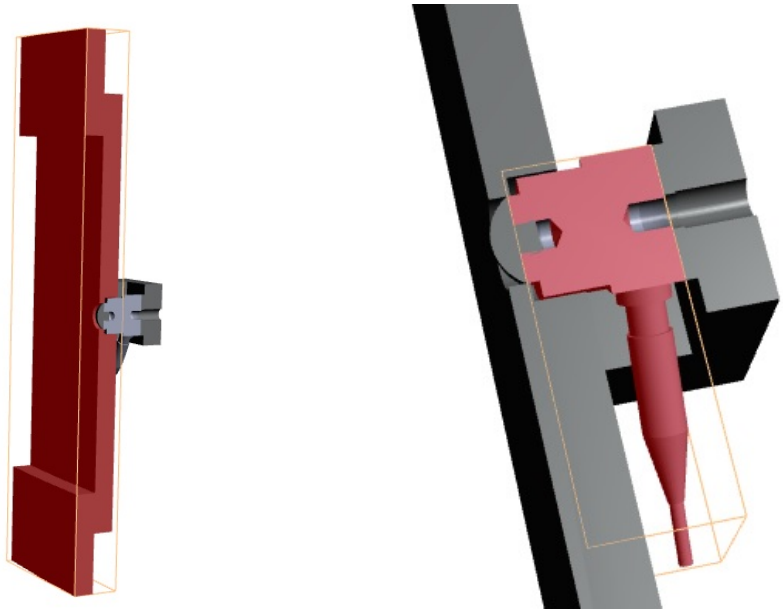

(a) Global transverse view of the metallic plate hosting a single asperity connected to a force transducer.

(b) Zoom of the connection between the asperity and the force tranducer.

Figure 3.1 – A single asperity is connected to a uni-axial force transducer situated behind the metallic plate integrated to the cylindrical concrete basis of the test rig.

### 3.2.2 Measurement of actual surface geometries

In this study, two geometric shapes of indenter are considered: spherical and conical. The spherical asperity is in fact a 3.50-mm-high cap of a sphere with a radius of 7.50 mm. Thus, its base radius is 6.35 mm. The conical one has a half-apex angle of 61.1°, a height of 3.50 mm and a base radius of 6.35 mm. Both asperities fit into a cylindrical cavity with a radius of 6.50 mm.

Although the position of the asperity tip with regard to the road surface could be calculated with the nominal thicknesses of the metallic flat washers inserted between the asperity and the force transducer, inaccuracy may be induced due to manufacture imperfections and mounting uncertainties. The contact force would vary sensitively with the value of the relative asperity height, denoted by $h$, which was of the order of magnitude of millimetres. Therefore, a 2D laser scanner (Micro-Epsilon Model scanCONTROL 2700-50) was used to assess more accurately the relative asperity heights for each measurement, as shown in Figure 3.2. By placing a transverse laser line that passed through the asperity tip, a list of scattered points whose positions described the surface geometries of the metallic plate and the asperity could be obtained. The plate being not curved in the transverse direction, its profile is approximated by two segments on the same straight line whose slope needs to be adjusted to bring the scanned profile to a horizontal position. The least squares fitting technique was applied to find a smooth circular curve for the profile of the spherical asperity and two straight lines for the profile of the conical asperity, respectively presented in Figures 3.3 and 3.4.

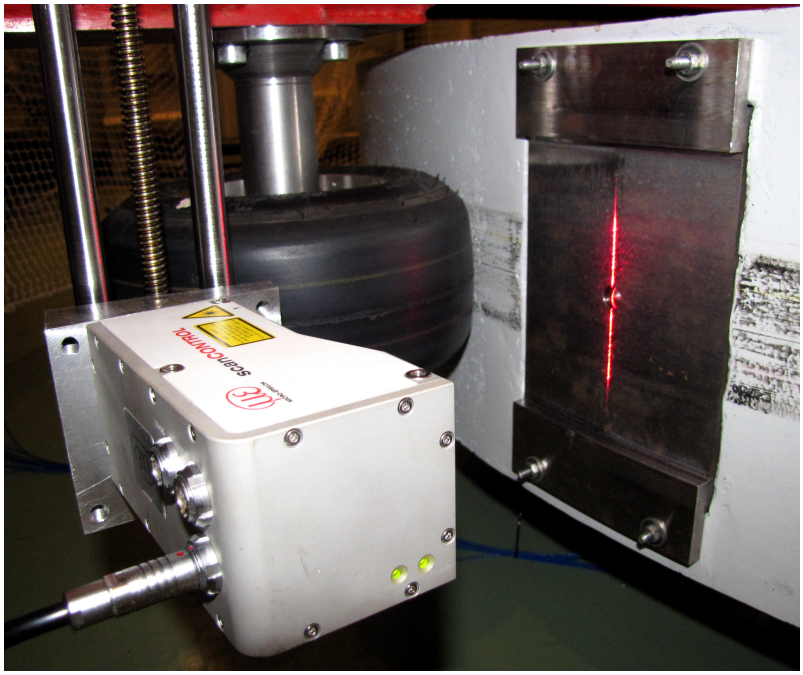

Figure 3.2 – Experimental set-up of the 2D laser profile scanner for measuring asperity height in the case of a single asperity.

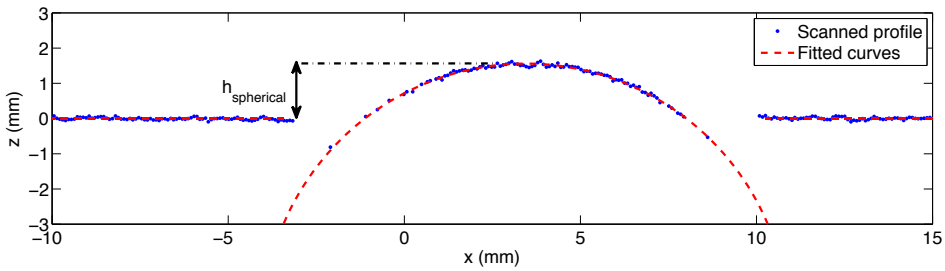


Figure 3.3 – An example of circular curve fitting the scanned profile of the spherical asperity at a relative height of 1.57 mm. The theoretical radius is 7.50 mm. The measured radius is 7.52 mm.

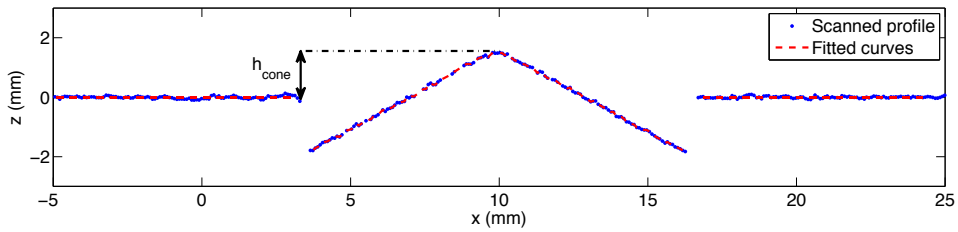


Figure 3.4 – An example of straight lines fitting the scanned profile of the conical asperity at a relative height of 1.61 mm. The theoretical half-apex angle is 61.1°. The measured half-apex angle is 61.4°.

Seven heights were measured for the spherical and the conical shapes. The relative asperity height $h$ is the distance between the asperity tip and the horizontal position of the plate profile. The relative heights determined for the two asperities are listed in Table 3.1. N.B.: The relative heights may be negative for low asperity positions.

Table 3.1 – Measured relative asperity heights $h$ for the spherical and the conical asperities.

| | | | | | | | |
|---|---|---|---|---|---|---|---|
| $h_{spherical}$ (mm) | -0.12 | 0.13 | 0.44 | 0.76 | 1.13 | 1.35 | 1.57 |
| $h_{conical}$ (mm) | -0.15 | 0.15 | 0.49 | 0.79 | 1.16 | 1.34 | 1.61 |

### 3.2.3 Measurement procedure and repeatability

Before starting a measurement of the contact force between the tyre and the asperity, it is essential to make sure that the tyre reaches a steady-state rolling regime, despite the small disturbance per revolution by the single asperity. First, the pneumatic jack applied a load to the tyre inwards along the radius of the test rig, thus normal to the rolling surface. An appropriate load value should be chosen to ensure a relatively large contact area with the road surface and would be maintained constant during an experiment. Then, the motor brought the steel beam to rotate around the centre of the test rig. Consequently, the tyre would start rolling on the concrete surface while the spindle rotated along with the beam. Finally, after an acceleration phase, the rolling had to continue for a while until the temperature at the surface of the tyre became stable before starting a measurement. This is due to a thermo-rheological effect that changes rubber's elastic modulus: the faster the tyre rolls, the higher the temperature rises and the less stiff the rubber becomes. For instance, for a total load of 1000 N, the surface temperature stabilises:

- between 34 °C and 35 °C at a rolling speed of 5 m/s;
- between 44 °C and 46 °C at a rolling speed of 10 m/s;
- between 46 °C and 50 °C at a rolling speed of 15 m/s.

The uni-axial force transducer under the asperity was connected to a data acquisition front-end (hardware: Brüel & Kjær PULSE front-end; software: Brüel & Kjær PULSE Labshop v. 14). A dynamic force exceeding a threshold value perceived by the transducer triggers a measurement. One measurement lasted 0.125 s to ensure that a complete impact force evolution was included in the time interval. The data acquisition front-end registered, with a fixed sampling frequency of 25600 Hz, the impact force history for each revolution as the tyre/road contact patch rolled over the asperity tip. The representativeness of measurements for one configuration was ensured by averaging measurements over multiple revolutions. The peak normal contact force was thus measured as the average of the maximum values of 100 impact force history curves. Figure 3.5 shows the 100 force history curves for one configuration for the spherical asperity.

As previously mentioned, one of the advantages of the test rig in comparison with in-situ measurement set-ups is that it permits tests to be performed under well-controlled laboratory conditions. The test rig is placed in an air-conditioned room. At the start of the beam rotations, and at the start and the end of one measurement, the tyre surface temperature, the room temperature and humidity were measured. While rolling, the tyre should be subjected to a constant load, have a constant speed and follow the same trajectory. Since these measurement conditions were controlled and monitored, the contact force detected for a given relative asperity height should not vary much from one test to another. This global repeatability of the apparatus was verified by performing three tests under the same measurement conditions but on three different days. Figure 3.6

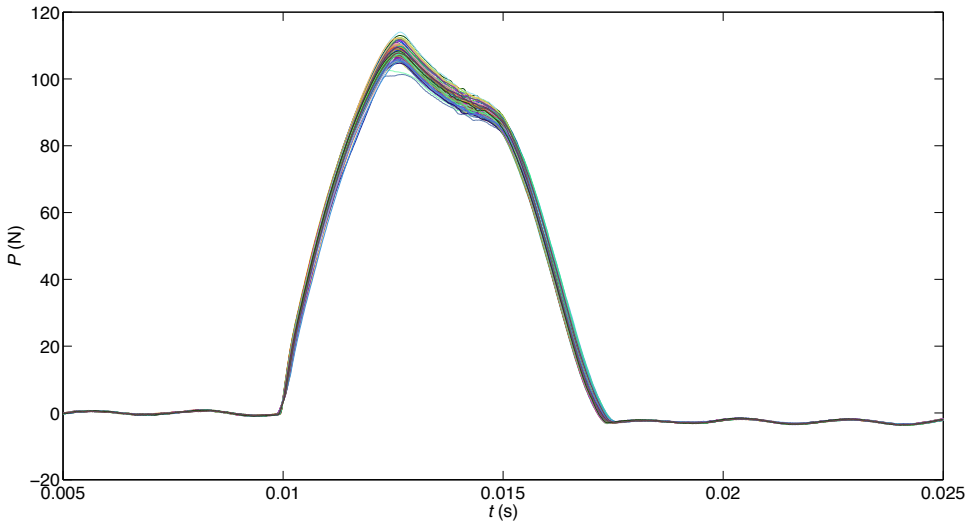


Figure 3.5 – An example of 100 time signals of the impact force evolution during impacts with the spherical asperity measured for the same configuration: a relative asperity height of 1.57 mm, a speed of 10 m/s and a load of 1000 N. The peak force is 107.5 ± 6.5 N.

shows the time signals measured in these three tests, respectively represented by solid, dash-dot and dashed lines. In this figure, the average contact force evolution is plotted versus the time. The measured curves reveal good repeatability of the tests. It can also be concluded from the figure that the lower the asperity is relative to the rolling surface, the shorter the contact time with asperity lasts.

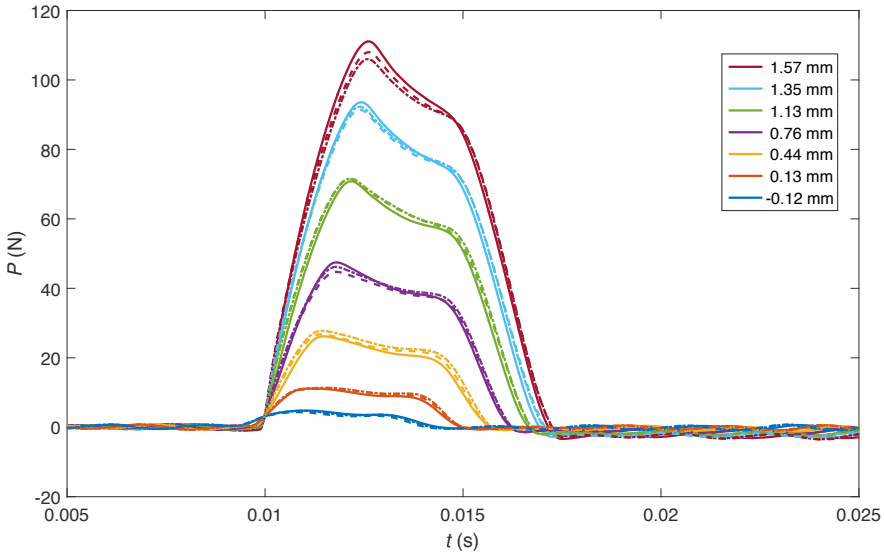


Figure 3.6 – Repeatability of the averaged time signals of contact forces measured for different relative heights of the spherical asperity. The three tests were carried out on different days (solid, dash-dot and dashed lines) but under the same conditions: a speed of 10 m/s and a load of 1000 N. The legend entries appear in the descending amplitude order of the curves in the figure.

Due to the high normal load on the tyre, the impact with the asperity should not cause the contact area to decrease significantly. Therefore, at the instant the normal tyre/asperity contact force reaches its peak value, the asperity should be completely located within the tyre/road contact patch. It is thus meaningful to take the peak value of impact force evolution over time as the peak contact force. Figure 3.7 shows repeatable experimental results in terms of peak contact force. The tyre surface temperatures were situated in the interval between 41 °C and 45 °C. Thus, the global repeatability of the test rig is verified. In addition, the error bars represent the standard deviations of results averaged over 100 revolutions. The variation of peak forces is small within the same test containing 100 revolutions.

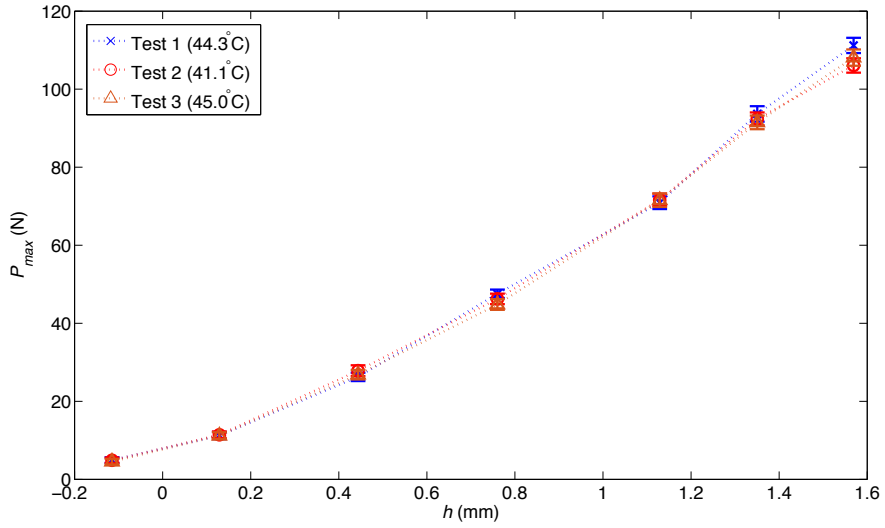


Figure 3.7 – Repeatability of experiments performed on the test rig. The three tests were carried out on different days but under the same conditions: a speed of 10 m/s and a load of 1000 N. The tyre temperature was measured for each test. Error bars are plotted for the three tests.

## 3.3 Experimental results

### 3.3.1 Influence of the geometric shapes of indenter

The influence of the geometric shapes was tested for the spherical and the conical indenters. In both cases, the tyre was brought to the same rolling speed of 10 m/s and subjected to a load of 1000 N. According to classical analytical solutions for static elastic contact, the force-indentation relationships for spherical [Hertz, 1882] and conical [Love, 1939] indenters can both be approximated by power laws but with distinct exponents. Under rolling conditions, different behaviours of the contact force as a function of the relative asperity height should also be expected, due to the significant influence of the geometric shape of indenter.

In Figure 3.8, time signals of contact force measured for a spherical asperity and a conical asperity of similar relative heights (1.57 mm for the spherical asperity and 1.61 mm for the conical one) are compared. Despite a substantial difference in magnitude, especially for peak forces, the contact duration $T_c$ is similar in both cases (close to 7.5 ms), and so is the signal shape.

A comparison of spectra of the resultant contact forces for a spherical asperity and a conical

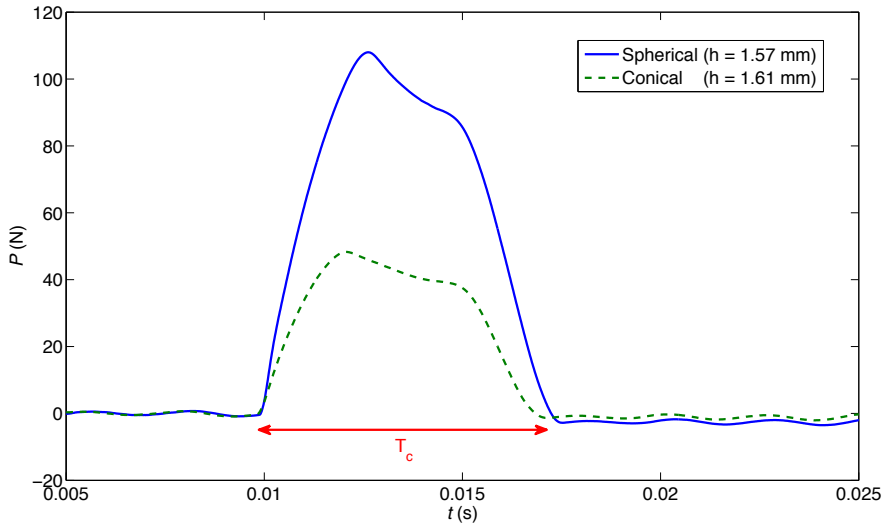


Figure 3.8 – Time signals of the contact force measured for a spherical asperity and a conical one of similar relative heights under the same conditions: a speed of 10 m/s and a load of 1000 N.

asperity of similar relative heights is given in Figure 3.9. In each calculation, a Blackman-Harris window was applied to the complete contact duration and the oscillations outside this time window were zero-padded. Each time signal in Figure 3.8 corresponds to an impact force pulse that can be approximated by a half-sine function. For such pulses, the frequency spectra remain flat up to a critical frequency equal to $1/T_c$ and then diminish and bounce [Ewins, 2000]. At multiples of $1/T_c$, wave peaks occur. This behaviour is verified for both curves in Figure 3.9 up to a frequency of $3/T_c$. For higher frequencies, the approximation by sine-function is no longer reliable, especially for the conical asperity.

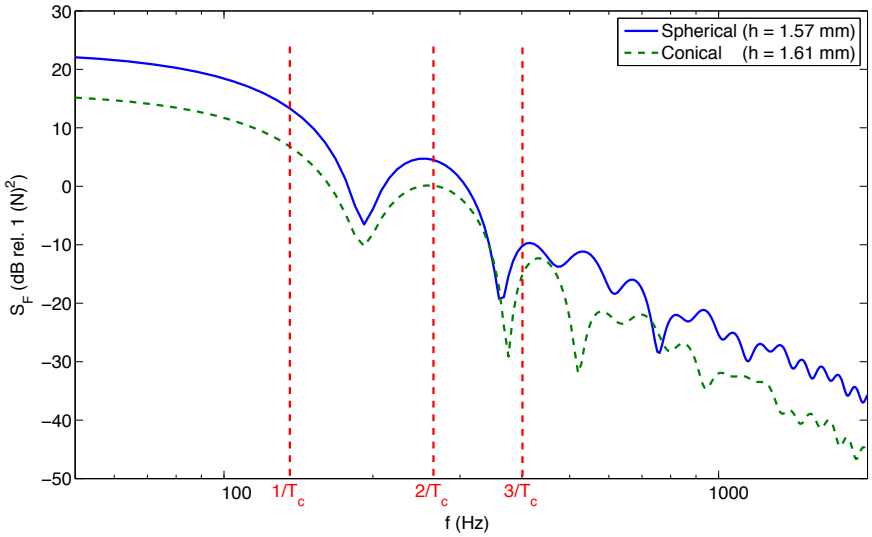


Figure 3.9 – Spectra $S_F$ of the resultant contact forces for a spherical asperity with a relative height of 1.57 mm and a conical asperity with a relative height of 1.61 mm. The rolling speed was 10 m/s and the load on the tyre was 1000 N, in both cases.

In Figure 3.10, the peak contact forces measured for the spherical and the conical asperities are plotted versus the relative asperity heights presented in Table 3.1 for comparison. The tyre surface temperatures were very close to 45 °C in both cases. However, the contact forces have significantly different behaviours. This will be discussed in the next section by comparison with a numerical model. For asperity tip positions slightly below the road surface, contact forces, albeit very weak, could still be detected. This fact implies that the part of the tyre covering the cylindrical cavity was able to penetrate into the latter due to the applied load and to come into contact with the asperity tip. To verify the validity of the half-space assumption in the Boussinesq theory of elastic contact, analytical solutions [Hertz, 1882, Love, 1939] are plotted by assuming an effective modulus of 8.7 MPa. The solution for a spherical asperity given by Hertz is:

$$P_{Hertz} = \frac{4}{3} E^* R^{0.5} \delta^{1.5}, \tag{3.1}$$

and the solution for a conical asperity given by Love is:

$$P_{Love} = \frac{2}{\pi} E^* tan(\theta) \delta^2. \tag{3.2}$$

Therefore, the theoretical exponents involved in these force-indentation relationships are 1.5 for a spherical asperity and 2 for a conical one. To take into account the partial penetration of tread rubber into the cavity, the curves are shifted by an assumed reference height $h_{ref}$ of -0.32 mm corresponding to the lowest asperity tip position relative to the rolling surface where the contact first occurs under the present loading conditions. Note that here $\delta \approx h + h_{ref}$. The experimental exponent are then calculated: 1.58 for the spherical asperity and 2.04 for the conical one. The good agreement between the experimental and the analytical results verifies, though roughly, the applicability of the Boussinesq contact theory in the present contact configuration. Although the existence of the cavity is not ideal for numerical modelling of the contact problem, it is inevitable in practice and will be included in the model in Subsection 3.4.1.

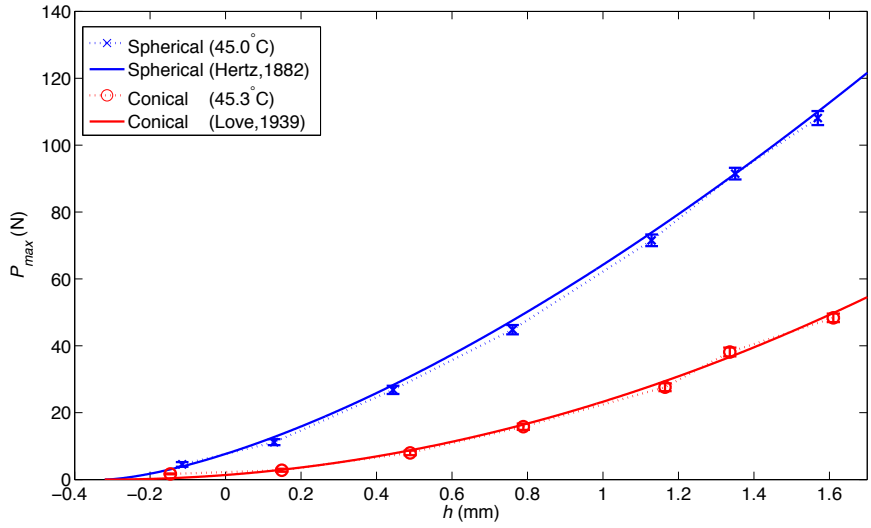


Figure 3.10 – Influence of geometric shapes of indenter. The tests were performed under the same conditions: a speed of 10 m/s and a load of 1000 N. The tyre temperature was measured for each test. Error bars are plotted for both tests. Classical analytical solutions by Hertz (sphere) and Love (cone) are plotted for comparison.

### 3.3.2 Influence of the total load

Tests were conducted to study the influences of the total load on the contact forces for a spherical asperity. Three loads, 500, 750 and 1000 N, were tested with the tyre rolling at 10 m/s.

The influence of normal loading condition on the time evolution of contact force is studied by plotting the time signals for the three loads on the tyre, measured for the highest relative height (1.57 mm) of the spherical asperity, as presented in Figure 3.11. The contact durations $T_c$ for 500, 750 and 1000 N are respectively 5.7, 6.8 and 7.6 ms. In Figure 3.12, the time is multiplied by the common rolling speed to represent the contact length. Therefore, the values for 500, 750 and 1000 N are respectively 0.057, 0.068 and 0.076 m. The contact length is influenced by the normal load, which is equally true under static loading condition: the higher the load, the greater the contact length (see Subsection 2.3.5). The shape of the signals is also influenced by the loading condition: as the load increases, the signal tends to have, after reaching the peak value, a longer phase of slow decrease in force value followed by a phase of faster decrease until end of contact.

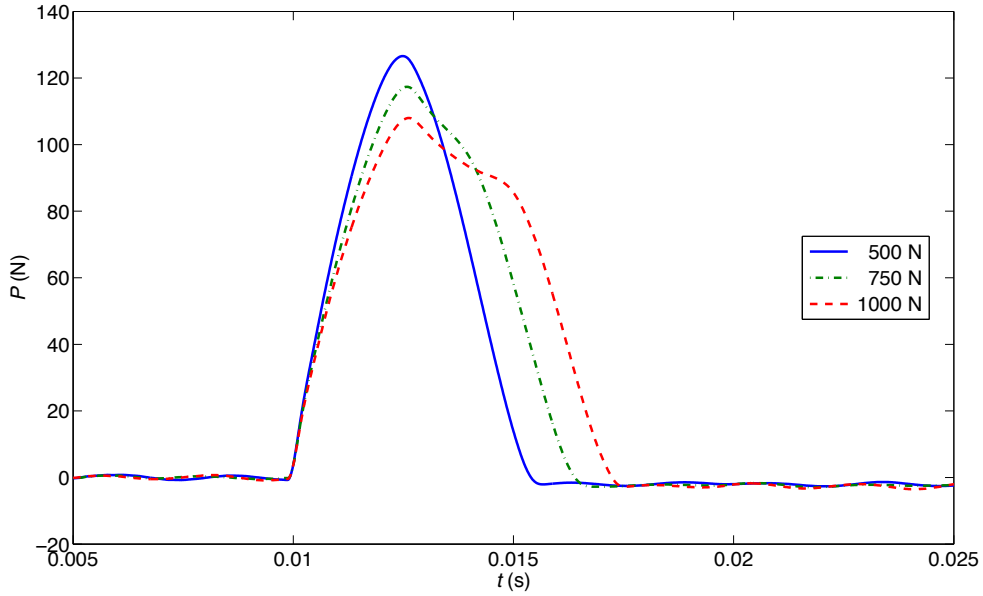


Figure 3.11 – Influence of the total load on the contact force. Three rolling speeds, respectively 500, 750 and 1000 N, were tested on the same day for the same rolling speed of 10 m/s.

A comparison of spectra of the resultant contact forces under the three loads is given in Figure 3.13. Based on the same method as used for analysing Figure 3.9, the approximation by sine-function can be applied to the three curves in Figure 3.13. The critical frequency is found near $1/T_c$ and wave peaks are found at multiples of $1/T_c$, at least up to $3/T_c$. Since $T_c$ increases with the load, the critical frequency decreases accordingly. Therefore, the greater the load, the shorter the flat part of the spectrum. The experimental result is in agreement with the theory.

The peak contact forces for the three loads are plotted versus the relative asperity heights, as represented in Figure 3.14. The tyre surface temperature was also measured for each test. The higher the load, the higher the tyre surface temperature and the lower the contact force. Numerical simulation results are presented in Subsection 3.4.1.2 to justify that it is the temperature rather than the force distribution that influences the peak contact force.

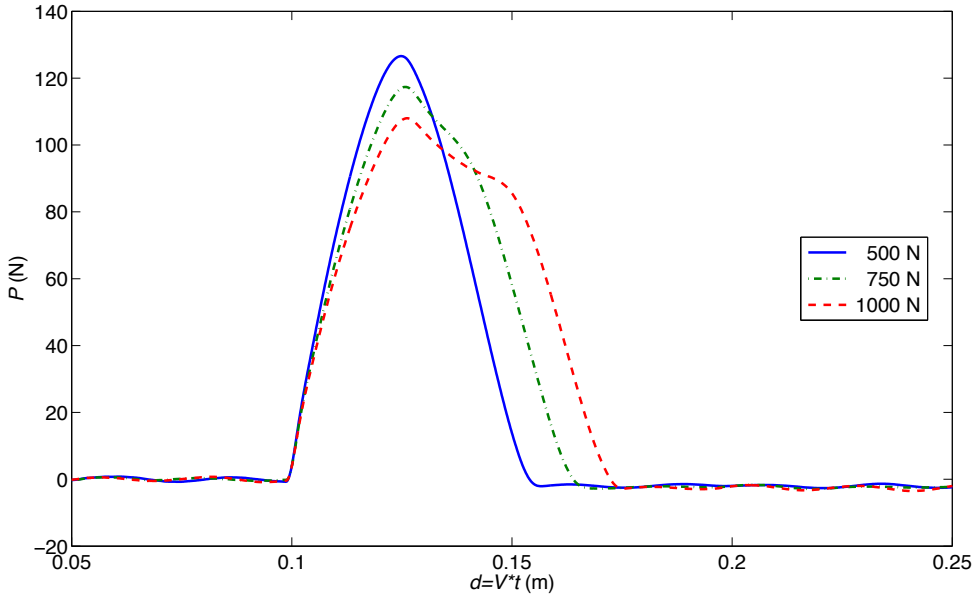


Figure 3.12 – Influence of the total load on the contact length. Three rolling speeds, respectively 500, 750 and 1000 N, were tested on the same day for the same rolling speed of 10 m/s. The time $t$ is multiplied by the respective rolling speed $V$ to represent the distance $d$ travelled during rolling.

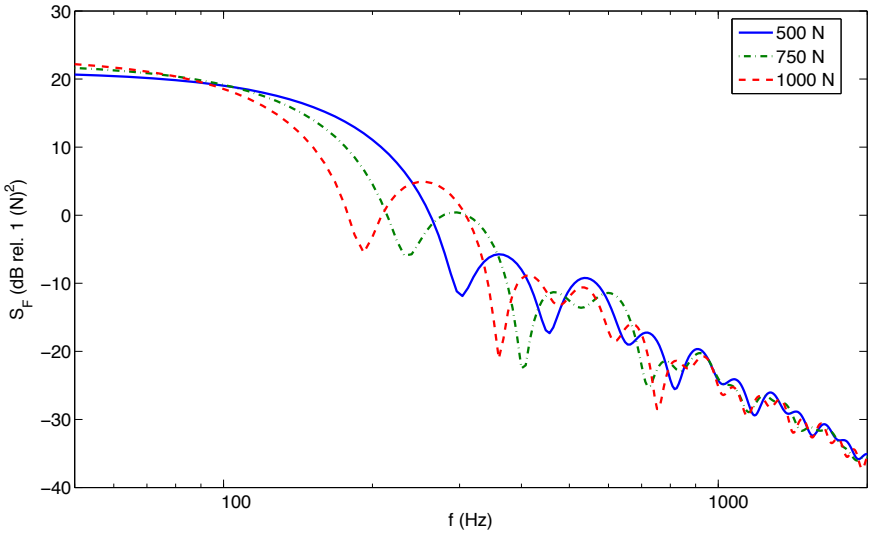


Figure 3.13 – Spectra $S_F$ of the resultant contact forces for total loads of respectively 500, 750 and 1000 N. The spherical asperity has a relative height of 1.57 mm. The rolling speed was 10 m/s.

### 3.3.3 Influence of the rolling speed

The influence of the rolling speed on the time evolution of the contact force is studied by plotting the time signals for three different rolling speed, respectively 5, 10 and 15 m/s, measured for the highest relative height of the spherical asperity, i.e. 1.57 mm, as presented in Figure 3.15.

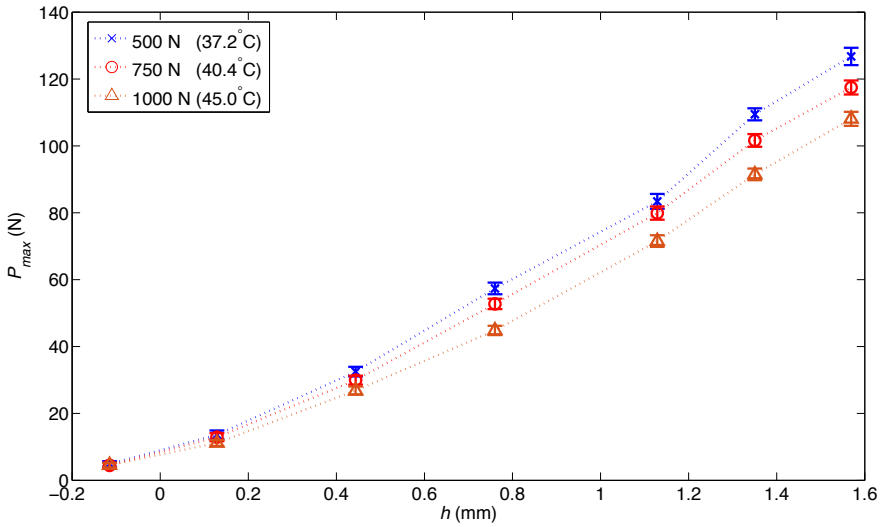


Figure 3.14 – Influence of the total load experienced by the tyre on the peak force. Three loads, respectively 500, 750 and 1000 N, were tested on the same day for the same rolling speed of 10 m/s. The tyre temperature was measured for each test. Error bars are plotted for the three loading conditions.

The contact durations $T_c$ for 5, 10 and 15 m/s are respectively 15.5, 7.6 and 5.3 ms. In Figure 3.16, the time is multiplied by each rolling speed to represent the contact length. The curves are shifted horizontally so that their peak values occur at the same position. The contact length is approximately the same for the three speeds and is close to 0.077 m. Therefore, the contact duration is inversely proportional to the rolling speed, which means that the contact is quasi-static. The peak contact forces are reached at the same position and are close in magnitude for 10 and 15 m/s, as also evidenced in the following in Figure 3.19.

A comparison of spectra $S_F$ of the resultant contact forces corresponding to the three rolling speeds is given in Figure 3.17. Take now 10 m/s as a reference speed $V_r$, the curve corresponding to the lower speed of 5 m/s is shifted to the left while having greater amplitudes at the first wave peaks. Reversely, the higher speed of 15 m/s causes the curve to be shifted to the right while having smaller amplitudes at peaks. By using an approach proposed in [Cesbron et al., 2009a] to regard the dynamic contact as quasi-static states, i.e. the resultant contact force is an invariant function of the position $Vt$, the spectral levels in Figure 3.17 can be linked to that of a reference speed. The modified spectrum $S^*_{F,i}$ for a given speed $V_i$ can be calculated as follows:

$$S^*_{F,i}(f) = S_{F,i}(f) + 20log_{10}(V_i). \tag{3.3}$$

By assuming that the resultant force $F$ is an invariant function of $V_i t$, the following relation should be verified:

$$S^*_{F,r}(f) = S^*_{F,i}(fV_i/V_r). \tag{3.4}$$

The modified spectra are represented in Figure 3.18 and are very similar in terms of magnitude up to 350 Hz. Therefore, the quasi-static nature of the contact is again verified.

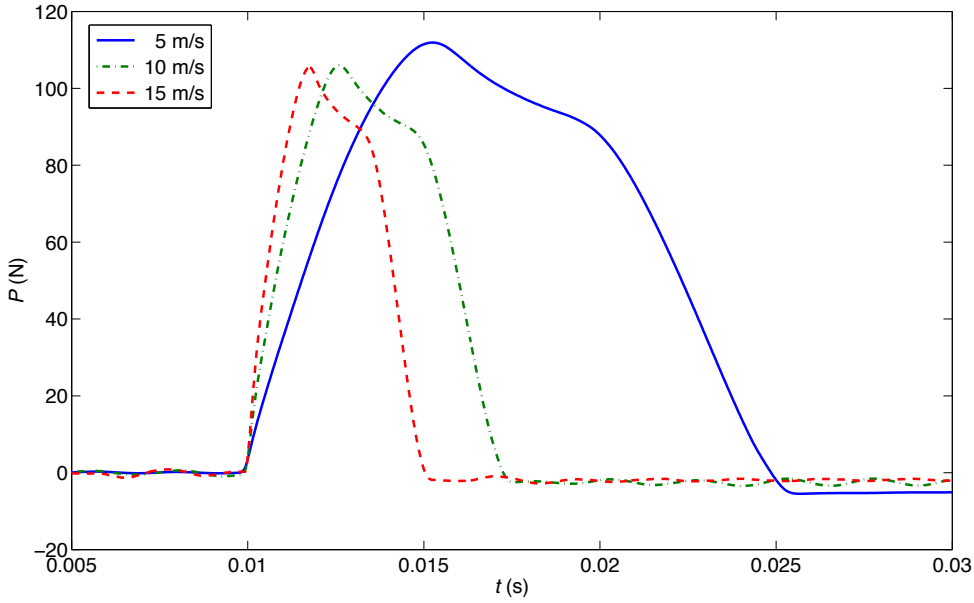


Figure 3.15 – Influence of the rolling speed on the contact force. Three rolling speeds, respectively 5, 10 and 15 m/s, were tested on the same day for the same load on the tyre of 1000 N.

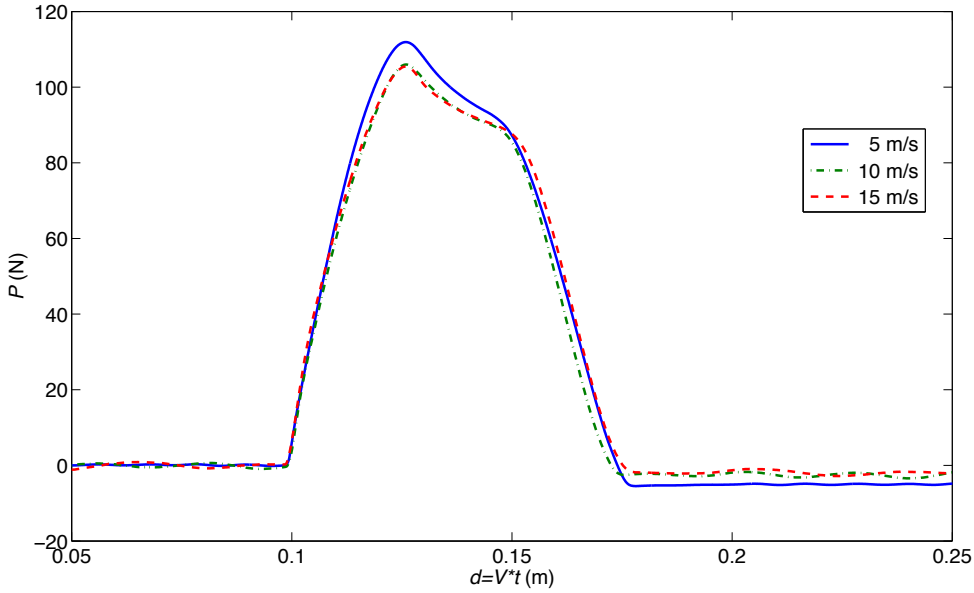


Figure 3.16 – Influence of the rolling speed on the contact length. Three rolling speeds, respectively 5, 10 and 15 m/s, were tested on the same day for the same load on the tyre of 1000 N. The time $t$ is multiplied by the respective rolling speed $V$ to represent the distance $d$ travelled during rolling.

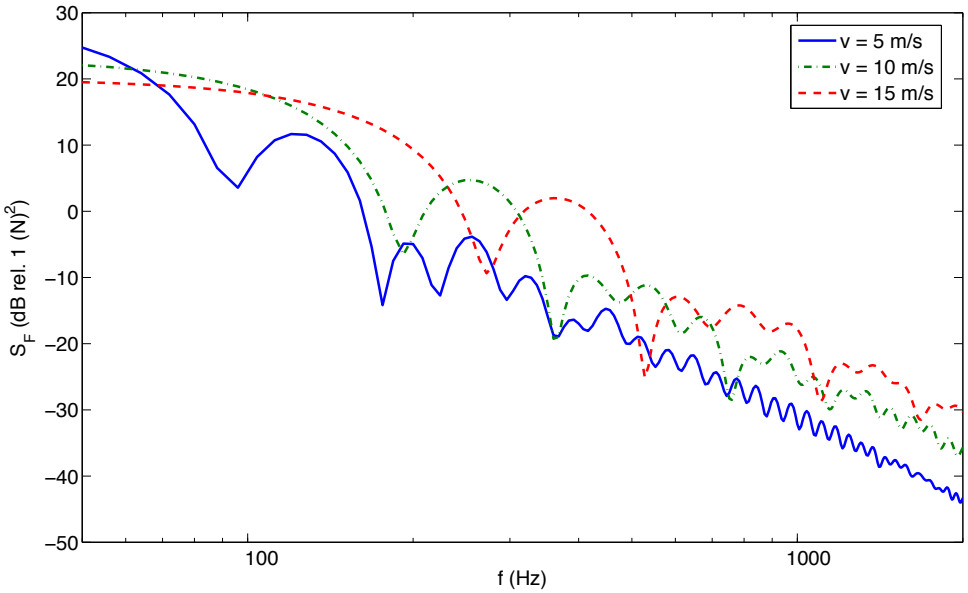


Figure 3.17 – Spectra $S_F$ of the resultant contact force at 5, 10 and 15 m/s. The spherical asperity has a relative height of 1.57 mm. The load on the tyre was 1000 N.

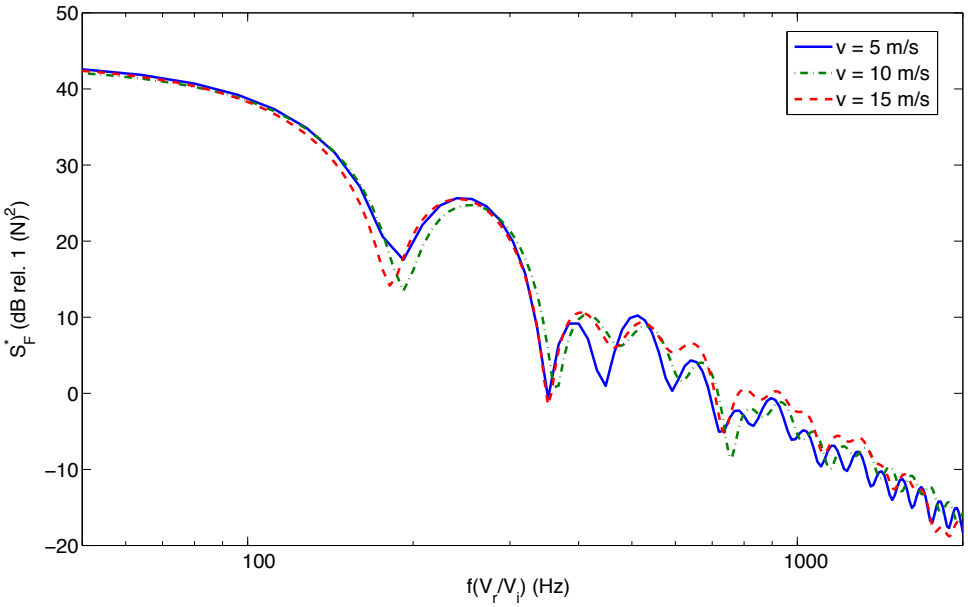


Figure 3.18 – Modified spectra $S_F^*$ of the resultant contact force at 5, 10 and 15 m/s with the reference speed $V_r$ = 10 m/s. The spherical asperity has a relative height of 1.57 mm. The load on the tyre was 1000 N.

The contact forces measured at seven relative asperity heights for rolling speeds of respectively 5, 10 and 15 m/s are given in Figure 3.19. The tyre surface temperature was measured for each test. The higher the speed, the higher the tyre surface temperature and the lower the contact force. As the speed rises, the contact force tends to stabilise. By comparing Figures 3.14 and 3.19,

it can be observed that, a change in load, which leads to a smaller change in temperature than a change in speed does, induces, meanwhile, a more pronounced change in contact force. This, again, supports the quasi-static nature of the contact.

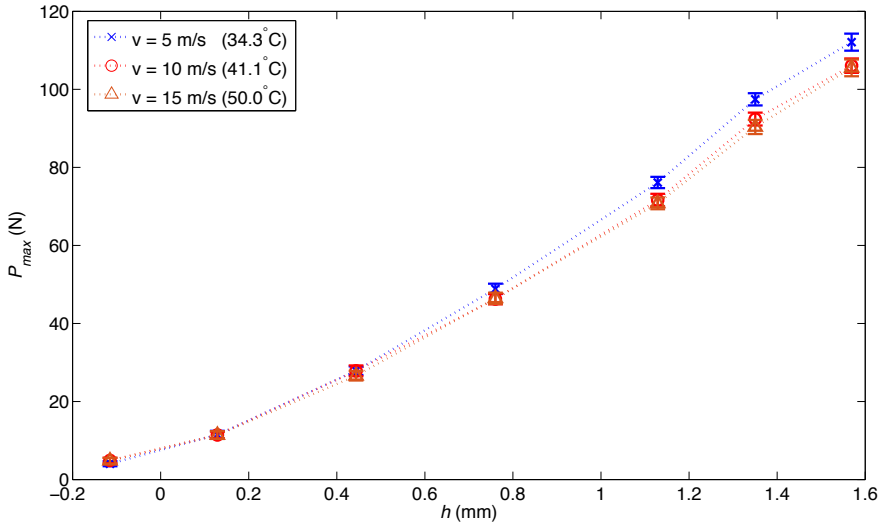


Figure 3.19 – Influence of the rolling speed on the peak force. Three rolling speeds, respectively 5, 10 and 15 m/s, were tested on the same day for the same load on the tyre of 1000 N. The tyre temperature was measured for each test. Error bars are plotted for the three rolling speeds.

### 3.3.4 Conclusions

The influences of several parameters have been analysed in this section. The asperity shape has a great influence on the contact. The experimental force-indentation relationships for a spherical asperity and a conical one follow the theoretical solutions by Hertz (sphere) and Love (cone), though shifted by a reference height $h_{ref}$. The exponents extracted from the measured data are close to those in the classical analytical solutions. Meanwhile, the total load and the rolling speed affect less the force-indentation relationship. By analysing the contact lengths and the force spectra for different rolling speeds, the quasi-static nature of the contact has been verified.

## 3.4 Contact model assessment

### 3.4.1 Elastic contact model

#### 3.4.1.1 Static contact patch calculations

Based on the assumptions that the contact is frictionless and that the tread of the tyre can be regarded as an elastic half-space, the tyre/road contact problem dealing with multiple asperities can be solved using the classical Matrix Inversion Method (MIM) [Johnson, 1985]. In this subsection, the validity of the elastic half-space assumption in the case of rolling contact with a single asperity is examined. To allow such comparisons to be performed, the assumption that the peak

force is reached when the tyre is right above the asperity tip is made. We first develop a numerical model to take the actual contact surface geometries, especially the existence of the cylindrical cavity, into account. Knowing the total load on the tyre, the contact pressure distribution within the tyre/road and tyre/asperity contact interfaces is calculated based on the elastic half-space assumption. Summing the pressure over the tyre/asperity contact area yields the peak normal contact force. Similar to the construction of experimental force-indentation relationships, numerical ones are established by plotting peak contact forces versus different relative asperity heights. Finally, they are compared with the experimental ones to evaluate the elastic half-space assumption for the prediction of peak forces under rolling conditions.

Thus, in the present section, the half-space assumption is applied to the reduced-sized tyre. The static contact with a rigid, smooth road surface including a cylindrical cavity inside which a rigid asperity is placed at the measured positions relative to the road surface is studied using the MIM. The actual curvatures of the road surface and the dimensions of the cavity and the asperity are taken into account in the model.

The detailed numerical procedure of the classical MIM can be found in [Cesbron and Yin, 2010]. In this study, the computation labour is reduced compared with the classical MIM by exploiting symmetries in the contact problem (see Appendix A). This optimisation not only simplifies the computation of the influence matrix, but also reduces the dimensions of matrices to be inverted in solving the matrix equation that combines the influence matrix and the equilibrium equation.

The dimensions of the mesh elements in this model are chosen to be 0.5 mm in both x (longitudinal) and y (transverse) directions. The estimated Young's modulus of 5 MPa used for calculating the static contact patches of the tyre, after rolling at 10 m/s and under a total load of 1000 N, in Figure 2.37 yields here relatively correct fits of contact forces to the experimental results. For the spherical asperity, the peak forces calculated for the measured relative asperity heights are compared with the experimental values in Table 3.2 for the configuration of a total load of 1000 N and a rolling speed of 10 m/s. The coefficients of variation of the measurements, defined as the ratio of standard deviation $\sigma(P_{max,exp})$ to peak contact force $P_{max,exp}$, range from 1.9% to 15.6% with a better precision for higher asperity positions. The numerical results for higher asperity positions agree better with the measured ones than those for lower positions.

Table 3.2 – Comparison of experimental results and numerical ones from the MIM for the spherical asperity. A Young's modulus of 5 MPa is calibrated for the configuration of a total load of 1000 N and a rolling speed of 10 m/s. The standard deviations $\sigma$ are given for the measured results.

| $h_{spherical}$ | (mm) | -0.12 | 0.13 | 0.44 | 0.76 | 1.13 | 1.35 | 1.57 |
|---|---|---|---|---|---|---|---|---|
| $P_{max,MIM}$ | (N) | 13.6 | 22.6 | 36.6 | 53.1 | 75.6 | 90.9 | 107.0 |
| $P_{max,exp}$ | (N) | 4.5 | 11.2 | 26.8 | 44.8 | 71.5 | 91.5 | 108.1 |
| $\sigma(P_{max,exp})$ | (N) | ± 0.7 | ± 0.9 | ± 1.2 | ± 1.4 | ± 1.7 | ± 1.8 | ± 2.1 |

A similar comparison is made for a total load of 500 N and a rolling speed of 10 m/s and is presented in Table 3.3. A change in total load necessitates solely a readjustment of the Young's modulus of the elastic half-space, as explained in Subsection 2.3.5. A modulus of 7 MPa is calibrated for the present loading condition and also coincides with the one used in Figure 2.37. A good agreement is found again for higher asperity positions between the calculated and the measured peak contact forces. Meanwhile, for lower positions, the elastic model yields better results for 500 N than for 1000 N.

Table 3.3 – Comparison of experimental results and numerical ones from the MIM for the spherical asperity. A Young's modulus of 7 MPa is calibrated for the configuration with a total load of 500 N and a rolling speed of 10 m/s. The standard deviations $\sigma$ are given for the measured results.

| $h_{spherical}$ | (mm) | -0.12 | 0.13 | 0.44 | 0.76 | 1.13 | 1.35 | 1.57 |
|---|---|---|---|---|---|---|---|---|
| $P_{max,MIM}$ | (N) | 9.8 | 20.1 | 37.2 | 58.3 | 87.5 | 107.2 | 128.8 |
| $P_{max,exp}$ | (N) | 4.9 | 13.6 | 32.5 | 57.4 | 83.4 | 109.4 | 126.7 |
| $\sigma(P_{max,exp})$ | (N) | ± 0.8 | ± 1.3 | ± 1.4 | ± 1.8 | ± 2.2 | ± 1.8 | ± 2.6 |

Numerical and experimental static contact pressure distributions are compared in Figures 3.20, and 3.21, respectively for relative heights of 0.44 and 1.57 mm. The experimental results remain qualitative, especially for 1.57 mm in which case the Fuji paper is considerably crumpled. For each relative height, calculations were performed based on the elastic half-space assumption for three loading conditions: 500, 750 and 1000 N. The corresponding Young's moduli are respectively 3.7, 3.3 and 2.9 MPa, same as those used in Figure 2.35, because the contact patches were measured with the tyre being at the room temperature. The contours of the numerical contact patches are superposed on the measured patches for comparison of dimensions.

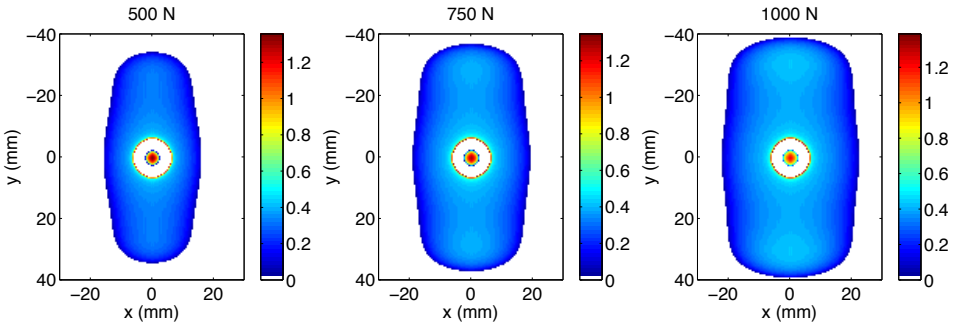


(a) Numerical contact patches

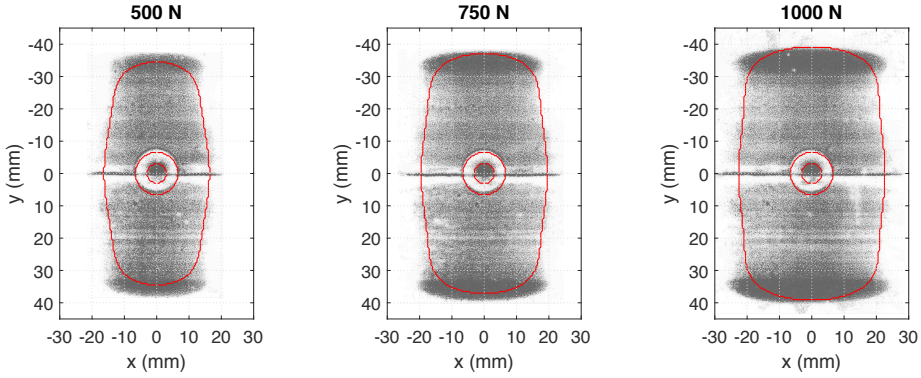


(b) Experimental contact patches

Figure 3.20 – Contact pressure distributions (in MPa) in the case of the spherical asperity at the relative height of 0.44 mm. The total loads are respectively 500, 750 and 1000 N. The corresponding Young's moduli are respectively 3.7, 3.3 and 2.9 MPa. The contours of the numerical contact patches are superposed on the measured patches for comparison of dimensions.

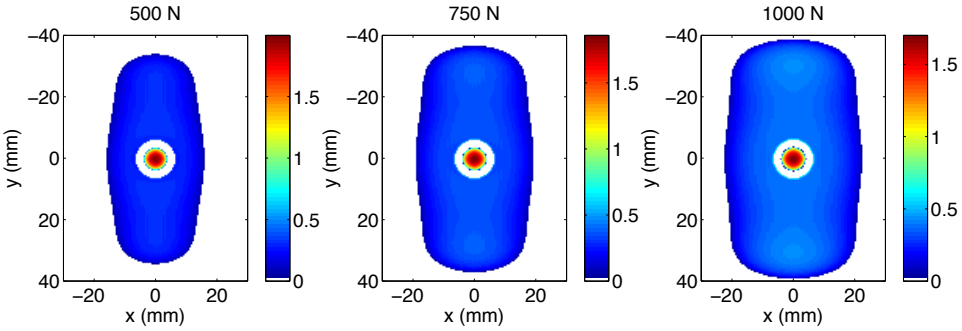


(a) Numerical contact patches

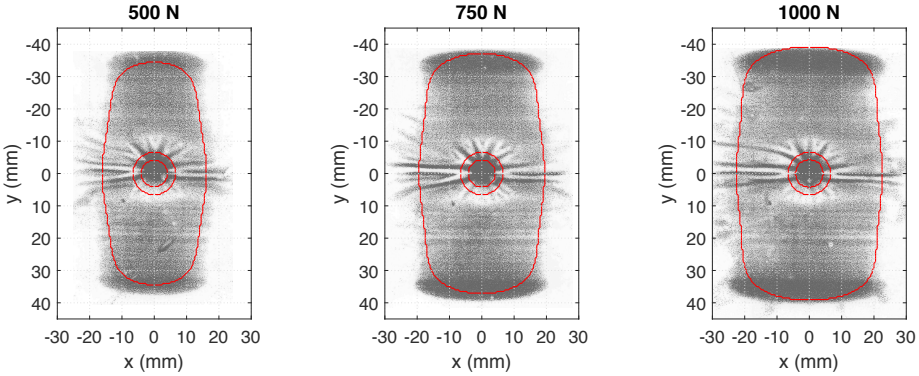


(b) Experimental contact patches

Figure 3.21 – Contact pressure distributions (in MPa) in the case of the spherical asperity at the relative height of 1.57 mm. The total loads are respectively 500, 750 and 1000 N. The corresponding Young's moduli are respectively 3.7, 3.3 and 2.9 MPa. The contours of the numerical contact patches are superposed on the measured patches for comparison of dimensions.

From the measured contact patches, it can be seen that for a fixed relative height of asperity, the total load does not affect significantly the contact area on the asperity. In addition, a similar influence of the sidewalls, when increasing the total load, on the contact pressure distribution to that in the configuration of the tyre loaded onto a flat surface, presented in Subsection 2.3.5, is observed. The higher pressure at the sidewalls is not well represented by the numerical model, with or without the asperity and the cylindrical cavity.

For the conical asperity, the peak forces calculated for the measured relative asperity heights are compared with the experimental values in Table 3.4. The coefficients of variation range from 2.7% to 16.1% with a better precision for higher asperity positions. The agreement is better than that for the spherical asperity (Table 3.2 for a total load of 1000 N and a rolling speed of 10 m/s) over the whole height range. An example of the numerical results is given in Figure 3.22.

The less desirable differences between the experimental and numerical results for lower asperity tip positions may have been induced by various factors. To enhance the agreement, the hyperelasticity of rubber and the sidewall effect could be taken into account in the model. Nevertheless, considering the simplicity of the numerical model, it provides satisfying predictions of contact forces for high asperities which interact more with the tyre than lower ones.

Table 3.4 – Comparison of experimental results and numerical ones from the MIM for the conical asperity. A Young's modulus of 5 MPa is calibrated for the configuration of a total load of 1000 N and a rolling speed of 10 m/s. The standard deviations $\sigma$ are given for the measured results.

| $h_{conical}$ | (mm) | -0.15 | 0.15 | 0.49 | 0.79 | 1.16 | 1.34 | 1.61 |
|---|---|---|---|---|---|---|---|---|
| $P_{max,MIM}$ | (N) | 2.9 | 6.8 | 13.1 | 20.4 | 32.2 | 38.8 | 50.5 |
| $P_{max,exp}$ | (N) | 1.7 | 2.8 | 8.0 | 15.8 | 27.6 | 38.1 | 48.4 |
| $\sigma(P_{max,exp})$ | (N) | ± 0.1 | ± 0.4 | ± 0.7 | ± 0.9 | ± 1.2 | ± 1.3 | ± 1.3 |

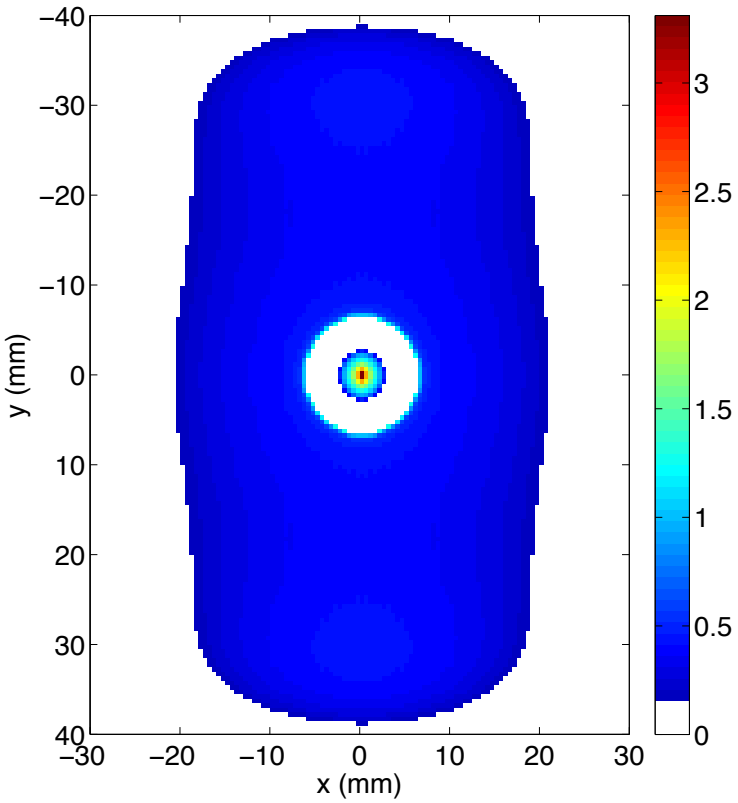


Figure 3.22 – Calculated contact pressure distribution (in MPa) in the case of the conical asperity at the relative height of 1.61 mm. The total load is 1000 N. The Young's modulus is 2.9 MPa.

#### 3.4.1.2 Influence of thermo-rheological properties

The tread rubber being a viscoelastic material, the temperature- and rate-dependences of its elastic modulus may influence the tyre/asperity contact force. As the load on the tyre increases, the tyre/road contact area also increases causing the rolling resistance to augment. The dissipated energy induces a rise in rubber temperature. Consequently, the storage modulus of tread rubber decreases which could explain the decrease in contact force in Figure 3.14. At low loading frequencies, the loss modulus rises with the frequency. Therefore, more energy is dissipated as the rolling speed rises. However, the decrease in storage modulus due to a rise in temperature is partially compensated by the fact that the modulus also increases with the frequency, which may explain the less pronounced influence of the rolling speed on the contact force in Figure 3.19.

Meanwhile, varying loads lead to varying force distributions on the metallic plate and the asperity. The possibility of the force distribution's being the main cause of the change in contact

force can be excluded by performing simulations using the MIM first without, then with consideration of the temperature-induced change in modulus. Figure 3.23 shows the results calculated with the same Young's modulus of 5 MPa for the three loads of 500, 750 and 1000 N. The variation of contact force does not follow the same tendency as in the experimental results. Figure 3.24 shows the results calculated with Young's moduli of 7, 6 and 5 MPa, respectively calibrated for the three loads of 500, 750 and 1000 N. In this instance, the numerical and experimental results are very close for higher asperity positions. Therefore, it may be concluded that the loading condition influences the contact force mostly via the temperature-dependence of rubber viscoelasticity.

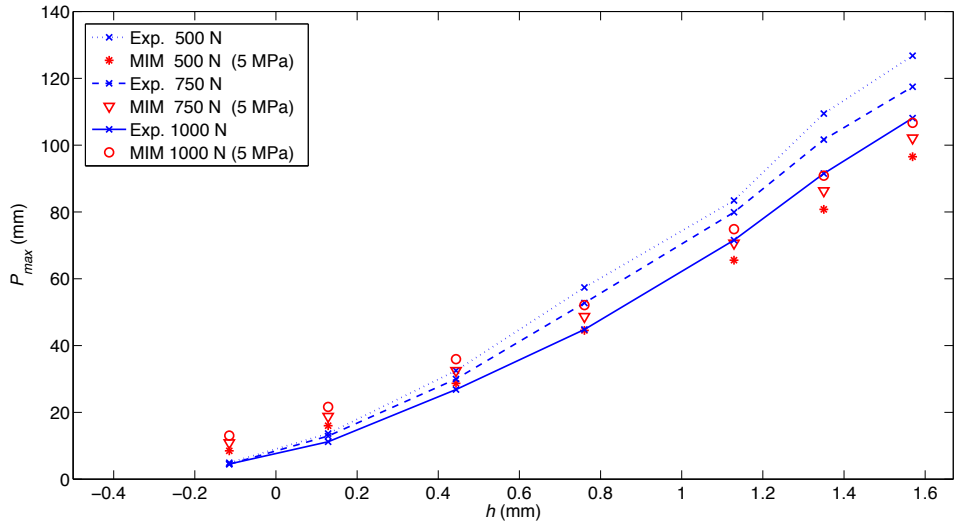


Figure 3.23 – Numerically calculated contact forces using the same Young's modulus of 5 MPa for the three loads of 500, 750 and 1000 N. The experimental curves in Figure 3.14 are plotted for comparison.

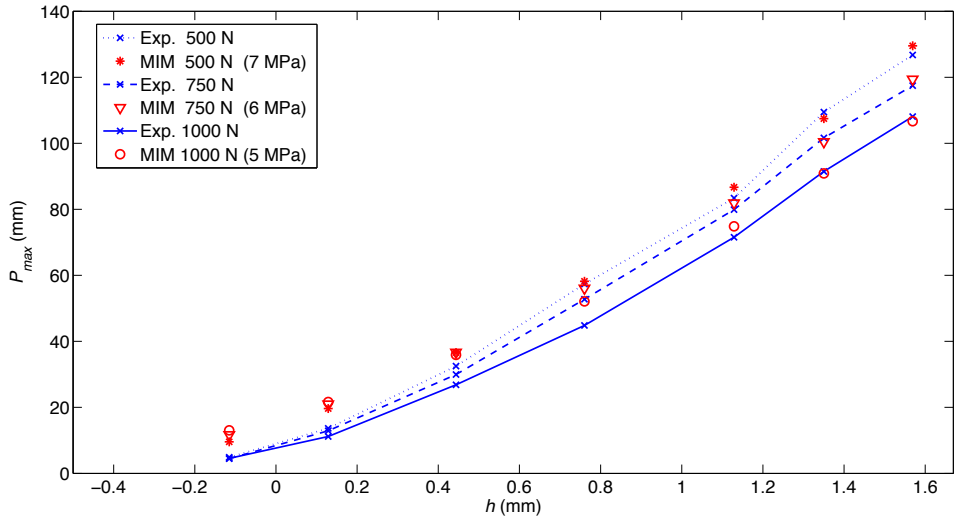


Figure 3.24 – Numerically calculated contact forces using Young's moduli of 7, 6 and 5 MPa respectively for the three loads of 500, 750 and 1000 N. The experimental curves in Figure 3.14 are plotted for comparison.

#### 3.4.1.3 Quasi-static calculations of the contact force evolution

Under the quasi-static assumption, the elastic contact model is used to calculate the contact force evolution for a series of positions along the tyre's rolling trajectory. To facilitate the description of the latter, the curvature of the rolling surface on the test rig is omitted in the model. Hence, the tyre rolls in a straight line at a chosen speed of 10 m/s. The dimensions of the mesh elements are respectively 1.25 mm in the rolling direction and 2.5 mm in the transverse direction. The tyre moves forward at a pace of 5 mm per time step.

Calculations are first performed for a total load of 500 N and a relative asperity height of 1.57 mm. The Young's modulus is 7 MPa. The numerical results of the contact force evolution are plotted along with the experimental curve in Figure 3.25 for comparison. The time is multiplied by the rolling speed to represent the distance travelled during rolling. The asperity tip position in the model is also represented. Note that the actual position of the tyre with respect to the rolling surface during the measurement is unknown. Thus, it is reasonable to place the positions where the peak forces occur in the experimental and the numerical curves to coincide with each other and then compare the shapes of the curves before and after reaching the maximum value. For 500 N, the contact duration with the asperity corresponds to 12 time steps in the numerical curve, which is symmetric and seems to be in agreement with the experimental curve. However, whether the actual asperity tip coincides with the one in the numerical model is still unclear.

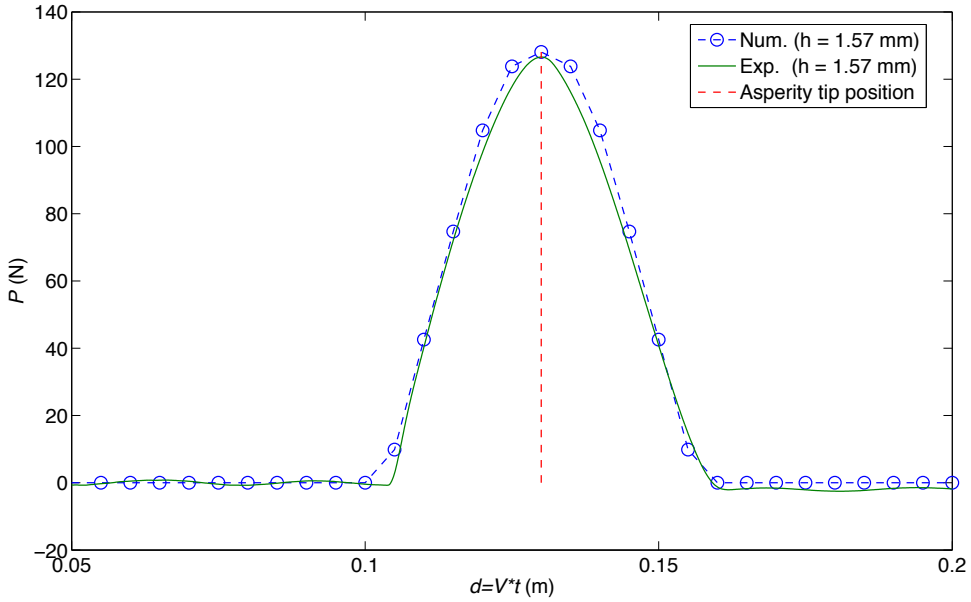


Figure 3.25 – Comparison of the contact force evolution, calculated using the elastic contact model, with the experimental curve in the case of a total load of 500 N and a rolling speed of 10 m/s. The time $t$ is multiplied by the rolling speed $V$ to represent the distance $d$ travelled during rolling. The positions where the peak forces occur are placed to coincide with each other.

Knowing that the experimental force evolution is strongly dissymmetric under high loads, calculations are then performed for a total load of 1000 N and a relative asperity height of 1.57 mm. The Young's modulus is 5 MPa. The comparison between the numerical and the experimental curves is illustrated in Figure 3.26. In this instance, the two curves do not have similar shapes; neither do they have the same contact duration.

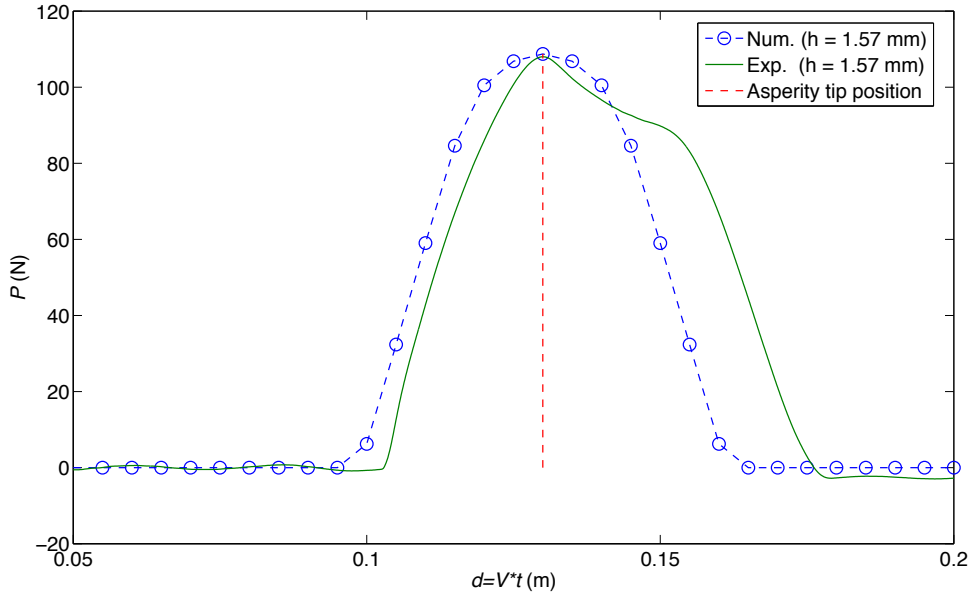


Figure 3.26 – Comparison of the contact force evolution, calculated using the elastic contact model, with the experimental curve in the case of a total load of 1000 N and a rolling speed of 10 m/s. The time $t$ is multiplied by the rolling speed $V$ to represent the distance $d$ travelled during rolling. The positions where the peak forces occur are placed to coincide with each other.

The elastic model fails to produce results with dissymmetry as in the measured contact force evolution, especially for high loads. Therefore, it would be necessary to introduce the viscoelasticity of rubber into the numerical model for rolling contact calculations.

## 3.4.2 Viscoelastic model

### 3.4.2.1 Viscoelastic stress-strain constitutive relations

To provide the theoretical ground of the memory effect due to the viscoelasticity of rubber involved in the tyre/road contact problem, a general formulation of viscoelastic stress strain constitutive relations is considered in the first place [Gurtin and Sternberg, 1962]. We assume isothermal conditions which can be physically interpreted as the stabilisation of tyre surface temperature so that constitutive model parameters are constant for the complete duration of the rolling problem to be analysed.

Consider the infinitesimal deformations at a point within a solid composed of a viscoelastic material which is said to have a memory. We make the hypothesis that the Cauchy stress tensor components $\sigma_{ij}$ depend on the complete past history of the Cauchy strain tensor components $\epsilon_{kl}$. This hereditary relation can be expressed in the form of a Stieltjes integral:

$$\sigma_{ij}(t) = \int_0^{\infty} \epsilon_{kl}(t-s)\, dG_{ijkl}(s) \quad or \quad \sigma_{ij}(t) = \epsilon_{kl} * dG_{ijkl}, \tag{3.5}$$

where $G_{ijkl}$ are components of a fourth order tensor and are called relaxation functions. The commutativity of the Stieltjes convolution allows the equation above to be written as follows:

$$\sigma_{ij}(t) = \int_0^t G_{ijkl}(t-\tau)\,\frac{d\epsilon_{kl}(\tau)}{d\tau}\,d\tau \quad or \quad \sigma_{ij}(t) = G_{ijkl} * d\epsilon_{kl}. \tag{3.6}$$

The inverse relation to Equation (3.6) leads to an alternative form of the stress strain relation:

$$\epsilon_{ij}(t) = \int_0^t J_{ijkl}(t-\tau)\,\frac{d\sigma_{kl}(\tau)}{d\tau}\,d\tau \quad or \quad \epsilon_{ij}(t) = J_{ijkl} * d\sigma_{kl}, \tag{3.7}$$

where $J_{ijkl}$ are components of a fourth order tensor and are called creep functions.

If we assume isotropy of the viscoelastic materials, the following expression obtains:

$$G_{ijkl} = \frac{G_2 - G_1}{3}\,\delta_{ij}\,\delta_{kl} + \frac{G_1}{2}\,(\delta_{ik}\,\delta_{jl} + \delta_{il}\,\delta_{jk}), \tag{3.8}$$

where $G_1$ and $G_2$ are respectively scalar relaxation functions in shear and isotropic compression and $\delta_{ij}$ the Kronecker delta. $G_1$ is typically associated with the stress deviator tensor $s_{ij}$ and the strain deviator tensor $e_{ij}$, respectively defined by:

$$s_{ij} = \sigma_{ij} - \frac{1}{3}\,\delta_{ij}\,\sigma_{kk}\,, \quad s_{kk} = 0, \tag{3.9}$$

$$e_{ij} = \epsilon_{ij} - \frac{1}{3}\,\delta_{ij}\,\epsilon_{kk}\,, \quad e_{kk} = 0, \tag{3.10}$$

where $\sigma_{kk}$ is the first stress invariant and $s_{kk}$ the first deviatoric stress invariant.

By separating the relaxation integral laws for shear and isotropic compression, the isotropic form of Equation (3.6) is split into two equations:

$$s_{ij} = G_1 * de_{ij}. \tag{3.11}$$

$$\sigma_{kk} = G_2 * d\epsilon_{kk}. \tag{3.12}$$

The corresponding creep integral laws are:

$$e_{ij} = J_1 * ds_{ij}. \tag{3.13}$$

$$\epsilon_{kk} = J_2 * d\sigma_{kk}, \tag{3.14}$$

where $J_1$ and $J_2$ are respectively scalar creep functions in shear and isotropic compression. By introducing the Laplace transform $\mathscr{L}$, defined by:

$$\mathscr{L}\{f(t)\}(s) = \int_0^\infty f(t)e^{-st}dt, \tag{3.15}$$

and using the property:

$$\mathscr{L}\{\phi * d\psi\}(s) = s\mathscr{L}\{\phi\}\mathscr{L}\{\psi\}, \tag{3.16}$$

the relationship between the relaxation and creep functions can be obtained from Equations (3.11) to (3.14):

$$\overline{J}_\alpha = (s^2\,\overline{G}_\alpha)^{-1}, \quad \alpha = 1, 2. \tag{3.17}$$

It is now expedient to use expressions of the isotropic relaxation functions in an analogous manner to those in the linear elasticity theory:

$$\mu(t) = G_1(t)/2, \tag{3.18}$$
$$k(t) = G_2(t)/3, \tag{3.19}$$

where $\mu(t)$ corresponds to the second Lamé parameter in elasticity and $k(t)$ the bulk modulus. This analogy between viscoelastic solutions and corresponding elastic solutions is termed elastic-viscoelastic correspondence principle. Elastic solutions are allowed to be converted into quasi-static viscoelastic ones by replacing elastic moduli by transformed viscoelastic properties [Christensen, 2012].

#### 3.4.2.2 Rolling contact formulation and discretisation

The 3D viscoelastic rolling contact has already been treated by Yin et al. [2015] in the travelling coordinate system of the contact patch. In this thesis, the contact pressure evolution is described in the fixed coordinate system of the road surface. Consider now the specific problem of viscoelastic rolling contact between a tyre and a road surface. The elastic solution of displacement along z-axis $u$ to a Boussinesq problem due to distributed pressure on an elastic half-space writes:

$$u(I) = \iint_{\Sigma_m} \frac{T(I,M)}{G}\, p(M)\, ds, \quad I \in \Sigma_m, \quad M \in \Sigma_c \tag{3.20}$$

where $\Sigma_c$ is the contact area, $G$ the shear modulus (also called the second Lamé parameter) and $T(I,M)$ the influence function defined as follows:

$$T(I,M) = \frac{1-\nu}{2\,\pi\, d(I,M)}, \tag{3.21}$$

where $\nu$ is the Poisson's ratio and $d(I,M) = \sqrt{(x_M - x_I)^2 + (y_M - y_I)^2}$ is the Euclidean distance between two point $I$ and $M$ in the xy-plane. The shear modulus $G$ considered here is an effective value taking into account the contributions of both solids. By assuming the shear modulus of the road material to be very large in front of that of the tyre rubber, the effective shear modulus could be considered equal to the rubber's shear modulus. The elastic half-space assumption is then readily applicable to the road surface by interchanging the shear moduli of both solids.

The elastic-viscoelastic correspondence principle is then applied to convert Equation (3.20) into a viscoelastic solution, written in Laplace transforms, to a contact problem in which the tyre is loaded onto the road surface without rolling:

$$\overline{u}(I,s) = \iint_{\Sigma_m} T(I,M)\, s\, \overline{J}(s)\, \overline{p}(M,s)\, ds. \tag{3.22}$$

When written in the Stieltjes integral form as in Equation (3.7), the equation above becomes:

$$u(I,t) = \int_0^t J(t-\tau)\,\frac{d}{d\tau}\left[\iint_{\Sigma_m} T(I,M)\,p(M,\tau)\,ds\right]d\tau, \quad I \in \Sigma_c(t), \quad M \in \Sigma_m, \tag{3.23}$$

where $t$ denotes the current time and $\tau$ varies between 0 and $t$. The vertical displacement $u$ due to the contact pressure history is evaluated within the current contact area $\Sigma_c(t)$. The maximum contact area $\Sigma_m$ comprises all points belonging to contact areas from the start of loading to the current time $t$. The pressure distribution $p(\tau)$ within $\Sigma_m$ is a function of the time variable $\tau$. $J(t)$ is the creep function converted from the relaxation function $G(t)$, analogous to the elastic shear modulus $G$ in Equation (3.20), through Equation (3.17).

The rolling conditions to be considered in the present problem are under the simplifying assumption that the friction at the contact interface can be neglected. Thus the rolling problem reduces to a sliding problem of a rigid solid representing the tyre loaded onto a viscoelastic half-space under a constant force. The kinematic conditions can be introduced by describing the spatial displacement of the contact area $\Sigma_c(t)$ relative to a global coordinate system fixed to the road surface as a function of time, i.e. in the Eulerian manner. A constant translational speed of $V_x$ along the x-axis is assumed for the tyre center.

Consider a point I belonging to the road surface whose xy-coordinates in the global coordinate system are denoted by $(X_I, Y_I)$. The total vertical displacement $u(I,t)$ observed at this point could be regarded as the summed contributions of contact pressure at all instants previous to $t$. Consider then a typical material point M within the tyre and belonging to the contact area for the whole contact duration. It has a fixed position in the local, travelling coordinate system fixed to the tyre center. Its coordinates in the global coordinate system at the initial instant are denoted by $(X_M, Y_M)$. The global coordinates in the xy-plane are therefore functions of the speed $V_x$ and the time variable $\tau$: $(X_M + V_x\,\tau, Y_M)$. The viscoelastic solution of $u(I,t)$ with consideration of the rolling conditions becomes:

$$u(I,t) = \int_0^t J(t-\tau)\,\frac{d}{d\tau}\left[\iint_{\Sigma_c(\tau)} T(I,M)\,p(M,\tau)\,ds\right]d\tau, \quad I \in \Sigma_c(t), \quad M \in \Sigma_c(\tau), \tag{3.24}$$

where

$$T(I,M) = \frac{1-\nu}{2\,\pi\,\sqrt{(X_I - X_M - V_x\,\tau)^2 + (Y_I - Y_M)^2}}. \tag{3.25}$$

The boundary conditions for solving the pressure distribution are as follows:

$$\begin{cases} \forall I \in \Sigma_c(t), & \delta(t) - z(I,t) - u(I,t) = 0 \quad \textit{and} \quad p(I,t) > 0 \\ \forall I \notin \Sigma_c(t), & \delta(t) - z(I,t) - u(I,t) > 0 \quad \textit{and} \quad p(I,t) = 0 \end{cases} \tag{3.26}$$

where $\delta(t)$ is the normal penetration of the tyre into the viscoelastic half-space yet to be determined, as the load is imposed in this problem. $z(I,t)$ represents the separation at point I and instant $t$ between the undeformed surfaces of the two bodies and can be written as the difference between the tyre surface geometry $z_t(I,t)$ and the road surface geometry $z_r(I,t)$. Since the

road is immobile, $z_r$ is independent of time. Hence, $z_r(I,t) \equiv z_r(I)$. On the contrary, $z_t(I,t)$, the z-coordinate of the projection point of I onto the tyre surface, is a function of speed $V_x$ and time $t$: $z_t(I,t) \equiv z_t(X_I, Y_I, t) = z_t(X_I - V_x\, t, Y_I, 0)$. Therefore, $z(I,t)$ is expressed as:

$$z(I,t) = z_t(X_I - V_x\, t, Y_I, 0) - z_r(X_I, Y_I). \tag{3.27}$$

The tyre surface geometry is obtained by rotating the outer contour of tyre cross-section around the axis parallel to the y-axis and passing through the tyre center. For the sake of simplicity, the outer contour within the global yz-plane containing the tyre center is considered. The geometry of the contour curve can be described by a polynomial curve $F(y)$ fitted to pass through several points whose positions relative to the tyre center are already measured. The polynomial curve $F(y)$ is shown in the left of Figure 3.27. For a given coordinate on the y-axis, the tyre contour geometry in the xz-plane, i.e. in the circumferential direction, is a circular arc to be calculated based on the transverse outer contour $F(y)$ of the tyre and the global coordinates $(X_P, Y_P, R_P)$ of the tyre center, with $R_P$ being the radius of the tyre. The circular contour in the xz-plane for $y = 0$ is shown in the right of Figure 3.27. For any point of xy-coordinates $(X, Y)$ on the tyre surface potentially in contact with the road surface, the z-coordinate $Z(X, Y)$ is involved in the following equation.

$$(R_P - F(Y))^2 = (X - X_P)^2 + (R_P - Z(X,Y))^2, \tag{3.28}$$

which leads to the solution of $Z$:

$$Z(X,Y) = R_P - \sqrt{(R_P - F(Y))^2 - (X - X_P)^2}. \tag{3.29}$$

Therefore, $z_t(X_I - V_x\, t, Y_I, 0)$ in Equation (3.27) can be expressed as:

$$z_t(X_I - V_x\, t, Y_I, 0) = Z(X_I - V_x\, t, Y_I). \tag{3.30}$$

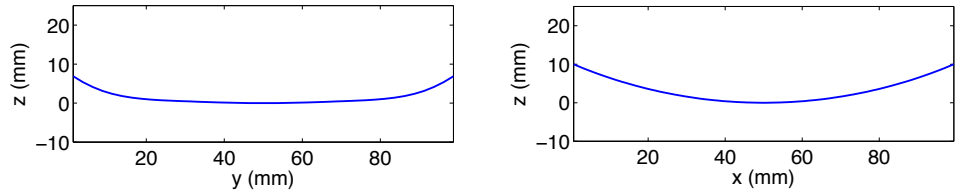


Figure 3.27 – Left: tyre contour along the transverse direction, described by a polynomial curve. Right: tyre contour along the circumferential direction, described by a circular arc.

The tyre surface is meshed with the same resolution as that of the road surface, with distinct spacings $dx$ and $dy$ along the x and the y directions, respectively. An example of the tyre surface geometry to be used in the viscoelastic rolling model is represented in Figure 3.28. Each mesh element is associated with its center point where the local displacement $u$, the separation $z$ between contact surfaces and the uniformly distributed pressure $p$ are evaluated.

To simulate the rolling contact with a prescribed loading for the complete rolling duration, to Equations (3.24), (3.25), (3.26) and (3.30) is added the following equation of equilibrium:

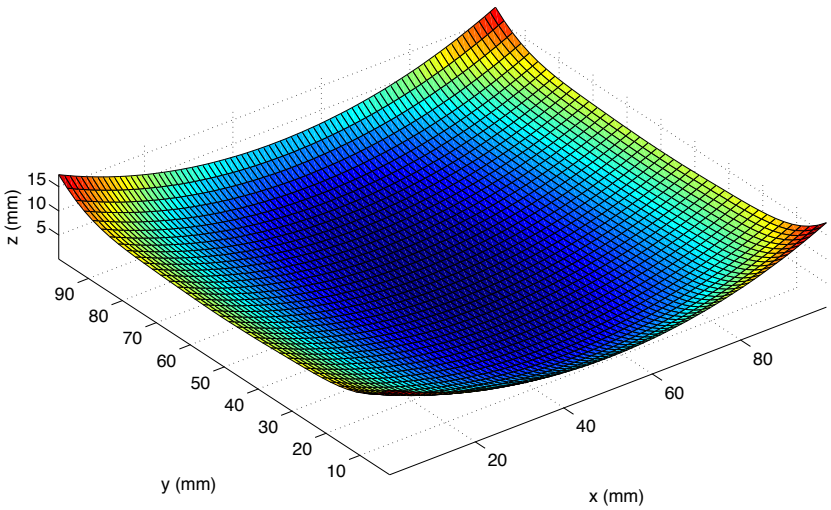


Figure 3.28 – Tyre surface geometry with the mesh used for the MIM calculation. The spacings are $dx = 1.25$ mm and $dy = 2.5$ mm.

$$P(t) = \int_{\Sigma_c(t)} p(t)\, ds. \tag{3.31}$$

The discretisation in space leads to the expression of the influence coefficient $T_{ij}$ to be calculated, using Love's result [Love, 2013], as the influence of a load associated to point $j$ on the element associated to point $i$ [Kozhevnikov et al., 2008].

To solve the time-dependent contact problem, a temporal discretisation is necessary in addition to the spatial discretisation. The total rolling duration $t$ is divided into $l$ time steps of duration $d\tau$. The creep function involved in Equation (3.24) becomes a right-continuous step function defined as follows:

$$J(t) = \sum_{k=1}^{l} J(kd\tau - d\tau)\, 1_{[kd\tau - d\tau, kd\tau[}(t), \tag{3.32}$$

where $1_{[kd\tau - d\tau, kd\tau[}(t)$ is the indicator function of interval $[kd\tau - d\tau, kd\tau[$ defined as:

$$1_{[kd\tau - d\tau, kd\tau)}(t) = \begin{cases} 1 & \text{if } t \in [kd\tau - d\tau, kd\tau[ \\ 0 & \text{if } t \notin [kd\tau - d\tau, kd\tau[ \end{cases} \tag{3.33}$$

Therefore, the displacement $u_i^l$ at point $i$ and time step $l$ is written in the following discretised form:

$$u_i^l = \sum_{k=1}^{l} J((l-k)d\tau) \sum_{j=1}^{n} T_{ij}\, [p_j^k - p_j^{k-1}], \tag{3.34}$$

where $p_j^k = p(X_j, Y_j, k\tau)$. By injecting the equation above into the discretised form of Equation (3.26) and placing the knowns on one side of the equal sign and the unknowns on the other side, the following equations obtain:

$$\delta^l - J(0) \sum_{j=1}^{n} T_{ij}\, p_j^l = z_i^l + v_i^{l-1}, \tag{3.35}$$

$$v_i^{l-1} = \sum_{k=1}^{l-1} J((l-k)d\tau) \sum_{j=1}^{n} T_{ij}\,[p_j^k - p_j^{k-1}] - J(0) \sum_{j=1}^{n} T_{ij}\, p_j^{l-1}, \tag{3.36}$$

where $T_{ij}$ with consideration of the rolling conditions is written as:

$$T_{ij} = \frac{1-\nu}{2\pi} \int_{Y_j^k-(dy/2)}^{Y_j^k+(dy/2)} \int_{X_j^k-(dx/2)}^{X_j^k+(dx/2)} \frac{dx\,dy}{\sqrt{(X_i - X_j - V_x\,d\tau)^2 + (Y_i - Y_j)^2}}, \tag{3.37}$$

with the same convention as in Equation (3.25) that the coordinates correspond to the initial instant.

#### 3.4.2.3 Results

Calculations are first performed for a total load of 500 N and a rolling speed of 10 m/s. The parameters of the model are very similar to those in the elastic model for contact force evolution. Only the elastic material properties are replaced by a viscoelastic constitutive model. It would be ideal to use the Prony series identified in Subsection 2.2.2. However, the Prony series is usually an expansion of the shear relaxation modulus. Calculating the creep compliance from a Prony series with multiple terms requires using Equation (3.17) to which there is no closed-form solution. Therefore, a Zener model (Figure 3.29) is used for the sake of simplicity. The creep compliance is expressed as:

$$J(t) = \frac{1}{E_\infty} - \frac{E_1}{E_\infty(E_1 + E_\infty)} e^{-t/\tau_1}, \tag{3.38}$$

where $\tau_1 = \eta(E_1 + E_\infty)/E_1E_\infty$ [Christensen, 2012]. The elastic moduli $E_\infty$ in the spring branch and $E_1$ in the Maxwell branch are assumed to be equal. After calibration, the long-term modulus $E_\infty = 4$ MPa and the characteristic time of the Maxwell branch $\tau = \eta/E_1 = 0.5$ ms.

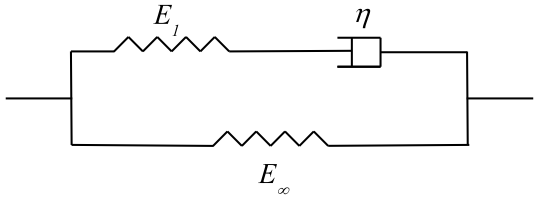


Figure 3.29 – Schematic view of the Zener model [Dubois et al., 2011].

The numerical results of contact force evolution are plotted, as a function of the distance, along with the experimental curve in Figure 3.30 for comparison. The calculated curve is clearly

no longer symmetric, as indicated by the deviation of the position where the peak force occurs from the asperity tip. The peak force is reached before the center of the tyre arrives right above the asperity tip. The contact pressure distributions are plotted for the instant of peak force and an instant after the contact with the asperity, respectively in the left and the right of Figure 3.31.

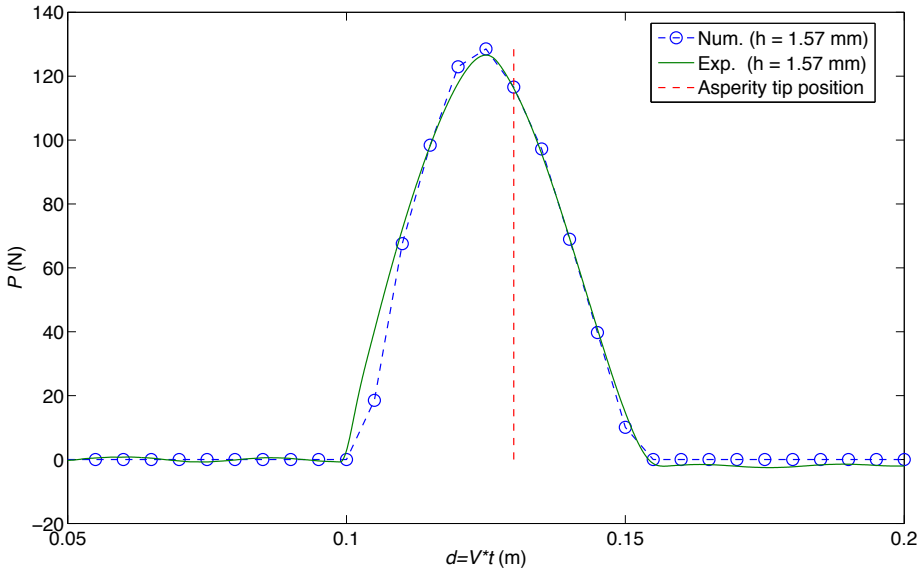


Figure 3.30 – Comparison of the contact force evolution, calculated using the viscoelastic contact model, with the experimental curve in the case of a total load of 500 N and a rolling speed of 10 m/s. The time $t$ is multiplied by the rolling speed $V$ to represent the distance $d$ travelled during rolling. The positions where the peak forces occur are placed to coincide with each other.

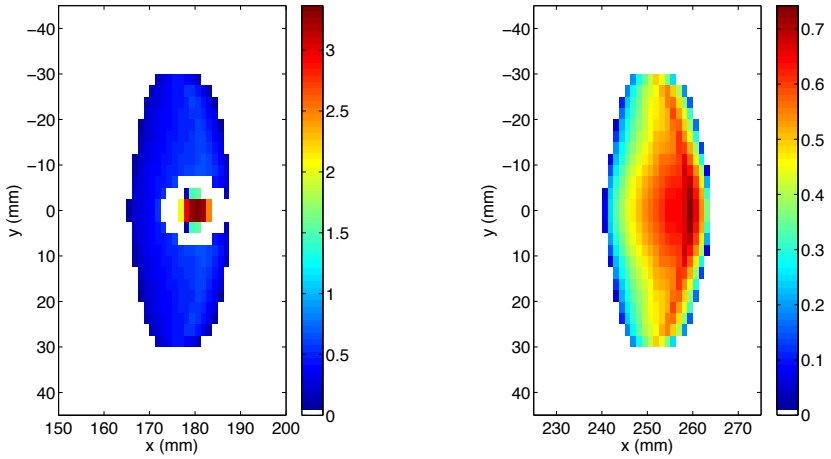


Figure 3.31 – Contact pressure distributions (in MPa) for (left) the instant of peak force and (right) an instant after the contact with the asperity.

To verify the convergence in the previous calculations, the model is reconfigured with a finer resolution in both space and time: the spacings $dx = 0.625$ mm instead of 1.25 mm, $dy = 1.25$ mm instead of 2.5 mm and the number of time step within the same total time is also doubled.

The contact force evolution and the pressure distribution are respectively depicted in Figures 3.32 and 3.33. It can be seen that the model already converges with a lower resolution which takes about 4 minutes for the calculation presented, while the finer version takes about 8 hours.

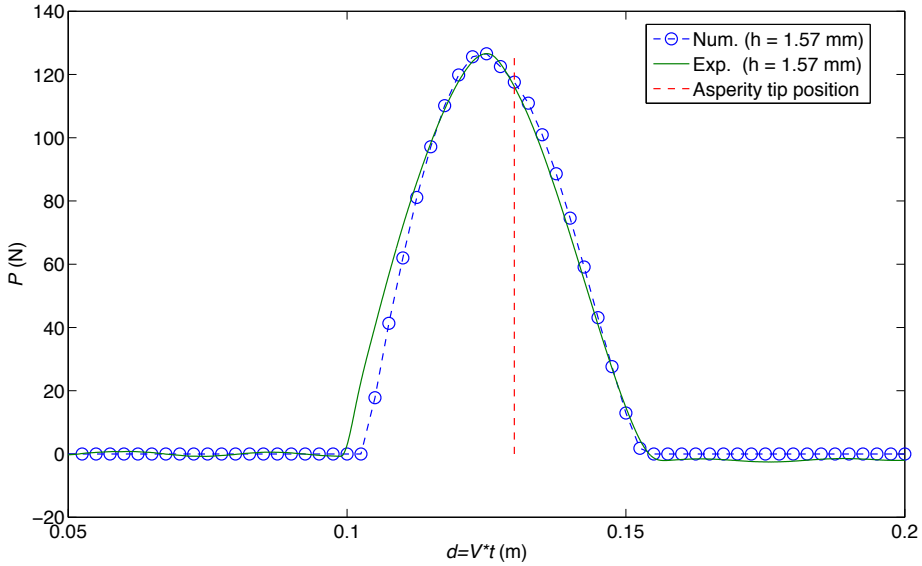


Figure 3.32 – Contact force evolution calculated using the viscoelastic contact model with a higher resolution in both time and space than for Figure 3.30.

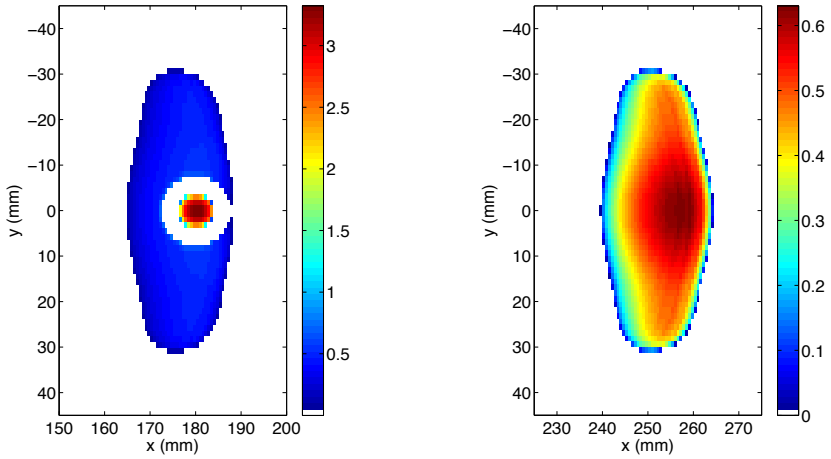


Figure 3.33 – Contact pressure distributions (in MPa), calculated with a higher resolution in both time and space than for Figure 3.31, for (left) the instant of peak force and (right) an instant after the contact with the asperity.

The viscoelastic model with lower resolution is then used to calculate the force evolution for different relative heights of the spherical asperity. The results are plotted in Figure 3.34 for comparison with experimental curves. The model predicts peak forces rather accurately for high asperity positions. For lower positions, the contact force on the asperity could be more easily affected by the pressure distribution that is not well represented by the model.

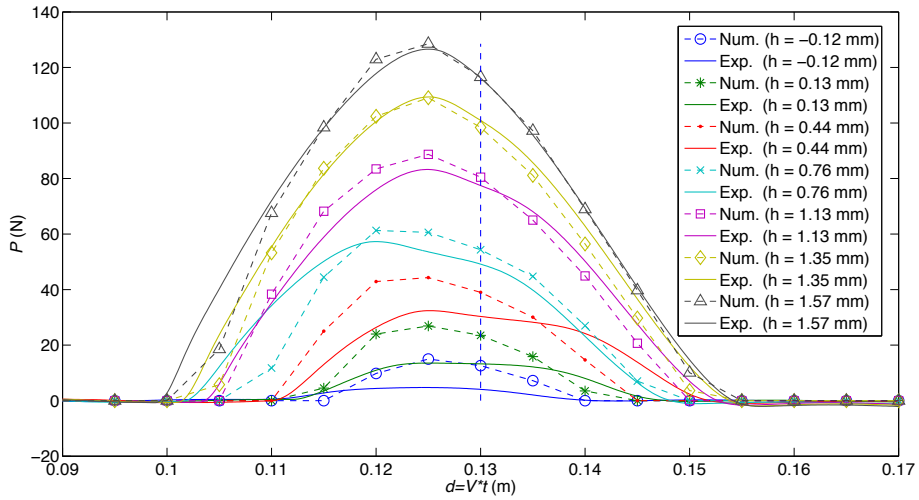


Figure 3.34 – Comparison of the contact force evolutions, calculated using the viscoelastic contact model for different relative heights of the spherical asperity, with the experimental curve in the case of a total load of 500 N and a rolling speed of 10 m/s. The positions where the peak forces occur are placed to coincide with each other.

This same model with $E_\infty = 2.8$ MPa is used to calculate the force evolution and the contact pressure distribution for a total load of 1000 N and a rolling speed of 10 m/s, as respectively shown in Figures 3.35 and 3.36. The discrepancy between the numerical and the experimental curves may be due to the use of an oversimplified constitutive model instead of the Prony series. The absence of the sidewall effect and the hyperelasticity in the model may also contribute to the inconsistency.

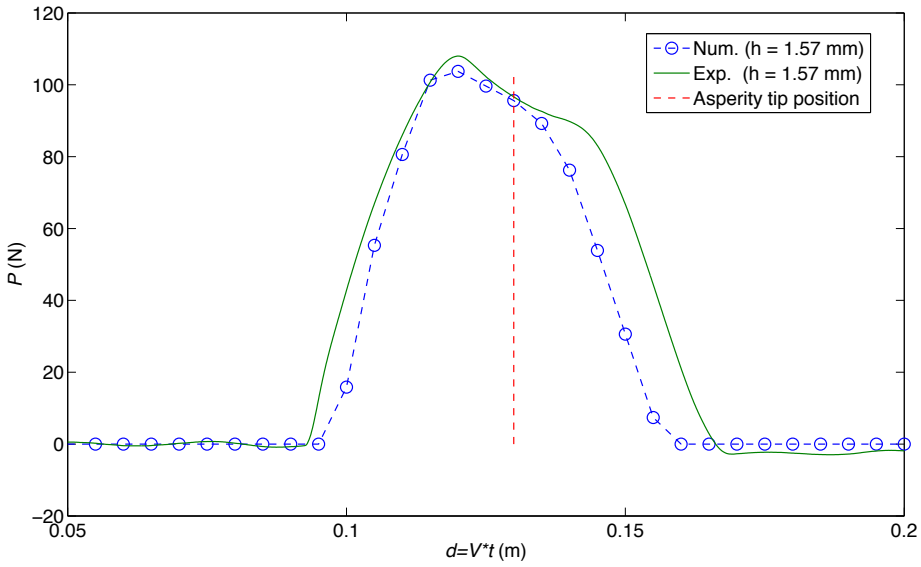


Figure 3.35 – Comparison of the contact force evolution, calculated using the viscoelastic contact model, with the experimental curve in the case of a total load of 1000 N and a rolling speed of 10 m/s. The positions where the peak forces occur are placed to coincide with each other.

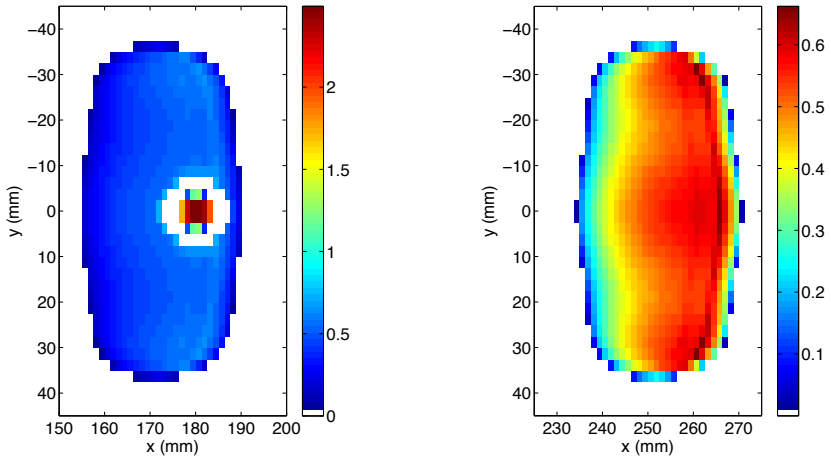


Figure 3.36 – Contact pressure distributions (in MPa) for (left) the instant of peak force and (right) an instant after the contact with the asperity.

## 3.5 Conclusions

This chapter deals with the investigations of dynamic contact forces between the reduced-sized tyre and a single asperity of simple geometric shape which is embedded in the rolling surface of the test rig and connected to a uni-axial force transducer. The latter, combined with the asperity, has the advantage of allowing direct measurements of the contact force, without interfacial layer, to be performed. The position of the asperity tip relative to the rolling surface is measured for 7 height levels for both a spherical asperity and a conical one. By comparing the measurement results for the same configuration but obtained on three different days, the repeatability of the tests is verified for the whole range of relative heights under consideration.

Next, tests are performed to study how factors like the geometric shapes of indenter, the total load and the rolling speed affect the dynamic contact, more precisely, from three aspects including the contact force evolution, the frequency content and the force-indentation relationship. The influence of the geometric shapes of indenter is studied through comparison of:

- the contact force evolutions, which shows that the spherical asperity induces greater contact forces than a conical asperity of similar relative height, while the signal shapes and the contact durations remain close;
- the frequency contents, which shows that the contact force evolution for the spherical asperity is better approximated by a half-sine function than the conical one is;
- the force-indentation relationships, which shows that the Boussinesq contact theory can be applied with adjusted indentation depths.

The influence of the total load is studied through comparison of:

- the contact force evolutions, which shows that a greater total load leads to a weaker peak force yet a wider contact patch in the rolling direction;
- the frequency contents, which shows that a higher load causes the resultant contact force to start to decrease significantly at a lower critical frequency, due to a longer contact duration;

- the force-indentation relationships, which shows that the load affects the contact force through a change in temperature at the surface of the tyre, changing the mechanical properties of the tread rubber.

The influence of the rolling speed is studied through comparison of:

- the contact force evolutions, which shows that the contact duration is inversely proportional to the rolling speed;
- the frequency contents, which shows that the resultant contact force is an invariant function of the position in the rolling direction;
- the force-indentation relationships, which shows that the rolling speed does not have a pronounced influence on the peak force.

The aforementioned conclusions concerning the influence of the rolling speed support the quasi-static nature of the contact.

Finally, numerical models based on the elastic or viscoelastic half-space assumption have been assessed in terms of how well they can be used to predict the contact force evolution and pressure distribution vis-à-vis the experimental results. For the elastic contact model, the assumption that the peak force is reached when the tyre is right above the asperity tip is made. Therefore, this configuration is employed in static contact calculations to evaluate the variations of the peak force and the contact pressure distribution for different relative heights of the asperity. With a carefully calibrated Young's modulus, the calculated peak contact forces are in good agreement with the measurement ones for high asperity position. However, the sidewall effect on the pressure distribution is not well represented by the elastic model. Quasi-static calculations of the contact force evolution show that the dissymmetry in the experimental curves is absent in the results from the elastic model. Consequently, a viscoelastic rolling contact model is formulated, and numerical results are obtained by using a Zener constitutive model. The model is most accurate for weak total loads and high asperity positions. Possible ways to improve the accuracy are to use the measured Prony series instead of a Zener model and/or to take into account the hyperelasticity and the sidewall effect in the model.

# Chapitre 4 : Contact dynamique avec plusieurs aspérités

Dans ce dernier chapitre, le banc d'essai est utilisé pour étudier les forces de contact dynamique entre le pneumatique de taille réduite et plusieurs aspérités de forme sphérique ou conique. Les essais sont réalisés en conditions de roulement. Comme au chapitre précédent, les forces de contact dynamique sont mesurées à l'aide d'un ensemble de capteurs de force piezo-électriques intégrés au bâti cylindrique du banc d'essai. Toutes les aspérités sont situées à la même hauteur, qui est contrôlée avec précision à l'aide d'une mesure par capteur à faisceau laser. La répétabilité des essais sur chaque aspérité est vérifiée à partir de 100 impacts successifs à une même vitesse de roulement. La symétrie des forces de contact par rapport à l'axe de roulement n'est pas parfaitement vérifiée en raison de défauts de montage du système et de l'apparition de forces de contact négatives sur certaines aspérités, dont l'origine reste à expliquer.

Les résultats expérimentaux sont ensuite présentés en s'intéressant à différents paramètres. Dans un premier temps, l'influence de la géométrie de l'aspérité sur la distribution des forces de contact dynamique est étudiée. Comme au chapitre 3, à hauteur équivalente, les forces de contact sur les sphères sont plus élevées que sur les cônes mais l'allure des signaux temporels est similaire et les durées de contact sont proches. L'influence de la charge totale sur la distribution des forces de contact dynamique est ensuite étudiée. La durée de contact augmente avec la charge totale, ce qui est cohérent avec la configuration d'une seule aspérité. Cependant, bien que l'évolution temporelle de la force de contact soit dissymétrique, le temps nécessaire pour atteindre la force maximale sur une aspérité est presque le même pour toutes les charges testées. Enfin, l'influence de la vitesse de roulement sur la force de contact est analysée. La nature quasi-statique du contact dynamique sur plusieurs aspérités est ainsi vérifiée par le fait que la durée de contact est inversement proportionnelle à la vitesse de roulement.

Dans la dernière partie du chapitre, la Méthode d'Inversion de Matrice (MIM) basée sur l'hypothèse de massif semi-infini est confrontée aux résultats expérimentaux. Le modèle élastique est premièrement testé en utilisant les modules d'Young recalés au chapitre précédent. Des empreintes de contact statique sont calculées pour différentes charges totales sur le pneumatique puis comparées aux empreintes mesurées à l'aide de papier Fuji. Les dimensions des empreintes et les aires de contact sur les aspérités sont assez bien estimées. Enfin, le problème de contact multi-aspérités avec roulement est résolu dans le cas viscoélastique en employant un modèle de Zener avec les mêmes paramètres recalés pour le contact avec une seule aspérité. L'accord essai/-calcul est meilleur pour les aspérités qui ont moins d'interactions avec les fortes concentrations de pressions de contact au niveau des flancs du pneumatique. Il pourrait aussi s'agir d'un effet des flancs et d'une limitation de l'hypothèse de massif semi-infini. Néanmoins, la dissymétrie des signaux temporels est bien estimée dans cette approche, ce qui est physiquement représentatif de l'interaction pneumatique/chaussée en conditions de roulement.

# Chapter 4

# Dynamic contact with multiple asperities

## 4.1 Introduction

In this chapter, the test rig is used to investigate the contact force between the reduced-sized pneumatic tyre and multiple asperities of spherical or conical shape under rolling conditions. All 16 asperities are have the same relative height and are arranged in several columns in the transverse direction. Triggering the force transducer connected to the first asperity to be in contact with the tyre activates simultaneously all other transducers. Section 4.2 explains how the asperities are arranged and presents the measured geometric properties of the spherical and the conical asperities. The measurement repeatability of the time signals is also verified in this section for all spherical asperities. In Section 4.3, experimental results are presented for studying the influences of different parameters on the peak contact force, such as the shape of the asperities, the total load and the rolling velocity. Section 4.4 concerns the contact model assessment in the case of multiple asperities and is divided into two parts. The first part concerns the comparison between experimental contact patches measured in static conditions under different total loads and solutions from a numerical model based on the elastic half-space assumption. In the second part, numerical results on all 16 asperities from a viscoelastic model are compared with experimental ones. Finally, concluding remarks are given.

## 4.2 Materials and Methods

### 4.2.1 Configurations for multiple contact analysis

In this configuration, the metallic plate hosting a single asperity described in Section 3.2 is replaced by another one which hosts 16 asperities of the same geometric shape. The 16 asperities are arranged in columns with one to four asperities per column in the transverse direction. A schematic view of the arrangement is depicted in Figure 4.1 in which the asperities in column 4 are highlighted as an example. Each of the asperities has a unique number and is screwed onto a uniaxial force transducer (PCB Model 208A12) which is embedded in the metallic plate. The force transducers are placed behind the metallic plate to facilitate the experimental set-up as illustrated in Figure 4.2. Each piezoelectric force transducer is triggered simultaneously with the one in column

1, positioned under the first asperity that comes into contact with the tyre in one revolution, and captures the dynamic normal force history throughout the contact duration on the corresponding asperity. The tyre comes into contact with the asperities once per revolution about the cylindrical axis of the test rig. The asperity tips are so placed that they all have the same height relative to the rolling surface, irrespective of the geometric shape of the asperities. However, the influence of the latter, the only factor related to the asperities, will be examined.

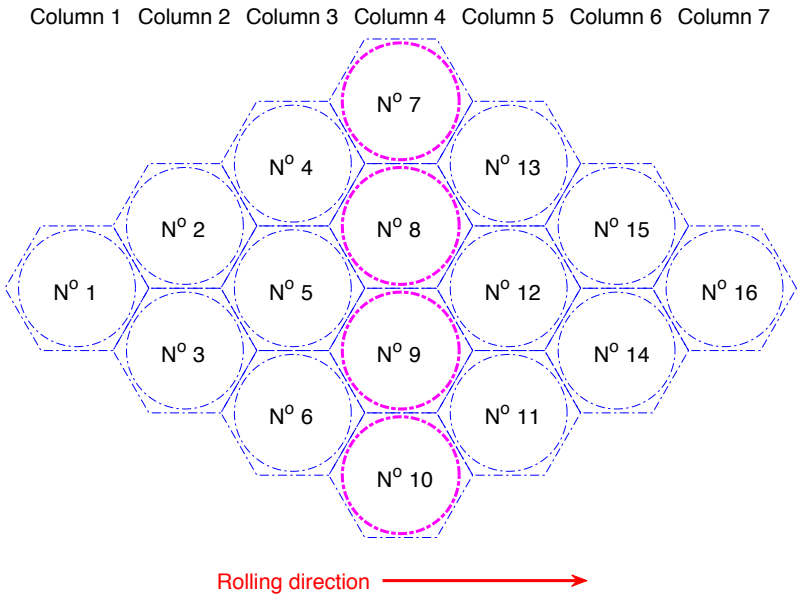


Figure 4.1 – Arrangement of the 16 asperities in 7 columns oriented in the transverse direction.

(a) Global view of the rolling surface on the metallic plate hosting multiple asperities.

(b) Zoom of the connection between the asperities and the force transducers.

Figure 4.2 – Global transverse view of the metallic plate hosting multiple asperities connected to force transducers.

### 4.2.2 Measurement of actual surface geometries

In this study, a 2D laser scanner (Micro-Epsilon Model scanCONTROL 2700-50) was used to assess more accurately the relative height of each asperity, as shown in Figure 4.3. By placing a transverse laser line that passed through the asperity tips belonging to the same column, a list of scattered points whose positions described the surface geometries of the metallic plate and the asperity could be obtained. The least squares fitting technique was applied to find a smooth circular curve for the profile of the spherical asperities and two straight lines for the profile of the conical asperities. Figure 4.4 shows the scanned profiles of the asperities belonging to column 4, in the cases of spherical and conical asperities. The fitting accuracy may be compromised due to the incomplete profile of the asperities on the two sides limited by the length of the laser line and the short segments between the asperities that can be used to find the horizontal position.

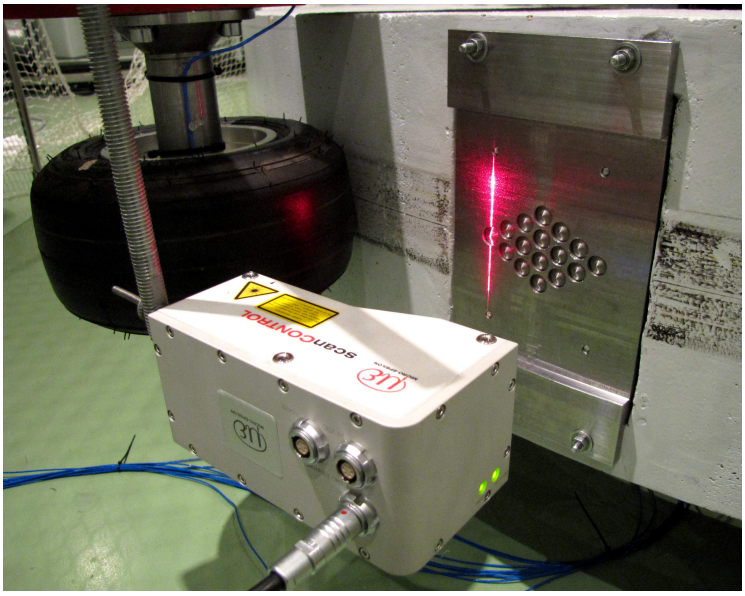


Figure 4.3 – Experimental set-up of the 2D laser profile scanner for measuring asperity height in the case of multiple asperities.

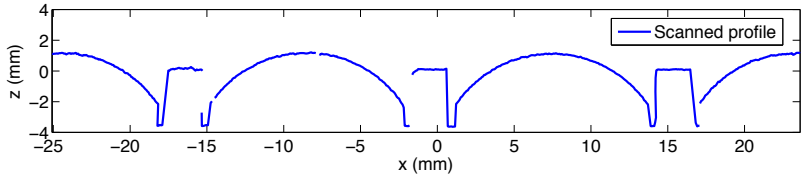


(a) Spherical asperities

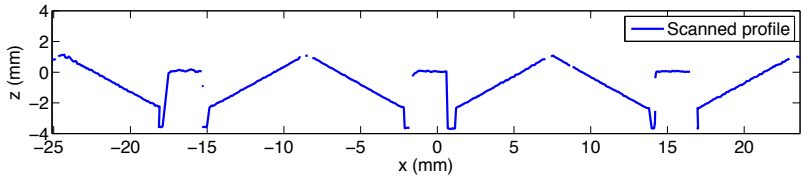


(b) Conical asperities

Figure 4.4 – Scanned profile of the asperities N$^{o}$ 7 to 10 belonging to column 4.

The relative heights and the radii of all 16 spherical asperities are respectively presented in Figures 4.5 and 4.6. The average relative height is 1.03 mm with a standard deviation of 0.05 mm. The average radius is 7.47 mm with a standard deviation of 0.09 mm while the theoretical radius is 7.50 mm.

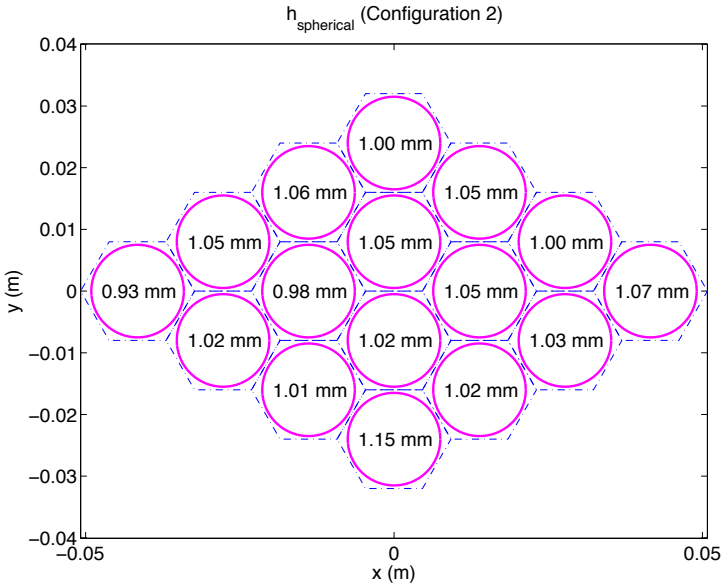


Figure 4.5 – Relative asperity heights measured for 16 spherical asperities. The tyre rolls along the x direction.

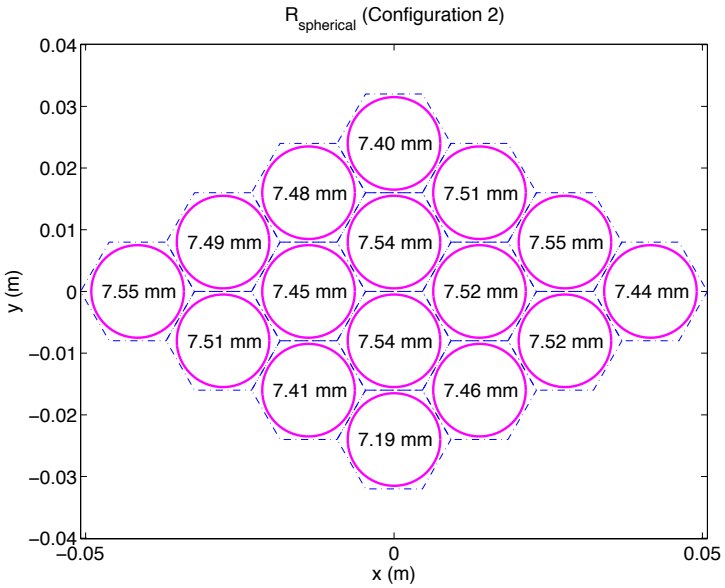


Figure 4.6 – Radii measured for 16 spherical asperities.

The relative heights and the half-apex angles of all 16 conical asperities are respectively presented in Figures 4.7 and 4.8. The average relative height is 1.03 mm with a standard deviation of 0.04 mm. The average half-apex angle is 61.2° with a standard deviation of 0.4° while the theoretical half-apex angle is 61.1°.

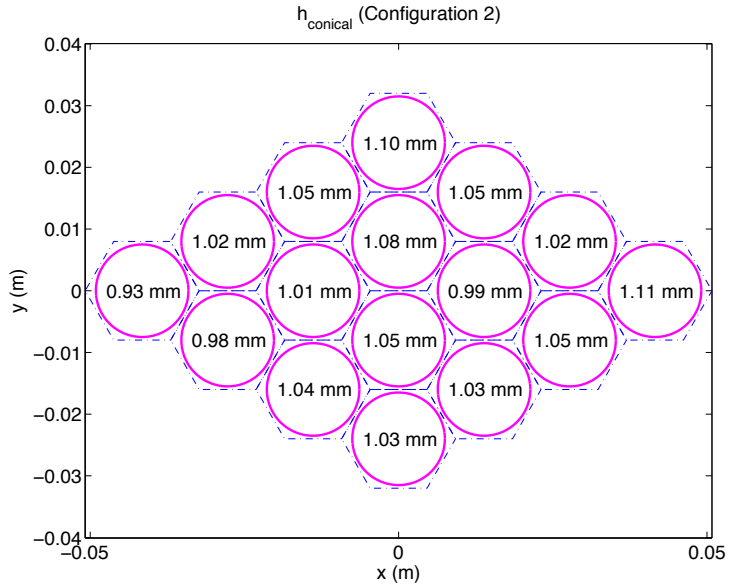


Figure 4.7 – Relative asperity heights measured for 16 conical asperities. The tyre rolls along the x direction.

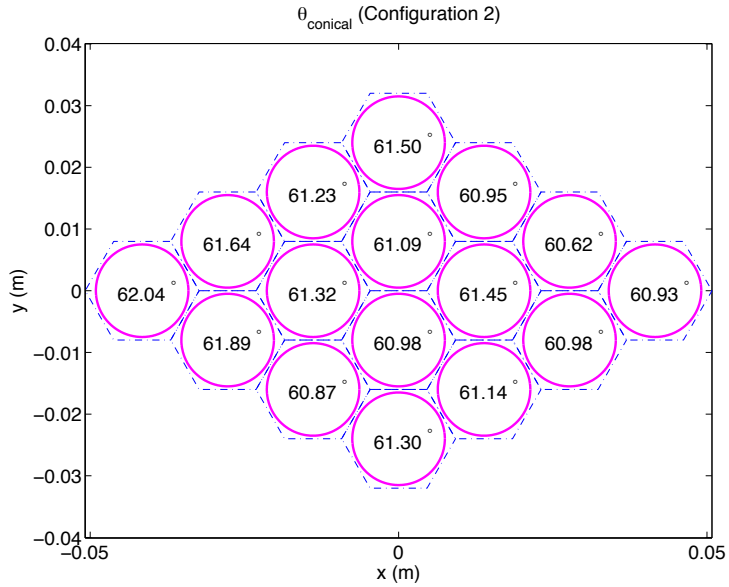


Figure 4.8 – Half-apex angles measured for 16 conical asperities.

### 4.2.3 Measurement repeatability

Similar to the single contact analysis, the repeatability of the measurements for multiple contact needs to be verified by comparing tests conducted on three different days. All three tests were performed for the same configuration: a total load of 1000 N and a rolling speed of 10 m/s. After a warm-up phase, the temperature at the surface of the tyre stabilises between 45 °C and 46 °C. Then, a test can be started for 100 revolutions. Figures 4.9 to 4.15 show, column by column, the time signals measured in these three tests, respectively represented by solid, dash-dot and dashed lines. The schematic drawing in the right of each figure indicates the positions of the

corresponding asperities. In these figures, the average contact force evolutions are plotted versus the time.

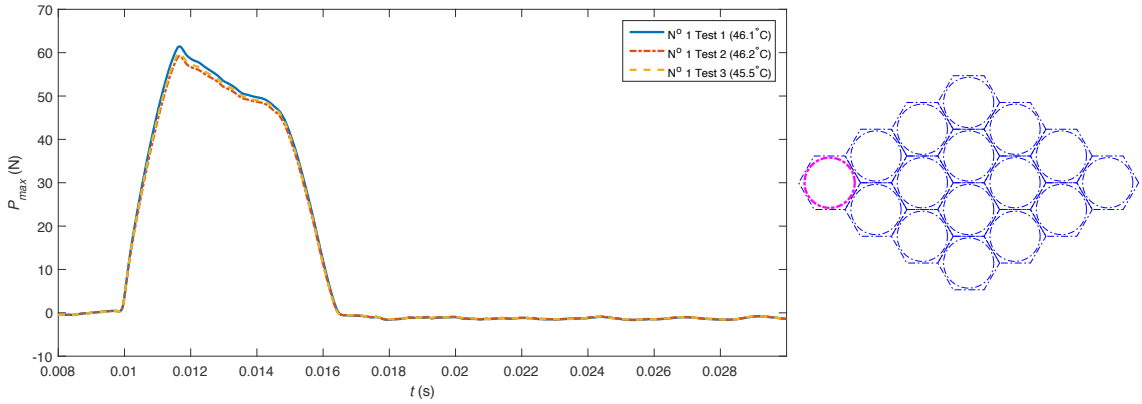


Figure 4.9 – Repeatability of the averaged time signal of contact force on the asperity N° 1 belonging to column 1. The three tests were carried out on different days (solid, dash-dot and dashed lines) but under the same conditions: a speed of 10 m/s and a load of 1000 N.

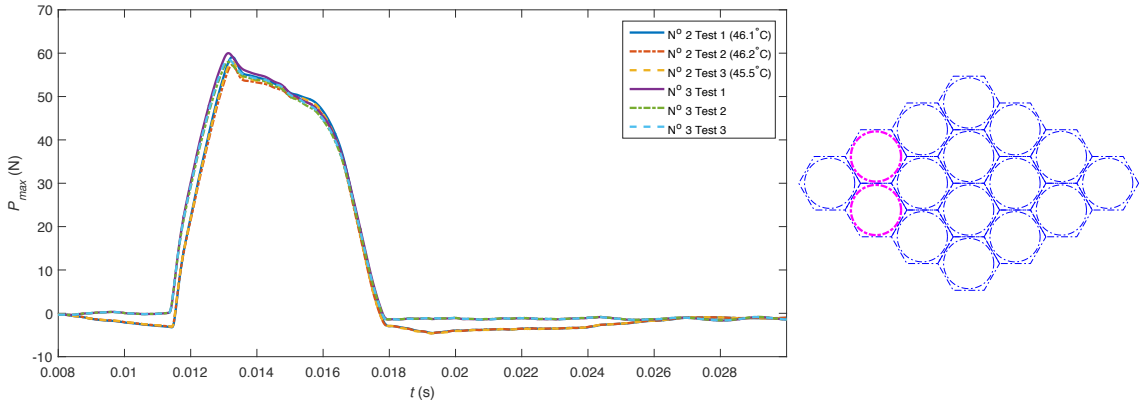


Figure 4.10 – Repeatability of the averaged time signals of contact force on the asperities N° 2 and N° 3 belonging to column 2.

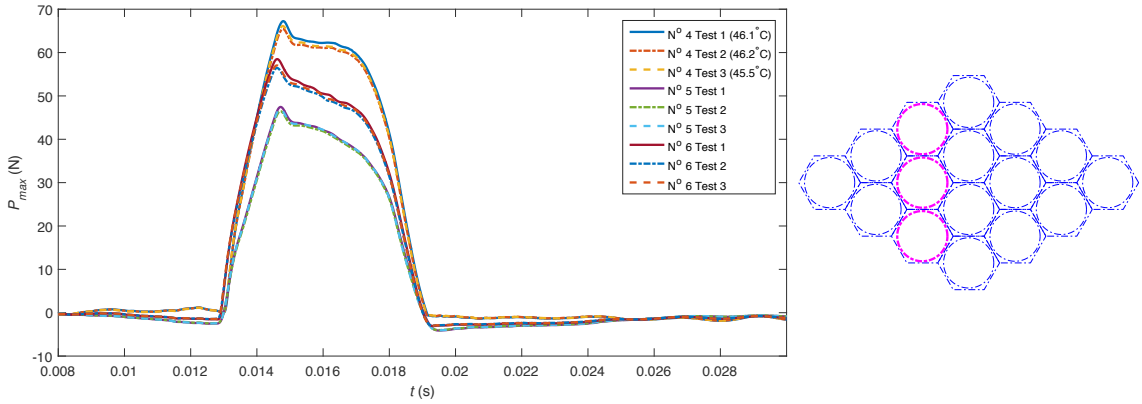


Figure 4.11 – Repeatability of the averaged time signals of contact force on the asperities N° 4, 5 and 6 belonging to column 3.

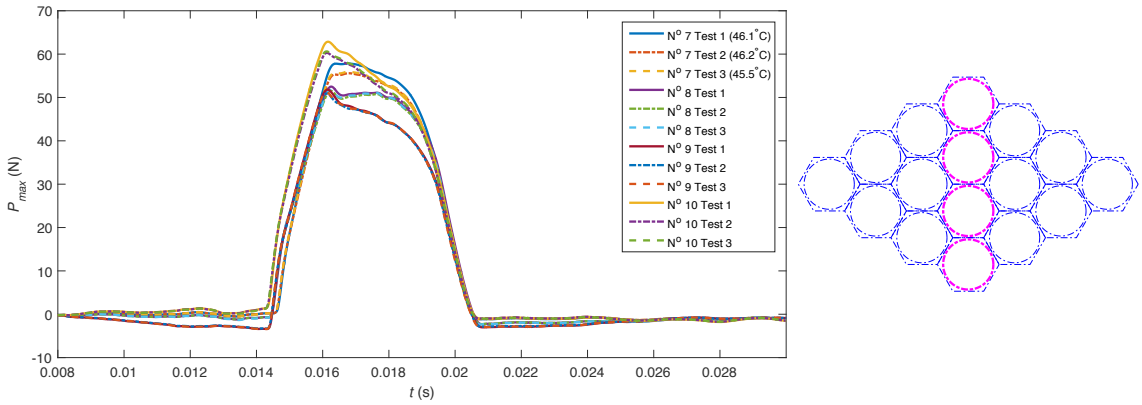


Figure 4.12 – Repeatability of the averaged time signals of contact force on the asperities N° 7, 8, 9 and 10 belonging to column 4.

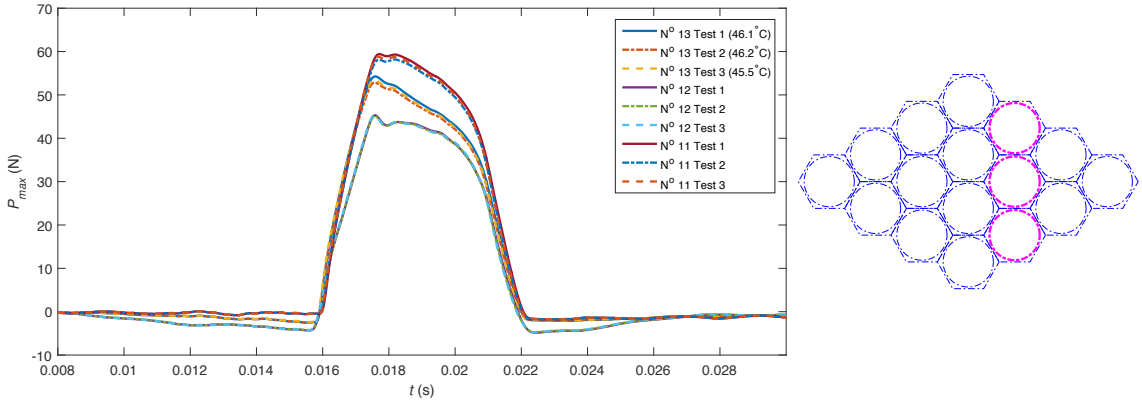


Figure 4.13 – Repeatability of the averaged time signals of contact force on the asperities N° 11, 12 and 13 belonging to column 5.

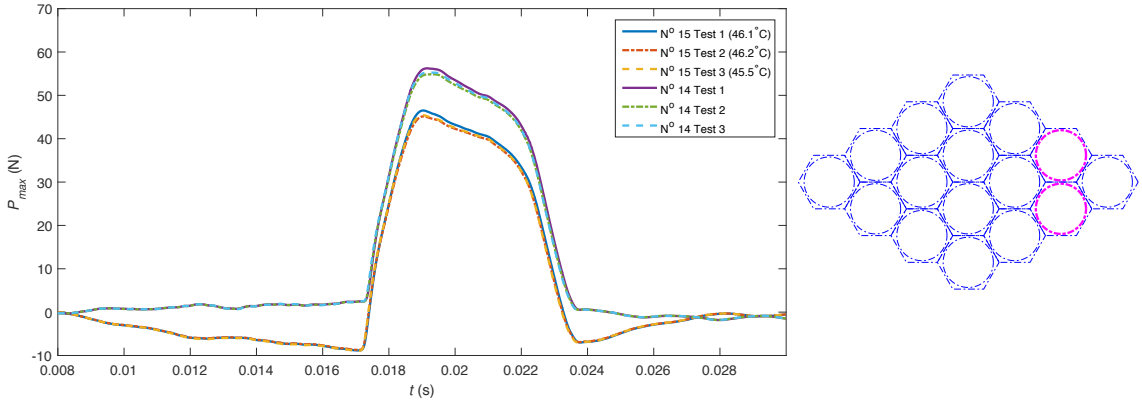


Figure 4.14 – Repeatability of the averaged time signals of contact force on the asperities N° 14 and N° 15 belonging to column 6.

The measured curves reveal good repeatability of the tests. Ideally, all the force transducers should measure compression forces between the tyre and the asperities and the time signals measured at asperities positions symmetrical about the axis passing through the summits of asperities N° 1, 5, 12 and 16 (along the rolling direction) should be identical. But in reality, the contact force from certain transducers (e.g. N° 15 in column 6) drops to a negative value just before the contact,

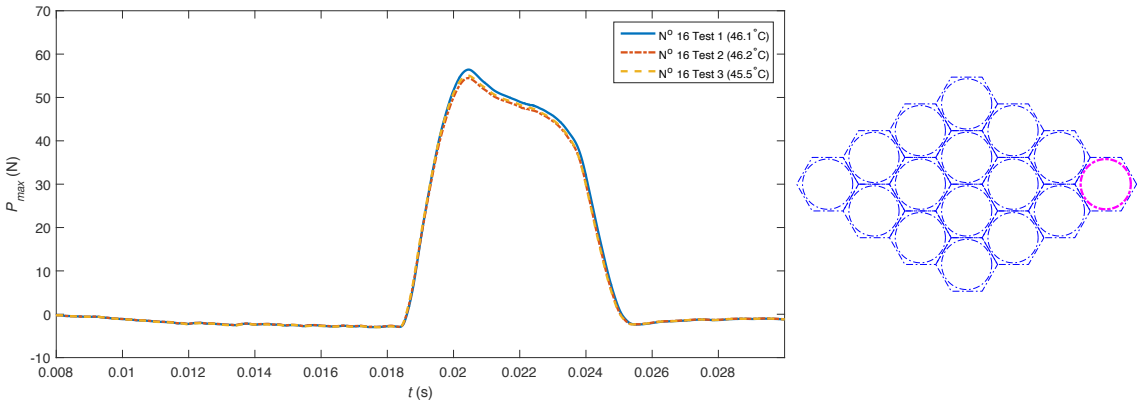


Figure 4.15 – Repeatability of the averaged time signal of contact force on the asperity N° 16 belonging to column 7.

becomes negative again at the end of the contact and finally returns to zero after the contact. This behaviour is also repeatable. The positions of the transducers have been interchanged and showed no influence on the negative forces at the initial asperities positions. Further investigations would be necessary to understand whether this is due to a tension force between the tyre and the asperity or a general acceleration in the negative direction of the transducer.

The symmetry along the rolling direction is verified for asperities N° 2 and 3. But for other asperities pairs, the comparison is less convincing which may be due to the difference of relative asperities heights or a non-symmetric loading of the tyre on the asperities. For asperities at mirror positions about column 4, e.g. asperities N° 1 and 16, there should be theoretically no symmetry in terms of the shape of time signal since the contact pressures distribution is dissymmetric during rolling due to the viscoelasticity of rubber.

## 4.3 Experimental results

### 4.3.1 Influence of the geometric shapes of indenter

The influence of the geometric shapes was tested for the spherical and the conical indenters. In both cases, the tyre was brought to the same rolling speed of 10 m/s and subjected to a load of 1000 N. In Figure 4.16, the time evolution of the contact forces on all 16 spherical asperities with scaled colours representing the magnitudes of the forces is plotted. For all 16 conical asperities, the results are given in Figure 4.17 with the same colour axis scaling as in Figure 4.16.

By comparing these two figures, it can be seen that the contact durations are similar for both geometric shapes of indenter, while the contact forces are significantly higher for spherical asperities. This observation is consistent with that made for Figure 3.8 in the case of a single asperity.

The contact force distribution on the spherical asperities is illustrated in Figure 4.18 for the average instant of peak force occurrence on asperities N° 7, 8, 9 and 10 belonging to column 4. This average instant corresponds to $t = 0.0163$ s in Figure 4.16, plotted as a blue dashed line. The tyre is mostly in contact with the asperities in column 2, 3 and 4 and is leaving contact with the asperity in column 1 and starting contact with the asperities in column 5. Generally, the asperities close to the borders parallel to the x-axis of the contact patches, i.e. asperities N° 7 and 10, are

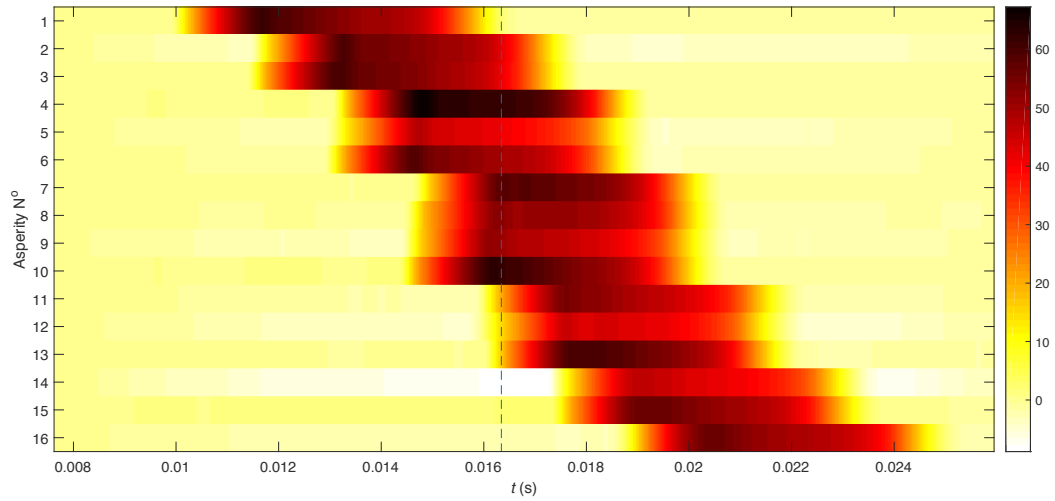


Figure 4.16 – Time evolution of the contact forces on all 16 spherical asperities with scaled colours representing the magnitudes of the forces. The total load is 1000 N. The rolling speed is 10 m/s.

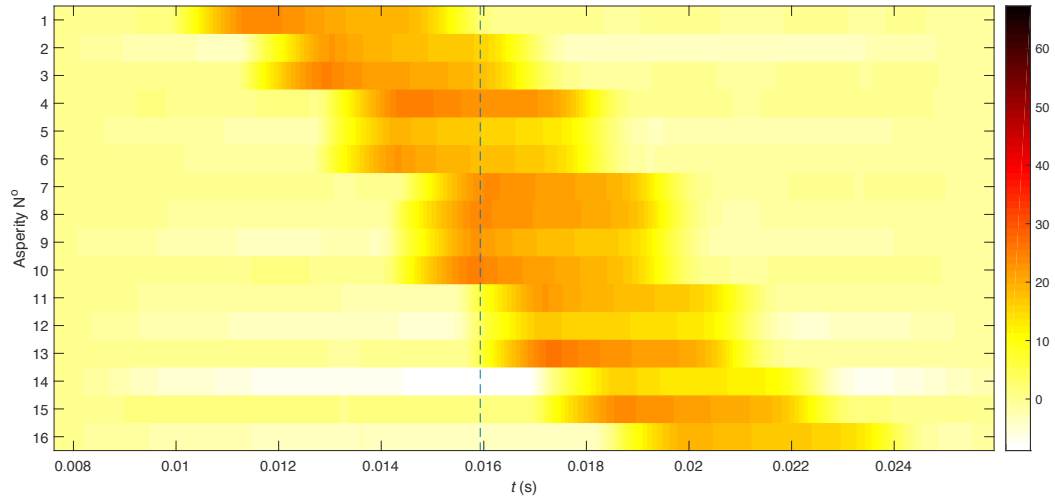


Figure 4.17 – Time evolution of the contact forces on all 16 conical asperities with scaled colours representing the magnitudes of the forces. The colour axis scaling is set to be equal to that of Figure 4.16. The total load is 1000 N. The rolling speed is 10 m/s.

subjected to higher forces than those close to the centre, i.e. asperities N° 8 and 9. This could be due to the high contact pressure concentration on the borders induced by the sidewall effect. The dissymmetry of the contact force distribution is also clearly visible.

The contact force distributions for all 16 conical asperities is shown in Figure 4.19. The blue dashed line in Figure 4.17 corresponding to $t = 0.0159$ s should be referred to for better understanding the contact situation which appears to be similar to the configuration of multiple spherical asperities, also with dissymmetry of the contact force distribution in the contact patch.

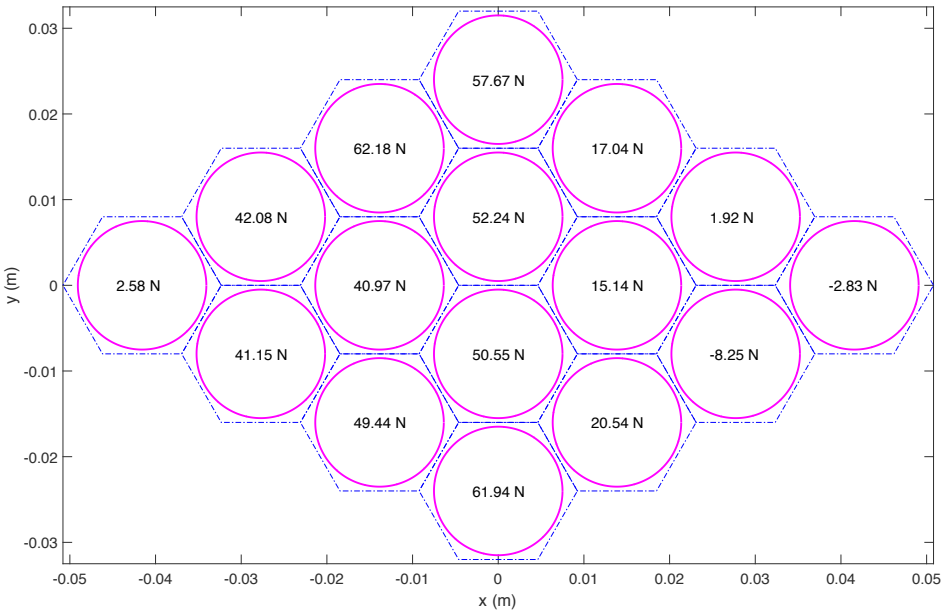


Figure 4.18 – Contact force distribution measured for 16 spherical asperities at the average instant of peak force occurrence on asperities N$^{o}$ 7, 8, 9 and 10 belonging to column 4.

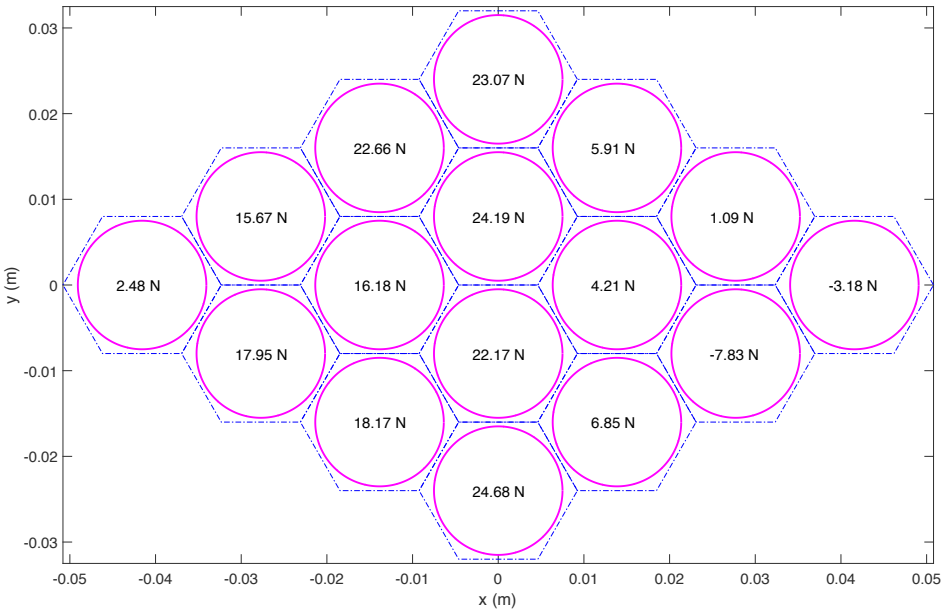


Figure 4.19 – Contact force distribution measured for 16 conical asperities at the average instant of peak force occurrence on asperities N$^{o}$ 7, 8, 9 and 10 belonging to column 4.

### 4.3.2 Influence of the total load

Tests were conducted to study the influences of the total load on the contact forces for spherical asperities. Three loads, 500, 750 and 1000 N, were tested with the tyre rolling at 10 m/s.

The time evolution of the contact forces on all 16 spherical asperities with scaled colours representing the magnitudes of the forces are plotted for total loads of 500, 750 and 1000 N, respectively in Figures 4.20, 4.21 and 4.22, using the same colour axis scaling. Comparison of these three figures shows that, with the same rolling speed, the contact duration is mainly determined by the total load and is almost independent of the asperity position: the higher the load, the longer the contact. This conclusion is consistent with that for the configuration of a single asperity. The peak contact force on each asperity appears early within the contact duration, implying that the peak force is reached in the leading part of the dynamic contact patch. The time to reach the peak force from the start of the contact with an asperity is nearly the same for the three loads, while the time to run through the trailing part of the contact patch is influenced by the loading condition.

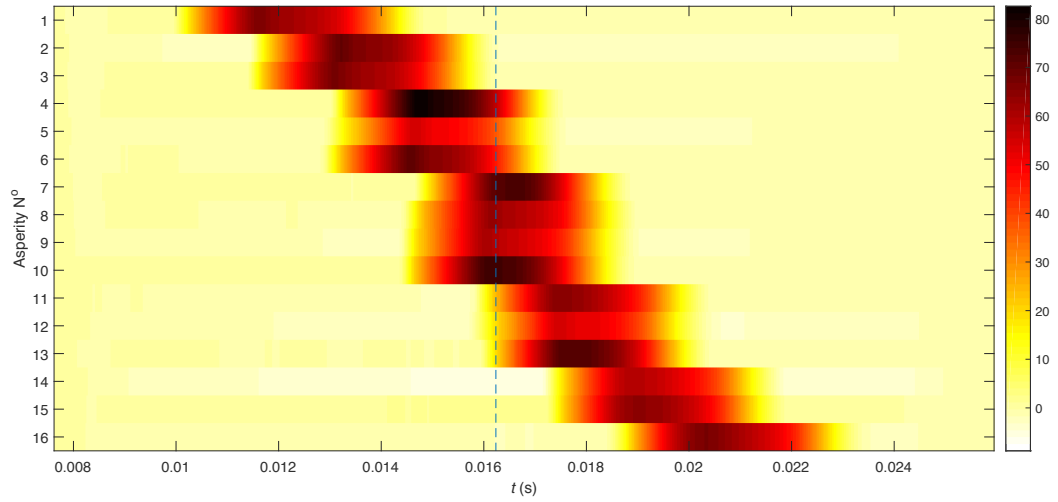


Figure 4.20 – Time evolution of the contact forces on all 16 spherical asperities with scaled colours representing the magnitudes of the forces. The total load is 500 N. The rolling speed is 10 m/s.

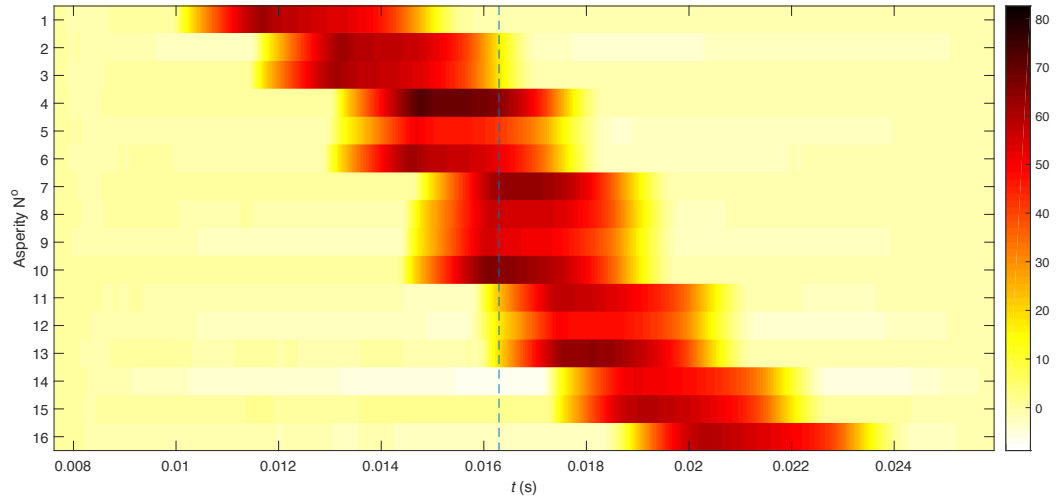


Figure 4.21 – Time evolution of the contact forces on all 16 spherical asperities with scaled colours representing the magnitudes of the forces. The colour axis scaling is set to be equal to that of Figure 4.20. The total load is 750 N. The rolling speed is 10 m/s.

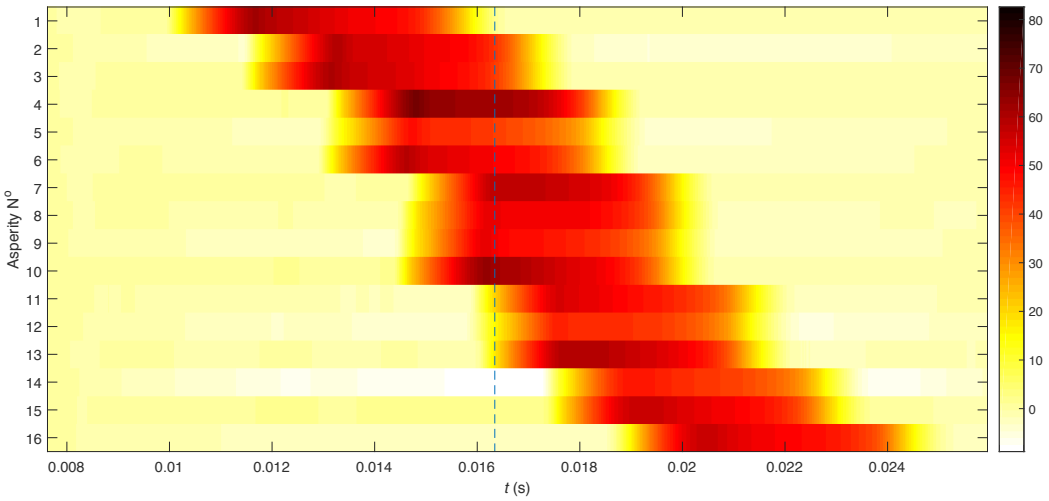


Figure 4.22 – Time evolution of the contact forces on all 16 spherical asperities with scaled colours representing the magnitudes of the forces. The colour axis scaling is set to be equal to that of Figure 4.20. The total load is 1000 N. The rolling speed is 10 m/s.

The contact force distribution on the spherical asperities for total loads of 500, 750 and 1000 N are plotted respectively in Figures 4.23, 4.24 and 4.25 for the average instants of peak force occurrence on asperities N° 7, 8, 9 and 10 belonging to column 4. Blue dashed lines are also added to Figures 4.20, 4.21 and 4.22 to represent these instants corresponding to $t = 0.0162$ s, 0.0163 s and 0.0163 s, respectively for 500, 750 and 1000 N. This also confirms that the time to reach the peak force is almost constant, irrespective of the load.

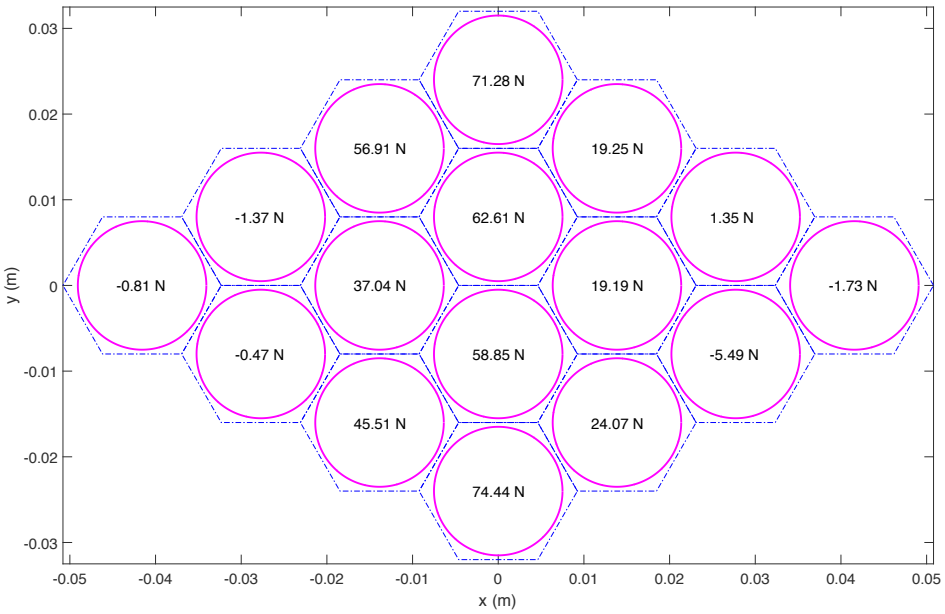


Figure 4.23 – Contact force distribution measured under 500 N for 16 spherical asperities at the average instant of peak force occurrence on asperities N° 7, 8, 9 and 10 belonging to column 4.

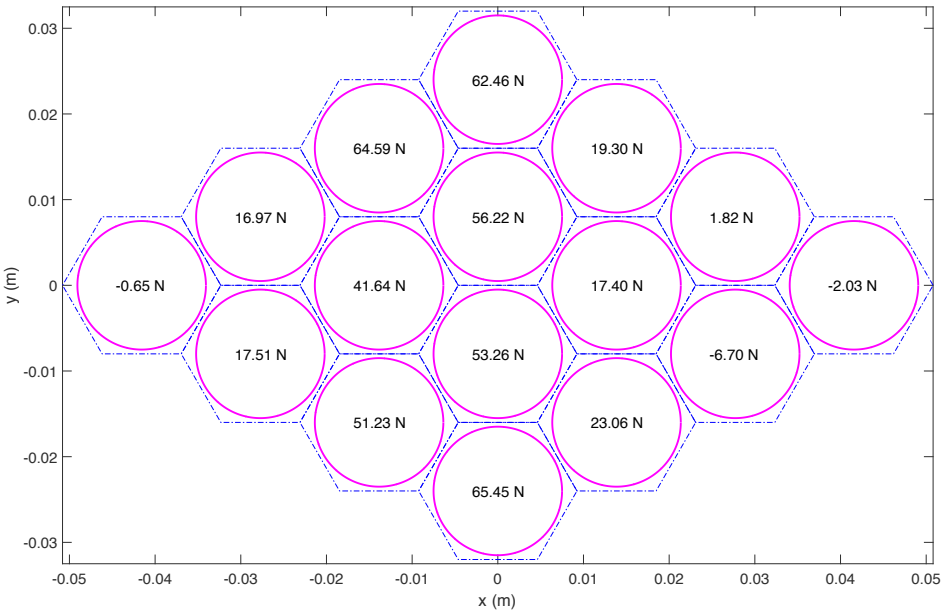


Figure 4.24 – Contact force distribution measured under 750 N for 16 spherical asperities at the average instant of peak force occurrence on asperities N$^{o}$ 7, 8, 9 and 10 belonging to column 4.

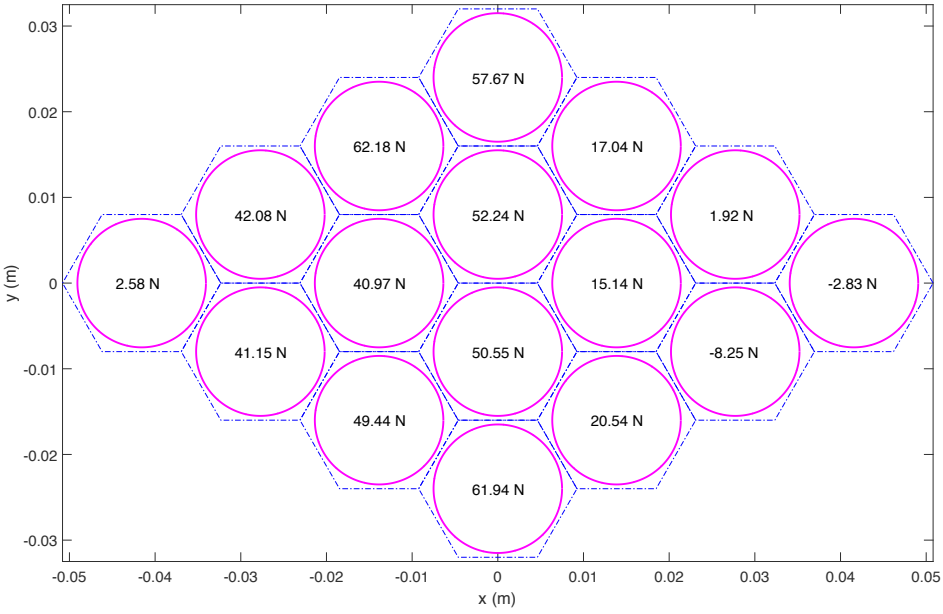


Figure 4.25 – Contact force distribution measured under 1000 N for 16 spherical asperities at the average instant of peak force occurrence on asperities N$^{o}$ 7, 8, 9 and 10 belonging to column 4.

According to Figures 4.23, 4.24 and 4.25, the tyre is in contact with asperities in column 3 and 4 and starts to come into contact with asperities in column 5. Concerning the asperities in column 2: under 500 N, the tyre in not in contact with them; under 750 N, the tyre is leaving

contact with them; under 1000 N, the tyre is still in contact with them. The peak forces in column 4 are highest under 500 N and are slightly higher under 750 N than 1000 N.

### 4.3.3 Influence of the rolling speed

The influence of the rolling speed is studied by plotting the time evolution of the contact forces on all 16 spherical asperities with scaled colours representing the magnitudes of the forces at 5, 10 and 15 m/s, respectively in Figures 4.26, 4.27 and 4.28, using the same colour axis scaling. The time is multiplied by each rolling speed to represent the rolling distance.

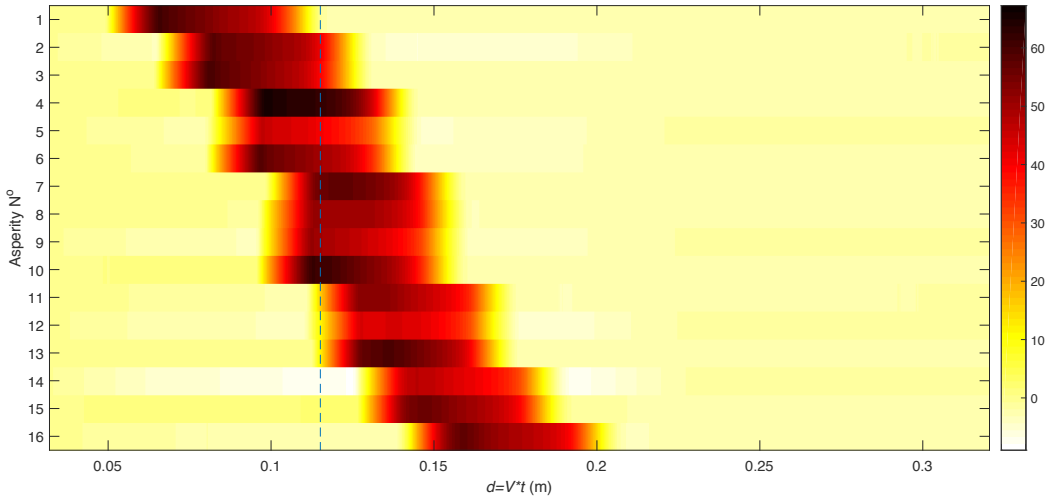


Figure 4.26 – Evolution of the contact forces on all 16 spherical asperities with scaled colours representing the magnitudes of the forces. The total load is 1000 N. The rolling speed is 5 m/s.

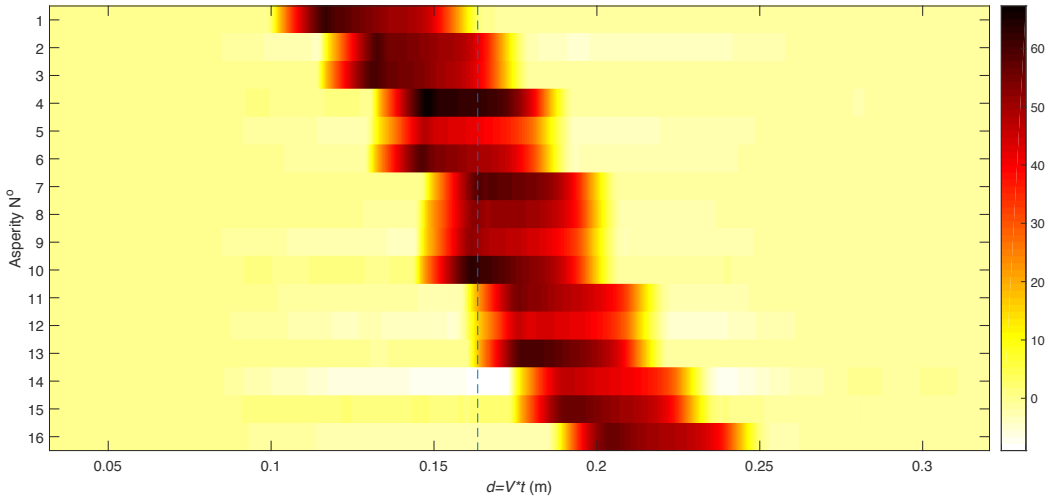


Figure 4.27 – Evolution of the contact forces on all 16 spherical asperities with scaled colours representing the magnitudes of the forces. The colour axis scaling is set to be equal to that of Figure 4.20. The total load is 1000 N. The rolling speed is 10 m/s.

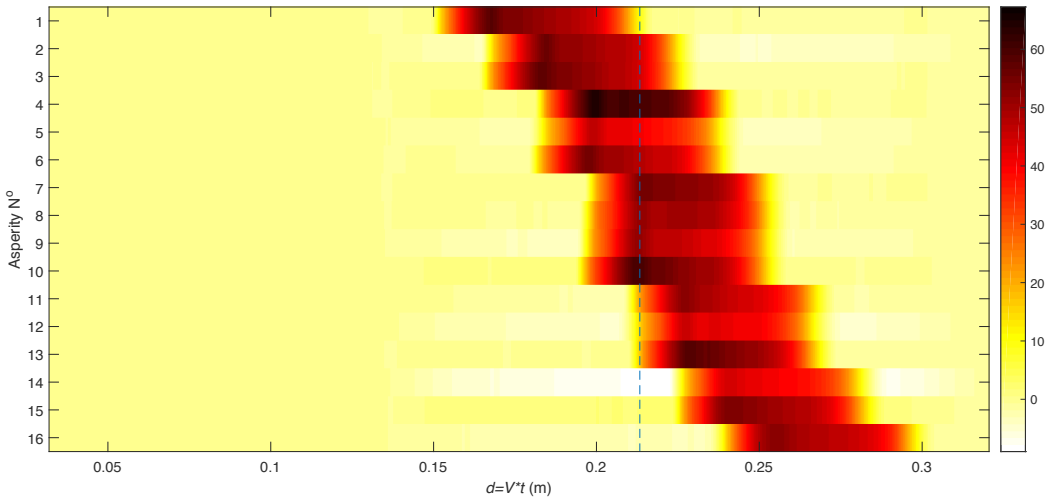


Figure 4.28 – Evolution of the contact forces on all 16 spherical asperities with scaled colours representing the magnitudes of the forces. The colour axis scaling is set to be equal to that of Figure 4.20. The total load is 1000 N. The rolling speed is 15 m/s.

The contact length with each asperity is almost constant for the three rolling speeds. Although the measurements are triggered at nearly the same time, when the time is multiplied by the respective rolling speed, the distance travelled by the tyre before touching the first asperity from the start of the contact force recording in each revolution is proportional to the rolling speed. The blue dashed lines in Figures 4.26, 4.27 and 4.28 indicate the respective distance of peak force occurrence on asperities N° 7, 8, 9 and 10 belonging to column 4, i.e. 0.115 m for 5 m/s, 0.163 m for 10 m/s and 0.213 m for 15 m/s. The difference of distances between 10 m/s and 5 m/s is 0.048 m and that between 15 m/s and 10 m/s is 0.050 m. These two values are very close and should correspond to the distance travelled from the start of one contact force recording until touching the first asperity. The fact that the resultant contact force is invariant with respect to the positions of the asperities suggests that the contact is of quasi-static nature.

A comparison of modified spectra $S^*_{F,i}$ are represented in Figures 4.29 to 4.35 respectively for the spherical asperities in column 1 to 7, by taking 10 m/s as a reference speed $V_r$ and regarding the dynamic contact as quasi-static states. For each asperity, the flat parts of the curves corresponding to different rolling speed coincide, and the first two wave peaks tend to appear at similar frequencies. Therefore, the quasi-static nature of the contact is again verified for the configuration of multiple asperities.

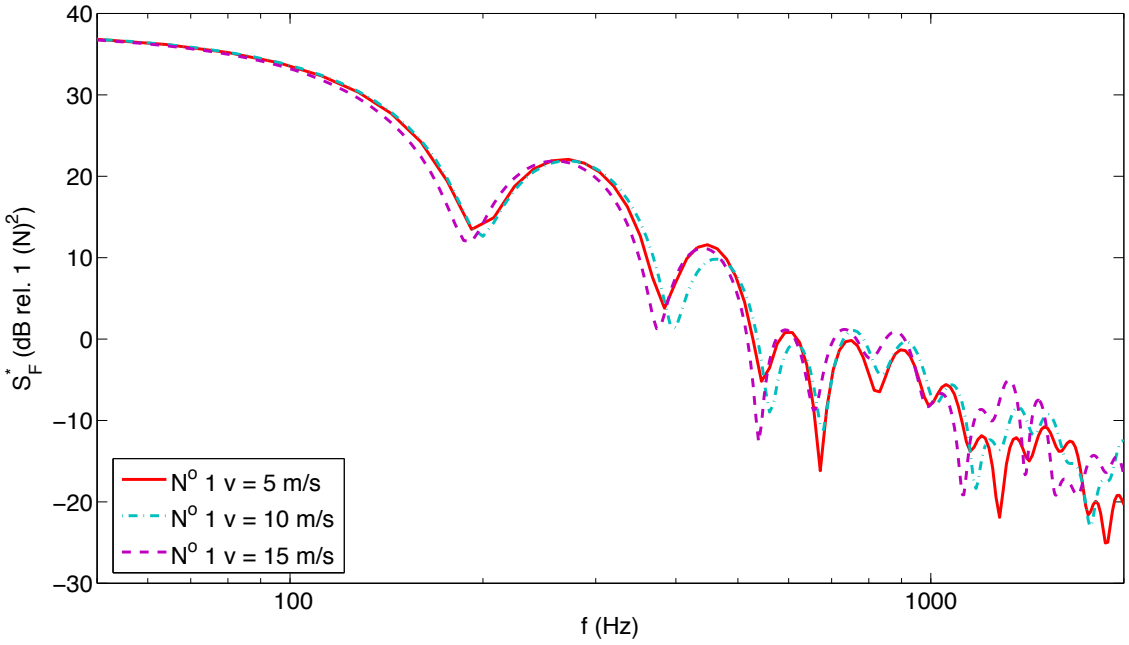


Figure 4.29 – Modified spectra $S_F^*$ of the resultant contact force on the spherical asperity placed in column 1 at 5, 10 and 15 m/s with the reference speed $V_r$ = 10 m/s. The load on the tyre was 1000 N.

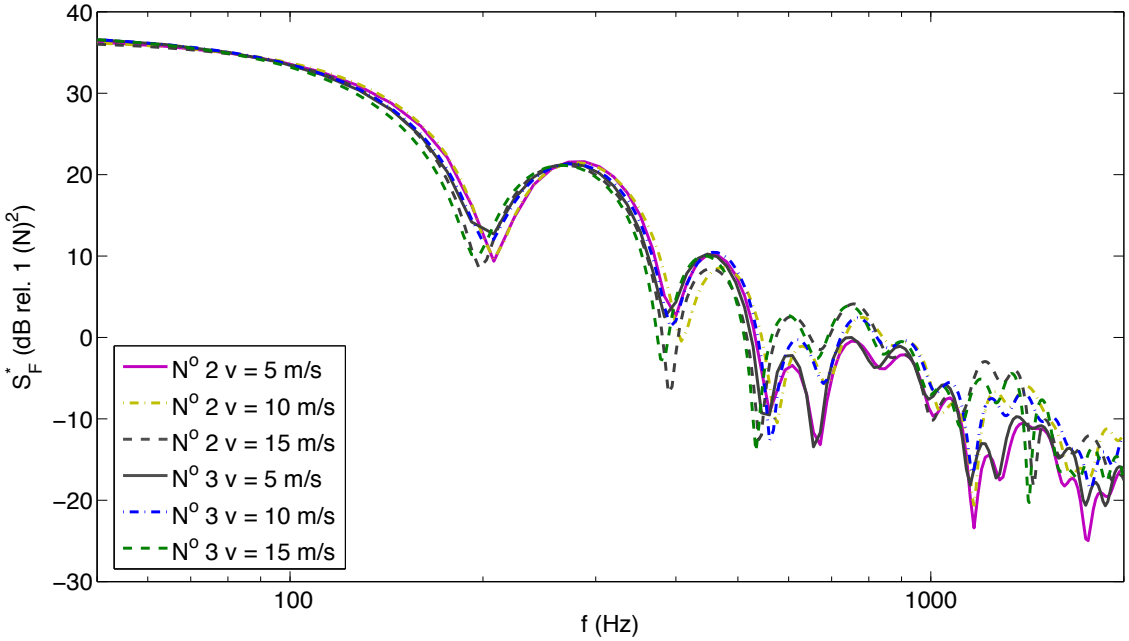


Figure 4.30 – Modified spectra $S_F^*$ of the resultant contact force on the spherical asperities placed in column 2 at 5, 10 and 15 m/s with the reference speed $V_r$ = 10 m/s. The load on the tyre was 1000 N.

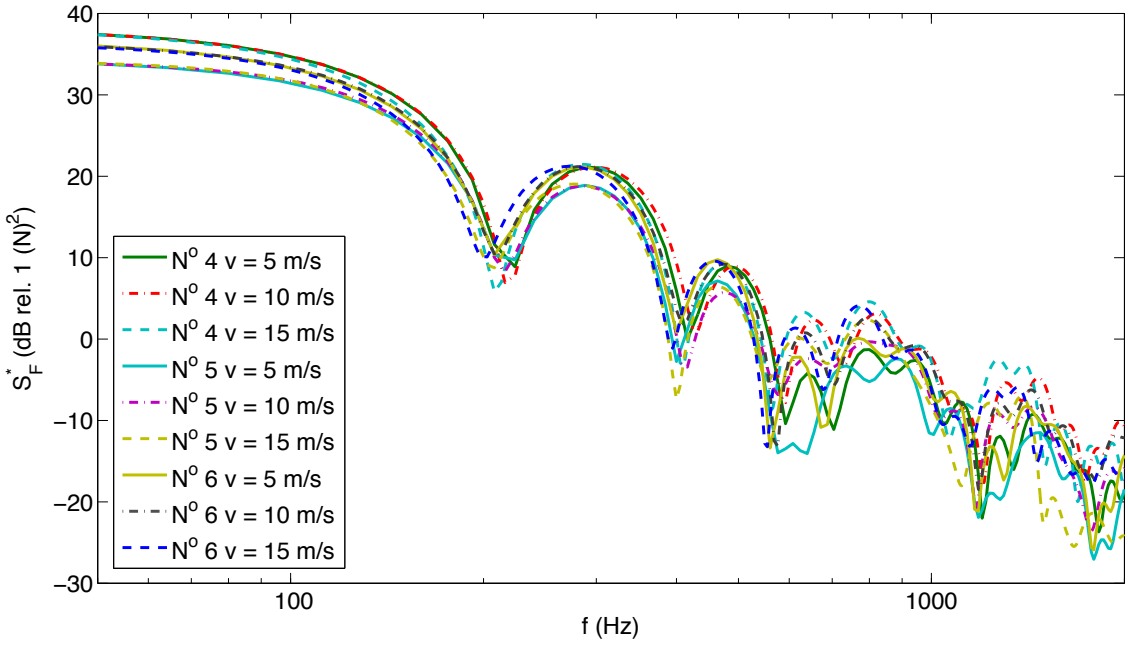


Figure 4.31 – Modified spectra $S_F^*$ of the resultant contact force on the spherical asperities placed in column 3 at 5, 10 and 15 m/s with the reference speed $V_r$ = 10 m/s. The load on the tyre was 1000 N.

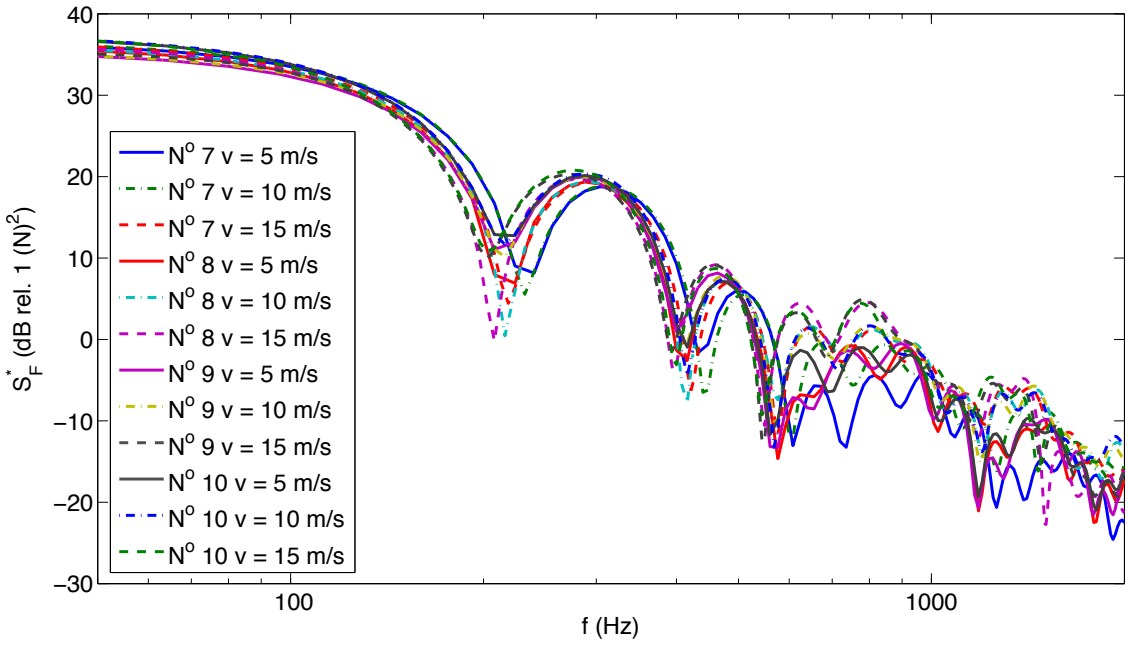


Figure 4.32 – Modified spectra $S_F^*$ of the resultant contact force on the spherical asperities placed in column 4 at 5, 10 and 15 m/s with the reference speed $V_r$ = 10 m/s. The load on the tyre was 1000 N.

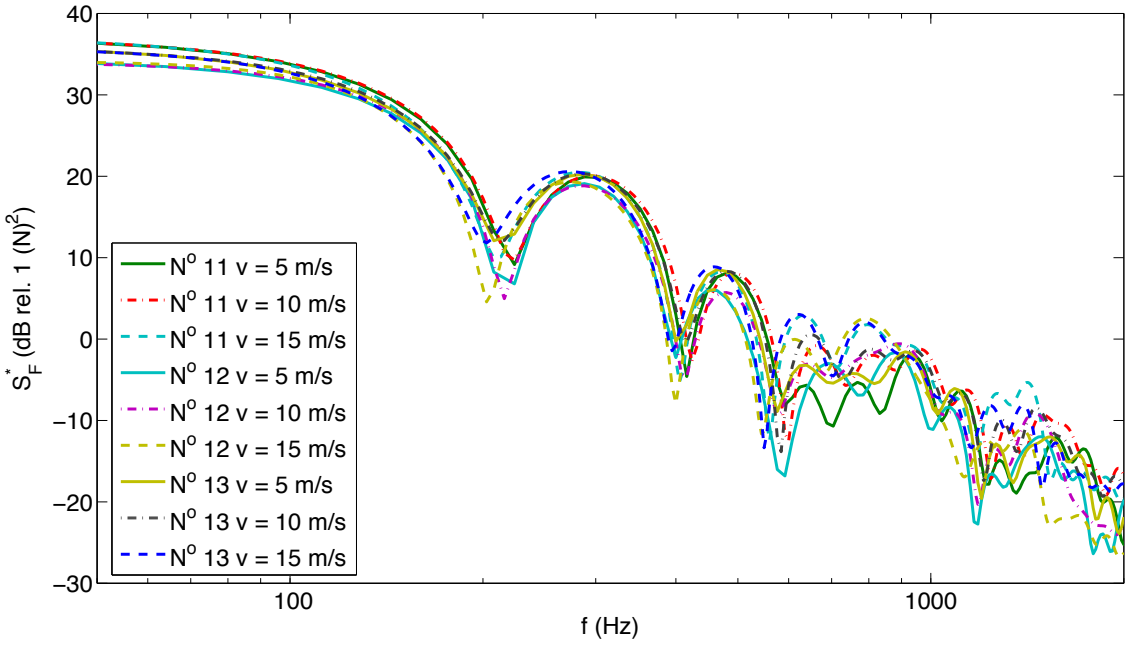


Figure 4.33 – Modified spectra $S_F^*$ of the resultant contact force on the spherical asperities placed in column 5 at 5, 10 and 15 m/s with the reference speed $V_r$ = 10 m/s. The load on the tyre was 1000 N.

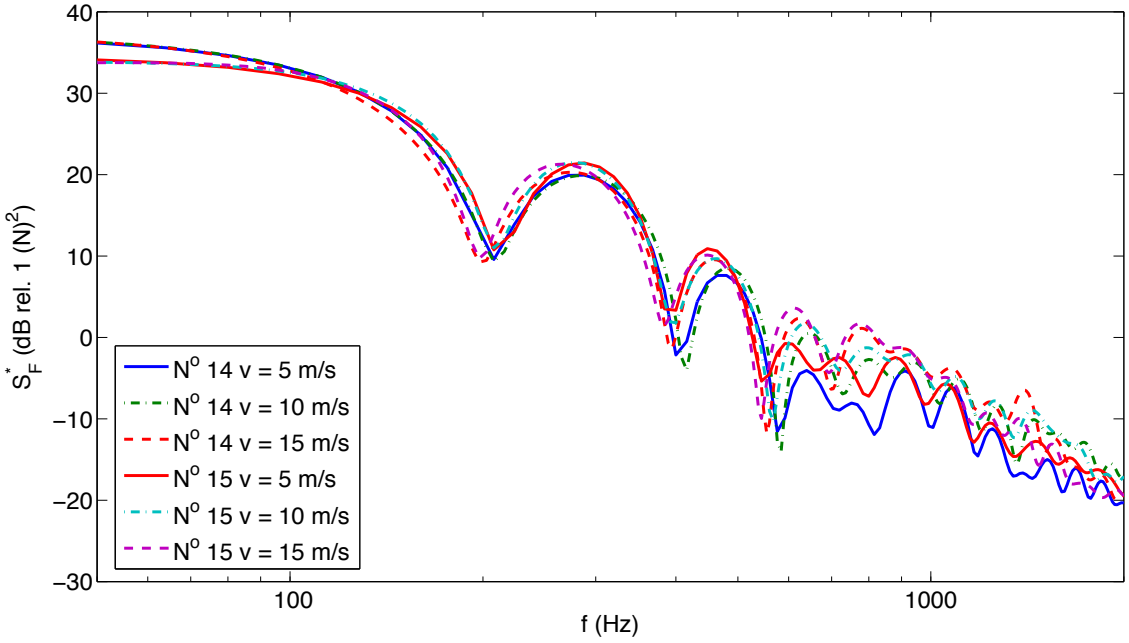


Figure 4.34 – Modified spectra $S_F^*$ of the resultant contact force on the spherical asperities placed in column 6 at 5, 10 and 15 m/s with the reference speed $V_r$ = 10 m/s. The load on the tyre was 1000 N.

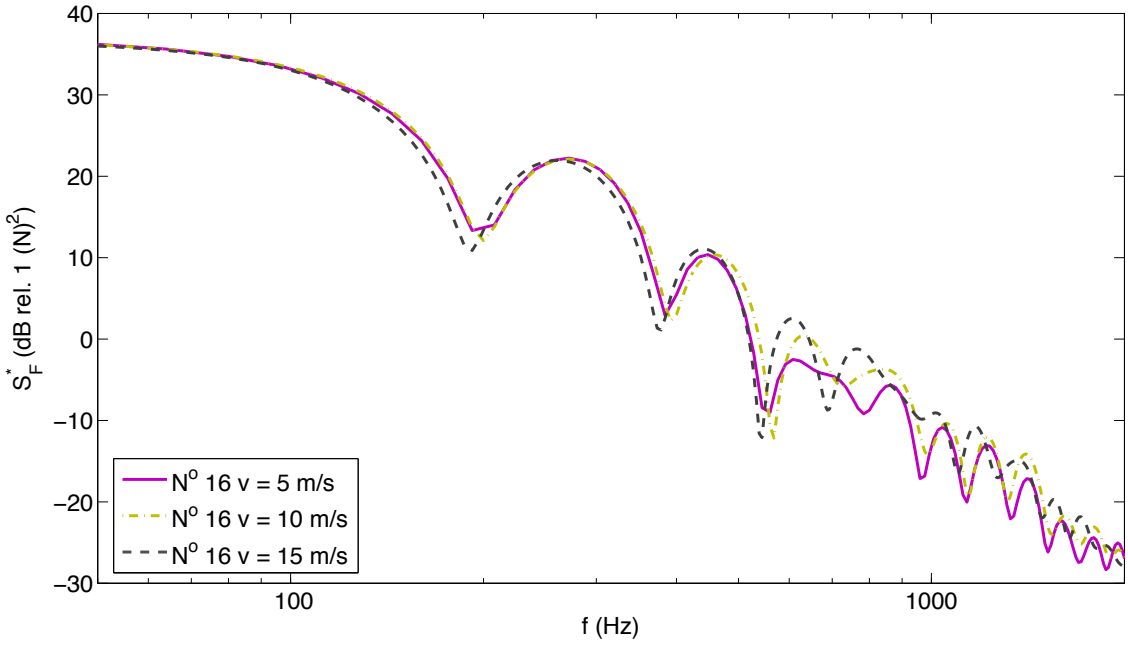


Figure 4.35 – Modified spectra $S_F^*$ of the resultant contact force on the spherical asperity placed in column 7 at 5, 10 and 15 m/s with the reference speed $V_r$ = 10 m/s. The load on the tyre was 1000 N.

### 4.3.4 Conclusions

The influences of several parameters have been analysed in this section. The asperity shape has a great influence on the contact in the case of multiple asperities. Generally, the asperities close to the borders parallel to the x-axis are subjected to higher forces than those close to the centre of the contact patch, possibly due to the sidewall effect. The total load affects the contact duration: the higher the load, the longer the contact. Meanwhile, the peak contact force is reached in the leading part of the contact patch, requiring almost the same amount of time. Therefore, the influence of the total load is more on the trailing part. Comparing the contact force evolution as a function of the rolling distance for each of the asperities for three rolling speed approves the quasi-static nature of the contact. This conclusion is further supported by the fact the modified spectra of the resultant contact force on all 16 spherical asperities are similar in shape up to 500 Hz.

## 4.4 Contact model assessment

### 4.4.1 Static contact patch calculations

In the present subsection, the half-space assumption is applied to the reduced-sized tyre. The static contact with a rigid, smooth road surface including 16 rigid spherical asperities inside cylindrical cavities placed at the measured positions is studied using the MIM. The actual curvatures of the road surface and the dimensions of the cavity and the asperity are taken into account in the model. The dimensions of the mesh elements in this model are chosen to be 0.5 mm in both x (longitudinal) and y (transverse) directions.

Numerical and experimental static contact pressure distributions are compared in Figures 4.36, 4.37 and 4.38, respectively for total loads of 500, 750 and 1000 N. The Young's moduli are the same as those used in Figures 3.20 and 3.21, i.e. 3.7, 3.3 and 2.9 MPa for 500, 750 and 1000 N, respectively. The contours of the numerical contact patches are added to the measured patches for comparison of dimensions. Despite the absence of high contact pressure concentration on the borders parallel to the x-axis, the elastic model estimates quite well the contact area on each of the asperities and the width of the contact patch along the rolling direction.

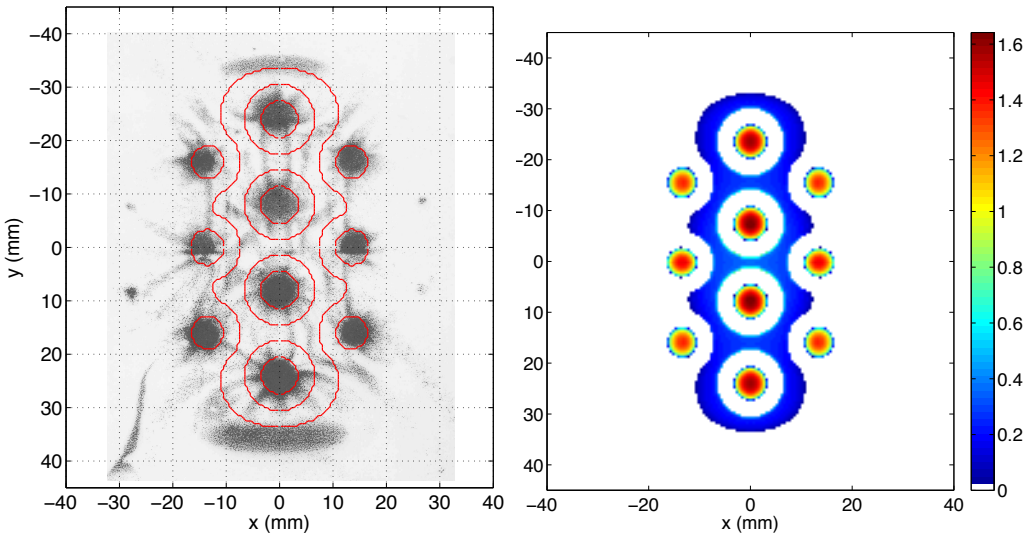


(a) Experimental contact patches (b) Numerical contact patches

Figure 4.36 – Contact pressure distributions (in MPa) in the case of 16 spherical asperities. The total load is 500 N. The Young's modulus is 3.7 MPa. The contour of the numerical contact patch is superposed on the measured patch for comparison of dimensions.

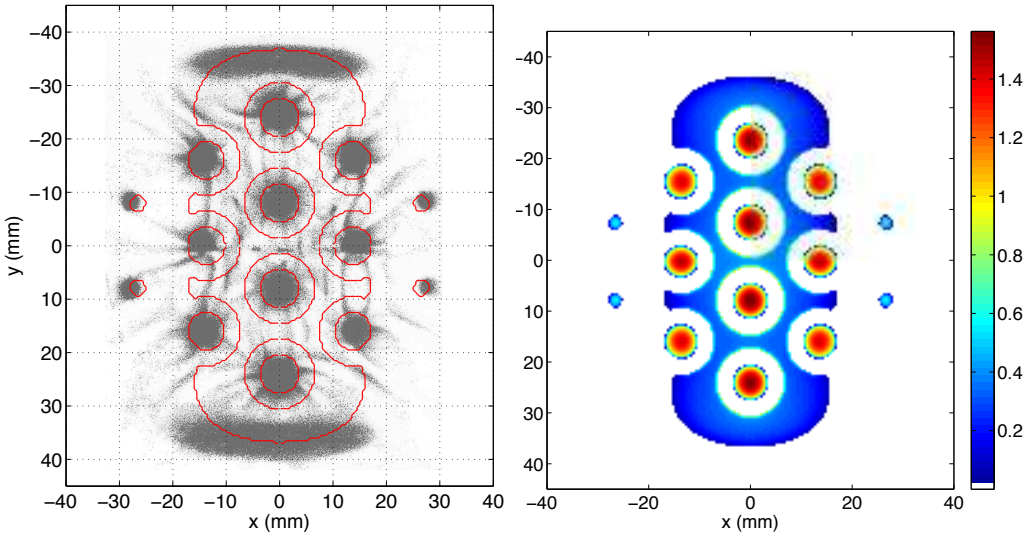


(a) Experimental contact patches (b) Numerical contact patches

Figure 4.37 – Contact pressure distributions (in MPa) in the case of 16 spherical asperities. The total load is 750 N. The Young's modulus is 3.3 MPa. The contour of the numerical contact patch is superposed on the measured patch for comparison of dimensions.

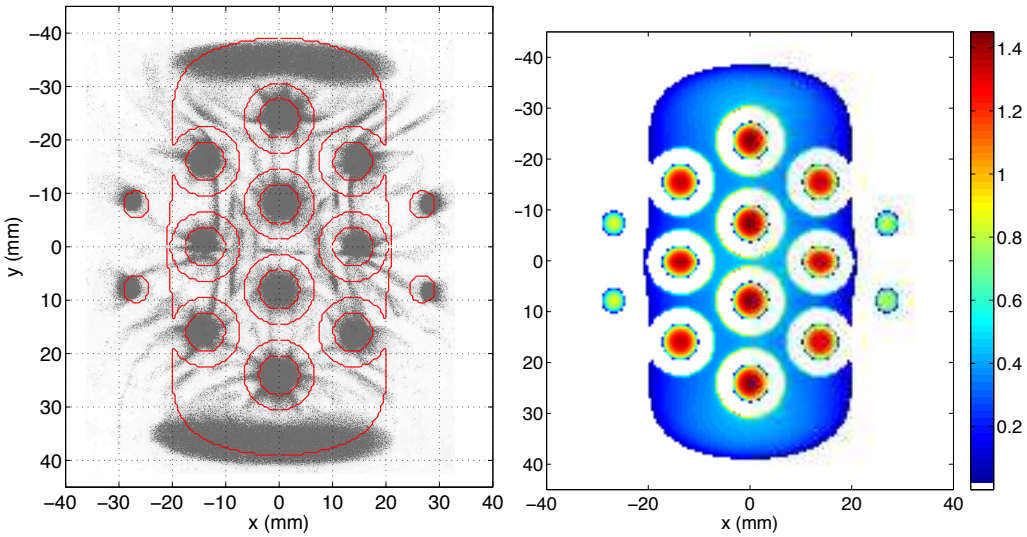


(a) Experimental contact patches (b) Numerical contact patches

Figure 4.38 – Contact pressure distributions (in MPa) in the case of 16 spherical asperities. The total load is 1000 N. The Young's modulus is 2.9 MPa. The contour of the numerical contact patch is superposed on the measured patch for comparison of dimensions.

### 4.4.2 Viscoelastic contact calculation

Calculations are performed for a total load of 500 N and a rolling speed of 10 m/s. The same Zener model parameters as in the case of a single asperity are used: the long-term modulus $E_\infty = 4$ MPa, the elastic modulus in the Maxwell branch $E_1 = 4$ MPa and the characteristic time of the Maxwell branch $\tau = \eta/E_1 = 0.5$ ms. The experimental and numerical peak contact forces on all 16 spherical asperities are plotted in Figure 4.39. Generally, the numerical model overestimates the peak forces on the asperities close to the centre (N$^o$ 5, 8, 9 and 12) and underestimates the peak forces on the asperities situated near the borders (N$^o$ 7 and 10). This problem can also be observed by comparing the numerical and experimental contact force evolution curves plotted in Figures 4.40 to 4.46 as functions of the distance, respectively for the spherical asperities in column 1 to 7. (Note that the numerical curves for asperities placed symmetrically about the x-axis are perfectly identical and thus coincide with each other.) Nevertheless, the time evolution of the calculated contact force is in accordance with the experiment. The dissymmetry of the signal is observed and the contact durations are quite similar on the full set of asperities.

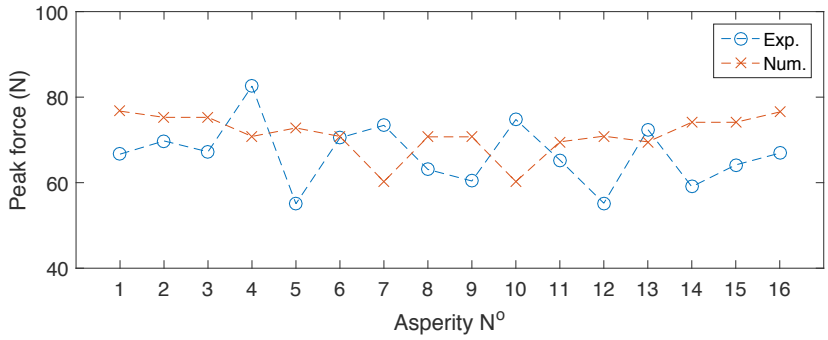


Figure 4.39 – Comparison of calculated and measured peak forces on all 16 spherical asperities.

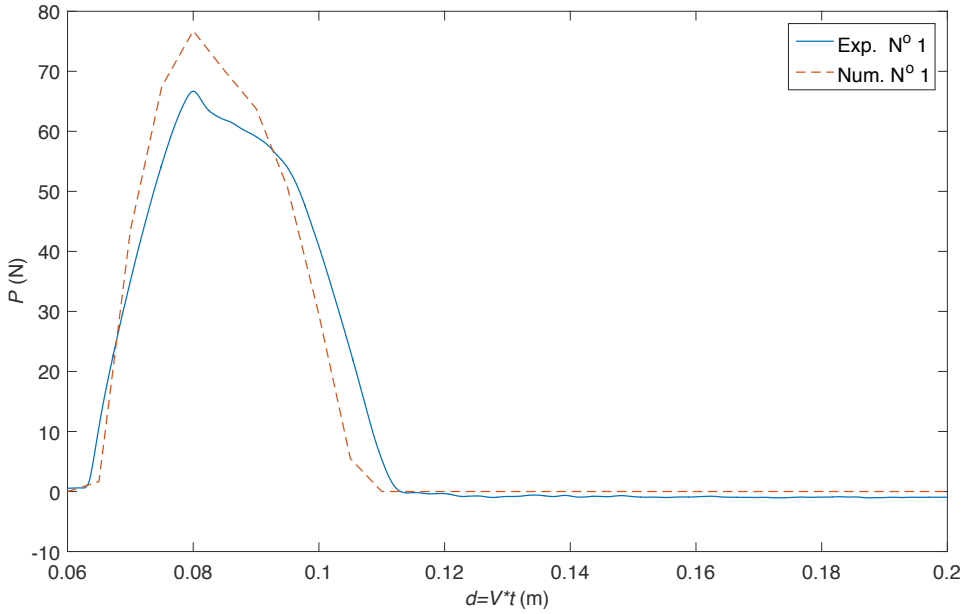


Figure 4.40 – Comparison of the contact force evolutions, calculated using the viscoelastic contact model, with the experimental curves for the spherical asperity in column 1 in the case of a total load of 500 N and a rolling speed of 10 m/s. The time $t$ is multiplied by the rolling speed $V$ to represent the distance $d$ travelled during rolling.

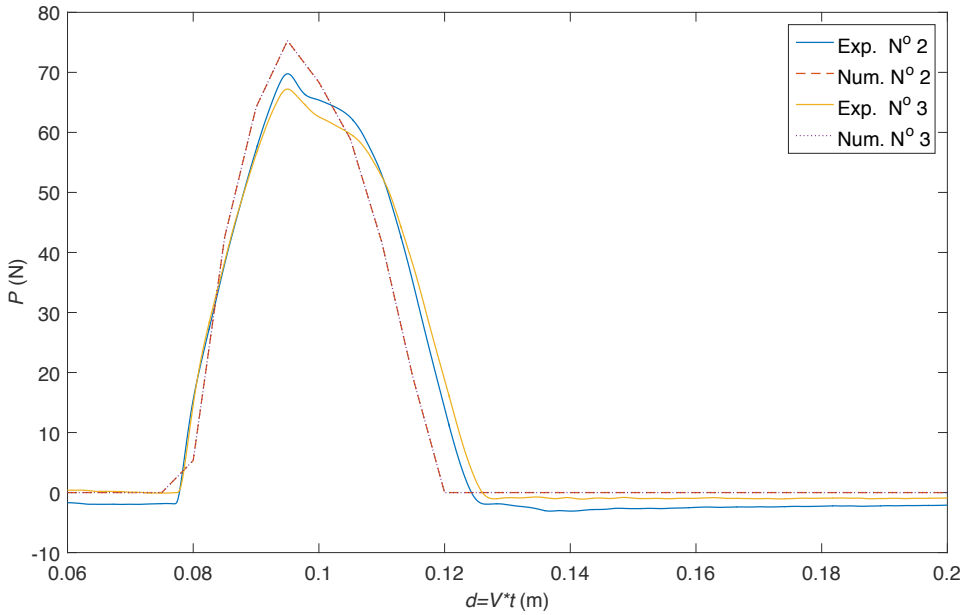


Figure 4.41 – Comparison of the contact force evolutions, calculated using the viscoelastic contact model, with the experimental curves for the spherical asperities in column 2 in the case of a total load of 500 N and a rolling speed of 10 m/s. The time $t$ is multiplied by the rolling speed $V$ to represent the distance $d$ travelled during rolling.

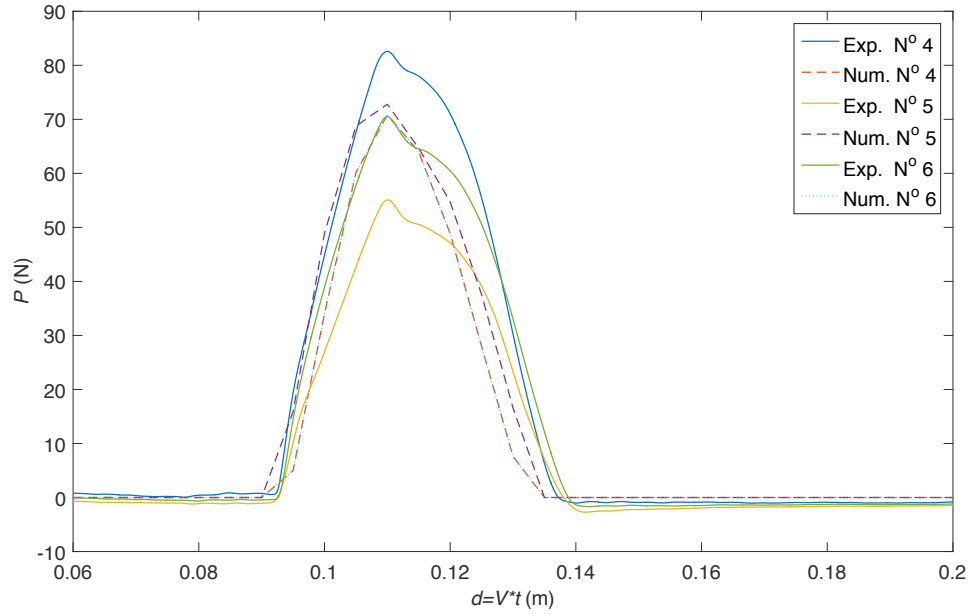


Figure 4.42 – Comparison of the contact force evolutions, calculated using the viscoelastic contact model, with the experimental curves for the spherical asperities in column 3 in the case of a total load of 500 N and a rolling speed of 10 m/s. The time $t$ is multiplied by the rolling speed $V$ to represent the distance $d$ travelled during rolling.

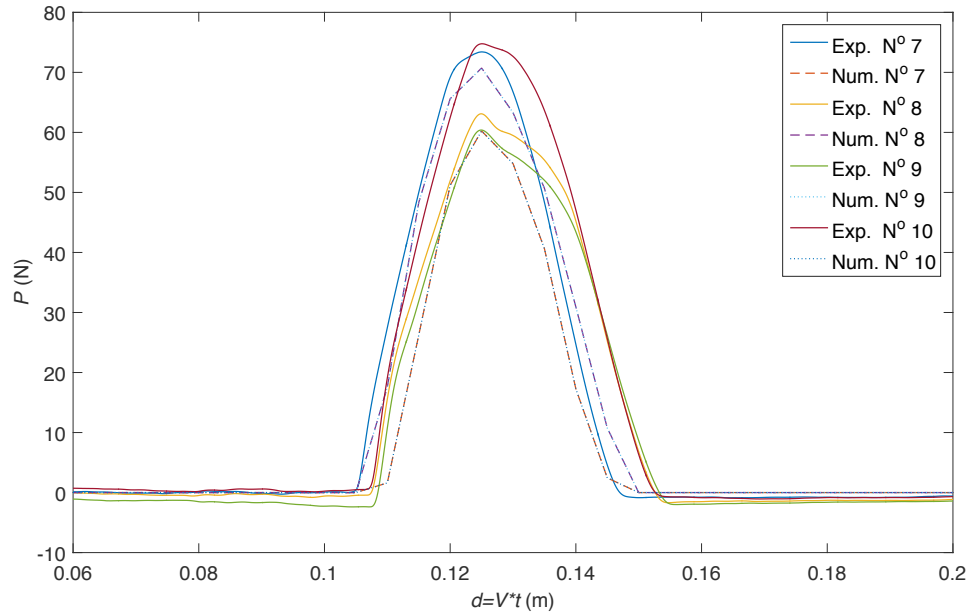


Figure 4.43 – Comparison of the contact force evolutions, calculated using the viscoelastic contact model, with the experimental curves for the spherical asperities in column 4 in the case of a total load of 500 N and a rolling speed of 10 m/s. The time $t$ is multiplied by the rolling speed $V$ to represent the distance $d$ travelled during rolling.

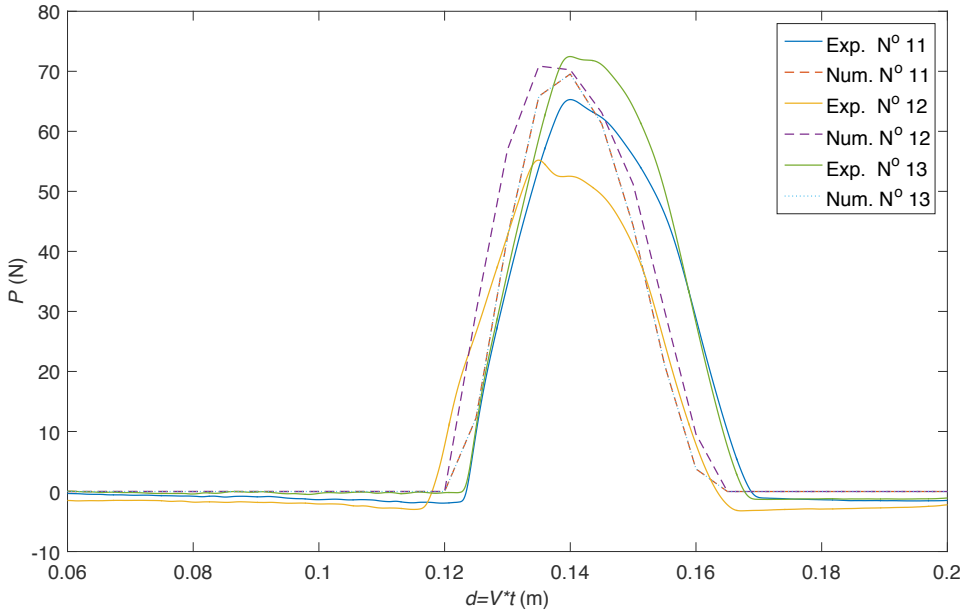


Figure 4.44 – Comparison of the contact force evolutions, calculated using the viscoelastic contact model, with the experimental curves for the spherical asperities in column 5 in the case of a total load of 500 N and a rolling speed of 10 m/s. The time $t$ is multiplied by the rolling speed $V$ to represent the distance $d$ travelled during rolling.

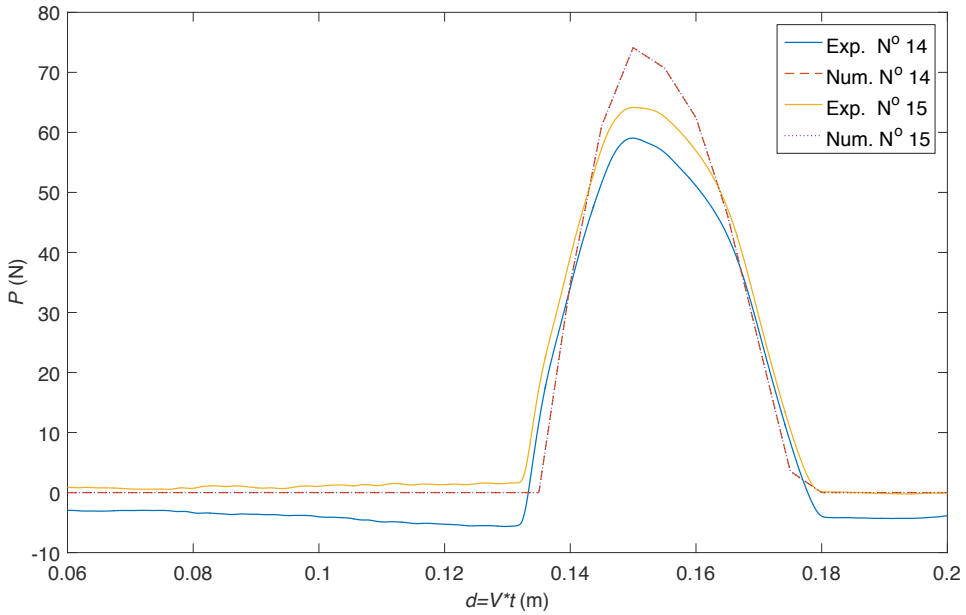


Figure 4.45 – Comparison of the contact force evolutions, calculated using the viscoelastic contact model, with the experimental curves for the spherical asperities in column 6 in the case of a total load of 500 N and a rolling speed of 10 m/s. The time $t$ is multiplied by the rolling speed $V$ to represent the distance $d$ travelled during rolling.

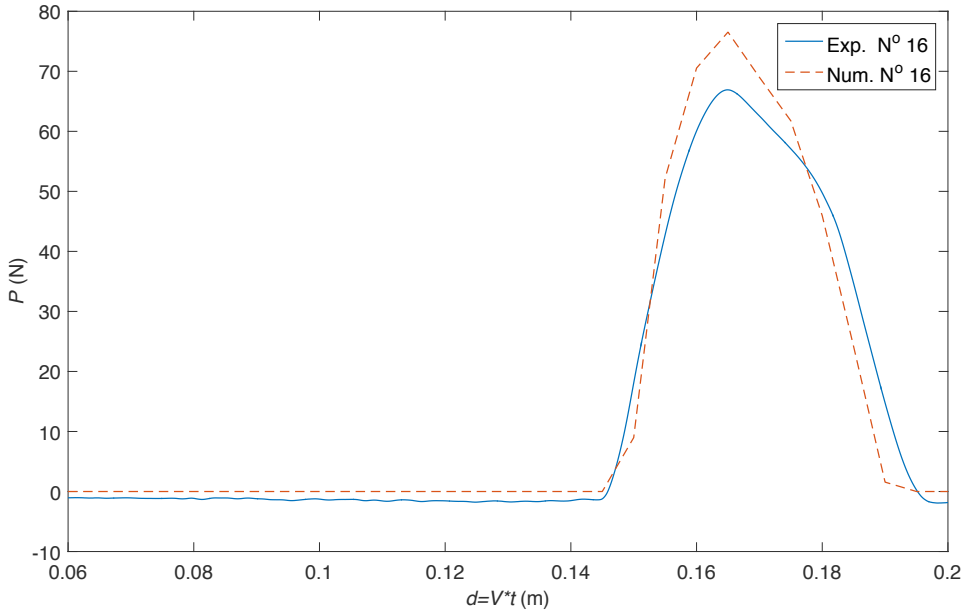


Figure 4.46 – Comparison of the contact force evolutions, calculated using the viscoelastic contact model, with the experimental curves for the spherical asperity in column 7 in the case of a total load of 500 N and a rolling speed of 10 m/s. The time $t$ is multiplied by the rolling speed $V$ to represent the distance $d$ travelled during rolling.

The contact pressure distributions are plotted for the instant of peak force occurrence in column 4 and an instant after the contact with the asperities, respectively in the left and the right of Figure 4.47. The contact patch has a higher pressure concentration in the leading part, which is in coherence with the results in the case of a single asperity and with experimental observations.

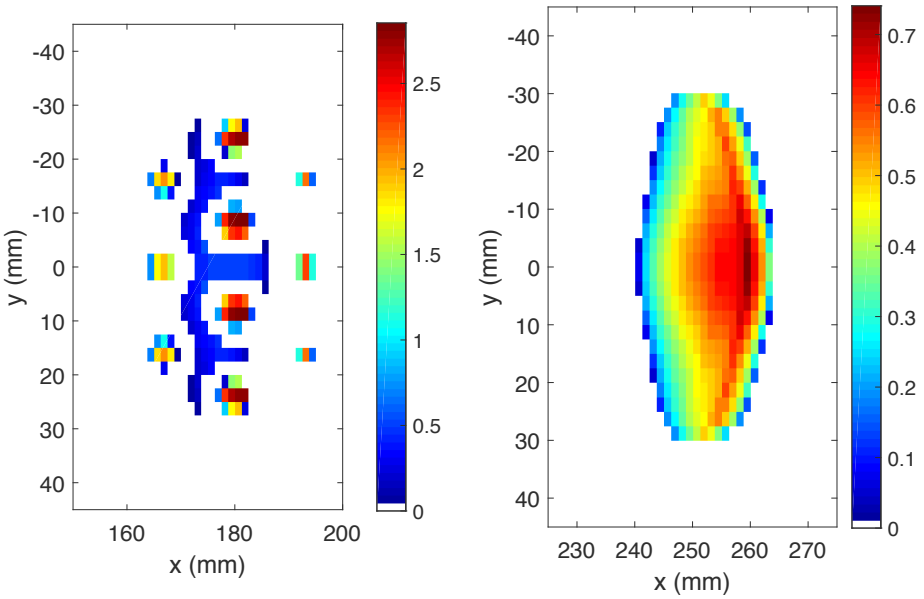


Figure 4.47 – Contact pressure distributions (in MPa) for (left) the instant of peak force occurrence in column 4 and (right) an instant after the contact with the asperities.

The dissymmetry is also visible from the numerical contact force evolution on all 16 spherical asperities plotted in Figures 4.48 with scaled colours representing the magnitudes of the forces. The corresponding experimental results are plotted in Figure 4.49 using the same colour axis scaling for comparison. The time is multiplied by each rolling speed to represent the rolling distance. The blue dashed lines represent the positions where the peak forces are reached for the asperities in column 4 in both figures. The distance axes are adjusted to have the two blue dashed lines appear at approximately the same position. The sidewall effect that is absent from the numerical model can be observed by comparing the contact force levels on asperities N$^o$ 7 to 10.

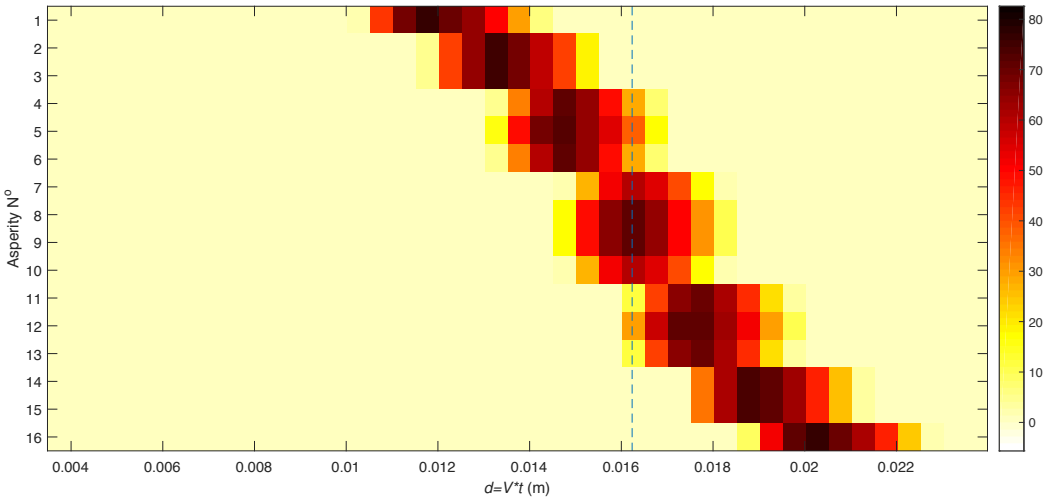


Figure 4.48 – Calculated evolution of the contact forces on all 16 spherical asperities with scaled colours representing the magnitudes of the forces. The total load is 500 N. The rolling speed is 10 m/s.

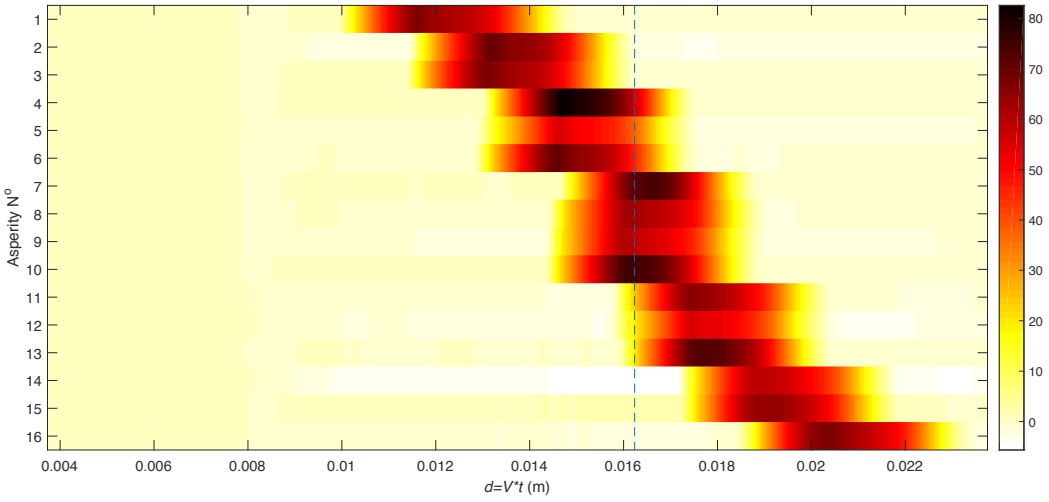


Figure 4.49 – Measured evolution of the contact forces on all 16 spherical asperities with scaled colours representing the magnitudes of the forces. The total load is 500 N. The rolling speed is 10 m/s.

The experimental and numerical contact forces on all 16 spherical asperities at the instants of peak force occurrence in column 3, 4 and 5 are respectively plotted in Figures 4.50, 4.51 and 4.52. Due to the negative forces that affect the peak force values and the abnormally high force level on certain asperities (e.g. N$^o$ 4) in the experimental results, the comparison is only qualitative. A general observation is that the comparison is better when the contact patch is less in contact with the asperities in column 4, especially N$^o$ 7 and 10 where the sidewall effect is most salient.

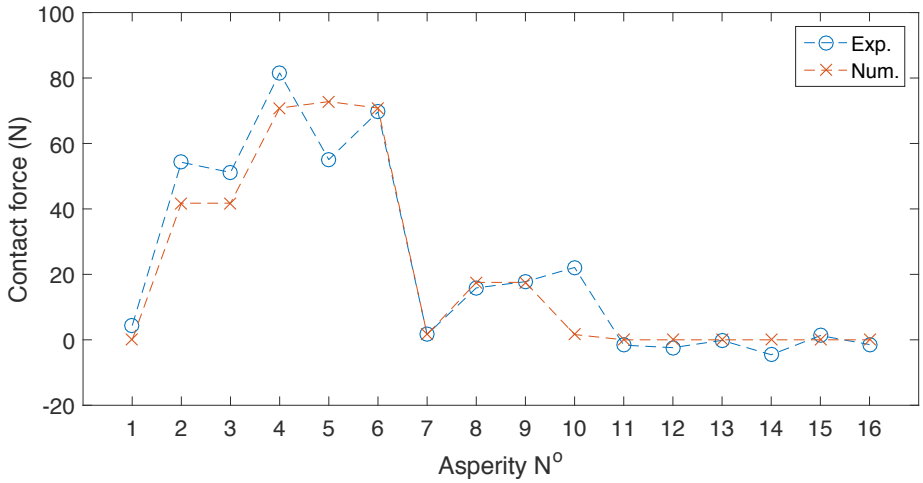


Figure 4.50 – Comparison of the calculated and the measured contact forces on all 16 spherical asperities at the instant of peak force occurrence in column 3.

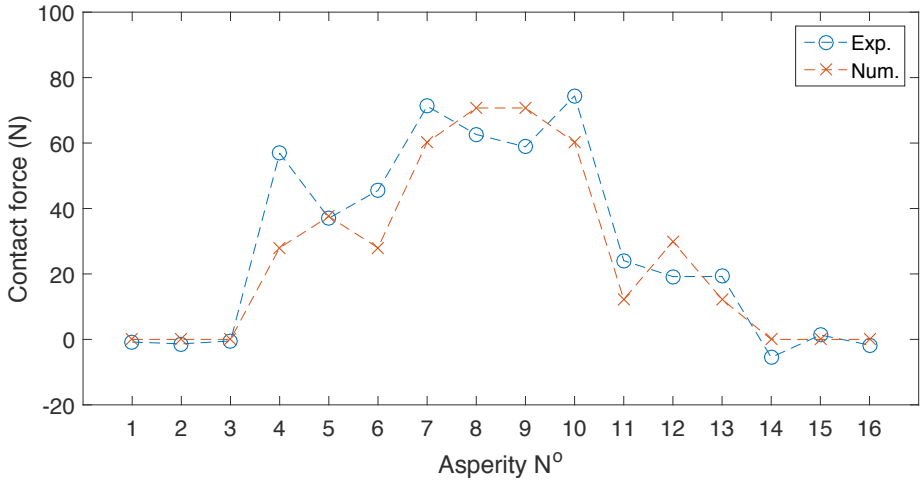


Figure 4.51 – Comparison of the calculated and the measured contact forces on all 16 spherical asperities at the instant of peak force occurrence in column 4.

## 4.5 Conclusions

This chapter deals with the investigations of dynamic contact forces between the reduced-sized tyre and multiple asperities. Measurements of the asperity geometries show that all the spherical or conical asperities are fabricated with good precision and have very similar geometric

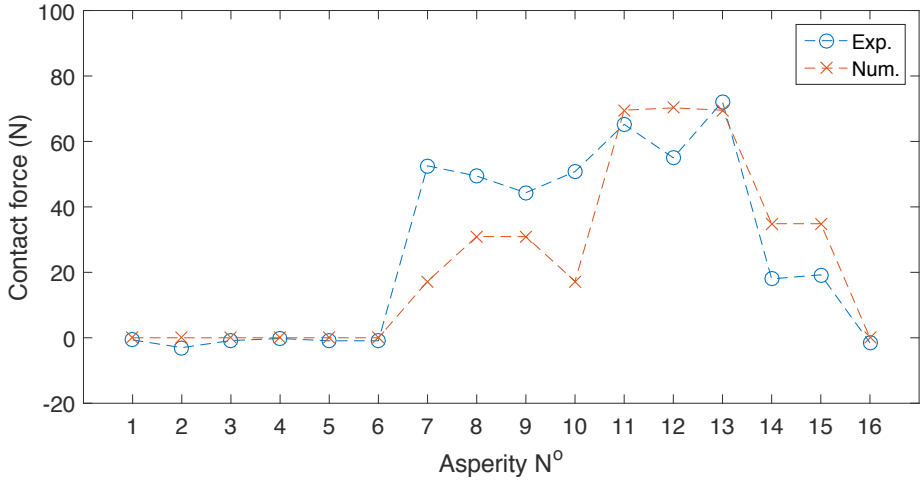


Figure 4.52 – Comparison of the calculated and the measured contact forces on all 16 spherical asperities at the instant of peak force occurrence in column 5.

properties and relative heights. By comparing the measurement results for the same configuration but obtained on three different days, the repeatability of the tests is verified for each asperity.

Next, tests are performed to study how factors like the geometric shapes of indenter, the total load and the rolling speed affect the dynamic contact, in the case of multiple asperities. The influence of the geometric shapes of indenter is first studied through comparison of the time evolutions of the contact forces on all 16 spherical and 16 conical asperities of similar height and then through comparison of the contact force distributions at the instant of peak force occurrence in the central column. The spherical asperities are subjected to significantly higher contact forces than the conical ones. Analogous approaches are used to examine the influence of the total load. A higher load leads to a longer contact duration. However, the time required to reach the peak force on an asperity from the start of the contact is almost independent of the load. Therefore, the total load changes mainly the size of the trailing part of the contact patch. To compare the contact force evolutions due to different rolling speeds, the time is multiplied by the speed to represent the distance travelled by the tyre. The rolling speed, at least up to 15 m/s, does not have a significant influence on the contact. Therefore, the contact is of quasi-static nature. The modified spectra of all 16 spherical asperities further confirm this conclusion.

Finally, numerical models based on the elastic or viscoelastic half-space assumption have been assessed. With the same Young's moduli identified for static contact analyses in previous chapters, the elastic contact model predicts well the dimensions of the contact patch and the contact areas on the asperities under different total loads. However, the sidewall effect on the contact pressure distribution is not well represented by the elastic half-space model. A viscoelastic rolling contact model with the same material properties as in the case of a single asperity is used to provide numerical results for comparison with experimental ones. The predicted contact forces differ from the measurements at positions where there is a high contact pressure concentration. This is probably due to the absence of the sidewall effect in the numerical model and a limitation of the half-space assumption. Nevertheless, the dissymmetry of the time signal is well assessed with the viscoelastic approach, which is physically representative of the tyre/road contact interaction during rolling.

# Conclusions and outlooks

Dynamic rolling contact between the tyre and the road has a great influence on the vibrational and aerodynamic mechanisms at the origin of tyre/road noise. Researches within the framework of this thesis have been focussed on the experimental study of tyre/road contact in rolling conditions by means of a specific laboratory test rig developed at Ifsttar. The measurements performed in well-controlled conditions have been used to assess the reliability of existing contact models in simplified contact configurations.

In Chapter 1, a literature survey on existing numerical and experimental researches on contact for tyre/road noise prediction has been carried out. The dynamic contact models are mostly based on a quasi-static description of the contact. The tread of the tyre is often approached by an elastic half-space that allows taking into account the interaction between contact points. A multi-asperity decomposition of the road surface has been proposed at Ifsttar and requires knowledge of the local contact laws on each asperity. For static loading conditions, experimental studies have validated the half-space assumption for simplified configurations between a rubber pad and spherical asperities. Static contact footprints between a pneumatic tyre and different rough surfaces have also been used to estimate the accuracy of the multi-asperity approach. In addition, measurements of dynamic contact forces on a test track, more difficult to achieve, showed a decrease of about 20% in contact area when rolling. This was attributed to the viscoelasticity of the rubber components of the tyre. However, these tests did not clearly demonstrate the quasi-static nature of the contact. Therefore, the simplifying assumptions of the dynamic contact model still remain to be validated experimentally. To this end, a special test rig was developed at Ifsttar to perform measurements under controlled conditions. Using this equipment, the objectives of the thesis have been focussed firstly on the study of the influence of the rolling speed on the dynamic contact forces and secondly on the study of the interaction between asperities and the distribution of dynamic contact forces in rolling conditions.

Chapter 2 has involved the characterisation of the vibrational and contact behaviours of the reduced-sized tyre to be used on the aforementioned test rig. Modal tests have been carried out, leading to the extraction of 8 modal frequencies between 280 and 1200 Hz and the corresponding damping ratios. A simplified FE tyre model was built to first simulate the vibrational nature of the tyre. By treating the tyre as elastic and homogeneous and by calibrating a Young's modulus, this model yielded modal frequencies that were in agreement with the experiment. However, the size of the numerical contact patch obtained was too small in the rolling direction. Thus, a more sophisticated model, taking into account the inner structure of the tyre and the properties of the different materials used in the tyre, including the measured viscoelasticity of the rubber, has been proposed. The new model offers a good compromise between the modal frequencies and the contact patch. The MIM, based on elastic half-space assumption, has also been used to predict the contact in static conditions between the tyre and the rolling surface on the test rig. The numerical model is time-efficient as the contact symmetries have been exploited. Real

contact patches have been measured using Fuji pressure-sensitive film. After adjusting the elastic Young's modulus for each configuration, the numerical model yields static contact patches of similar shapes and dimensions to the measured ones. Meanwhile, it provides lesser accuracy in terms of contact pressure distribution for high loads, which could be due to the oversimplifying elastic half-space assumption and the underestimation of the sidewall effect. Contact patches have also been measured for different contact configurations to study the influences of factors such as the curvature of the test rig, the total load, the rolling speed and the consequent change in temperature at the tyre surface.

Chapter 3 has dealt with the investigations of dynamic contact forces between the reduced-sized tyre and a single asperity of spherical or conical shape. The repeatability of the tests was checked for the whole range of relative heights of the asperity. Experimental results have been presented by focussing on different parameters. First, the influence of the geometry of the asperity on the dynamic contact force has been studied. At equivalent height, the contact force on the sphere is larger than on the cone but the shape of time signals is very similar and contact durations are very close. The relationship between the maximum contact force and the relative height of the asperity has been studied for both geometries and is consistent with Boussinesq's theory. The influence of the total load on the dynamic contact force has also been studied. The maximum amplitude of the force decreases when the load increases, while the contact time decreases with the load, which is consistent with the contact prints measured statically. Finally, the influence of the rolling speed on the contact force has been analysed. It appears that the contact duration is inversely proportional to the speed and that the spectra at different speeds, modified in frequency, coincide up to 350 Hz. These results illustrate the quasi-static nature of the dynamic contact on a single asperity. Finally, numerical models based on the elastic or viscoelastic half-space assumption have been compared with experimental results. For the elastic contact model, with a carefully calibrated Young's modulus, the calculated peak contact forces are in good agreement with measurements for high asperity position. However, the sidewall effect on the pressure distribution is not well represented. Quasi-static calculations of the contact force evolution show that the dissymmetry in the experimental curves is absent in the results from the elastic model. Consequently, a viscoelastic rolling contact model has been formulated, and numerical results have been obtained by using a Zener constitutive model. The model is most accurate for weak total loads and high asperity positions. Possible ways to improve the accuracy are to use the measured Prony series instead of a Zener model and/or to take into account the hyperelasticity and the sidewall effect in the model.

In Chapter 4, the dynamic contact force between the reduced-sized tyre and multiple asperities of spherical or conical shape has been investigated. The asperities are all identical and located at the same relative height. The repeatability of the tests has been checked for the full set of asperities. The influences of different parameters have been studied experimentally. First, the influence of the geometry of the asperities on the contact forces has been examined, through comparison of the time evolutions of the contact forces on all 16 spherical and 16 conical asperities and also through comparison of the contact force distributions at the instant of peak force occurrence on a set of asperities with common positions. The contact forces on the spherical asperities are significantly higher than on the conical ones located at the same positions. Analogous approaches have been used to study the influence of the total load. Similar to the case of a single asperity, the contact duration increases with the total load. The contact forces on the asperities change in a dissymmetric manner in time. Nevertheless, the time necessary to reach the peak force from the start of contact with an asperity is almost constant, irrespective of the load. Therefore, the load affects rather the length of the trailing part of the contact patch. Finally, the influence of the rolling speed, up to 15 m/s, has been investigated for the full set of spherical asperities. Both the evolution of the contact force as a function of the distance travelled by the tyre and the modified spectra of

the resultant contact forces approve the quasi-static nature of the contact. The measurements also provided elements for assessing numerical models based on the elastic or viscoelastic half-space assumption in the case of multiple asperities. With the same Young's moduli calibrated in Chapter 3, the elastic contact model estimates quite well the dimensions of the contact patch and the contact areas on the asperities under different loads. Finally, a viscoelastic rolling contact model has been configured with the same material properties calibrated in the case of a single asperity. The numerical results are in better agreement with the experimental ones at positions where there is less interaction with the high contact pressure concentration on the borders of the contact patch. The discrepancies may be due to the absence of the sidewall effect in the model and a limitation of the half-space assumption. Nevertheless, the dissymmetry of the time signal is well assessed with the viscoelastic approach, which is physically representative of the tyre/road contact interaction during rolling.

Considering the work that has been performed during the thesis, the following aspects could be further investigated to improve the dynamic contact model:

- use the finite-element model of the reduced-sized tyre for calculating the influence matrix used in contact calculation in replacement of the analytical matrix based on half-space assumption;
- use a creep function based on the generalised Kelvin model instead of the Zener model to improve the description of viscoelasticity in the model and improve the agreement between the calculated and measured time signals;
- perform measurements on the test rig for single and multiple asperities of random shapes to validate the multi-asperity approach for actual road surfaces;
- scale laboratory results in simplified configurations to realistic conditions.

Furthermore, the test rig opens several outlooks within the field of tyre/road interaction, among which are investigation of air-pumping mechanisms in simplified configurations, measurement of noise or rolling resistance in laboratory for calibrating prediction tools, academic research for acoustical optimisation of road surface properties.

# Bibliography


P. Andersson and K. Larsson. Validation of a high frequency three-dimensional tyre model. *Acta acustica united with acustica*, 91(1):121–131, 2005.

P. Andersson, K. Larsson, F. Wullens, and W. Kropp. High frequency dynamic behaviour of smooth and patterned passenger car tyres. *Acta Acustica united with Acustica*, 90(3):445–456, 2004.

P.B.U. Andersson and W. Kropp. Time domain contact model for tyre/road interaction including nonlinear contact stiffness due to small-scale roughness. *Journal of Sound and Vibration*, 318 (1):296–312, 2008.

T. Beckenbauer, P. Klein, J.-F. Hamet, and W. Kropp. Tyre-road noise prediction: A comparison between the speron and hyrone models-part 1. *Journal of the Acoustical Society of America*, 123(5):3388–3388, 2008.

H.C. Booij and G.P.J.M. Thoone. Generalization of Kramers-Kronig transforms and some approximations of relations between viscoelastic quantities. *Rheologica Acta*, 21(1):15–24, jan 1982.

J. Boussinesq. *Application des potentiels à l'étude de l'équilibre et du mouvement des solides élastiques*. Gauthier-Villars, 1885.

Q.-H. Bui. *Étude numérique de l'influence de la texture de chaussée sur la résistance au roulement*. PhD thesis, École des Ponts ParisTech, 2014.

J. Cesbron. *Influence de la texture de chaussée sur le bruit de contact pneumatique/chaussée*. PhD thesis, École Centrale de Nantes - Université de Nantes, 2007.

J. Cesbron and H.P. Yin. Contact analysis of road aggregate with friction using a direct numerical method. *Wear*, 268(5-6):686–692, 2010.

J. Cesbron, F. Anfosso-Lédée, D. Duhamel, H.P. Yin, and D. Le Houédec. Prediction of contact stresses for tyre/road noise modelling. In *Proceedings of Euronoise 2006*, Tampere, Finland, 2006.

J. Cesbron, F. Anfosso-Lédée, H.P. Yin, D. Duhamel, and D. Le Houédec. Influence of road texture on tyre/road contact in static conditions. *Road Materials and Pavement Design*, 9(4):689–710, 2008.

J. Cesbron, F. Anfosso-Lédée, D. Duhamel, H.P. Yin, and D. Le Houédec. Experimental study of tyre/road contact forces in rolling conditions for noise prediction. *Journal of sound and vibration*, 320(1):125–144, 2009a.

J. Cesbron, H.P. Yin, F. Anfosso-Lédée, D. Duhamel, D. Le Houédec, and Z.Q. Feng. Numerical and experimental study of multi-contact on an elastic half-space. *International Journal of Mechanical Sciences*, 51(1):33–40, 2009b.

J. Cesbron, G. Dubois, F. Anfosso-Lédée, and H.P. Yin. Tyre/road noise: Influence of multi-asperity road surface properties on tyre-road contact stresses. *Noise Control Engineering Journal*, 61(4):400–406, 2013.

E. Chailleux, G. Ramond, C. Such, and C. de La Roche. A mathematical-based master-curve construction method applied to complex modulus of bituminous materials. *Road Materials and Pavement Design*, 7(sup1):75–92, jan 2006.

E. Chailleux, C. de La Roche, and J.-M. Piau. Modeling of complex modulus of bituminous mixtures measured in tension/compression to estimate secant modulus in indirect tensile test. *Mater Struct*, 44(3):641–657, sep 2010.

R. Christensen. *Theory of viscoelasticity: an introduction*. Elsevier, 2012.

T.G. Clapp, A.C. Eberhardt, and C.T. Kelley. Development and validation of a method for approximating road surface texture-induced contact pressure in tire-pavement interaction. *Tire Science and Technology*, 16(1):2–17, 1988.

Dassault Systèmes. Abaqus 6.14 online documentation, 2014.

G. Dubois. *Modèle de contact dynamique pneumatique chaussée par approche multi-aspérités : application au bruit de roulement*. PhD thesis, Ecole Centrale de Nantes - ECN, 2012.

G. Dubois, J. Cesbron, H.P. Yin, and F. Anfosso-Lédée. Macro-scale approach for rough frictionless multi-indentation on a viscoelastic half-space. *Wear*, 272(1):69–78, 2011.

G. Dubois, J. Cesbron, H.P. Yin, and F. Anfosso-Lédée. Numerical evaluation of tyre/road contact pressures using a multi-asperity approach. *International Journal of Mechanical Sciences*, 54 (1):84–94, 2012.

G. Dubois, J. Cesbron, H.P. Yin, F. Anfosso-Lédée, and D. Duhamel. Statistical estimation of low frequency tyre/road noise from numerical contact forces. *Applied Acoustics*, 74(9):1085–1093, 2013.

EEA. Noise in Europe 2014. Technical report, European Environment Agency, 2014.

D.J. Ewins. *Modal testing: theory, practice, and application*. Research Studies Press, sep 2000. ISBN 9780863802188.

L. Fritschi, L. Brown, R. Kim, D. Schwela, and S. Kephalopolous. *Burden of disease from environmental noise: Quantification of healthy years life lost in Europe*. World Health Organisation, 2011.

P. Gatti. *Applied structural and mechanical vibrations*. Informa UK Limited, feb 2014.

M.E. Gurtin and E. Sternberg. On the linear theory of viscoelasticity. *Archive for Rational Mechanics and Analysis*, 11(1):291–356, 1962.

J.-F. Hamet. Tire/road noise: time domain green's function for the orthotropic plate model. *Acta Acustica united with Acustica*, 87(4):470–474, 2001.

J.-F. Hamet and M. Bérengier. Acoustical characteristics of porous pavements: a new phenomenological model. In *Proceedings of Inter-Noise 1993*, Leuven, Belgium, 1993.

H. Hertz. Über die Berührung fester elastischer Körper. *Journal für die reine und angewandte Mathematik*, 92:156–171, 1882.

K. Iwao and I. Yamazaki. A study on the mechanism of tire/road noise. *JSAE review*, 17(2): 139–144, 1996.

K.L. Johnson. *Contact Mechanics*. Cambridge University Press (CUP), 1985.

J.J. Kalker. *Three-dimensional elastic bodies in rolling contact*, volume 2. Springer Science & Business Media, 2013.

P. Kindt, P. Sas, W. Desmet, and F. De Coninck. Experimental modal analysis of radial tires under different boundary conditions. In *Proceedings of the 2006 International Congress on Sound and Vibration*, page 223, jul 2006.

P. Kindt, D. Berckmans, F. De Coninck, P. Sas, and W. Desmet. Experimental analysis of the structure-borne tyre/road noise due to road discontinuities. *Mechanical Systems and Signal Processing*, 23(8):2557–2574, 2009a.

P. Kindt, P. Sas, and W. Desmet. Measurement and analysis of rolling tire vibrations. *Optics and Lasers in Engineering*, 47(3):443–453, 2009b.

P. Klein and J.-F. Hamet. Road texture and rolling noise: an envelopment procedure for tire-road contact. Technical report, 2004.

I. Kozhevnikov, D. Duhamel, H.P. Yin, J. Cesbron, and F. Anfosso-Lédée. A new algorithm for computing the indentation of a rigid body of arbitrary shape on a viscoelastic half-space. *International Journal of Mechanical Sciences*, 50(7):1194–1202, 2008.

I.F. Kozhevnikov, D. Duhamel, H.P. Yin, and Z.Q. Feng. A new algorithm for solving the multi-indentation problem of rigid bodies of arbitrary shapes on a viscoelastic half-space. *International Journal of Mechanical Sciences*, 52(3):399–409, 2010.

W. Kropp. *Ein Modell zur Beschreibung des Rollgeräusches eines unprofilierten Gürtelreifens auf rauher Straßenoberfläche*. PhD thesis, T. U. Berlin, 1992.

W. Kropp, K. Larsson, F. Wullens, P. Andersson, F.-X. Bécot, and T. Beckenbauer. The modelling of tyre/road noise - a quasi three-dimensional model. In *Proceedings of the 2001 International Congress and Exhibition on Noise Control Engineering*, The Hague, The Netherlands, 2001.

W. Kropp, P. Sabiniarz, H. Brick, and T. Beckenbauer. On the sound radiation of a rolling tyre. *Journal of Sound and Vibration*, 331(8):1789–1805, 2012.

A. Kuijpers and G. van Blokland. Tyre/road noise models in the last two decades: a critical evaluation. In *Proceedings of the 2001 International Congress and Exhibition on Noise Control Engineering*, The Hague, The Netherlands, 2001.

L.E. Kung, W. Soedel, T.Y. Yang, and L.T. Charek. Natural frequencies and mode shapes of an automotive tire with interpretation and classification using 3-D computer graphics. *Journal of Sound and Vibration*, 102(3):329–346, October 1985. ISSN 0022-460X.

K. Larsson and W. Kropp. A high-frequency three-dimensional tyre model based on two coupled elastic layers. *Journal of sound and vibration*, 253(4):889–908, 2002.

F. Liu, M.P.F. Sutcliffe, and W.R. Graham. Prediction of tread block forces for a free-rolling tyre in contact with a rough road. *Wear*, 282:1–11, 2012.

A.E.H. Love. The stress produced in a semi-infinite solid by pressure on part of the boundary. *Philosophical Transactions of the Royal Society of London. Series A, Containing Papers of a Mathematical or Physical Character*, 228:377–420, 1929.

A.E.H. Love. Boussinesq's problem for a rigid cone. *The Quarterly Journal of Mathematics*, (1): 161–175, 1939.

A.E.H. Love. *A treatise on the mathematical theory of elasticity*, volume 1. Cambridge University Press, 2013.

R. Meftah. *Une approche par formalisme de green réduit pour le calcul des structures en contact dynamique : application au contact pneumatique/chaussée*. PhD thesis, École des Ponts ParisTech, 2011.

R. Meftah, D. Duhamel, J. Cesbron, and H.P. Yin. Une méthode rapide pour calculer un produit de convolution avec une fonction de green : application au problème de contact dynamique. In *CSMA 2011, 10e Colloque National en Calcul des Structures*, Presqu'île de Giens, France, 2011.

J. Périsse. A study of radial vibrations of a rolling tyre for tyre-road noise characterisation. *Mechanical Systems and Signal Processing*, 16(6):1043–1058, 2002.

J.R.M. Radok. Visco-elastic stress analysis. *Quarterly of Applied Mathematics*, 15(2):198–202, 1957.

A. Sameur. *Modèle de contact pneumatique/chaussée pour la prévision du bruit de roulement*. PhD thesis, École des Ponts ParisTech, 2004.

U. Sandberg. Tyre/road noise - myths and realities. In *Proceedings of the 2001 International Congress and Exhibition on Noise Control Engineering*, The Hague, The Netherlands, 2001.

I.N. Sneddon. The relation between load and penetration in the axisymmetric boussinesq problem for a punch of arbitrary profile. *International Journal of Engineering Science*, 3(1):47–57, 1965.

L. Vincent and P. Soille. Watersheds in digital spaces: an efficient algorithm based on immersion simulations. *IEEE transactions on pattern analysis and machine intelligence*, 13(6):583–598, 1991.

A. von Meier, G. van Blockland, and G. Descornet. The influence of texture and sound absorption on the noise of porous road surfaces. In *Proceedings of Second International Symposium on Road Surface Characteristics*, Berlin, Germany, 1992.

J. Winroth, P.B.U. Andersson, and W. Kropp. Importance of tread inertia and damping on the tyre/road contact stiffness. *Journal of Sound and Vibration*, 333(21):5378–5385, 2014.

F. Wullens. Modelling of the local deformation at the tyre/road contact for the prediction of forced tyre vibrations and air pumping. In *Proceedigns of Euronoise 2003*, Naples, Italy, 2003.

F. Wullens and W. Kropp. A three-dimensional contact model for tyre/road interaction in rolling conditions. *Acta Acustica united with Acustica*, 90(4):702–711, 2004.

F. Wullens and W. Kropp. Wave content of the vibration field of a rolling tyre. *Acta acustica united with acustica*, 93(1):48–56, 2007.

H.P. Yin, J. Cesbron, and Q.H. Bui. A new formulation for solving 3-d time dependent rolling contact problems of a rigid body on a viscoelastic half-space. *Mechanics Research Communications*, 64:8–14, 2015.

# Appendix A

# Validation of the optimised MIM in the case of a spherical indenter

The essential idea of the MIM goes as follows. The Boussinesq problem at $\Sigma$, the surface of the half-space, is governed by the following relationships:

$$\forall M \in \Sigma, \quad u(M) = \int_{\Sigma} T(M,S)p(S)d\Sigma\,, \tag{A.1a}$$

$$\forall (M(x,y), S(x',y')) \in \Sigma^2, \quad T(M,S) = \frac{1-\nu^2}{\pi E \sqrt{(x-x')^2 + (y-y')^2}}\,, \tag{A.1b}$$

where $u$ is the displacement at the surface of the half-space, $p$ is the normal contact pressure and $T$ is the Boussinesq's influence function with $E$ the Young's modulus and $\nu$ the Poisson's coefficient of the half-space. The points within the contact area should satisfy Equation (A.2a); those outside, Equation (A.2b):

$$\forall M \in \Sigma_c\,, \quad g(M) = 0 \quad \text{and} \quad p(M) > 0\,, \quad \text{Contact} \tag{A.2a}$$

$$\forall M \in \bar{\Sigma}_c\,, \quad g(M) > 0 \quad \text{and} \quad p(M) = 0\,, \quad \text{Separation} \tag{A.2b}$$

where $\Sigma_c$ is the contact area and $\bar{\Sigma}_c$ is the non-contact area ($\Sigma = \Sigma_c \cup \bar{\Sigma}_c$ and $\Sigma_c \cap \bar{\Sigma}_c = \emptyset$). $g(M) = u(M) + \tilde{g}(M)$ is the gap function with $\tilde{g}(M) = \delta + z_t(M) - z_r(M)$ where $\delta$ is the global penetration between the contacting bodies, $z_r$ describes the height of the road surface and $z_t$ the height of the tyre. Commonly, the total load $P$ applied to the tyre is specified which provides the additional equilibrium equation:

$$-P = \int_{\Sigma} p(S)d\Sigma\,. \tag{A.3}$$

The surface of the half-space is meshed into $n$ identical rectangular pressure elements of dimensions $h_x$ by $h_y$ and centred around points $M_i$ ($i \in [1,n]$) of coordinates $(x_i, y_i)$. On each element $i$, the normal displacement denoted by $u(M_i) = u_i$ and the normal contact pressure $p(M_i) = p_i$ are assumed constant. Thus, Equation (A.1a) is rewritten in a matrix form:

$$\mathbf{Ap} = \mathbf{b}\,, \tag{A.4}$$

where $\mathbf{A}$ is the influence matrix in which any element $A_{ij}$ is calculated as follows:

$$\forall (i,j) \in [1,n]^2\,,\ A_{ij} = \int_{y_j - h_y/2}^{y_j + h_y/2} \int_{x_j - h_x/2}^{x_j + h_x/2} T(x_i, y_i; \xi, \eta) d\xi d\eta\,. \tag{A.5}$$

By integrating Equation (A.5), Equation (A.6) obtains.

$$A_{ij} = \frac{(1-\nu)}{2\pi G}[F(u_2, v_2) - F(u_1, v_2) - F(u_2, v_1) + F(u_1, v_1)]\,, \tag{A.6}$$

where $F(u,v)$ and $u_1$, $u_2$, $v_1$, $v_2$ are given by:

$$F(u,v) = v\ln(u + \sqrt{u^2+v^2}) + u\ln(v + \sqrt{u^2+v^2})\,, \tag{A.7a}$$
$$u_1 = x_j - h_x/2 - x_i\,, \tag{A.7b}$$
$$u_2 = x_j + h_x/2 - x_i\,, \tag{A.7c}$$
$$v_1 = y_j - h_y/2 - y_i\,, \tag{A.7d}$$
$$v_2 = y_j + h_y/2 - y_i\,. \tag{A.7e}$$
$$\tag{A.7f}$$

Combining Equations (A.3) and (A.5) results in Equation (A.8) expressed in matrix form. Equation (A.8) is solved by means of an iterative algorithm in order to satisfy the contact conditions. The contact area is overestimated in the first instance. Matrix $\mathbf{A}$ is inverted in each iteration to compute the contact pressure distribution. After each iteration, the negative pressures are replaced by zero. The procedure goes on until all the elements within the contact area calculated have positive pressure.

$$\begin{pmatrix} A_{11} & \cdots & A_{1n} & 1 \\ \vdots & \ddots & \vdots & \vdots \\ A_{n1} & \cdots & A_{nn} & 1 \\ 1 & \cdots & 1 & 0 \end{pmatrix} \begin{Bmatrix} p_1 \\ \vdots \\ p_n \\ \delta \end{Bmatrix} = \begin{Bmatrix} z_{r,1} - z_{t,1} \\ \vdots \\ z_{r,n} - z_{t,n} \\ \frac{-P}{h_x h_y} \end{Bmatrix} \tag{A.8}$$

To check the validity of the optimised MIM proposed in Subsection 2.3.3, this method is used to solve the contact problem in a special case where a perfect elastic half-space is in contact with a rigid spherical indenter. The Young's modulus $E$ of the half-space is chosen to be 5 MPa, the Poisson's ratio $\nu$ 0.5. The indenter is a hemisphere with a radius R of 7.5 mm. The optimised MIM reduces the memory usage during processing, thus allows a much finer mesh grid of the contact surface. In the present contact problem, the dimensions $h_x$ and $h_y$ of the mesh elements are both 0.5 mm. Figure A.1 shows the contact pressure distribution over one quarter of the contact surface between an elastic half-space and a rigid spherical indenter. The fine mesh grid leads to a good resolution in terms of contact pressure, revealing the roundness of the contact area contour. Two aspects are considered in the comparison of the semi-analytical results with classical theoretical solutions given by Hertz [1882] and Sneddon [1965]: the relationship between the contact force $P$

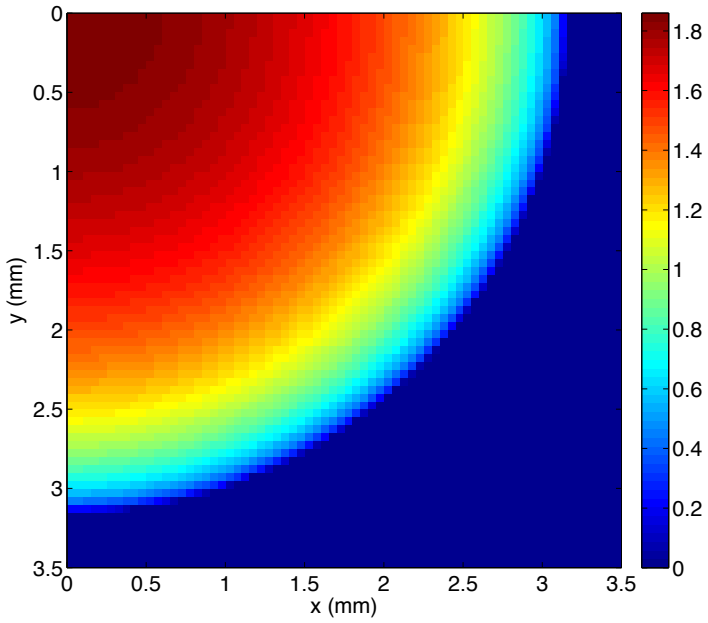


Figure A.1 – Contact pressure distribution (in MPa) over one quarter of the contact surface between an elastic half-space and a rigid spherical indenter.

and the indentation depth $\delta$ and the evolution of the contact pressure $p$ along the radial direction in the base plane of the indenter.

The contact law based on the Hertzian non-adhesive contact theory for a paraboloidal indenter is as follows:

$$P = \frac{4}{3} E^* R^{\frac{1}{2}} \delta^{\frac{3}{2}} , \tag{A.9}$$

where the effective elastic modulus $E^* = E/(1-\nu^2)$.

Sneddon proposed a solution in the case of spherical indenters:

$$P = \frac{1}{2} E^* \left( (a^2 + R^2) \ln\left(\frac{R+a}{R-a}\right) - 2aR \right) , \tag{A.10}$$

where $a$ denotes the radius of the contact area. The indentation depth $\delta$ is expressed in terms of $a$ and $R$:

$$\delta = \frac{1}{2} a \ln\left(\frac{R+a}{R-a}\right) . \tag{A.11}$$

The three contact laws are plotted in Figure A.2. Globally, all the three solutions are in very good agreement with each other. The Hertzian solution start to diverge from the other two from $\delta \approx$ 1.2 mm which corresponds to 1.6 times the sphere radius. The solution proposed by Sneddon still holds beyond this depth because it gives a better approximation of the deformed surface geometry of the elastic half-space.

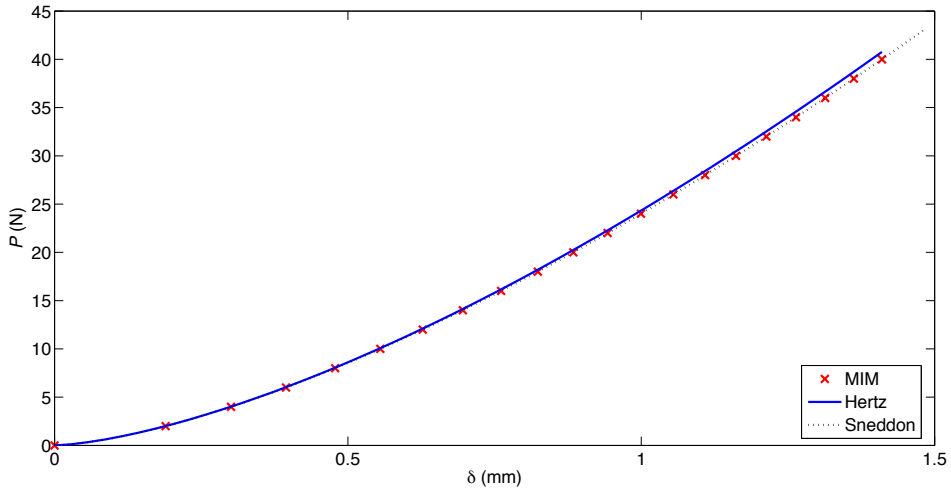


Figure A.2 – Contact law between an elastic half-space and a rigid spherical indenter calculated using the optimised MIM compared with classical solutions given by Hertz and Sneddon.

UNIVERSITE BRETAGNE LOIRE

Centrale Nantes

# Thèse de Doctorat

Yuanfang ZHANG

## Titre de la thèse : Étude sur banc d'essai des forces de contact dynamique pneumatique/chaussée à l'origine du bruit de roulement

## Title of thesis: Study on a test rig of dynamic tyre/road contact forces at the origin of rolling noise

**Résumé**

Les modèles de contact dynamique pour le bruit de roulement reposent souvent sur une hypothèse quasi-statique et une approximation de massif semi-infini pour le pneu. L'objectif de la thèse est de vérifier ces hypothèses par la mesure de forces de contact sur un banc d'essai constitué d'un pneu lisse de taille réduite roulant sur un bâti cylindrique. Au préalable, l'analyse modale expérimentale du pneu permet d'identifier des modes propres de formes classiques. Bien qu'un modèle éléments finis basé sur une section de pneu homogène élastique donne des modes satisfaisants, une section hétérogène hyper-viscoélastique permet d'obtenir un bon compromis entre vibrations et contact statique. La force de contact dynamique lors du roulement du pneu sur une seule aspérité sphérique ou conique est ensuite mesurée. La relation entre la force maximale et la hauteur de l'aspérité est conforme aux lois de contact théoriques. La durée de contact sur l'aspérité est inversement proportionnelle à la vitesse. Les calculs de contact basés sur un massif semi-infini élastique permettent d'approcher correctement la force maximale mesurée pour les fortes hauteurs d'aspérités, mais pas pour les faibles. La dissymétrie du signal temporel de force est bien modélisée en introduisant la viscoélasticité dans le modèle. Les forces de contact dynamique mesurées entre le pneu et plusieurs aspérités de formes simples confirment les résultats précédents, démontrant dans l'ensemble la nature quasi-statique du contact roulant. Toutefois, les forces calculées sont sous-estimées sur les bords de l'aire de contact, montrant une limitation de l'hypothèse de massif semi-infini pour décrire la structure du pneu.

**Mots-clés**
Contact dynamique pneumatique/chaussée, analyse modale, viscoélasticité, mesures de forces de contact, contact roulant, banc d'essai pneumatique/chaussée, bruit de roulement

**Abstract**

The dynamic contact models for tyre/road noise are often based on a quasi-static assumption and a half-space approximation for the tyre. The aim of the thesis is to assess these assumptions by measuring contact forces on a test rig composed of a smooth reduced-sized tyre rolling on a cylindrical basis. Beforehand, the experimental modal analysis of the tyre allows the identification of eigenmodes of classical shapes. Although a finite element model based on a homogeneous elastic tyre section yields satisfactory modes, a hyper-viscoelastic heterogeneous section provides a good compromise between vibrations and static contact. The dynamic contact force on a single spherical or conical asperity during rolling of the tyre is then measured. The relationship between the maximum force and the height of the asperity is consistent with theoretical contact laws. The contact duration on the asperity is inversely proportional to the speed. The contact calculations based on an elastic half-space assumption lead to a proper estimation of the maximum force measured on high asperity heights, but not on low asperity heights. The dissymmetry of the force time signal is well modelled by introducing the viscoelasticity in the model. The dynamic contact forces measured between the tyre and several asperities of simple shapes confirm the previous results, demonstrating the quasi-static nature of the rolling contact. However, the calculated forces are underestimated at the edges of the contact area, showing a limitation of the half-space assumption to describe the tyre structure.

**Key Words**
Dynamic tyre/road contact, modal analysis, viscoelasticity, contact forces measurements, rolling contact, tyre/road test rig, tyre/road noise